ELECTRON CLOUD STUDIES FOR CERN PARTICLE ACCELERATORS AND SIMULATION CODE DEVELOPMENT

Doctoral Thesis by: Giovanni Iadarola

Università degli Studi di Napoli Federico II, Napoli, Italy
Dipartimento di Ingegneria Elettrica e Tecnologie dell'Informazione (DIETI)
Dottorato di Ricerca in Ingegneria Elettrica

Tutor: Prof. Giovanni Miano

CERN-THESIS-2014-047
23/05/2014

European Organization for Nuclear Research, Geneva, Switzerland
Beams Department, Accelerators and Beam Physics Group (BE-ABP)

Supervisor: Dr. Giovanni Rumolo

March 2014

Giovanni Iadarola: *Electron cloud studies for CERN particle accelerators and simulation code development,* © March 2014

Ai miei genitori, Lina e Nicola,
con amore e riconoscenza.

ACKNOWLEDGMENTS

It has been a great pleasure for me to do my PhD at CERN under the supervision of Giovanni Rumolo. I really want to thank Giovanni for proposing to me an extremely interesting project, for introducing me to the fascinating fields of accelerator physics and collective effects, for giving me the right guidelines and advices while granting me time, resources and freedom to develop my own ideas and proposals, for the day by day support and motivation, and just for the fun of working together.

I would also like to thank my University Tutor Prof. Giovanni Miano, for giving me the possibility of working in this interesting field, for sharing with me his deep knowledge on electromagnetism and computational physics, for the important advices and support he gave me during, and also before, this PhD.

It was also a great experience to work side by side with Hannes Bartosik. I am indebted to him for many invaluable discussions, for several contributions to this work, for all I learnt in the countless hours we spent together working in the control room and, most importantly, for his sincere friendship.

I would like to thank my Section Leader Elias Metral and many members of the HSC section for their important support and for discussions.

I also want to thank Gianluigi Arduini for sharing with us his great experience on electron cloud effects and for coordinating and supporting the electron cloud studies at the SPS and the LHC.

Important support for these studies also came from the LHC Injectors Upgrade (LIU) project. In particular I would like to thank the PS Upgrade Coordinator Simone Gilardoni and the SPS Upgrade Coordinator Brennan Goddard.

I had very fruitful discussions with Mauro Taborelli, on the subjects of Secondary Electron Emission and Electron Cloud Effects.

During the development of PyECLOUD I profited from important advice from Chandra Bhat, Octavio Dominguez, Kevin Li, Humberto Maury Cuna and Frank Zimmermann.

All the studies and machine experiments presented in this work would not have been possible without the help and support from several experts from the different CERN departments, for calculations, machine and measurements setup, data collection and post processing. In particular, there are some people I would like to mention explicitly.

For the LHC activities: J. Esteban Muller and Elena Shaposhnikova (bunch-by-bunch energy loss estimations from stable phase measurements); Laurent Tavian and Serge Claudet (heat load measurement from the cryogenic system); Vincent Baglin (vacuum observations); Federico Roncarolo and George Trad (BSRT measurements); Riccardo De Maria, Wolfgang Hofle and Daniel Valuch (beam position measurements); Danilo Banfi and Tatiana Pieloni (transverse emittance estimation from specific luminosity); Carlo Zannini (impedance heating estimations); Riccardo De Maria and Rogelio Tomas (optics and aperture information).

For the PS activities: Sergio Rioja Fuentelsaz (electron cloud measurements and simulations), Christina Yin Vallgren, Fritz Caspers and Edgar Mahner (shielded pickup measurements); Mauro Pivi and Guido Sterbini (transverse instability measurements); Heiko Damerau and Steven Hancock (RF setup and measurements).

For the SPS activities: Mounir Mensi, Holger Neupert and Mauro Taborelli (strip detectors and shielded pickup measurements); Leonid Kopylov and Mauro Taborelli (vacuum pressure measurements); Theodoros Argyropoulos, Thomas Bohl, Juan Esteban Muller, Christos Lazaridis, Elena Shaposhnikova, Helga Timko (RF setup and measurements), Ana Guerrero (wire scanner measurements).

Finally I would like to express my gratitude to the LHC and injectors operator crew for their fundamental support to the machine studies.

CONTENTS

INTRODUCTION 1

I MODELING AND SIMULATION OF ELECTRON CLOUD EFFECTS IN PARTICLE ACCELERATORS 5

1 ELECTRON CLOUD (EC) IN PARTICLE ACCELERATORS: BASIC CONCEPTS AND MECHANISMS 7
- 1.1 Primary electron production mechanisms . . . 8
- 1.2 Secondary electron emission . . . 9
  - 1.2.1 Scrubbing: SEY reduction with the electron dose . . . 11
- 1.3 The EC buildup mechanism . . . 12
- 1.4 Effects of externally applied magnetic fields . . . 19
- 1.5 Impact of EC effects on the accelerator's performances . . . 20

2 MODELING AND SIMULATION OF THE ELECTRON CLOUD BUILDUP WITH THE PYECLOUD CODE 23
- 2.1 PyECLOUD: overall structure . . . 23
- 2.2 Macroparticle size management . . . 24
- 2.3 The chamber module . . . 26
- 2.4 The beam . . . 27
- 2.5 Primary electrons: residual gas ionization . . . 30
- 2.6 Primary electrons: photoemission due to synchrotron radiation . . . 31
- 2.7 The space charge field of the EC . . . 32
- 2.8 Tracking of the electrons . . . 34
- 2.9 Impacts of the electrons on the chamber's wall . . . 38
- 2.10 Some considerations on the achieved simulation performances . . . 40

II ELECTRON CLOUD STUDIES AT THE LHC 43

3 THE LARGE HADRON COLLIDER (LHC) 45
- 3.1 Machine layout and beam properties . . . 46
- 3.2 Production of the LHC beam in the injector complex . . . 50

4 SIMULATION STUDIES FOR THE MAIN LHC ARC COMPONENTS 53
- 4.1 Dipole magnets . . . 53
- 4.2 Quadrupole magnets . . . 57
- 4.3 Relative contributions to heat loads . . . 60
- 4.4 Effect of bunch intensity . . . 61
- 4.5 Effect of bunch length in dipole magnets . . . 63
- 4.6 Effect of transverse size variation in dipole magnets . . . 65
- 4.7 Impact of the low energy part of the SEY curve . . . 69
- 4.8 Simulation studies for a doublet scrubbing beam in the LHC . . . 71

5 ELECTRON CLOUD OBSERVATIONS AND EXPERIMENTAL STUDIES AT THE LHC 75
- 5.1 EC observations and mitigation with beams with 50 ns and larger bunch spacing 75
- 5.2 EC observations and studies with beams with 25 ns spacing in 2011 . . . 79

5.2.1 Heat load measurements and reconstruction of the SEY evolution in the dipole chambers . . . 81
5.2.2 Beam observations: bunch by bunch energy loss . . . 84
5.2.3 Beam observations: transverse instabilities . . . 88
5.2.4 Beam observations: transverse emittance growth and particle losses . . . 92
5.3 EC observations and studies with beams with 25 ns spacing in 2012 . . . 95
5.3.1 Injection tests . . . 96
5.3.2 The scrubbing run with 25 ns beams: goals and strategy . . . 98
5.3.3 The scrubbing run with 25 ns beams: beam observations . . . 100
5.3.4 The scrubbing run with 25 ns beams: heat load evolution . . . 104
5.3.5 Heat load and beam energy loss during the energy ramp . . . 107
5.3.6 EC observations during the high energy stores . . . 111
5.3.7 Test fills at injection energy after high energy stores . . . 116
6 ELECTRON CLOUD EFFECTS IN COMMON CHAMBERS 121
6.1 The LHC Insertion Regions . . . 121
6.2 The inner triplets . . . 123
6.2.1 PyECLOUD simulation studies . . . 125
6.2.2 Machine observations . . . 128
6.2.3 Simulation studies for the High Luminosity Upgrade . . . 130
6.3 The 800 mm common chamber in IR2 . . . 135

III ELECTRON CLOUD STUDIES FOR THE LHC INJECTORS 139
7 ELECTRON CLOUD STUDIES FOR THE CERN PROTON SYNCHROTRON 141
7.1 PyECLOUD simulation studies . . . 143
7.2 Shielded pickup measurements . . . 146
7.2.1 Comparison against simulation . . . 148
7.3 Transverse instabilities . . . 149
7.4 Low EC RF voltage program . . . 151
8 ELECTRON CLOUD STUDIES FOR THE CERN SUPER PROTON SYNCHRONTRON (SPS) 153
8.1 PyECLOUD simulation studies . . . 153
8.2 Experimental studies: an overview . . . 158
8.3 Experimental studies: beam observations . . . 160
8.3.1 *Nominal* 25 ns LHC beam in the SPS . . . 160
8.3.2 *Ultimate* 25 ns LHC beam in the SPS - on the flat bottom . . . 163
8.3.3 Test with large bunch intensity and Q20 optics . . . 164
8.4 Experimental studies: vacuum observations . . . 166
8.4.1 Effect of the beam intensity . . . 166
8.4.2 Effect of losses . . . 169
8.4.3 Effect of the filling pattern . . . 173
8.5 Experimental studies: measurements with dedicated EC equipment . . . 173
8.5.1 Shielded pickup . . . 173
8.5.2 Strip detectors . . . 176
8.6 Doublet scrubbing beam . . . 184
SUMMARY AND CONCLUSIONS 187

BIBLIOGRAPHY 193

ACRONYMS

BCMS Batch Compression Merging and Splittings

BCT Beam Current Transformer

BLM Beam Loss Monitor

BPM Beam Position Monitor

BSRT Beam Synchrotron Radiation Telescope

CDF Cumulative Distribution Function

CoM Center of Mass

EC Electron Cloud

ECM Electron Cloud Monitor

EYTS End of Year Technical Stop

FBCT Fast Beam Current Transformer

FD Finite Difference

HL-LHC High Luminosity LHC

IP Interaction Point

IR Insertion Region

LIU LHC Injectors Upgrade

LHC Large Hadron Collider

LS1 Long Shutdown 1

MD Machine Development

MP MacroParticle

MKI LHC injection kicker

ppb protons per bunch

PIC Particle In Cell

PS Proton Synchrotron

PSB Proton Synchrotron Booster

RF Radio Frequency

SAM Stand Alone Module

SEY Secondary Electron Yield

SPS Super Proton Synchrotron

INTRODUCTION

In a particle accelerator free electrons in the beam chambers can be generated by different mechanisms like the ionization of the residual gas or the photoemission from the chamber's wall due to the synchrotron radiation emitted by the beam. The electromagnetic field of the beam can accelerate these electrons and project them onto the chamber's wall. According to their impact energy and to the Secondary Electron Yield (SEY) of the surface, secondary electrons can be generated. Especially when the accelerator is operated with closely spaced bunches of positively charged particles, this mechanism can drive an avalanche multiplication process of the electrons with the formation of a so called Electron Cloud (EC) in the chamber. The presence of a large electron density in the beam pipe as well as of a strong electron flux on the chamber's wall can limit the achievable performance of the accelerator through different effects like transverse instabilities, transverse emittance growth, particle losses, vacuum degradation and heating of the chamber's surface.

EC effects have been recognized among the major performance limitations for the Large Hadron Collider (LHC), presently the world's largest and most powerful particle accelerator and collider, built by the European Organization for Nuclear Research (CERN) in a 27 km underground tunnel across the Franco-Swiss border near Geneva, Switzerland.

EC effects were observed at the LHC during the first three years of beam operation (Run 1, 2010-2012), becoming more and more severe while moving to tighter bunch spacing. EC effects with 50 ns bunch spacing could be successfully mitigated through beam induced scrubbing (reduction of the SEY by means of electron bombardment) and this bunch spacing could be used for most of the integrated luminosity production with 7 - 8 TeV Center of Mass (CoM) energy in 2011-12. After the 2013-14 machine shutdown (LS1) the LHC will be able to run at 13-14 TeV CoM energy and it will be necessary to move to the design bunch spacing of 25 ns in order to reach the design luminosity within the pileup limits required by the LHC experiments. Up to now, the 25 ns beam has been used only for test purposes and EC effects proved to be significantly more severe compared to the 50 ns case.

The present thesis work addresses EC effects in the LHC and its injector accelerators chain in terms of both numerical simulations and machine experiments. Particular emphasis is put on beams with 25 ns bunch spacing.

In particular, the analysis of EC observations in the LHC and its injectors have raised new challenges for the EC build-up simulations. For a correct understanding of machine observations it is often necessary to deal with beams with thousands of bunches and with non-idealities like non-uniform bunch populations and bunch lengths along the beam. Beside the usual simulation scenarios of field free regions and dipole magnets, also more complex situations needed to be addressed, like the EC buildup in quadrupoles or combined function magnets and with two counter-rotating beams in the same chamber. Moreover, the demand for extensive parameter scans gave quite stringent requirements in terms of speed and reliability.

CERN's long experience in the EC build-up simulation, mostly carried out with the ECLOUD code, developed and maintained at CERN since 1997, proved instrumental to respond to the newly arisen needs. However, due to its non-modular structure and to the programming

language (FORTRAN 77), the existing ECLOUD code did not appear to be suitable to be extended to fulfill the aforementioned requirements. It was therefore decided to follow a different strategy and write a fully reorganized code, in a more modern and flexible language, considering that the initial effort would be compensated by a significantly increased efficiency in development and debugging.

The new code has been called PyECLOUD, since it is almost entirely written in Python and inherits the physical models of the ECLOUD code. During the development all the known issues of the ECLOUD code were addressed and new features were introduced, necessary to deal with the complex scenarios described above. Modifications on numerical model and implementation were introduced practically everywhere, and key modules of the code, i.e. the MacroParticle (MP) Size Management, the electron space charge evaluation, the MP tracker and the electron/wall interaction have been completely redesigned. The new code has been applied for a full characterization of the EC formation in the main LHC components (including those with the two counter-rotating beams in the same chamber) with respect to different to surface properties (SEY) and beam configurations.

In parallel with this modeling and simulation work, an intense experimental activity was carried out, which involved the LHC and the last two synchrotrons of its injector chain, i.e. the Proton Synchrotron (PS) and the Super Proton Synchrotron (SPS), and had three main goals:

1. The qualification of the EC formation in the three accelerators and of its impact on the quality of the proton beam;
2. The collection of experimental data for the validation and the improvement of our simulation models;
3. The definition and experimental validation of possible EC mitigation strategies.

As already stated before, at the LHC, EC effects represent the main limitation to the use of the nominal bunch spacing of 25 ns. Experiments with this type of beam took place for the first time in 2011 and more extensively towards the end of the 2012 run. The main goals were to investigate these limitations and to study the process of beam scrubbing as a possible mitigation for future operation. These tests included a 3.5 day scrubbing run at 450 GeV, few test ramps with 25 ns beams in order to study EC effect at high energy (4 TeV), and a pilot physics run with low emittance 25 ns beams. During this period it was possible to collect measurements on several EC observables, e. g. transverse positions for the first seconds after injection, heat load on the cryogenic sections, bunch by bunch intensity, transverse emittance and stable phase. The careful analysis of these data significantly improved our understanding on the EC buildup in the LHC and on its impact on machine performance and beam quality, both at injection and collision energy.

Concerning the LHC injectors, both at the PS and at the SPS, several "direct" e-cloud measurements could be collected under different beam conditions (bunch intensity, length, number and spacing) using dedicated devices installed in the rings. Moreover we could observe and qualify the impact of the EC on the vacuum pressure and on the quality of the beams in terms of transverse instabilities, beam losses, emittance growth. For the SPS, the possibility of preparing a dedicated beam for the EC mitigation through beam induced scrubbing has been studied. PyECLOUD simulations have been performed to compare different options and the most promising, the so-called "doublet" beam has been experimentally validated in the accelerator.

The thesis is organized in three parts. Part I introduces the main concepts and mechanisms involved in the EC formation and describes in detail our simulation model and its implementation in the PyECLOUD code. Part II addresses the EC effects in the LHC, covering both simulation and experimental studies, with a dedicated chapter focusing on EC effects in the common regions where the two beams share the same chamber. Finally Part III describes simulation and experimental studies on EC effects in the LHC injectors.

Part I

MODELING AND SIMULATION OF ELECTRON CLOUD EFFECTS IN PARTICLE ACCELERATORS

1

ELECTRON CLOUD (EC) IN PARTICLE ACCELERATORS: BASIC CONCEPTS AND MECHANISMS

Secondary electron emission in resonance with an alternating electric field can lead to avalanche electron multiplication. The underlying mechanism is called multipactor effect. Although desirable for some applications [1], it is usually associated with deleterious effects, such as voltage breakdown in radio frequency (RF) devices, outgassing, surface heating [2–4].

In the case of a particle accelerator operated with closely spaced bunches multipactor effects can occur in the beam chambers leading to the formation of so called Electron Clouds (ECs) with several negative effect on the machine performances [5–9]. EC effects have been observed in several accelerators all over the world, much more commonly in those operated with positively charged particles (e. g. positrons, protons, heavy ions), and are presently among the major performance limitations for high energy colliders, like the Relativistic Heavy Ion Collider (RHIC) in the USA [10], the KEKB electron positron collider in Japan [11], the DAΦNE electron positron collider in Italy [12] and, more recently, the CERN Large Hadron Collider (LHC) as it will be extensively discussed in this thesis.

A qualitative picture of the EC buildup at a section of an accelerator operated with bunches of positively charged particles is sketched in Fig. 1.1 (see also [13]). The circulating beam particles can produce electrons due to different mechanisms, e. g. ionization of the residual gas in the beam chamber or photoemission from the chamber's wall due to the synchrotron radiation emitted by the beam. These are called "primary or seed electrons". Seeds are attracted by the passing particle bunch and can be accelerated to energies up to several hundreds of eV. When an electron with this energy impacts the wall, "secondary electrons" are likely to be emitted. The secondaries have energies up to few tens of eV and, if they impact the wall with these energies, they are either absorbed or elastically reflected but cannot produce any sec-

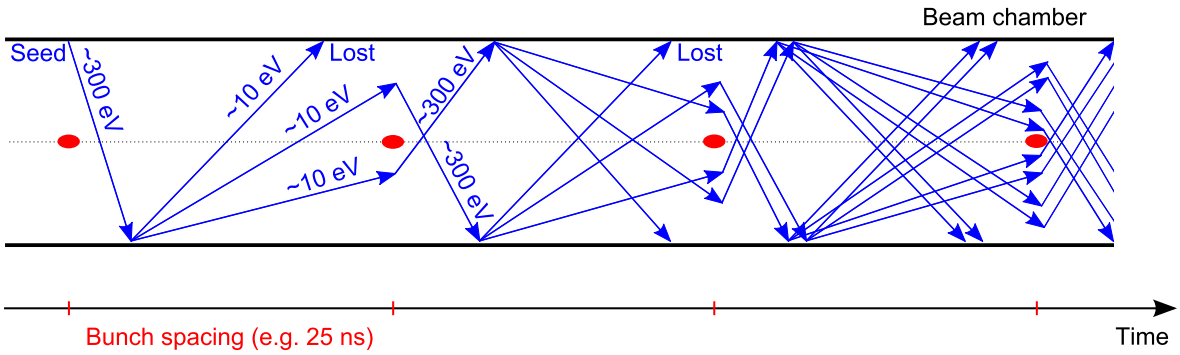

Figure 1.1: Schematic of the formation of an electron cloud in a particle accelerator (a similar sketch can be found in [13]).

ondary. On the other hand, if they survive until the passage of the following bunch they can in turn be accelerated, projected onto the wall and produce secondaries. This can trigger an avalanche multiplication effect which builds up the EC during the passage of an entire bunch train.

The present chapter will introduce the different phenomena involved in the formation of an EC, will then describe the main features of the EC buildup mechanism, and finally review how the presence of ECs in the beam chambers can affect the performances of a particle accelerator.

1.1 PRIMARY ELECTRON PRODUCTION MECHANISMS

We will consider the two production mechanisms for the primary electrons relevant for CERN accelerators, namely the ionization of the residual gas and the photoemission due to synchrotron radiation:

- **Residual gas ionization:** The particle beam can ionize the molecules of the residual gas in the beam chambers (where vacuum pressures are typically below 10^{-8} mbar) producing free electron-ion pairs. The local electron and ion production rate per unit volume in the beam chamber is given by:

$$\frac{dn_{\text{ion}}}{dt} = \sigma_{\text{ion}} n_{\text{gas}} \phi_p \tag{1.1}$$

  where σ_{ion} is the ionization cross section of the residual gas [14], n_{gas} is the residual gas density (supposed to be uniform in space and constant on the time scale of few beam revolutions), and ϕ_p is the beam particle flux (per unit area). The cross section differs for the different gas species composing the residual gas, it ranges between 1 and 2 Mbarn for CO and N_2 gases, and about 0.2 Mbarn for H_2. These numbers refer to singly charged particles at ultrarelativistic energies ($\beta_{\text{rel}} \simeq 1$). In the case of beams of fully ionized atoms, σ_{ion} increases roughly with the square of the atomic number of the beam particle and of the gas atoms and it is higher for lower beam energies [15].

- **Photoemission due to synchrotron radiation:** Synchrotron radiation is the emission of photons that occurs when a particle beam undergoes a transverse acceleration [16, 17], for example in a bending magnet. The total power emitted by the beam due to the bending dipoles of a synchrotron can be written as:

$$P = \frac{q\gamma_{\text{rel}}^4}{3\varepsilon_0 \rho} I_{\text{beam}} \tag{1.2}$$

  where q is the charge, γ_{rel} is the relativistic factor, I_{beam} is the beam current. The photon spectrum extends up to the so called "critical energy", given by:

$$E_c = 3\frac{\hbar c \gamma_{\text{rel}}^3}{2\rho} \tag{1.3}$$

  where $\hbar$ is the reduced Planck constant. If the beam energy, and therefore γ_{rel}, is large enough, a non negligible fraction of the photons have energy larger than the work function of the beam chamber's material. In this case the impinging photons have enough

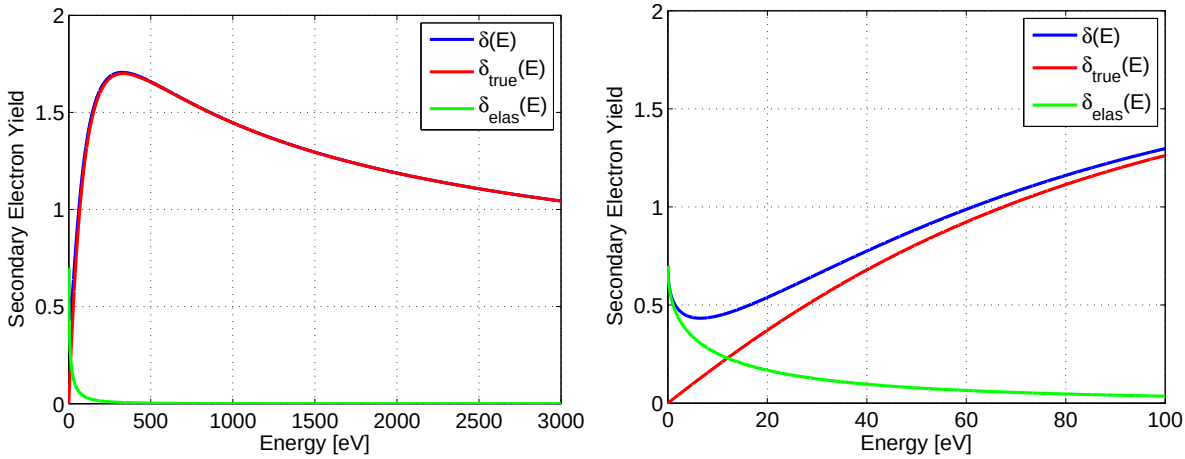

Figure 1.2: Left: SEY curve for $\delta_{\max} = 1.7$ - elastic component $\delta_{\text{elas}}(E)$, "true secondary" component $\delta_{\text{true}}(E)$, and total $\delta(E)$. Right: zoom on the low energy region.

energy to extract electrons from the chamber's wall (photoelectric effect [18]). These electrons are typically called "photoelectrons" and, for sufficiently large beam energy, can constitute the main source of primary electrons in the buildup of the EC. The synchrotron radiation is emitted in the direction tangent to the beam trajectory, with a radiation pattern which is a cone becoming narrower when γ_{rel} increases. Only a part of the photons are absorbed, and therefore can produce photoelectrons, at their first impact on the vacuum chamber, the others are reflected, sometimes more than once, by the metallic surface of the beam chamber. In the past important efforts have been spent in the modeling of this phenomenon, in order to get the distribution of the photons impacting the chamber's wall [19, 20]. The "Photoelectron Yield" of the beam chambers, i. e. the probability of electron emission per impinging photon, has also been characterized with several measurement campaigns (for the LHC see for example [21]).

1.2 SECONDARY ELECTRON EMISSION

The model for the Secondary Electron Emission which has been used for all the calculations presented in this thesis is based on extensive studies, relying mainly on laboratory measurements, which were carried out on the copper surface of the LHC beam chambers at CERN and in other research institutes [22–26].

The process is described through the Secondary Electron Yield (SEY) of the surface which is defined as the ratio between the electron current impinging the wall and the corresponding emitted current, and is a function of the energy of the impacting electrons:

$$\delta(E) = \frac{I_{\text{emit}}}{I_{\text{imp}}(E)} \tag{1.4}$$

A typical SEY curve is presented in Fig. 1.2. This quantity can in turn be decomposed in two main components:

$$\delta(E) = \delta_{\text{elas}}(E) + \delta_{\text{true}}(E) \tag{1.5}$$

where $\delta_{\text{elas}}(E)$ and $\delta_{\text{true}}(E)$ correspond respectively to electrons which are elastically reflected by the surface and to the so called "true secondaries".

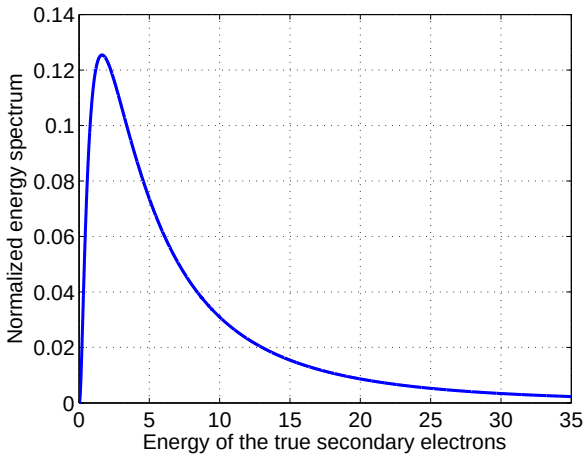

Figure 1.3: Energy distribution of the true secondary electrons.

The first component, corresponding to the green curve in Fig. 1.2, has the form:

$$\delta_{\text{elas}}(E) = R_0 \left(\frac{\sqrt{E} - \sqrt{E + E_0}}{\sqrt{E} + \sqrt{E + E_0}} \right)^2 \tag{1.6}$$

where, for the LHC beam chambers, we use the values $R_0 = 0.7$ and $E_0 = 150\,\text{eV}$ for the two free parameters of the model [24]. The electrons corresponding to this component of the SEY elastically interact with the surface and are emitted with the same energy with which they impacted on the surface.

The "true secondary" component, plotted in red in Fig. 1.2, has the form:

$$\delta_{\text{true}}(E) = \delta_{\text{max}} \frac{s \dfrac{E}{E_{\text{max}}}}{s - 1 + \left(\dfrac{E}{E_{\text{max}}} \right)^s} \tag{1.7}$$

where, for the LHC beam chambers, we use the values $s = 1.35$ and $E_{\text{max}} = 332\,\text{eV}$. At $E = E_{\text{max}}$ the SEY curve reaches a maximum at the value:

$$\delta(E_{\text{max}}) \simeq \delta_{\text{true}}(E_{\text{max}}) = \delta_{\text{max}}. \tag{1.8}$$

The parameter δ_{max} is strongly dependent on the surface material, roughness and history (see Sec. 1.2.1) and plays a key role in the EC buildup, as we will see in Sec. 1.3. In the following it will be often referred to simply as the "SEY parameter".

True secondary electrons are emitted with a cosine angular distribution with respect to the direction normal to the surface and their energy spectrum is well fitted by a "lognormal" distribution:

$$\frac{d\,n_{\text{true}}}{d\,E} = \frac{1}{E\,\sigma_{\text{true}}\sqrt{2\pi}} e^{-\dfrac{(\ln(E) - \mu_{\text{true}})^2}{2\sigma_{\text{true}}^2}} \tag{1.9}$$

where, for the LHC beam chambers, we use the values $\sigma_{\text{true}} = 1.0828$ and $\mu_{\text{true}} = 1.6636$, which correspond to the distribution plotted in Fig. 1.3.

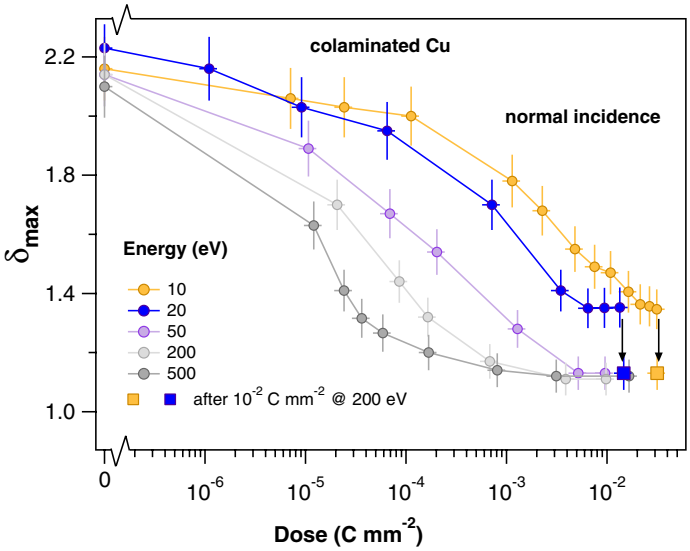

Figure 1.4: $\delta_{\max}$ as a function of the dose for different impinging electron energies at normal incidence on colaminated Cu of the LHC beam screen. The squares represent the $\delta_{\max}$ values measured after an additional electron dose of 1.0×10^{-2} C/mm^2 at 200 eV [27].

The SEY depends also on the angle of incidence of the impinging electron (θ, defined with respect fo the normal to the surface). In order to take this effect into account, the parameters $E_{\max}$ and $\delta_{\max}$ are rescaled as a function of the angle of incidence using the following relations:

$$\begin{aligned} E_{\max}(\theta) &= E_{\max}(\theta = 0)\,(1 - 0.7\,(1 - \cos\theta)) \\ \delta_{\max}(\theta) &= \delta_{\max}(\theta = 0)\, e^{\frac{(1-\cos\theta)}{2}} \end{aligned} \tag{1.10}$$

1.2.1 *Scrubbing: SEY reduction with the electron dose*

Experimental studies have shown that the SEY of many materials tends to decrease when the surface is exposed to prolonged electron irradiation. This effect is called "SEY conditioning" or "scrubbing" and has been investigated in detail in [27, 28] and references therein. Figure 1.4, for example, shows the dependence of the SEY parameter on the applied electron dose for different energies of the impinging electrons.

These observations suggested that EC effects in an accelerator can be self-mitigating, as the electron bombardment from the EC itself can lower the SEY of the chamber walls and gradually, in turn, reduce the amount of EC (process commonly referred as "beam induced scrubbing"). This is typically achieved during dedicated periods (Scrubbing Runs) during which the accelerator is operated in a configuration that should maximize EC in the chambers. In the past this strategy already proved effective to mitigate the EC effects observed at the CERN Super Proton Synchrotron (SPS) when operated with LHC type beams (see [29] and references therein).

Figure 1.5 shows the result of an experiment performed in the SPS in order to directly study beam induced scrubbing effects. The special setup allowed the in-situ measurement of

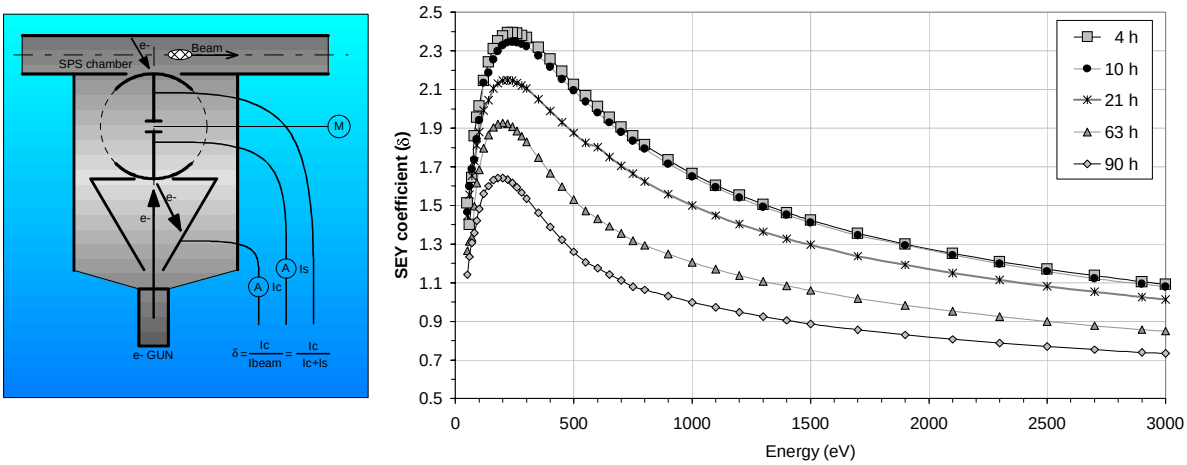

Figure 1.5: Left: Schematic view of the in-situ SEY detector installed in the SPS in 2002. Right: Decrease of the SEY of a copper sample exposed to the bombardment of the electrons from the cloud in the SPS as a function of the time of exposure to the LHC-type beam [30].

the SEY evolution on a portion of the vacuum chamber exposed to the beam. Measurements taken at different stages showed the gradual reduction of the SEY during a Scrubbing Run.

1.3 THE EC BUILDUP MECHANISM

We will now present a simple analytical model, which allows identifying the main features of the EC buildup process.

Let us consider a train of uniformly spaced bunches passing at a certain section of an accelerator, which does not contain any electron before the passage of the first bunch. Let n_0 be the number of primary electrons generated by a single bunch passage and n_i the number of electrons in the chamber at the instant t_i right before the passage of the i-th bunch. We can define $\delta_{\text{eff},i}$ such that:

$$n_{i+1} = \delta_{\text{eff},i}\, n_i + n_0 \tag{1.11}$$

where $\delta_{\text{eff},i}\, n_i$ is the number of electrons generated by the interaction of the EC with the chamber's wall (such a quantity can also be negative, when the wall acts like a net electron absorber).

The quantity $\delta_{\text{eff},i}$ can be directly related to the SEY of the chamber's surface $\delta(E)$ and to the energy spectrum of the impacting electrons, since we can write:

$$n_{i+1} = n_i + \int_0^{\infty} \int_{t_i}^{t_{i+1}} \Phi(E,t)\,(\delta(E) - 1)\, dt\, dE + n_0 \tag{1.12}$$

where

$$\Phi(E,t) = \frac{dn}{dE} \tag{1.13}$$

is the instantaneous energy spectrum of the electrons impinging the wall. If we define the normalized energy spectrum for the the i-th bunch passage as:

$$\phi_i(E) = \frac{1}{n_i} \int_{t_i}^{t_{i+1}} \Phi(E,t) dt \tag{1.14}$$

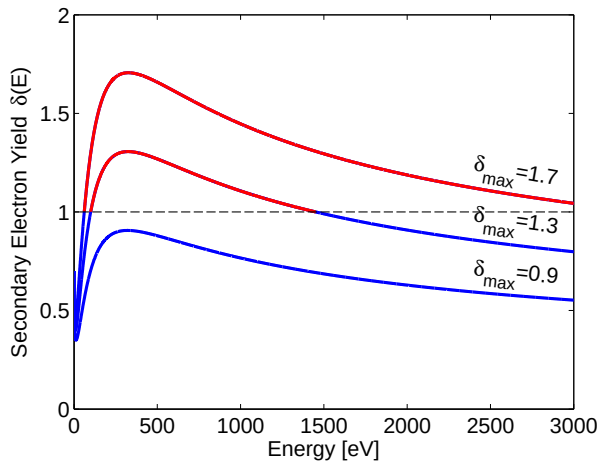

Figure 1.6: SEY curve for different values of the $\delta_{\max}$ parameter. The values for which the material behaves as electron absorber or emitter are plotted in blue and red respectively.

we can rewrite the Eq. 1.12 as:

$$n_{i+1} = n_i \left(1 + \int_0^\infty \phi_i(E)\,(\delta(E) - 1)\,dE\right) + n_0 \tag{1.15}$$

and, comparing against Eq. 1.11, we obtain:

$$\delta_{\text{eff},\,i} = 1 + \int_0^\infty \phi_i(E)\,(\delta(E) - 1)\,dE \tag{1.16}$$

The meaning of this equation is quite intuitive: the SEY curve can be divided in two regions, one in which $\delta(E) < 1$ and the wall acts as an electron absorber, and the other in which $\delta(E) > 1$ and the wall acts as an electron emitter. The two regions are shown in blue and red respectively in Fig. 1.6, for different values of $\delta_{\max}$. Looking at Eq. 1.16 we observe that, if the electron flux $\phi_i(E)$ lies mainly in the $\delta(E) < 1$ region, then the integral is negative, $\delta_{\text{eff},\,i} < 1$, and the chamber's wall behaves like a net absorber. On the other hand, if $\phi_i(E)$ lies manly in the $\delta(E) > 1$ region than the integral is positive, $\delta_{\text{eff},\,i} > 1$, and the chamber's wall behaves like a net emitter.

If the electrons do not influence each other's trajectory, which means that the Coulomb forces between them are negligible, then we can assume that $\phi_i(E)$ does not depend on the bunch index:

$$\phi_i(E) = \phi(E) \tag{1.17}$$

and hence the same holds for $\delta_{\text{eff},\,i}$:

$$\delta_{\text{eff},\,i} = \delta_{\text{eff}} \tag{1.18}$$

In these conditions by recursively applying Eq. 1.11 we find:

$$n_i = n_0 \sum_{k=1}^{i} \delta_{\text{eff}}^k \tag{1.19}$$

which is a partial sum of a geometric series and can be written as:

$$n_i = n_0 \frac{1 - \delta_{\text{eff}}^i}{1 - \delta_{\text{eff}}} \tag{1.20}$$

From this expression we can recognize two different regimes:

- When $\delta_{\text{eff}} < 1$ we observe that, for sufficiently large i, n_i tends to the constant value:

  $$n_i \simeq \frac{n_0}{1 - \delta_{\text{eff}}} \tag{1.21}$$

  which is essentially an equilibrium condition between primary electron production and electron absorption at the chamber's wall. We will therefore call this condition **"seed accumulation regime"** .

- When $\delta_{\text{eff}} > 1$ we observe an exponential growth of the number of electrons in the chamber, i. e. for sufficiently large i:

  $$n_i \simeq n_0 \frac{\delta_{\text{eff}}^i}{\delta_{\text{eff}} - 1} \tag{1.22}$$

  which is indeed an avalanche multiplication of the electrons driven by the secondary emission. We will therefore call this condition **"multipacting regime"**. In this case other mechanisms intervene to limit the number of electrons to a finite value, as it will be explained later in this section.

In order to explore the validity of this simple model we used the PyECLOUD code (which will be described in detail in Chapter 2) to simulate the EC buildup in the very simple case of a cylindrical chamber (radius 22 mm, i. e. the horizontal size of the LHC arc beams screen) without any externally applied magnetic field, with nominal LHC bunch parameters, and a uniform train of 25 ns spaced bunches. For the analysis of these results it is also useful to introduce few other quantities, namely the total electron flux on the chamber's wall:

$$F_i = \int_0^\infty \int_{t_i}^{t_{i+1}} \Phi(E, t)\, dt\, dE \tag{1.23}$$

and the fractions of the impacting electrons which lie in the region of the SEY curve where the wall acts as an electron absorber or electron emitter, respectively:

$$F_{\text{absor},i} = \int_{\{E:\, \delta(E)<1\}} \int_{t_i}^{t_{i+1}} \Phi(E, t)\, dt\, dE \tag{1.24a}$$

$$F_{\text{emit},i} = \int_{\{E:\, \delta(E)>1\}} \int_{t_i}^{t_{i+1}} \Phi(E, t)\, dt\, dE \tag{1.24b}$$

The simulation results for the case $\delta_{\text{max}} = 1.1$ are shown in Fig. 1.7. In particular, the blue curve in the top plot shows the evolution of n_i. In the middle plot we compare two ways of estimating the $\delta_{\text{eff},i}$ coefficients from the simulation results, i. e. using both the recursive formula 1.11 and using the simulated bunch-by-bunch electron spectra to evaluate the integral in Eq. 1.16. The two estimates are very consistent, showing that the angular dependence of the SEY, which is included in the simulation (see Sec. 2.9) but not in the estimate of Eq. 1.16, is in this case negligible.

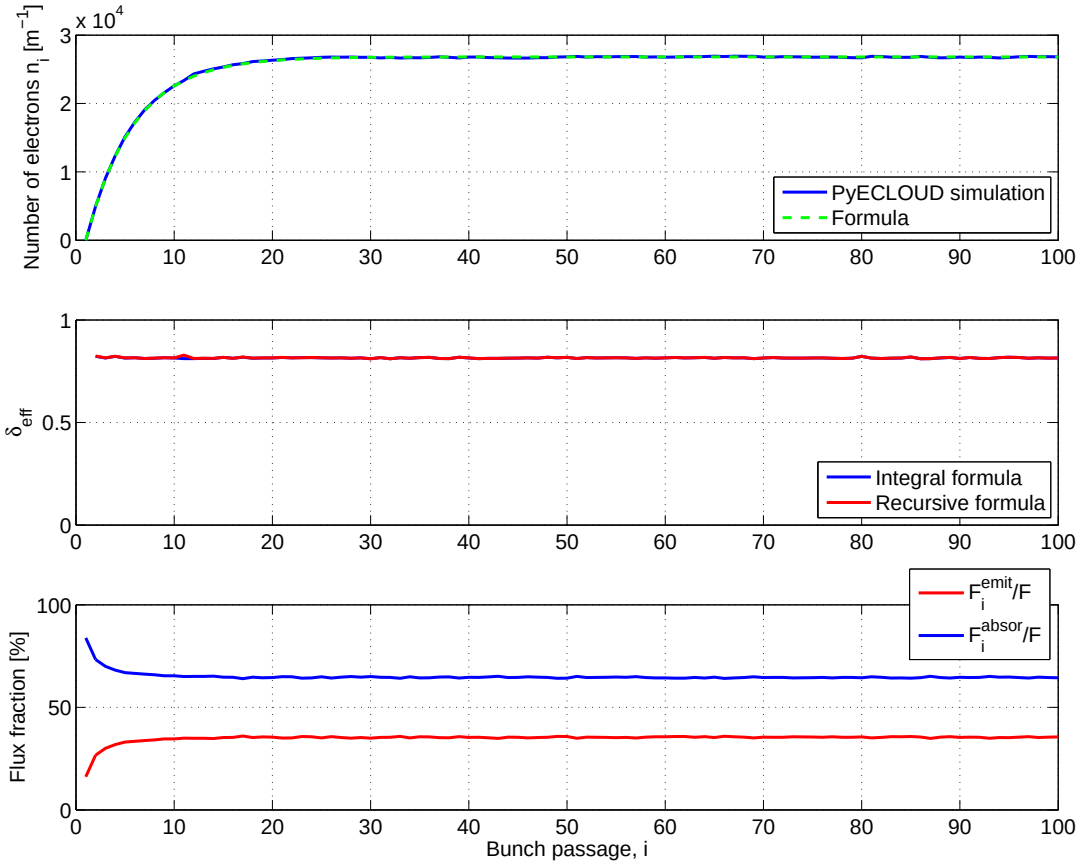

Figure 1.7: Simulated EC buildup for $\delta_{\max} = 1.1$. Top: number of electrons before each bunch passage (directly from simulation - blue - and estimated from Eq. 1.20 - dashed green). Center: δ_{eff} (both from the integral formula 1.16 and the recursive formula 1.11). Bottom: fractions of the electron energy spectrum falling in the absorber/emitter regions of the SEY curve.

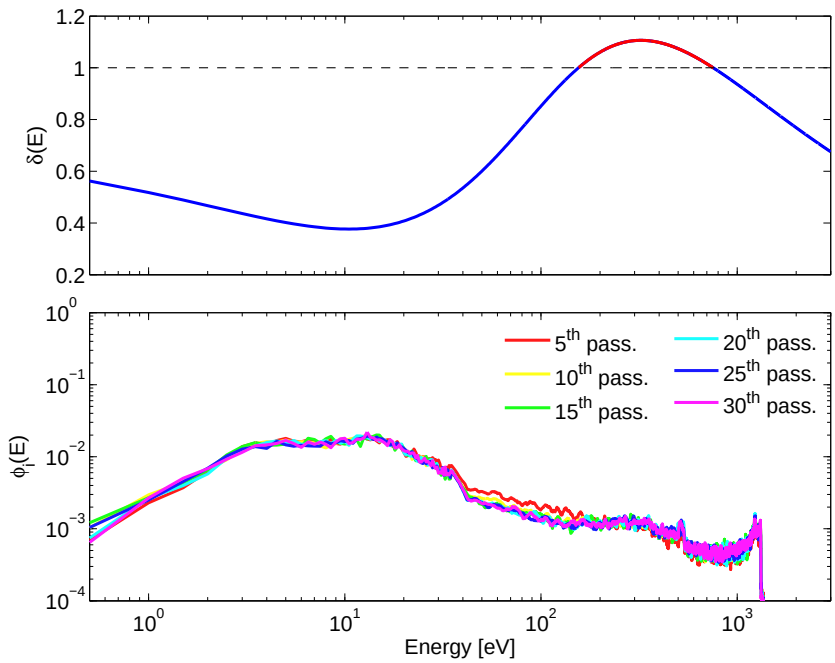

Figure 1.8: Simulated EC buildup for $\delta_{\max} = 1.1$. Top: SEY curve. Bottom: energy spectrum $\phi_i(E)$ for different bunch passages.

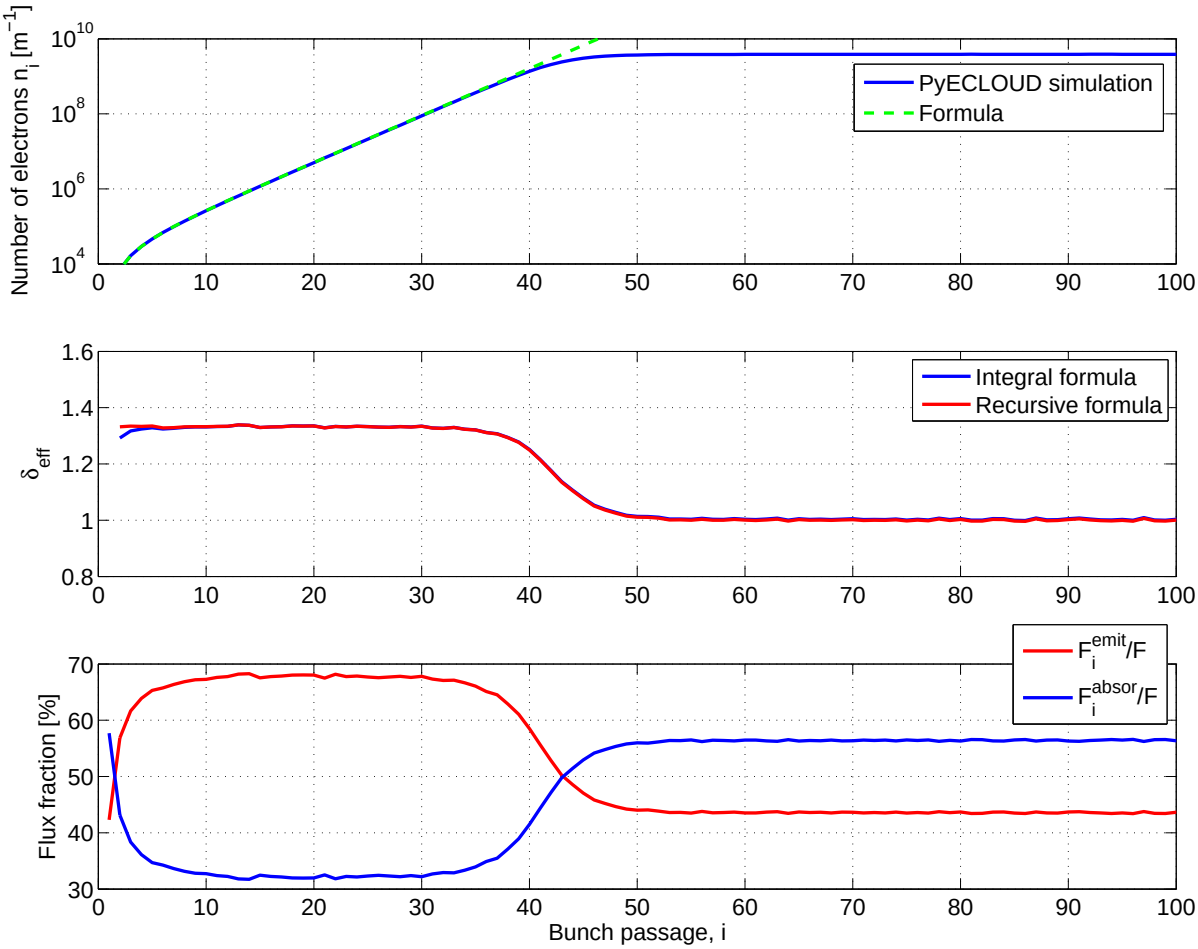

Figure 1.9: Simulated EC buildup for $\delta_{max} = 1.75$. Top: number of electrons before each bunch passage (directly from simulation - blue - and estimated from Eq. 1.20 - dashed green). Center: δ_{eff} (both from the integral formula 1.16 and the recursive formula 1.11). Bottom: fractions of the electron energy spectrum falling in the absorber/emitter regions of the SEY curve.

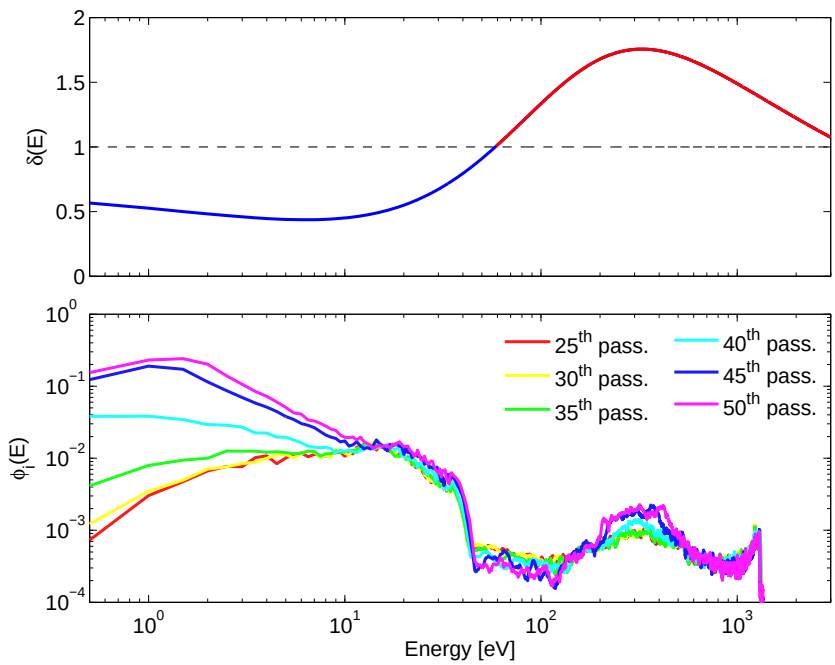

Figure 1.10: Top: SEY curve. Bottom: energy spectrum $\phi_i(E)$ for different bunch passages.

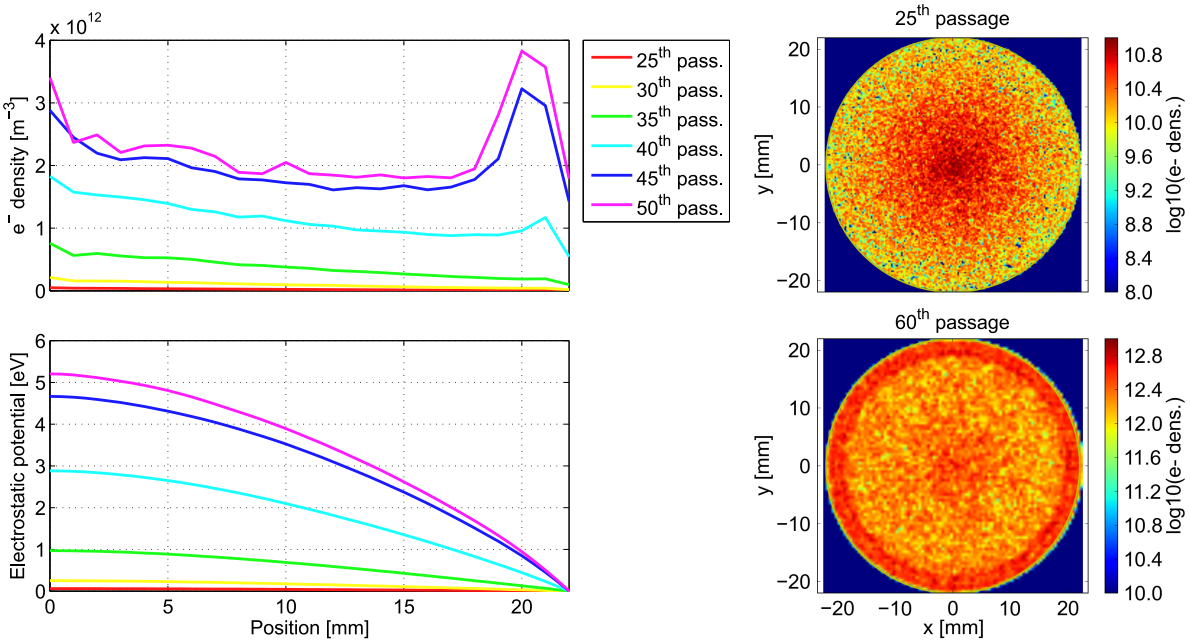

Figure 1.11: Simulated EC buildup for $\delta_{\max} = 1.75$. Left: electron density and electrostatic potential as a function of the distance from the center and of the bunch passage. Right: two snapshots of the electron density in the chamber, one taken right before a bunch passage during the exponential rise (top) and one taken right before a bunch passage during the saturation phase (bottom).

We observe $\delta_{\text{eff},i}$ is practically constant and smaller than one, which means we are in the seed accumulation regime. This is confirmed by Fig. 1.7 (bottom), which shows that F_{absorb} is significantly larger than F_{emit}, and by Fig. 1.8 which shows that the energy spectrum $\phi_i(E)$ is the same all along the simulation (i. e. the condition of Eqs. 1.17 is fulfilled) and lies mainly in the energy region for which the wall behaves as an electron absorber. In Fig. 1.7 (top) we can observe that, in this case, the simulated buildup is perfectly described the Eq. 1.20, with the average estimated δ_{eff}.

We now repeat the same procedure for the case $\delta_{\max} = 1.75$, the results are presented in Figs. 1.9 and 1.10. In these plots we can recognize two different stages, one going from the first passage up to around the 45th, and the second from that point onward. In the first stage the condition 1.17 is again verified but now $\delta_{\text{eff},i}$ is larger than one, which means we are in the multipacting regime. Indeed the energy spectrum $\phi_i(E)$ lies mainly in the energy region where the wall behaves like a net electron emitter, as confirmed by Figs. 1.9 (bottom) and 1.10. In this case Eq. 1.20 predicts an exponential growth of the number of electrons, which is exactly what is observed Fig. 1.9 (top).

Later on we observe that the evolution of n_i deviates from the expected exponential growth and finally "saturates" to a constant value, which is larger than the equilibrium value reached in the seed accumulation regime by several orders of magnitude (compare Figs. 1.7 and 1.9). By looking at Fig. 1.10 we observe that during this transition the condition 1.17 is not fulfilled anymore since one can notice a strong increase in the number of electrons hitting the wall with extremely low energy (< 10 eV). We also observe that the electron flux becomes dominated by the fraction lying in the net absorber region (see Fig. 1.9 - bottom) and that the effect of this change in the electron spectrum is that the parameter $\delta_{\text{eff},i}$ drops to one (see Fig. 1.9 - middle).

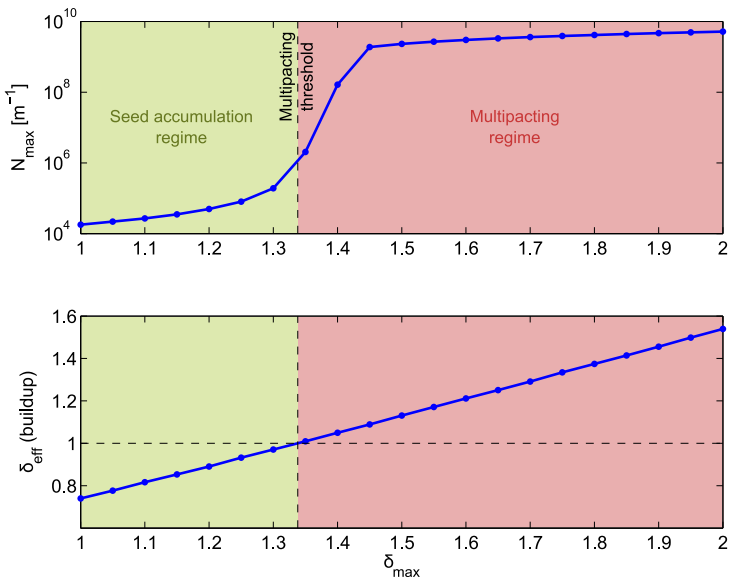

Figure 1.12: Maximum number of electrons in the chamber and δ_{eff} coefficient as a function of th SEY parameter.

The reason of this change can be understood considering the fact that most of true secondary electrons are emitted with energies of the order of few eV (see Fig. 1.3), and therefore, if they impact on the wall before being accelerated by a bunch passage, they have a high chance to be absorbed (the wall acts as net absorber for these energies, see Fig. 1.10 - top). Fig. 1.11 shows how the electron density and the electrostatic potential evolve during the buildup (all plots correspond to snapshots taken right before the passage of the corresponding bunch).

During the first stages the electron density is quite modest, and, as a result, the electrostatic potential in the chamber (with respect to the wall) is smaller then 1 eV. In these conditions most of the true secondaries are practically free to move in the chamber. Due to their initial velocity they drift towards the center and have a high chance of avoiding to impact on the wall before the next bunch passage.

As the electron density in the chamber increases, so does also the electrostatic potential which means that the forces due to "space charge" effects within the EC itself become increasingly stronger. Around the 45th bunch passage the true secondaries emitted by the wall see a potential barrier comparable to their kinetic energy and therefore tend to be confined in a region close to the chamber's wall. As a consequence the electron density assumes a ring like shape (see Fig. 1.11) and the probability that low energy electrons reach the wall before the next passage strongly increases.

This causes the change in the energy spectrum observed in Fig. 1.10 towards an equilibrium condition such that:

$$\int_0^\infty \phi_i(E)\,(\delta(E)-1)\,dE = 0 \tag{1.25}$$

Here electron emission and absorption at the wall perfectly balance one another and therefore $\delta_{\text{eff},i} = 1$ (see Eq. 1.16).

Figure 1.12 shows how the maximum number of electrons in the chamber and the δ_{eff} coefficient in the first stage of the buildup simulation (before space charge effects become

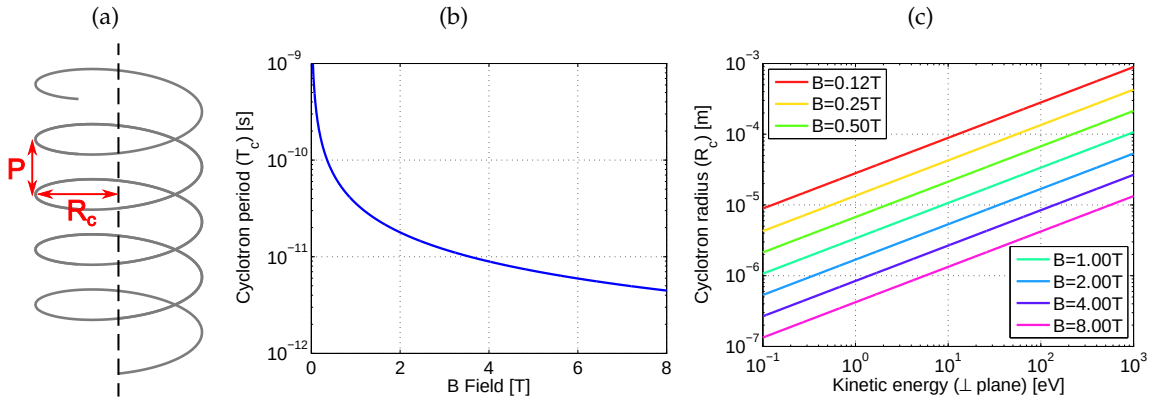

Figure 1.13: (a) Helicoidal trajectory of an electron moving in a uniform vertical magnetic field. (b) Cyclotron period as a function of the magnetic field. (d) Cyclotron radius as a function of the magnetic field and of kinetic energy associated to the motion in the plane orthogonal to the field lines.

significant) depend on the SEY parameter δ_{max}. The value of δ_{max} for which $\delta_{\text{eff}} = 1$ is called **"multipacting threshold"** and separates the seed accumulation and the multipacting regimes. The multipacting threshold can be easily recognized also on the number of electrons in the the beam chamber (see Fig. 1.12 - top) since around this point an increase of several orders of magnitude is observed with respect to the seed accumulation regime. This kind of dependence is observed also on many other quantities related to the EC in the chamber, e. g. the electron flux on the wall, the electron density at the beam position, the energy deposition onto the wall. Typically, if δ_{max} is below the multipacting threshold and therefore no avalanche multiplication is occurring, the EC is practically harmless for the machine performance, unless very strong seeding mechanisms are present.

1.4 EFFECTS OF EXTERNALLY APPLIED MAGNETIC FIELDS

The features of the EC buildup are strongly influenced by externally applied magnetic fields, like those present in bending and focusing magnets of a particle accelerator.

It is simple to prove [31] that a non-relativistic electron moving in a uniform magnetic field of magnitude B (as for example in the case of a bending magnet) follows an helicoidal trajectory around the field lines. The revolution period, the radius (also called "cyclotron period" and "cyclotron radius" respectively) and the pitch of the helix (see Fig. 1.13 - a) are respectively given by:

$$T_c = \frac{2\pi m}{qB} \tag{1.26a}$$

$$R_c = \frac{m v_\perp}{qB} \tag{1.26b}$$

$$P = v_\parallel T_c = \frac{2\pi v_\parallel m}{qB} \tag{1.26c}$$

where q and m are respectively the charge and the mass of the electron and $v_\parallel$ and $v_\perp$ are the magnitudes of the components of the velocity vector in the direction parallel and orthogonal to the field lines respectively. Figure 1.13 (b) shows the dependence of the electron cyclotron

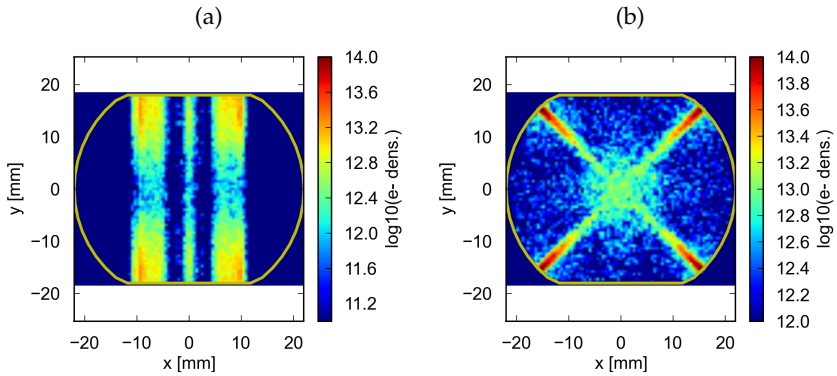

Figure 1.14: Snapshots of the electron cloud density in a dipole (a) and a quadrupole (b) magnet of the LHC (See Secs. 4.1 and 4.2 for more details).

period on the applied magnetic field. In all the bending magnets discussed in this thesis B is in the range [0.1 T, 8 T], hence the cyclotron period is always much smaller than the bunch spacing and than the bunch length (which, for example, are 25 ns and 1 ns respectively for the nominal LHC beam at 7 TeV).

Figure 1.13 (c) shows the dependence of the cyclotron radius on the kinetic energy associated to the motion in the plane orthogonal to the field (i. e. $\frac{1}{2}\, mv_{\perp}^2$) and on the applied magnetic field. In a typical EC buildup, the total kinetic energy of an electron is typically not larger than 2 keV (see for example the energy spectra in Figs. 1.8 and 1.10), which implies that, in all cases of interest for this work, the cyclotron radius never exceeds few millimeters. This means that the electrons are practically constrained to move around the field lines. Electrons trapped by different filed lines will receive different kicks from the passing bunches, corresponding to different efficiencies for the multipacting process. This generates characteristic patterns of the electron density, as for example, the one shown in Fig. 1.14 (a).

Similar effects are observed also in quadrupole magnets. For example, with the chamber and beam parameters of LHC, the electron density shows an x-like shape as shown in Fig. 1.14 (b) (see Sec. 4.2 for the details). In the case of quadrupoles, the presence of a magnetic field gradient can also trigger electron trapping mechanisms which can make the EC buildup even more severe [32].

1.5 IMPACT OF EC EFFECTS ON THE ACCELERATOR'S PERFORMANCES

The presence of EC in the beam chamber can limit the achievable performance of a particle accelerator through different effects which will be briefly reviewed in the following:

- **Transverse beam instabilities**: the forces exerted by the EC on the particle beam can drive transverse instabilities (e. g. exponentially growing oscillation of the particle around the nominal trajectory). Both "coupled bunch" instabilities and intra-bunch motion [33] can be observed leading to fast transverse emittance blowup and particle losses, which in many cases can prevent a safe operation of the accelerator. Due to the important high frequency content, the conventional transverse feedback systems are usually ineffective in controlling EC induced instabilities. Better results can be obtained introducing

Landau damping [33] through high chromaticity settings or using octupole magnets, typically at expense of transverse emittance preservation and beam lifetime [34, 35].

- **Incoherent beam effects:** even when transverse instabilities can be avoided (either because the EC density is low enough, or thanks to Landau damping) the interaction of the beam with the EC can drive incoherent effects e. g. slow emittance blow up, particle losses, transverse tune spread, which are particularly worrying in storage rings and particle colliders where the aim is to store the beam in the ring for a very long time (several hours) while preserving the beam quality.

- **Vacuum degradation:** the electron flux on the chamber's wall stimulates the desorption of gas molecules from the surface which results in an increased residual gas density in the beam chamber, and therefore in a pressure increase. This has several deleterious effects like larger equipment irradiation, worse background in the experimental areas, increased probability of breakdown in high voltage devices like kickers or electrostatic septa, and impact on the beam lifetime [36].

- **Heat load:** the electrons also deposit energy on the chamber's wall. While this effect is typically negligible in room temperature accelerator components, it can become a serious issue in devices operating at cryogenic temperature like the superconducting magnets of the LHC, where the EC induced heat load can reach the cooling capacity limit of the cryogenic system [37].

- **Impact on beam diagnostics:** The presence of an unforeseen electron flux can induce malfunctions on beam diagnostics devices like pickups and Beam Position Monitors (BPMs) [38].

All these effects have been observed at the LHC and in its injector chain, as will be discussed in Parts II and III of this thesis.

2

MODELING AND SIMULATION OF THE ELECTRON CLOUD BUILDUP WITH THE PYECLOUD CODE

The analysis of EC observations in the LHC and its injectors have raised new challenges for the EC build-up simulations. For a correct understanding of machine observations it is often necessary to deal with beams with thousands of bunches and with non idealities like non uniform bunch populations and bunch lengths along the beam. Beside the usual simulation scenarios of field free regions and dipole magnets, also more complex situations needed to be addressed, like the EC buildup in quadrupoles or combined function magnets and with two counter-rotating beams in the same chamber. Moreover, the demand for extensive parameter scans gave quite stringent requirements in terms of speed and reliability.

CERN has a long experience in the EC build-up simulation, mostly carried out with the ECLOUD code, developed and maintained at CERN since 1997 [13, 39–41]. Unfortunately, due to its non modular structure and to the programming language (FORTRAN 77), this code did not appear to be suitable to fulfill the aforementioned requirements. We decided to undertake a different strategy and to write a fully reorganized code, in a more modern and powerful language, considering that the initial effort would be compensated by a significantly increased efficiency in development and debugging. The new code has been called PyECLOUD, since it is almost entirely written in Python and inherits the physical models of the ECLOUD code.

During the development we addressed all the known issues of the ECLOUD code and we introduced the new features, necessary to deal with the complex scenarios described before. Modifications on numerical model and implementation were introduced practically everywhere, and key modules of the code, i. e. the MacroParticle (MP) Size Management, the electron space charge evaluation, the MP tracker and the electron/wall interaction have been completely redesigned. Substantial improvements in terms of reliability, accuracy, speed and usage flexibility were immediately evident.

The present chapter will present our model for the simulation of the EC buildup and its implementation in the PyECLOUD code. Several examples of its usage in EC studies for the LHC and its injector chain will then be presented in Parts II and III.

2.1 PYECLOUD: OVERALL STRUCTURE

PyECLOUD is a 2D code that simulates the EC buildup in a thin slice around a certain section of a particle accelerator (having longitudinal coordinate s along the machine).

Electrons are grouped in MPs in order to achieve a reasonable computational burden and the dynamics of the MP system is simulated following the flow diagram sketched in Fig. 2.1.

At each time step, seed electrons due to residual gas ionization and/or to photoemission (see Sec. 1.1), are generated with a number consistent with the passing beam slice (see

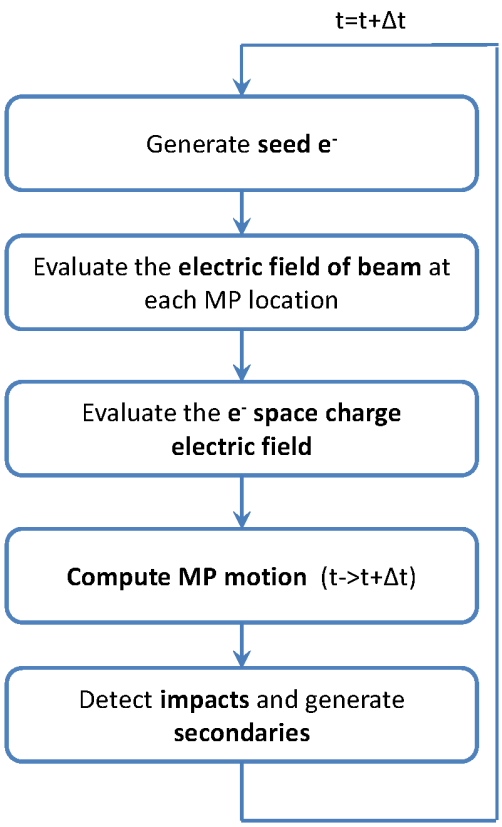

Figure 2.1: Flowchart representing PyECLOUD main loop.

Secs. 2.5 and 2.6). Then the electric field acting on each MP is evaluated: the field of the beam is precomputed on a suitable rectangular grid and obtained at each MP location by a linear interpolation (see Sec. 2.4), while the electron space charge contribution is calculated by a classical Particle In Cell (PIC) algorithm (see Sec. 2.7). Once the total electric field at each MP location is known, MP positions and momenta are updated by integrating the equation of motion. At this stage the presence of an externally applied magnetic field can also be taken into account (see Sec. 2.8). At each time step, a certain number of MPs can hit the wall. In these cases a proper model of the secondary emission process is applied to generate charge, energy and angle of the emitted electrons. According to the size of the corresponding emitted charge, a rescaling of the impinging MP can be performed or new MPs can be emitted (see Sec. 2.9).

2.2 MACROPARTICLE SIZE MANAGEMENT

One of the peculiarities of the EC buildup process is the fact that, due to the exponential rise driven by multipacting (see Sec. 1.3), the number of electrons can spread several orders of magnitude along the passage of the bunch train (see Fig. 2.2 - top). As a consequence, it is impossible to choose a MP size which is suitable for the entire simulation, allowing both a satisfactory description of the phenomena and a computationally affordable number of MPs at every stage of the simulation. The MP size management in PyECLOUD has been modified from the ECLOUD concept and will be briefly described in the following.

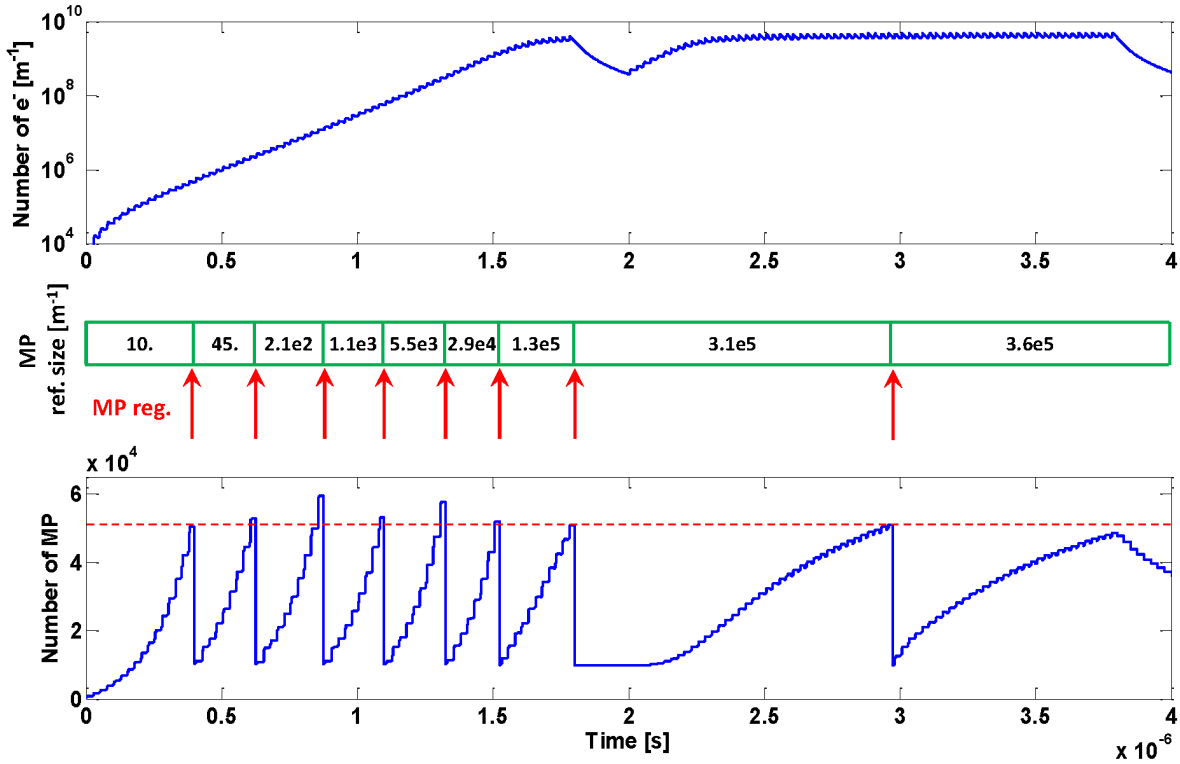

Figure 2.2: Top: evolution of the number of electrons in the beam pipe for an LHC type beam with 25 ns bunch spacing in the SPS (2 trains of 72 bunches. MBB type magnet); middle: evolution of the reference MP size; bottom: evolution of the number of MPs, the regeneration threshold is highlighted in red.

MP sizes are not enforced throughout the simulation process but are determined step by step by "decisions" taken during the execution. For this purpose a target MP size n_{ref}, dynamically adapted during the simulation, is employed to control the number of electrons per MP. In particular:

- The size of MPs generated by seed mechanisms is exactly n_{ref} (see also Secs. 2.5 and 2.6);
- When a MP hits the wall, it is simply rescaled according to the SEY if the emitted charge is below $1.5\,n_{\text{ref}}$, otherwise "true" secondary MPs are generated so that the resulting MP size is as close as possible to n_{ref} (see also Sec. 2.9);
- Once per bunch passage, a cleaning procedure is performed, which deletes the MPs with charge lower than $10^{-4} n_{\text{ref}}$.

The target MP size n_{ref} is changed whenever the total number of MPs becomes larger than a certain threshold defined by the user (typical value $\sim 10^5$), which means that the computational burden has become too high. When this happens, a **regeneration** of the set of MPs is applied, by performing the following procedure (see Fig. 2.2):

- Each MP is assigned to a cell of a uniform grid in the 5-D phase space (x, y, v_x, v_y, v_z) obtaining an approximation of the phase space distribution of the electron gas;

- The new n_{ref} is chosen in order to get a target number of MPs (typically 5-10 times smaller than the regeneration threshold), which still allows for an accurate simulation but with a more reasonable computational effort;
- A new set of MPs, having the new reference size, is generated according to the computed distribution.

The preservation of the entire phase space is very important in EC build-up simulation since the dynamics imparted by passing bunches generates very distinctive velocity distributions at the different time steps and the conservation of few specific lower order moments (e. g. total charge, total energy) might not guarantee a sufficient accuracy.

Several numerical test have shown that the errors on the total charge and the total energy which are introduced by this procedure, are about 1% at the first time step after the regeneration and they become even smaller after the first bunch passage following the regeneration.

2.3 THE CHAMBER MODULE

Beam chambers in particle accelerators can be of very different shapes as witnessed by the variety of chamber profiles installed in CERN synchrotrons (as we will show in Parts II and III of this thesis). It was therefore very important to make the code as flexible as possible with respect to this aspect and allow easy implementation of new shapes. In PyECLOUD this was accomplished by exploiting the object oriented features of the Python language. The beam chamber is defined essentially as a Python object with two member functions (the reference system is chosen such that the plane (x, y) is the transverse plane):

(1) The function "IsOutside(x,y)" allows to check if a point (x,y) is internal or external to the chamber;

(2) The function "ImpactPointAndNormal(xin, yin, xout, yout)", given two points P_{in} and P_{out}, respectively internal and external to the chamber, computes the crossing point between the segment $P_{\text{in}}P_{\text{out}}$ and the chamber's profile and, in this point, provides the unit vector normal to the profile and pointing towards the inside of the chamber.

An efficient implementation of these functions was found to be crucial for the code performances since they are called an extremely large number of times ($\sim 10^{10}$ checks) during a typical simulation. Special attention must also be paid to the algorithm robustness with respect to precision issues, which may arise when particles are extremely close to the chamber's surface or when they impact on the chamber's wall with a grazing angle.

Two chamber modules are already implemented in PyECLOUD, one for an elliptical profile and one for a generic convex polygon (with vertexes specified by the user). Other shapes can be simulated by developing a new chamber module, respecting the specifications highlighted before, without any need for further changes in other parts of the code.

For the case of the elliptic profile, the two methods can be easily implemented using analytic formulas. Concerning the case in which the chamber profile is a convex polygon the implemented algorithms will be briefly described in the following.

The user provides the coordinates of the vertexes of the polygon, which will be denoted as $\{V_1, V_2, \ldots, V_N\}$. In the initialization stage the code computes for each edge the normal unit vector pointing inward the chamber, these will be denoted as $\{\hat{\mathbf{n}}_1, \hat{\mathbf{n}}_2, \ldots, \hat{\mathbf{n}}_N\}$.

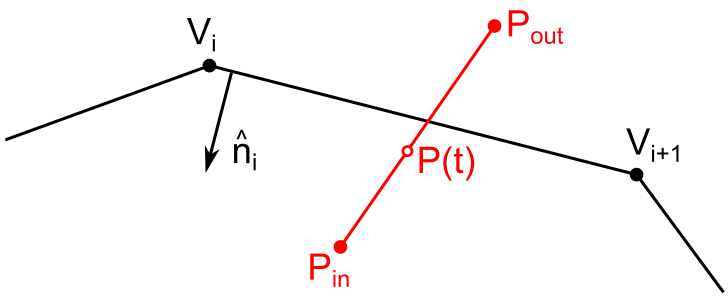

Figure 2.3: Intersection between a segment $P_{\text{in}}P_{\text{out}}$ and an edge af a convex polygon.

It can be proved [42] that a point P lies outside the polygon if for at least one edge the condition holds:

$$(P - V_i) \cdot \hat{\mathbf{n}}_i < 0 \tag{2.1}$$

which is the condition we use to implement the "IsOutside(x,y)" function.

For the implementation of the "ImpactPointAndNormal(xin, yin, xout, yout)", let us consider the case in which, given two points P_{in} and P_{out}, respectively internal and external to the chamber, we want to find the crossing point between the segment $P_{\text{in}}P_{\text{out}}$ and the chamber profile. We parametrize the segment $P_{\text{in}}P_{\text{out}}$ as:

$$P(t) = P_{\text{out}}t + P_{\text{in}}(1 - t) \quad \text{with } t \text{ in } [0, 1] \tag{2.2}$$

Looking at Fig. 2.3 we observe that, if $P(t)$ is the crossing point between $P_{\text{in}}P_{\text{out}}$ and the edge V_iV_{i+1}, the following condition must be fulfilled:

$$(P(t) - V_i) \cdot \hat{\mathbf{n}}_i = 0 \tag{2.3}$$

Substituting the 2.2 into the 2.3 we obtain:

$$t = \frac{(V_i - P_{\text{in}}) \cdot \hat{\mathbf{n}}_i}{(P_{\text{out}} - P_{\text{in}}) \cdot \hat{\mathbf{n}}_i} \tag{2.4}$$

Such a quantity can be indeed computed for all the edges of the polygon, providing the crossing point between the *lines* identified by the edge and the segment $P_{\text{in}}P_{\text{out}}$. It is possible to prove [42] that an effective way of finding the crossing point between the segment and the polygon is to compute the quantity 2.4 for all the edges and then search for the minimum non negative value. The index of the edge corresponding to such a minimum (the impact edge) is also computed, in order to select the appropriate normal unit vector from the list precalculated at the initialization stage.

2.4 THE BEAM

In PyECLOUD the beam is assumed ultra-relativistic ($\beta_{\text{rel}} = 1$) and its distribution is assigned *a priori* and not affected by the EC ("rigid beam" approximation - on the time scale of an EC buildup simulation this condition is always satisfied). We assume that the beam particle distribution can be factorized as follows (quite realistic in modern synchrotrons):

$$\rho(x, y, s, t) = \lambda(s - ct)\rho_{\perp}(x, y) \tag{2.5}$$

The transverse distribution $\rho_\perp(x,y)$ is chosen such that:

$$\int_A \rho_\perp(x,y)dxdy = 1 \tag{2.6}$$

where A is the transverse section of the beam pipe, and therefore $\lambda(s-ct)$ is the line charge density at the section s at the instant t.

For a charge traveling at the speed of light in the s direction, the electric and magnetic fields are purely transverse:

$$\mathbf{E}\cdot\hat{\mathbf{i}}_s = 0 \tag{2.7a}$$
$$\mathbf{B}\cdot\hat{\mathbf{i}}_s = 0 \tag{2.7b}$$

and are related by [16]:

$$\mathbf{B} = \frac{\hat{\mathbf{i}}_s \times \mathbf{E}}{c} \tag{2.8}$$

The Lorentz force acting on an electron is given by:

$$\mathbf{F} = -q\left(\mathbf{E} + \mathbf{v}_e \times \mathbf{B}\right) \tag{2.9}$$

where q is the elementary charge and $\mathbf{v}_e$ is the electron velocity. Since in the EC buildup the electrons are always non relativistic ($|\mathbf{v}_e| \ll c$) the effect of the magnetic field of the beam can be neglected.

For the computation of the electric field generated by the distribution 2.5 we start from the special case:

$$\lambda(s-ct) = \delta(s-ct) \tag{2.10}$$

the corresponding electric field has the form [16]:

$$\mathbf{E}_\delta(x,y,s,t) = \mathbf{E}_\perp(x,y)\delta(s-ct) \tag{2.11}$$

Projecting the Maxwell's equation

$$\nabla\times\mathbf{E} = -\frac{\partial\mathbf{B}}{\partial t} \tag{2.12}$$

along the s axis and using the 2.7b we find:

$$\frac{\partial E_{\perp y}}{\partial x} - \frac{\partial E_{\perp x}}{\partial y} = 0 \tag{2.13}$$

Using the 2.7a we can write:

$$\nabla\cdot\mathbf{E}_\delta(x,y,s,t) = \nabla\cdot\left[\mathbf{E}_\perp(x,y)\delta(s-ct)\right] = \left[\nabla\cdot\mathbf{E}_\perp(x,y)\right]\delta(s-ct) \tag{2.14}$$

Using this relation and the 2.5 we can rewrite the Maxwell's equation:

$$\nabla\cdot\mathbf{E} = \frac{\rho}{\varepsilon_0} \tag{2.15}$$

as:

$$\frac{\partial E_{\perp x}}{\partial x} + \frac{\partial E_{\perp y}}{\partial y} = \frac{\rho_\perp}{\varepsilon_0} \tag{2.16}$$

The transverse field $\mathbf{E}_\perp$ can be calculated combining the Eqs. 2.13 and 2.16 with perfect electric boundary conditions on the chamber's surface:

$$\begin{cases} \dfrac{\partial E_{\perp y}}{\partial x} - \dfrac{\partial E_{\perp x}}{\partial y} = 0 & \text{(2.17a)} \\ \dfrac{\partial E_{\perp x}}{\partial x} + \dfrac{\partial E_{\perp y}}{\partial y} = \dfrac{\rho_\perp}{\varepsilon_0} & \text{(2.17b)} \\ \hat{\mathbf{n}} \times \mathbf{E}_\perp = 0 \quad \text{on the boundary} & \text{(2.17c)} \end{cases}$$

which are identical to the case of a 2D (z-invariant) electrostatics problem.

The electric field due to the distributed source given by Eq. 2.5 can be obtained from the 2.11 through convolution:

$$\mathbf{E}(x, y, s, t) = \mathbf{E}_\perp(x, y)\lambda(s - ct) \tag{2.18}$$

Based on this considerations, the computation of the electric field of the beam at the MP locations can be performed in three stages:

1. **Computation of the transverse field map:** in the initialization stage the field $\mathbf{E}_\perp(x, y)$ is computed, by solving the system 2.17, and the field components at the nodes a uniform grid covering the beam chamber are then stored.

2. **Field gather:** the field map is interpolated at the MP locations (using the same interpolation algorithm which will be presented in detail in Sec. 2.7 in the case of the electron space charge field).

3. **Rescaling:** the values are rescaled according to the longitudinal beam density at the current time step obtaining at each MP location the field exerted by the beam:

$$\mathbf{E}_\perp\left(x_{\mathrm{MP}}, y_{\mathrm{MP}}\right)\lambda(s - ct) \tag{2.19}$$

In PyECLOUD the transverse beam distribution is assumed to be Gaussian (quite realistic for most synchrotrons):

$$\rho_\perp(x, y) = \frac{1}{2\pi\sigma_x\sigma_y} e^{-\left(\frac{x^2}{2\sigma_x{}^2} + \frac{y^2}{2\sigma_y{}^2}\right)} \tag{2.20}$$

When the chamber's profile is elliptical the beam electric field $\mathbf{E}_\perp(x, y)$ can be evaluated analytically using the Bassetti-Erskine formula and image charges to account for the effect of the boundary [43, 44]. In all other cases, the system 2.17 is solved numerically using the Finite Difference (FD) algorithm, which is also employed for the electron space charge field calculation (it will be presented in detail in Sec. 2.7). An example showing the quantities $\rho_\perp(x, y)$, $|\mathbf{E}_\perp(x, y)|$, $E_{\perp,x}(x, y)$, $E_{\perp,y}(x, y)$ for the nominal LHC beam at injection energy inside the arc beam screen is shown in Fig. 2.4.

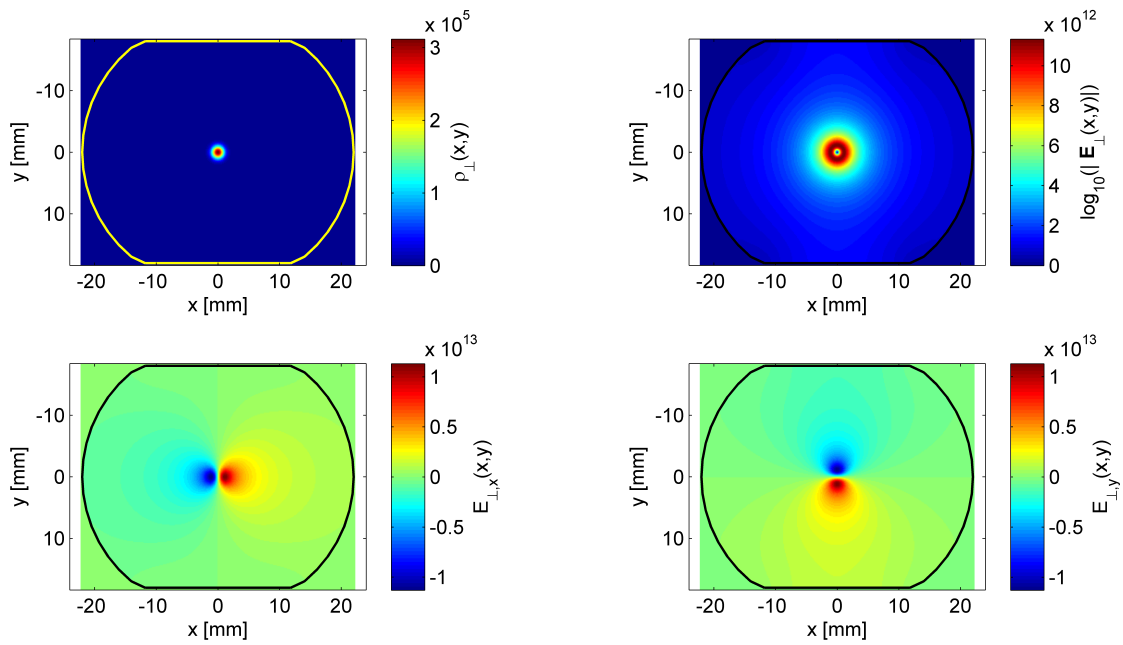

Figure 2.4: The quantities $\rho_\perp(x,y)$, $|\mathbf{E}_\perp(x,y)|$, $E_{\perp,x}(x,y)$, $E_{\perp,y}(x,y)$ for the nominal LHC beam at injection energy inside the arc beam screen.

2.5 PRIMARY ELECTRONS: RESIDUAL GAS IONIZATION

As we already described in Sec. 1.1, the local electron production rate in the beam chamber due to residual gas ionization is given by:

$$\frac{dn_{\text{ion}}}{dt\,dA\,ds} = \sigma_{\text{ion}} n_{\text{gas}} \phi_p(x,y,s,t) \tag{2.21}$$

where dA is an infinitesimal area around (x,y), σ_{ion} is the ionization cross section of the residual gas [14], n_{gas} is the residual gas density (supposed to be uniform in space and constant on the time scale of few beam revolutions), and ϕ_p is the beam particle flux (per unit area). Assuming that the beam is ultrarelativistic and factorized as in Eq. 2.5 we can write:

$$\phi_p(x,y,s,t) = c\rho(x,y,s,t) = c\rho_\perp(x,y)\lambda(s-ct) \tag{2.22}$$

and substituting in the 2.21 we obtain:

$$\frac{dn_{\text{ion}}}{dt\,dA\,ds} = \sigma_{\text{ion}} n_{\text{gas}} c\rho_\perp(x,y,s,t)\lambda(s-ct) \tag{2.23}$$

which shows that the produced electrons have both the same transverse distribution and time dependence of the beam. Using the 2.6 and the 2.23 we can write the number of electrons per unit length produced in each timestep Δt as:

$$\Delta n_{\text{ion}} = \sigma_{\text{ion}} n_{\text{gas}} c\lambda(s-ct)\Delta t \tag{2.24}$$

The number of MPs to be generated at each timestep can be therefore estimated as:

$$N_{\text{ion}}^{MP} = \left\lfloor \frac{\Delta n_{\text{ion}}}{n_{\text{ref}}} \right\rfloor + u \tag{2.25}$$

where u is a random variable which can be 0 or 1 with probability:

$$P\left(u=1\right)=\frac{\Delta n_{\text{ion}}}{n_{\text{ref}}}-\left\lfloor\frac{\Delta n_{\text{ion}}}{n_{\text{ref}}}\right\rfloor \tag{2.26}$$

This is done in order to avoid populating the chamber with very small MPs and keep the MP size as close as possible to n_{ref} (see also Sec. 2.2). The generated MPs have therefore size n_{ref} and are distributed within the chamber according to $\rho_{\perp}(x,y)$.

2.6 PRIMARY ELECTRONS: PHOTOEMISSION DUE TO SYNCHROTRON RADIATION

Concerning the primary electron generation due to photoemission (see Sec. 1.1), the number k_{PE} of photoeletrons to be generated per beam particle and per unit length along the beam trajectory is specified by the user. Therefore the number of electrons per unit length to be generated at each time step is given by:

$$\Delta n_{\text{PE}}=k_{\text{PE}}c\lambda(s-ct)\Delta t \tag{2.27}$$

and, like in the case of the ionization of the residual gas, the number of MPs to be generated is given by:

$$N_{\text{PE}}^{MP}=\left\lfloor\frac{\Delta n_{\text{PE}}}{n_{\text{ref}}}\right\rfloor+u \tag{2.28}$$

where u is a random variable which can be 0 or 1 with probability:

$$P\left(u=1\right)=\frac{\Delta n_{\text{PE}}}{n_{\text{ref}}}-\left\lfloor\frac{\Delta n_{\text{PE}}}{n_{\text{ref}}}\right\rfloor \tag{2.29}$$

Also in this case, the particles have size n_{ref}. According to a reflection fraction set by the user the MPs to be generated are divided into two sets, i.e. those generated by photons coming directly from the beam, and those generated by photons which have been reflected one or more times on the beam chamber. The two have different distributions on the surface of the beam chamber. The model we employ for the LHC arc magnets is implemented as follows:

- **Non-reflected photons:** the angle of emission θ_{PE} is generated uniformly in the interval $[-\theta_{\text{max}},\theta_{\text{max}}]$ specified by the user. In order to keep the algorithm general with respect to the chamber shape, the MP location is determined by calling the chamber module (see Sec. 2.3) in order to find the crossing point between the chamber's profile and a segment going from the beam location to the point of coordinates $(R_{\text{PE}}\cos\theta_{\text{PE}}, R_{\text{PE}}\sin\theta_{\text{PE}})$, where R_{PE} is the radius of a circle external to the chamber (see Fig. 2.5 left).

- **Reflected photons:** the angular distribution with respect to the impact point of the direct synchrotron light (angle ψ_{PE} in Fig. 2.5 right) is defined by the user in terms of Cumulative Distribution Function (CDF) $F(\psi_{\text{PE}})$. The angle ψ_{PE} can be generated as:

  $$\psi_{\text{PE}}=F^{-1}(u) \tag{2.30}$$

  where u is a random number uniformly generated in the interval $[0,1]$. Again to keep the algorithm independent from the chamber's geometry the MP location is determined by using the chamber module in order to get the crossing point between the chamber's profile and a segment going from the direct syncrhotron light impact point $(x_{0\,PE},0)$ an a point of coordinates $(-2R_{\text{PE}}\cos\psi_{\text{PE}}+x_{0\,PE}, 2R_{\text{PE}}\sin\psi_{\text{PE}})$ (see Fig. 2.5 right).

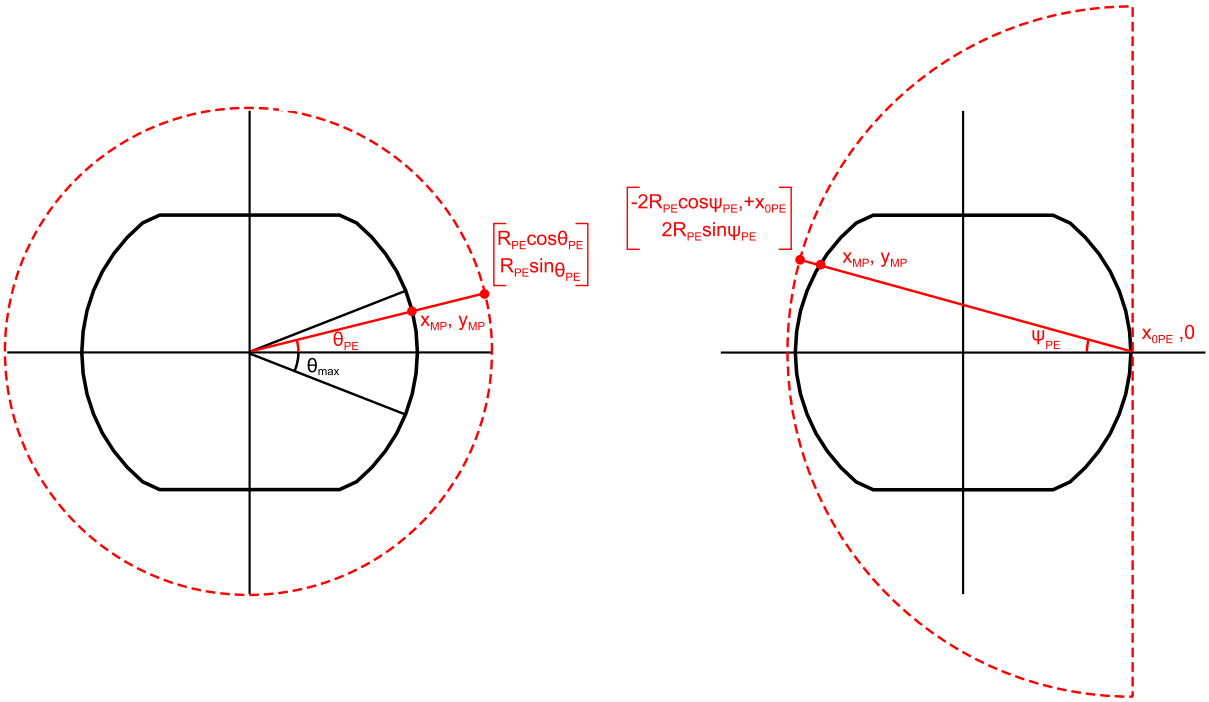

Figure 2.5: Position generation algorithm for photoelectrons from non-reflected (left) and reflected (right) photons.

For both sets the kinetic energy is generated with a Gaussian distribution, truncated to positive values, where mean and standard deviation are defined by the user. The angle of emission with respect to the normal to the chamber's surface is generated uniformly in the interval $\left[0, \frac{\pi}{2}\right]$, and the azimuthal angle uniformly in $[0, 2\pi]$ (this procedure will be explained in more details in the case of MPs generated from secondary emission in Sec. 2.9).

2.7 THE SPACE CHARGE FIELD OF THE EC

For the computation of the electric field due to space charge forces within the EC we use a classical Particle In Cell (PIC) algorithm. We define over the beam chamber's section a square grid of equally spaced points with grid size Δh and $N_x \times N_y$ nodes. The grid extends slightly outside the chamber shape (by at least Δh). The electric field calculation at the MP locations is performed as follows:

(1) **MP scatter:** The charge of each MP is distributed to the four neighbouring nodes of the grid to obtain a discrete approximation of the charge distribution. For this purpose, a first order (area weighting) algorithm is employed.

In particular, for a MP at the location $(x_{\mathrm{MP}}, y_{\mathrm{MP}})$ carrying charge n_{MP}, the indexes of the neighbouring grid nodes can be computed as (see Fig. 2.6):

$$i = \left\lfloor \frac{x_{\mathrm{MP}} - x_0}{\Delta h} \right\rfloor, \quad j = \left\lfloor \frac{y_{\mathrm{MP}} - y_0}{\Delta h} \right\rfloor \tag{2.31}$$

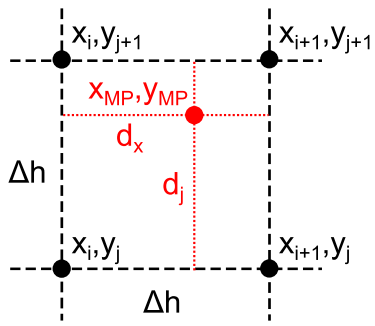

Figure 2.6: Nodes and distances involved in the MP scatter and field gather stages of the space charge field calculation.

where x_0, y_0 is the bottom left corner of the grid. Then the auxiliary distances d_x and d_y (see Fig. 2.6) are computed as:

$$d_x = x_{\mathrm{MP}} - x_0 - i\Delta h, \quad d_y = y_{\mathrm{MP}} - y_0 - j\Delta h \tag{2.32}$$

and the charge density matrix is updated as follows:

$$\rho_{i,j} = \rho_{i,j} + \frac{q\, n_{\mathrm{MP}}}{\Delta h}\left(1 - \frac{d_x}{\Delta h}\right)\left(1 - \frac{d_y}{\Delta h}\right) \tag{2.33a}$$

$$\rho_{i+1,j} = \rho_{i+1,j} + \frac{q\, n_{\mathrm{MP}}}{\Delta h}\left(\frac{d_x}{\Delta h}\right)\left(1 - \frac{d_y}{\Delta h}\right) \tag{2.33b}$$

$$\rho_{i,j+1} = \rho_{i,j+1} + \frac{q\, n_{\mathrm{MP}}}{\Delta h}\left(1 - \frac{d_x}{\Delta h}\right)\left(\frac{d_y}{\Delta h}\right) \tag{2.33c}$$

$$\rho_{i+1,j+1} = \rho_{i+1,j+1} + \frac{q\, n_{\mathrm{MP}}}{\Delta h}\left(\frac{d_x}{\Delta h}\right)\left(\frac{d_y}{\Delta h}\right) \tag{2.33d}$$

(2) **Electrostatic potential computation:** the electrostatic potential $\phi(x, y)$ (defined such that $\mathbf{E} = -\nabla\phi$) is solution of the Poisson equation with homogeneous boundary conditions:

$$\begin{cases} \nabla^2\phi(x,y) = -\dfrac{\rho(x,y)}{\varepsilon_0} & \text{(2.34a)} \\ \phi(x,y) = 0 \qquad \text{on the boundary} & \text{(2.34b)} \end{cases}$$

The differential equation 2.34a is discretized on the grid defined before using the Finite Difference (FD) method (second order):

$$\frac{\phi_{i-1,j} + \phi_{i,j-1} - 4\phi_{i,j} + \phi_{i+1,j} + \phi_{i,j+1}}{\Delta h^2} = -\frac{\rho_{i,j}}{\varepsilon_0} \tag{2.35}$$

The chamber module (see Sec. 2.3) is used to identify the nodes of the grid that fall inside the chamber. At this nodes the Eq.2.35 is enforced, while on the others we impose the zero potential condition:

$$\phi_{i,j} = 0 \tag{2.36}$$

The grid nodes are ordered following a lexicographical rule:

$$\{\rho_{1,1}, \rho_{2,1}, \ldots, \rho_{N_x,1}, \rho_{1,2}, \rho_{2,2}, \ldots, \rho_{N_x,N_y}, \ldots, \ldots, \rho_{1,N_y}, \rho_{2,N_y}, \ldots, \rho_{N_x,N_y}\} \tag{2.37}$$

so that the Eqs. 2.35 and 2.36 can be put matrix form:

$$\underline{\underline{A}}\underline{\phi} = \frac{1}{\varepsilon_0}\underline{\rho} \tag{2.38}$$

where $\underline{\underline{A}}$ is a $N_x N_y \times N_x N_y$ sparse matrix. By solving the system of linear equations it is possible to obtain the electrostatic potential at the nodes of the grid.

(3) **Electric field computation:** the electric field at the internal nodes of the grid can be computed using a central difference formula:

$$(E_x)_{i,j} = -\frac{\phi_{i+1,j} - \phi_{i-1,j}}{2\Delta h}, \quad (E_y)_{i,j} = -\frac{\phi_{i,j+1} - \phi_{i,j-1}}{2\Delta h} \tag{2.39}$$

For boundary nodes a forward difference formula has is adopted.

(4) **Field gather:** again a first order interpolation algorithm is used to obtain the electric field at each MP location:

$$\begin{aligned}\mathbf{E}\left(x_{\mathrm{MP}}, y_{\mathrm{MP}}\right) =& \mathbf{E}_{i,j}\left(1-\frac{d_x}{\Delta h}\right)\left(1-\frac{d_y}{\Delta h}\right) + \mathbf{E}_{i+1,j}\left(\frac{d_x}{\Delta h}\right)\left(1-\frac{d_y}{\Delta h}\right) \\ &+ \mathbf{E}_{i,j+1}\left(1-\frac{d_x}{\Delta h}\right)\left(\frac{d_y}{\Delta h}\right) + \mathbf{E}_{i+1,j+1}\left(\frac{d_x}{\Delta h}\right)\left(\frac{d_y}{\Delta h}\right)\end{aligned} \tag{2.40}$$

In typical simulations the changes of the charge distribution are relatively slow, therefore the electric field map is not updated at each time step but every few ($\sim$ 10) steps in order to speed-up the simulation. The matrix of the linear system in Eq. 2.38 depends only on the chamber's shape and on the defined grid and it is therefore constant all along the buildup simulation. Hence a consistent speed-up can be obtained by pre-computing and storing the its LU factorization in the initialization stage [45, 46].

Figure 2.7 shows the results of the different stages of the space charge calculation for the EC in the circular chamber of a quadrupole magnet.

2.8 TRACKING OF THE ELECTRONS

In Sec. 1.4 we observed that in bending or focusing magnets the electrons perform a fast cyclotron motion around the magnetic field lines. For the values of magnetic field and kinetic energy which are typically involved, within few cyclotron periods the electrons explores a region in which electric and magnetic fields can be assumed to be constant and uniform. Based on these considerations we have developed a tracking algorithm based on the solution of the equation of motion for an electron moving in uniform static electromagnetic field, which can be written, together with the relevant initial condition, as follows:

$$\begin{cases} \dfrac{d\mathbf{v}}{dt} = -\dfrac{q}{m}\left(\mathbf{E} + \mathbf{v}\times\mathbf{B}\right) & \text{(2.41a)} \\ \mathbf{v}(0) = \mathbf{v}_0 & \text{(2.41b)} \\ \mathbf{r}(0) = \mathbf{r}_0 & \text{(2.41c)} \end{cases}$$

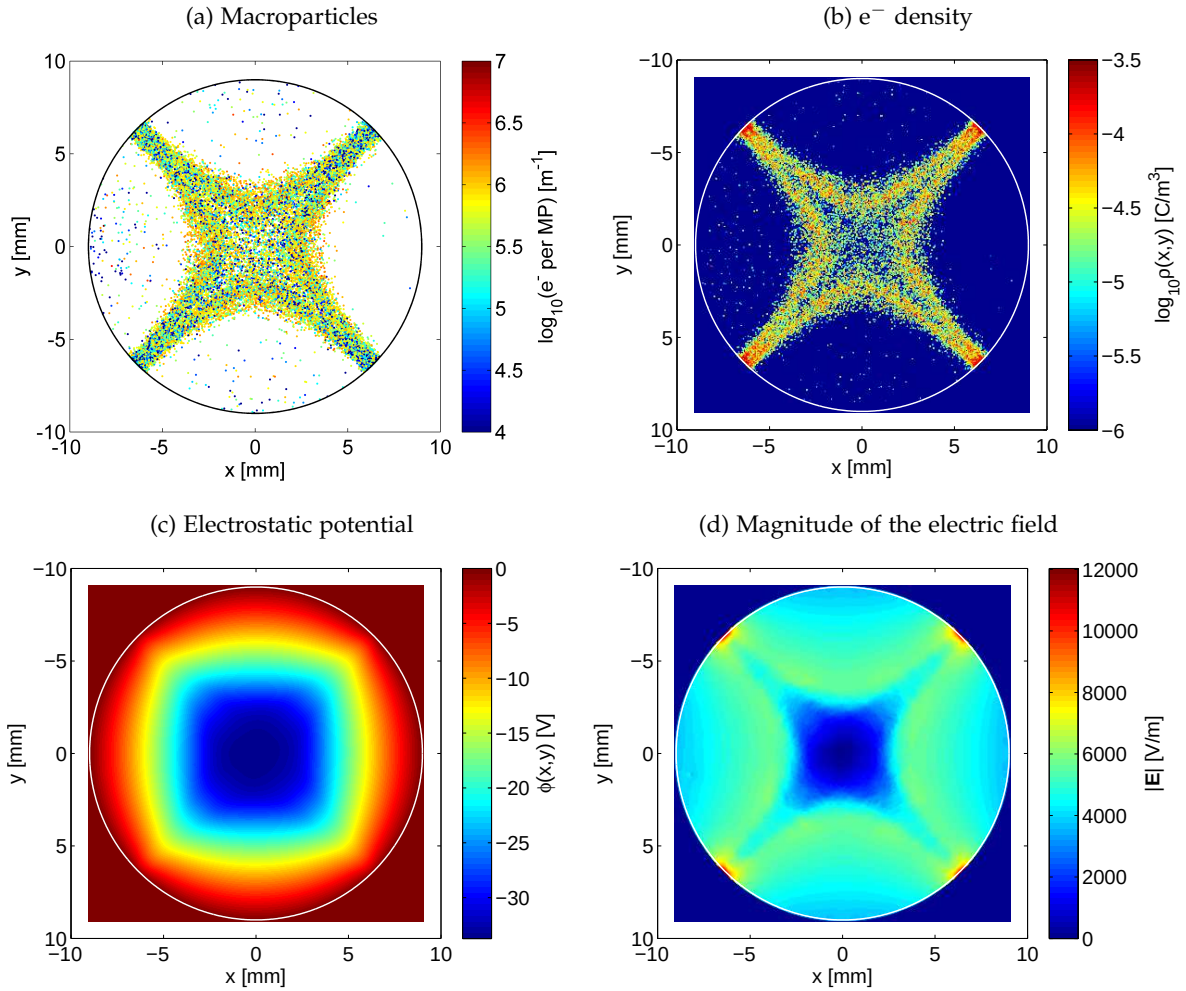

Figure 2.7: The different stages of the space charge calculation for the EC in the circular chamber of a quadrupole magnet (simulation for the positron Damping Ring of the CLIC linear collider).

for a generic particle having charge $-q$ (for an electron q is positive) and mass m. We are interested in the case in which electric and magnetic fields are purely transverse:

$$E_z = 0, \quad B_z = 0 \tag{2.42}$$

we can therefore rewrite the 2.41a as:

$$\begin{cases} \dfrac{dv_x}{dt} = -\dfrac{q}{m}\left(E_x - v_z B_y\right) & (2.43a) \\ \dfrac{dv_y}{dt} = -\dfrac{q}{m}\left(E_y + v_z B_x\right) & (2.43b) \\ \dfrac{dv_z}{dt} = -\dfrac{q}{m}\left(-B_x v_y + B_y v_x\right) & (2.43c) \end{cases}$$

By deriving the 2.43c we obtain:

$$\frac{d^2 v_z}{dt^2} = -\frac{q}{m}\left(-B_x \frac{dv_y}{dt} + B_y \frac{dv_x}{dt}\right) \tag{2.44}$$

and using the 2.43a and 2.43b:

$$\frac{d^2 v_z}{dt^2} + \left(\frac{q}{m}\right)^2 \left(B_x^2 + B_y^2\right) v_z = \left(\frac{q}{m}\right)^2 \left(B_y E_x - B_x E_y\right) \tag{2.45}$$

We define the cyclotron frequency ω_c as:

$$\omega_c = \frac{|q|}{m}\sqrt{B_x^2 + B_y^2} = \frac{|q|}{m}\,|\mathbf{B}| \tag{2.46}$$

and rewrite the 2.45 as:

$$\frac{d^2 v_z}{dt^2} + \omega_c^2 v_z = \left(\frac{q}{m}\right)^2 \left(B_y E_x - B_x E_y\right) \tag{2.47}$$

All the solutions of this equation can be written as:

$$v_z(t) = \tilde{A}\cos(\omega_c t) + \tilde{B}\sin(\omega_c t) + v_z^*(t) \tag{2.48}$$

where $v_z^*(t)$ is a particular solution of 2.47. Since the RHS of 2.47 is constant, a strategy to find a possible $v_z^*(t)$ is to look for a constant solution of 2.47. By doing so we find:

$$v_z^*(t) = \frac{\left(B_y E_x - B_x E_y\right)}{|\mathbf{B}|^2} \tag{2.49}$$

and therefore we can rewrite the 2.48 as:

$$v_z(t) = \tilde{A}\cos(\omega_c t) + \tilde{B}\sin(\omega_c t) + \frac{\left(B_y E_x - B_x E_y\right)}{|\mathbf{B}|^2} \tag{2.50}$$

By imposing the initial condition $v_z(0) = v_{0z}$ (obtained projecting the 2.41b along z), we find:

$$\tilde{A} = v_{0z} - \frac{\left(B_y E_x - B_x E_y\right)}{|\mathbf{B}|^2} \tag{2.51}$$

and we can rewrite the 2.50 as:

$$v_z(t) = v_{0z}\cos(\omega_c t) + \tilde{B}\sin(\omega_c t) + \frac{\left(B_y E_x - B_x E_y\right)}{|\mathbf{B}|^2}\left(1 - \cos(\omega_c t)\right) \tag{2.52}$$

By evaluating the 2.43c at $t = 0$, we find:

$$\left.\frac{dv_z}{dt}\right|_{t=0} = -\frac{q}{m}\left(-B_x v_{0y} + B_y v_{0x}\right) \tag{2.53}$$

We can obtain $\tilde{B}$ deriving the 2.52 and replacing the result in 2.53, obtaining:

$$\tilde{B} = -\frac{\left(B_y v_{0x} - B_x v_{y0}\right)}{|\mathbf{B}|} \tag{2.54}$$

Substituting in the 2.52 we obtain:

$$v_z(t) = v_{0z}\cos(\omega_c t) - \frac{\left(B_y v_{0x} - B_x v_{y0}\right)}{|\mathbf{B}|}\sin(\omega_c t) + \frac{\left(B_y E_x - B_x E_y\right)}{|\mathbf{B}|^2}\left(1 - \cos(\omega_c t)\right) \tag{2.55}$$

$z(t)$ can be obtained by integration:

$$z(t) = z_0 + \int_0^t v_z(t')\, dt' \tag{2.56}$$

which gives:

$$z(t) = z_0 + \frac{v_{0z}}{\omega_c} \sin(\omega_c t) + \frac{(B_y v_{0x} - B_x v_{y0})}{|\mathbf{B}|\, \omega_c} (\cos(\omega_c t) - 1) + \frac{(B_y E_x - B_x E_y)}{|\mathbf{B}|^2} \left(t - \frac{\sin(\omega_c t)}{\omega_c} \right) \tag{2.57}$$

Integrating the 2.43a and 2.43b between 0 and t, and using the 2.56 we obtain the other two components of the velocity:

$$v_x(t) = v_{0x} - \frac{q}{m} \left(E_x t - B_y \left(z(t) - z_0 \right) \right) \tag{2.58a}$$

$$v_y(t) = v_{0y} - \frac{q}{m} \left(E_y t + B_x \left(z(t) - z_0 \right) \right) \tag{2.58b}$$

The components $x(t)$ and $y(t)$ of the trajectory can be obtained by integration of the 2.58a and 2.58b. In order to minimize the computational burden it is useful at this point to introduce the auxiliary quantity:

$$z^P(t) = \int_0^t \left(z(t') - z_0 \right)\, dt' \tag{2.59}$$

From the 2.57 this is given by:

$$z^P(t) = \frac{v_{0z}}{\omega_c^2} (1 - \cos(\omega_c t)) + \frac{(B_y v_{0x} - B_x v_{y0})}{|\mathbf{B}|\, \omega_c} \left(\frac{\sin(\omega_c t)}{\omega_c} - t \right) + \frac{(B_y E_x - B_x E_y)}{|\mathbf{B}|^2} \left(\frac{t^2}{2} + \frac{\cos(\omega_c t)}{\omega_c^2} \right) \tag{2.60}$$

and $x(t)$ and $y(t)$ can then be written as:

$$x(t) = x_0 + v_{x0} t - \frac{q}{m} \left(E_x \frac{t^2}{2} - B_y z^P(t) \right) \tag{2.61a}$$

$$y(t) = y_0 + v_{y0} t - \frac{q}{m} \left(E_y \frac{t^2}{2} + B_x z^P(t) \right) \tag{2.61b}$$

Based on these results, the tracking algorithm implemented in PyECLOUD performs the following steps to update the position and velocity of a MP, given the electric and magnetic field at the MP location:

(1) **Compute $v_z(t_{n+1})$ using the 2.55:**

$$\begin{aligned} v_z(t_{n+1}) =& v_z(t_n) \cos(\omega_c \Delta t) - \frac{(B_y v_x(t_n) - B_x v_y(t_n))}{|\mathbf{B}|} \sin(\omega_c \Delta t) \\ &+ \frac{(B_y E_x - B_x E_y)}{|\mathbf{B}|^2} (1 - \cos(\omega_c \Delta t)) \end{aligned} \tag{2.62}$$

(2) **Compute $z(t_{n+1})$ using the 2.57:**

$$\begin{aligned} z(t_{n+1}) =& z(t_n) + \frac{v_z(t_n)}{\omega_c} \sin(\omega_c \Delta t) + \frac{(B_y v_x(t_n) - B_x v_y(t_n))}{|\mathbf{B}|\,\omega_c} (\cos(\omega_c \Delta t) - 1) \\ &+ \frac{(B_y E_x - B_x E_y)}{|\mathbf{B}|^2} \left(\Delta t - \frac{\sin(\omega_c \Delta t)}{\omega_c} \right) \end{aligned} \tag{2.63}$$

(3) **Compute $v_x(t_{n+1})$ and $v_y(t_{n+1})$ using the 2.58:**

$$v_x(t_{n+1}) = v_x(t_n) - \frac{q}{m} \left(E_x \Delta t - B_y \left(z(t_{n+1}) - z(t_n) \right) \right) \tag{2.64a}$$

$$v_y(t_{n+1}) = v_y(t_n) - \frac{q}{m} \left(E_y \Delta t + B_x \left(z(t_{n+1}) - z(t_n) \right) \right) \tag{2.64b}$$

(4) **Compute $z^P(t_{n+1})$ using the 2.60:**

$$\begin{aligned} z^P(t_{n+1}) =& \frac{v_z(t_n)}{\omega_c^2} (1 - \cos(\omega_c \Delta t)) + \frac{(B_y v_x(t_n) - B_x v_y(t_n))}{|\mathbf{B}|\,\omega_c} \left(\frac{\sin(\omega_c \Delta t)}{\omega_c} - \Delta t \right) \\ &+ \frac{(B_y E_x - B_x E_y)}{|\mathbf{B}|^2} \left(\frac{\Delta t^2}{2} + \frac{\cos(\omega_c \Delta t)}{\omega_c^2} \right) \end{aligned} \tag{2.65}$$

(5) **Compute $x(t_{n+1})$ and $y(t_{n+1})$ using the 2.61:**

$$x(t_{n+1}) = x(t_n) + v_x(t_n)\Delta t - \frac{q}{m} \left(E_x \frac{\Delta t^2}{2} - B_y z^P(t_{n+1}) \right) \tag{2.66a}$$

$$y(t_{n+1}) = y(t_n) + v_y(t_n)\Delta t - \frac{q}{m} \left(E_y \frac{\Delta t^2}{2} + B_x z^P(t_{n+1}) \right) \tag{2.66b}$$

As opposed to purely numerical integration methods like the Boris or the Runge-Kutta algorithms [47], this approach does not force to take a time step much shorter than the cyclotron period, with significant advantages in terms of computational effort.

2.9 IMPACTS OF THE ELECTRONS ON THE CHAMBER'S WALL

PyECLOUD detects and handles he impacts of MPs onto the chamber's wall using the following procedures:

(1) **Impact detection:** the chamber module (see Sec. 2.3) is queried in order to detect which MPs drifted outside the chamber at the last time step.

(2) **MP backtracking:** for all the MPs found outside the chamber, the impact point on the chamber is calculated by the chamber module, as the crossing point between the chamber's profile and the segment joining the MP position at the current and previous time steps[1]. For the i-th MP, such a point will be indicated as $\mathbf{r}_i^{\text{emit}}$. The chamber module also provides for each $\mathbf{r}_i^{\text{emit}}$, the unit vector $\hat{\mathbf{n}}_i$ normal to the chamber's surface at the impact point and pointing towards the inside.

1 Actually the MP is backtracked slightly inside the chamber in order to avoid numerical issues, occurring with MP exactly on the chamber's edge. The amount of such "over-backtracking" is defined by the user as a compromise between accuracy and robustness.

(3) **Computation of the impact parameters:** For each impacting MP the following parameters, which are relevant for the Secondary Emission process, have to be loaded or computed:

- the *total charge* n_i^{imp} carried by the MP;
- the *velocity vector* $\mathbf{v}_i^{\text{imp}}$is simply the result of the the last tracking step (see Sec. 2.8);
- the *kinetic energy* (per electron) is simply given by:

$$E_i^{\text{imp}} = \frac{1}{2} m \left| \mathbf{v}_i^{\text{imp}} \right|^2 \tag{2.67}$$

- the *impact angle* θ_i^{imp} is calculated as:

$$\theta_i^{\text{imp}} = acos \left(- \frac{\mathbf{v}_i^{\text{imp}} \cdot \hat{\mathbf{n}}_i}{\left| \mathbf{v}_i^{\text{imp}} \right|} \right) \tag{2.68}$$

(4) **Secondary Emission:** the parameters computed at the previous stage are provided to a secondary emission module which returns, for each MP, the *total emitted charge* n_i^{emit} given by:

$$n_i^{\text{emit}} = \delta \left(E_i^{\text{imp}}, \theta_i^{\text{imp}} \right) n_i^{\text{imp}} \tag{2.69}$$

and a flag stating if the MP should be treated as an elastically reflected electron or as a true secondary electron. In particular, the probability that the MP is treated as elastically reflected is given by (see also Sec. 1.2):

$$P_i^{\text{refl}} = \frac{\delta_{\text{refl}} \left(E_i^{\text{imp}} \right)}{\delta_{\text{true}} \left(E_i^{\text{imp}}, \theta_i^{\text{imp}} \right) + \delta_{\text{refl}} \left(E_i^{\text{imp}} \right)} \tag{2.70}$$

(5) **Elastic reflection:** for the elastically reflected MPs the velocity of the emitted particle is given by:

$$\mathbf{v}_i^{\text{emit}} = \mathbf{v}_i^{\text{imp}} - 2 \left(\mathbf{v}_i^{\text{imp}} \cdot \hat{\mathbf{n}}_i \right) \hat{\mathbf{n}}_i \tag{2.71}$$

(6) **True secondaries:** for the MP behaving like true secondaries it is possible to have $n_i^{\text{emit}} > n_i^{\text{imp}}$. In some of these cases it will be necessary to spread the emitted charge over more than one MP in order to stay close to the reference MP size n_{ref} (see Sec. 2.2). The number of MP to be emitted is therefore computed as:

$$N_i^{MP} = \left\lfloor \frac{n_i^{\text{emit}}}{n_{\text{ref}}} \right\rfloor \tag{2.72}$$

For each of the emitted MPs the kinetic energy E_i^{imp} is generated following the lognormal distribution presented in Sec. 1.2 and, from this, the magnitude of the corresponding velocity vector is calculated as by:

$$v_i^{\text{emit}} = \sqrt{2 \frac{E_i^{\text{imp}}}{m}} \tag{2.73}$$

The angle of emission θ_i^{emit} with respect to $\hat{\mathbf{n}}_i$ is generated in the interval $\left[0, \frac{\pi}{2}\right]$ with a $cos\,\theta$ distribution, and the azimuthal angle ϕ_i^{emit} with respect to the z direction is generated uniformly in the interval $[0, 2\pi]$. Then the components of $\mathbf{v}_i^{\text{emit}}$ are given by:

$$\begin{aligned} v_{i\,x}^{\text{emit}} &= v_i^{\text{emit}} \left(\cos\,\theta_i^{\text{emit}}\,\hat{n}_{i\,x} + \sin\,\theta_i^{\text{emit}}\,\sin\,\phi_i^{\text{emit}}\,\hat{n}_{i\,y}\right) \\ v_{i\,y}^{\text{emit}} &= v_i^{\text{emit}} \left(\cos\,\theta_i^{\text{emit}}\,\hat{n}_{i\,y} - \sin\,\theta_i^{\text{emit}}\,\sin\,\phi_i^{\text{emit}}\,\hat{n}_{i\,x}\right) \\ v_{i\,z}^{\text{emit}} &= v_i^{\text{emit}} \sin\,\theta_i^{\text{emit}}\,\cos\,\phi_i^{\text{emit}} \end{aligned} \tag{2.74}$$

2.10 SOME CONSIDERATIONS ON THE ACHIEVED SIMULATION PERFORMANCES

The passage from ECLOUD to PyECLOUD had a significant impact on the performances both in terms of accuracy and of computational efficiency. Fig. 2.8 shows a comparison between the two codes in terms of convergence properties with respect to the time step chosen for the simulation. While in ECLOUD it is quite difficult to achieve a good convergence, PyECLOUD gives a good estimate of the total number of electrons in the chamber already for relatively large time steps ($\sim$ 0.1 ns) while a satisfactory convergence is obtained for a time step of the order of 25 ps.

For the same test cases the simulation time required by the two codes is reported in Tab. 2.1 showing that the improvements introduced in PyECLOUD had also a positive impact on the code efficiency.

Furthermore, the new code has been designed in order to offer an increased usage flexibility, allowing to deal with irregular beam structures e. g. non uniform bunch intensity and/or bunch length along the bunch train, irregular bunch spacings and bunch profiles.

Thanks to these new features, PyECLOUD has been already largely applied at CERN for several EC simulation studies for the LHC and its injector chain [48–51]. In particular, as described in detail in Sec. 5.2.1, PyECLOUD simulations have been used to reconstruct the evolution of the SEY of the chambers in the LHC arcs, from the measurement of the heat load deposited on the beam screen of the cryogenic magnets. The new code also allows us to estimate the bunch by bunch energy loss due to the interaction of the beam with the EC and to export the electron distribution seen by each bunch. The first feature allowed us to benchmark the results against bunch by bunch stable phase measurements (see Sec. 5.2.2) while the second was used, together with HEADTAIL simulations, to analyze the instabilities observed in the LHC with 25 ns bunch spacing (see Sec. 5.2.3).

Simulation studies have also addressed the EC formation in the common vacuum chambers of the LHC. Examples of this kind of application will be described in Chapter 6, showing the capability of PyECLOUD to deal with beams made of thousands of bunches with irregular spacings.

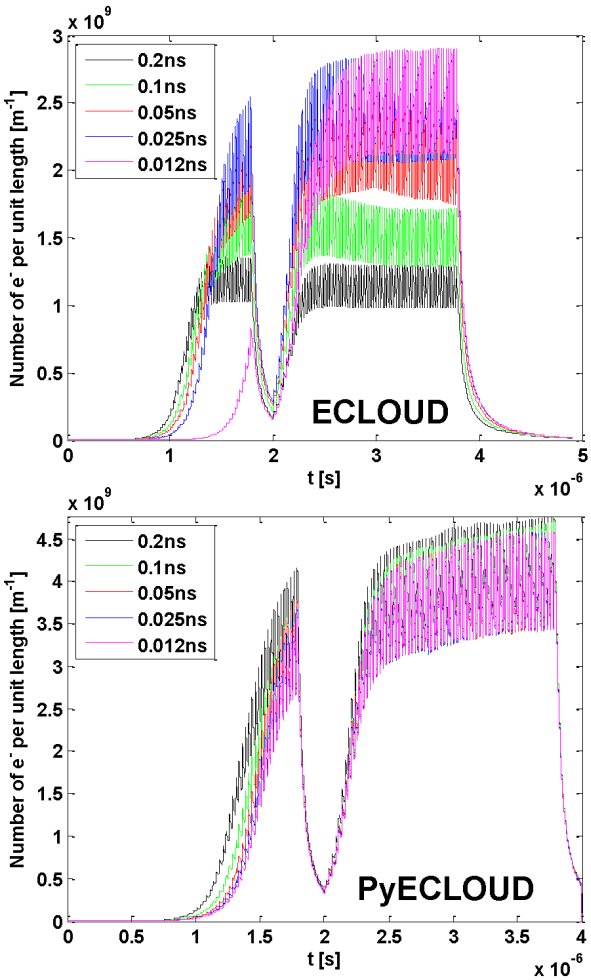

Figure 2.8: Electron cloud build-up simulations for different time steps in ECLOUD (top) and PyECLOUD (bottom). Simulated case: SPS MBB bending magnet, 26 GeV, two trains of 72 bunches with 225 ns gap, 25ns bunch spacing, 1.1×10^{11} protons per bunch.

	Processing time	
Time step [ps]	ECLOUD	PyECLOUD
200	29 min	12 min
100	1 h 27 min	13 min
50	1 h 45 min	24 min
25	3 h 7 min	40 min
12	4 h 15 min	1 h 6 min

Table 2.1: Computation time required by ECLOUD and PyECLOUD for the simualtions in Fig. 2.8.

Part II

ELECTRON CLOUD STUDIES AT THE LHC

3

THE LARGE HADRON COLLIDER (LHC)

The Large Hadron Collider (LHC) is the world's largest and most powerful particle collider. It was built by the European Organization for Nuclear Research (CERN) from 1998 to 2008 with the aim of testing the predictions of different theories of particle and high-energy physics, and in particular of proving (or disproving) the existence of the theorized Higgs particle and of the large family of new particles predicted by supersymmetric theories.

The LHC was built in collaboration with over 10,000 scientists and engineers from over 100 countries, as well as hundreds of universities and laboratories. It lies in a 27 km underground tunnel, on average 100 m deep, across the Franco-Swiss border near Geneva, Switzerland.

As of 2014, the LHC remains one of the largest and most complex experimental facilities ever built. Its synchrotron is designed to accelerate and collide two counter-rotating particle beams of either protons at up to an energy of 7 TeV, or lead nuclei up to 574 TeV per nucleus.

The collision products are analyzed by four major experiments located in large caverns excavated at the LHC's intersection points (ATLAS, CMS, LHCb and ALICE) and by few other much smaller detectors for very specialized research (e. g. TOTEM, LHCf).

Collision data were anticipated to be produced at an unprecedented rate of tens of petabytes per year, to be analyzed by a grid-based computer network infrastructure connecting 140 computing centers in 36 countries (by 2012 the LHC Computing Grid was the world's largest computing grid, comprising over 170 computing facilities in a worldwide network across 36 countries).

The LHC operation with beam started on 10 September 2008, with proton beams successfully circulated in the main ring of the LHC for the first time but 9 days later a faulty electrical connection led to the rupture of a liquid helium enclosure, causing both a magnet quench and several tons of helium gas escaping with explosive force. This incident delayed further operations by 14 months. On November 20, 2009 proton beams were successfully circulated again, with the first recorded proton-proton collisions occurring 3 days later at the injection energy of 450 GeV per beam. On March 30, 2010, the first collisions took place between two 3.5 TeV beams, setting a world record for the highest-energy man-made particle collisions, and the LHC began its planned research program. The LHC operated at 3.5 TeV per beam in 2010 and 2011 and at 4 TeV in 2012. It operated for two months in 2013 colliding protons with lead nuclei, and went into shutdown for maintenance and consolidation in order to increase beam energy to 6.5 TeV per beam, with beam operation restart planned for early 2015.

By 2013, the LHC had recorded the first observations of the very rare decay of the B_s meson into two muons ($B_s^0 \to \mu^+\mu^-$) (a major test of supersymmetry), created a quark-gluon plasma, and discovered two previously unobserved particles, i. e. the $\chi_b(3P)$ bottomonium state and a massive 125 GeV boson which has been confirmed to be the long-sought Higgs boson

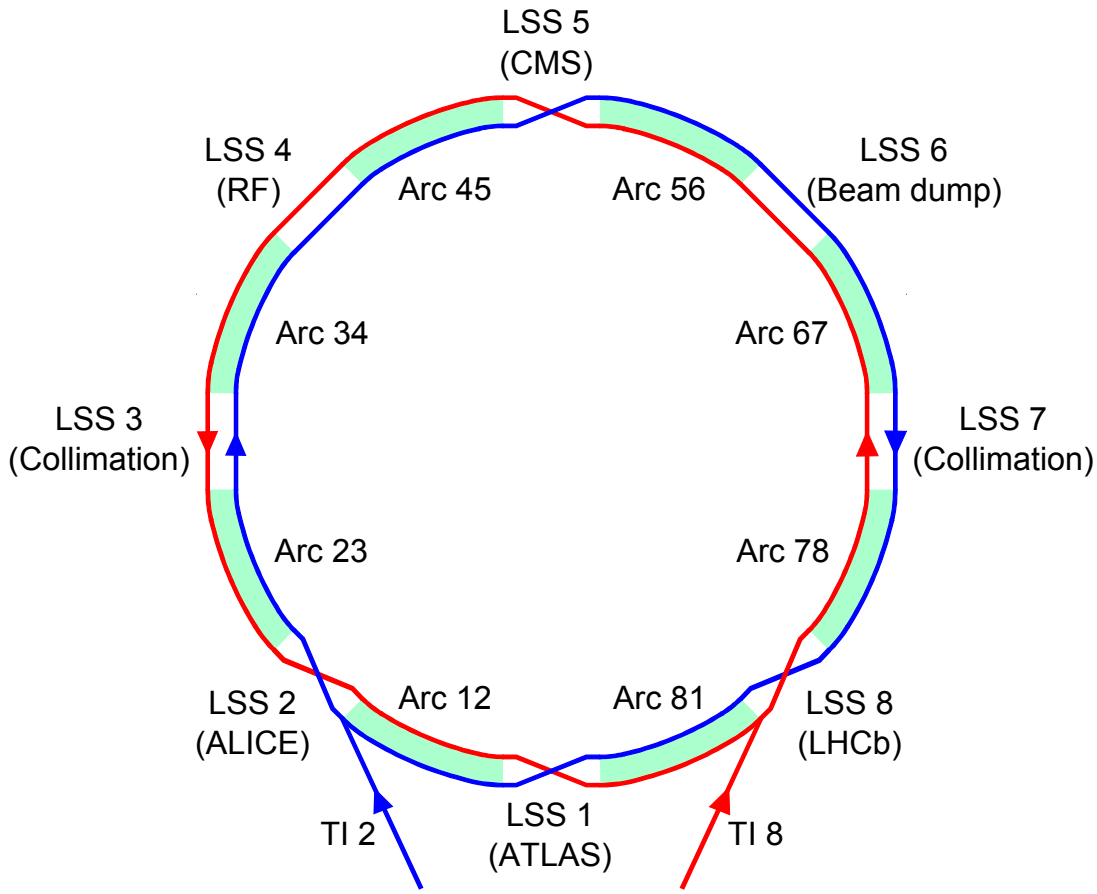

Figure 3.1: Schematic layout of the LHC. Beam 1 circulates clockwise and Beam 2 counter-clockwise.

(following this observation, the 2013 Nobel Prize was awarded to Peter Higgs and Francois Englert who theorized the existence of this particle in 1964).

A detailed description of the main features and subsystem of the LHC can be found in [52]. In the following sections we will briefly recall those which are more relevant with respect to the present thesis work.

3.1 MACHINE LAYOUT AND BEAM PROPERTIES

The LHC is designed as a proton-proton collider with separate magnet fields and vacuum chambers, with common sections (where the two beams circulate in the same chamber) only at the insertion regions where the experimental detectors are located. The two beams share an approximately 130 m long common beam pipe along the interaction regions (IRs).

Since there is not enough room for two separate rings of magnets in the tunnel (which was previously hosting the LEP collider), the LHC uses twin bore magnets which consist of two sets of coils and beam channels within the same mechanical structure and cryostat.

The LHC has eight arcs and straight sections (see Fig. 3.1). Each straight section is approximately 528 m long and can serve as an experimental or utility insertion. The two high luminosity experimental insertions are located at diametrically opposite straight sections: the ATLAS experiment is located at point 1 and the CMS experiment at point 5. Two more experimental insertions are located at point 2 and point 8 which also contain the injection systems

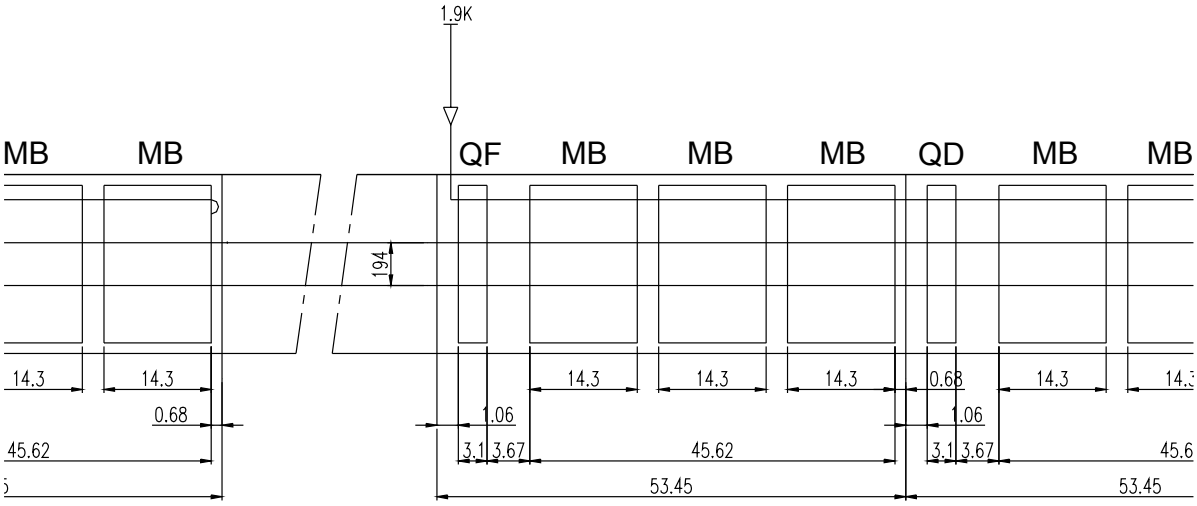

Figure 3.2: Schematic layout of an LHC arc half-cell.

for Beam 1 and Beam 2, respectively. The beams only cross from one magnet bore to the other at these four locations (a more detailed description of the four experimental insertion regions will be presented in Chapter 6). The remaining four straight sections do not have beam crossings. Insertion 3 and 7 contain the collimation systems. Insertion 4 contains two RF systems, one independent system for each LHC beam. The straight section at point 6 contains the beam dump insertion where the two beams are vertically extracted from the machine using a combination of horizontally deflecting fast-pulsed magnets and vertically-deflecting septum magnets. Each beam features an independent abort system.

The arcs of LHC lattice are made of 23 regular arc cells (classical FODO lattice [53]). The arc cells are 106.9 m long and are made out of two 53.45 m long half cells each of which contains four main magnets (see Fig. 3.2), i. e. one 3.1 m long quadrupole magnet and three 14.3 m long dipole magnets.

The two apertures for Ring 1 and Ring 2 are separated by 194 mm. The two coils in the dipole magnets are powered in series and all dipole magnets of one arc form one electrical circuit. The quadrupoles of each arc form two electrical circuits: all focusing quadrupole magnets in Ring 1 and Ring 2 are powered in series and all defocusing quadrupole magnets of Beam 1 and Beam 2 are powered in series. The optics of Beam 1 and Beam 2 in the arc cells is therefore strictly coupled via the powering of the main magnetic elements.

The section of the LHC arc dipole is shown in Fig. 3.3 where one can see the separate bores for the two counter-rotating beams. The superconducting coils operate at 1.9 K, which is also the temperature of the circular vacuum pipe (the *cold bore*), directly in contact with the coils. A stainless steel *beam screen* is inserted in the cold bore, hold with low thermal conductance supports and cooled with a liquid helium circuit. The function of the beam screen is to absorb and remove the beam induced heating due to the longitudinal beam coupling impedance of the screen itself, to synchrotron radiation and to EC effects. In order to increase the surface conductivity (and therefore to reduce impedance related effects) the beam screen is colaminated with copper. The section of the beam screen installed in the LHC arc dipole and quadrupole magnets is show in Fig. 3.4

The main parameters of the LHC machine and of the design proton beam are reported in Tab. 3.1. The proton bunches in the machine are spaced by 25 ns (corresponding to about 7.5 m

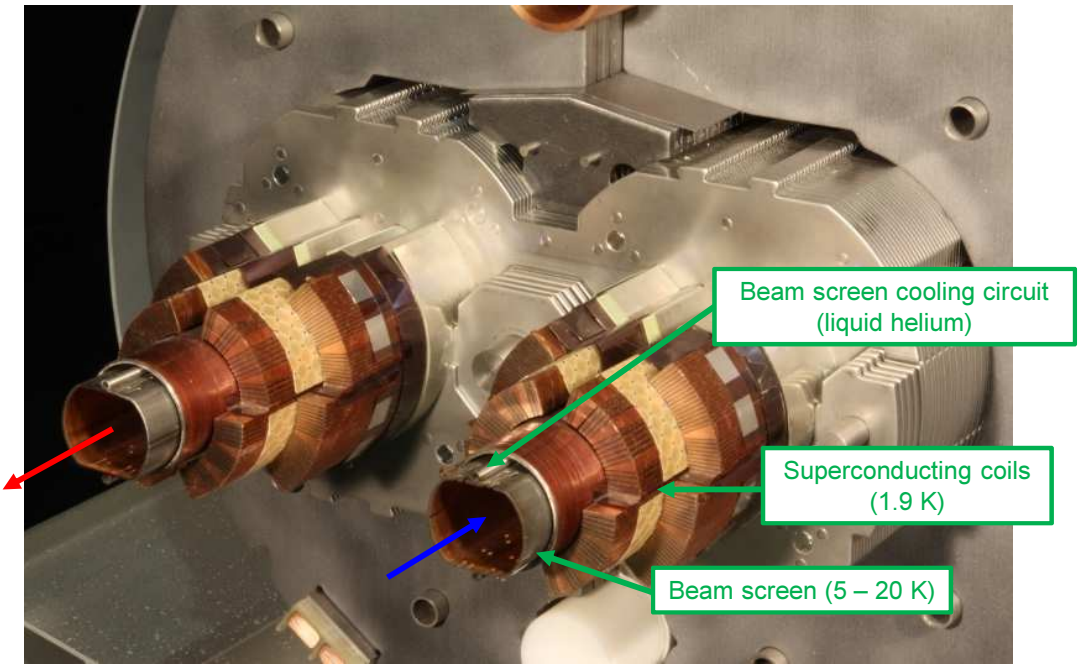

Figure 3.3: Section of an LHC arc dipole magnet.

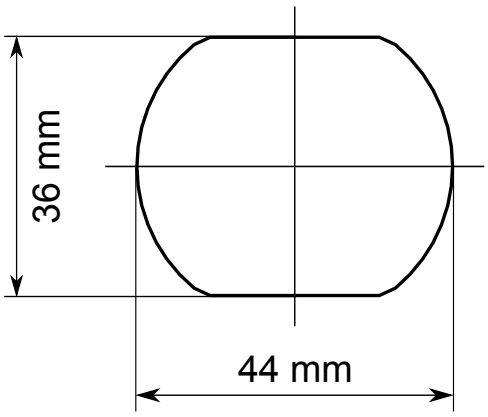

Figure 3.4: Transverse profile of the LHC arc beam screen.

		Injection	Collision
Proton momentum	[GeV/c]	450	7000
Relativistic gamma		479.6	7461
Number of particles per bunch		1.15×10^{11}	
Number of bunches		2808	
Bunch spacing	[ns]	25	
Longitudinal emittance (4σ)	[eVs]	1.0	2.5
Transverse normalized emittance	[$\mu mrad$]	3.5	3.75
RMS beam size in arc	[mm]	1.19	0.3
RMS energy spread $\delta E/E_0$	[10^4]	3.06	1.129
RMS bunch length	[cm]	11.24	7.55
Synchrotron radiation power per ring	[W]	6.15×10^2	3.6×10^3
Field of main bends	[T]	0.535	8.33
Maximum dispersion in arc	[m]	$2.018(h)/0.0(v)$	
Minimum horizontal dispersion in arc	[m]	0.951	
Maximum β in arc	[m]	$177(h)/180(v)$	
Minimum β in arc	[m]	$30(h)/30(v)$	
Horizontal tune		64.28	64.31
Vertical tune		59.31	59.32
Revolution frequency	[kHz]	11.245	
RF frequency	[MHz]	400.8	
Harmonic number		35640	
Total RF voltage	[MV]	8	16
Synchrotron frequency	[Hz]	61.8	21.4

Table 3.1: Main parameters of the LHC machine and of its proton beam.

since the particles' velocity is extremely close to the speed of light). They are not uniformly distributed along the ring but organized as shown in Fig. 3.5. The bunches are grouped in several trains, each corresponding to a different injection from the injector complex (see Sec. 3.2). The trains are separated by gaps of 925 ns, i. e. the rise time of the LHC Injection Kicker (MKI). Each train is in turn composed by two or four batches of 72 bunches. The batches are separated by gaps of 225 ns, i. e. the risetime of the SPS (see Sec. 3.2) injection kicker (MKP). A gap of 3 μs (abort gap) is left at the tail of the beam in order to allow for a clean extraction to the beam dump. At the head of the LHC beam there is a short train of 12 bunches which is the first injected in the machine for safety reasons.[1]

The LHC ran with a beam energies of 3.5 TeV in 2011 and of 4 TeV in 2012. Due to several considerations, and in particular to be less sensitive to EC effects, during this period the

1 This safety measure was not included in the LHC design. For this reason the presented filling pattern features 2748 bunches against the 2808 foreseen in the design.

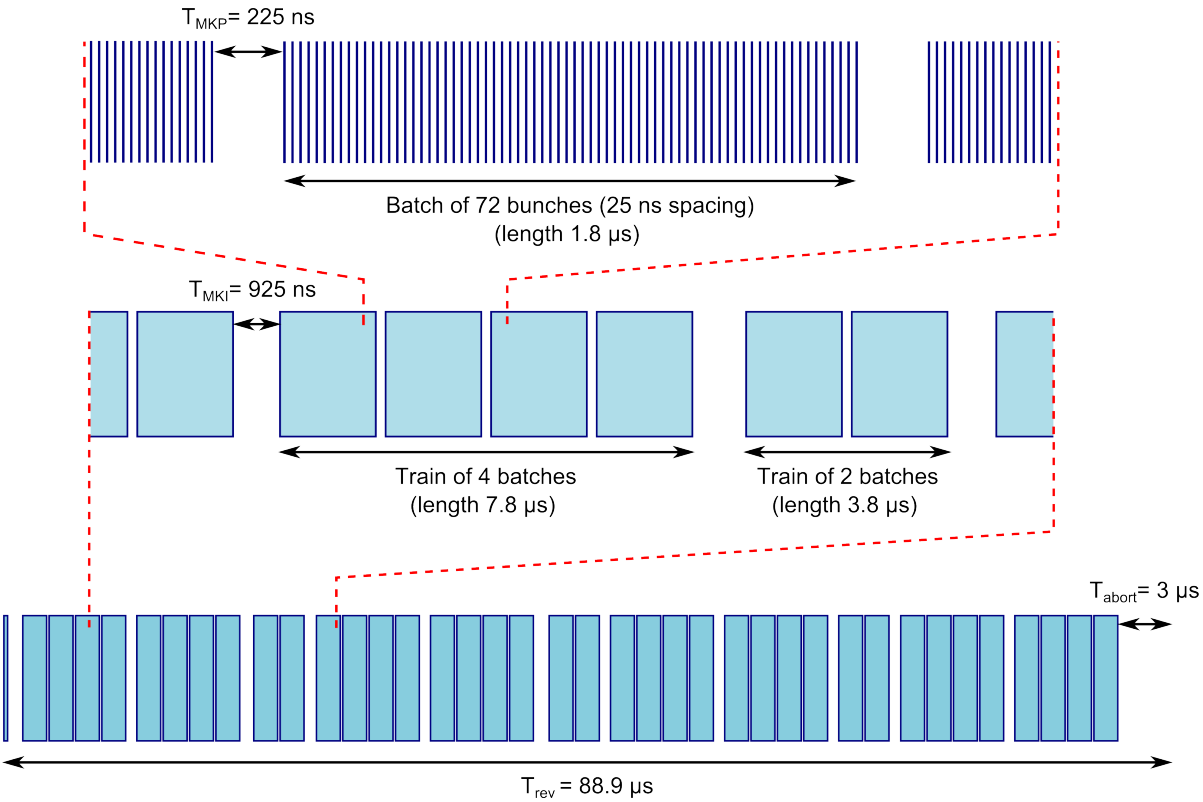

Figure 3.5: Longitudinal structure of one of the LHC beams.

machine was operated mainly with a bunch spacing of 50 ns. Apart from minor changes, the filling pattern was obtained from the one presented in Fig. 3.5 by suppressing the odd bunches in half of the trains and the even bunches in the other half (allowing for head on collisions in ATLAS, CMS and LHCb). With this bunch spacing the injectors were capable of delivering beams with intensities of up to 1.7×10^{11} ppb and transverse emittances as small as $2.4\mu m$ allowing for a compensation of the loss in collision rate (luminosity) due to the smaller number of bunches (1374). Moreover it was decided to run with bunch lengths of about 1.3 ns, slightly larger than nominal, since this was found to be beneficial with respect to beam induced heating in several machine elements.

3.2 PRODUCTION OF THE LHC BEAM IN THE INJECTOR COMPLEX

The 450 GeV/c proton beam injected into the LHC is produced using a chain of four particle accelerators (see Fig. 3.6).

Protons are produced by a duoplasmatron source and accelerated up to a kinetic energy of 50 MeV by the **Linac2** linear accelerator.

The 50 MeV protons are injected into the first circular machine of the chain, the **Proton Synchrotron Booster (PSB)** having 157 m circumference. The PSB is a synchrotron made of four superimposed rings. Right after the injection in the machine the protons in each ring are captured in one bunch by the RF system at the harmonic number h=1 and accelerated up to a kinetic energy of 1.4 GeV.

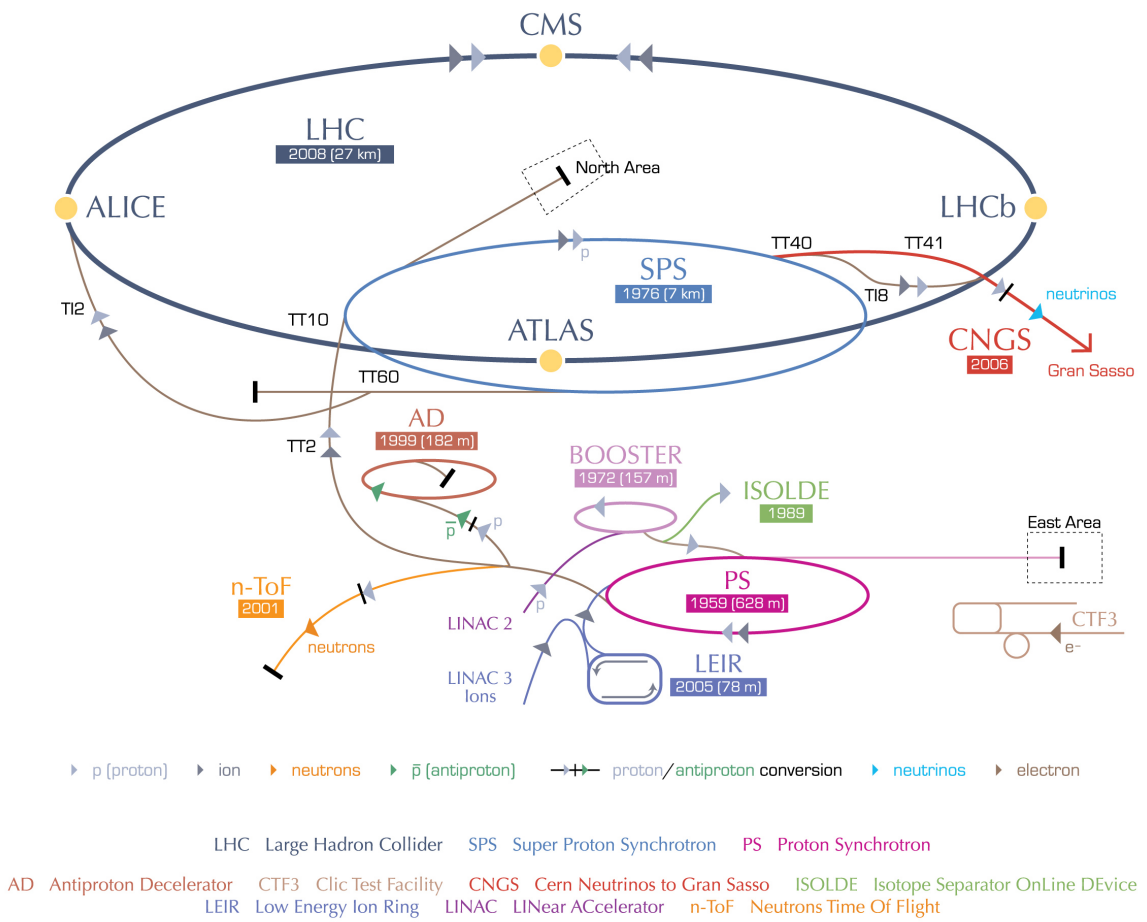

Figure 3.6: The CERN accelerator complex.

The 1.4 GeV proton bunches from the four rings of the PSB are then transferred to the **Proton Synchrotron (PS)** having 628 m circumference. The PSB can provide beam to the PS with a repetition time of 1.2 s. Two subsequent PSB cycles are used for injecting six proton bunches (four from the first injection and two from the second one) into the PS on a harmonic number h=7. Right after the second injection an RF manipulation called triple bunch splitting is performed in order to obtain from the six bunches on the h=7 harmonic, 18 bunches on h=21. The h=21 RF system is used to accelerate the beam up to a particle momentum 26 GeV/c. The 18 bunches, spaced by about 100 ns, then undergo two further bunch splitting stages, i. e. from h=21 to h=42, giving 36 bunches with 50 ns spacing, and from h=42 to h=84 giving the final configuration with 72 bunches with 25 ns spacing. After a bunch shortening stage, the bunches are extracted towards the next ring of the chain, the **Super Proton Synchrotron (SPS)** having 7 km circumference. The PS can provide LHC-type beams to the SPS with a repetition time of 3.6 s.

Two or four batches of 72 bunches with 25 ns spacing are stored in the SPS ring at 26 GeV/c, accelerated up to 450 GeV and transferred to the LHC. The SPS can provide a bunch train to the LHC with a minimum repetition time of about 20 s.

The production scheme for beams with 50 ns spacing is very similar to that for 25 ns beams, the major difference being the suppression of the last bunch splitting stage in the PS.

4

SIMULATION STUDIES FOR THE MAIN LHC ARC COMPONENTS

The dipole and quadrupole magnets of the cryogenic arcs constitute about 75% of the total length of the LHC. The presence of an EC in the beam chambers of these magnets can strongly impact the performance of the machine. The heat load due to the electrons impacting the beam screen can be comparable to the available cooling power, which results in a limitation of the maximum beam intensity that can be stored and, therefore, on the luminosity. Moreover, due to the extent of the integrated length, the presence of a consistent electron density in these chambers can have serious detrimental effects on the beam quality, especially at injection energy, inducing transverse instabilities, transverse emittance growth, and proton loss.

Therefore an extensive PyECLOUD simulation campaign has been performed in order to study the EC buildup in these magnets and its dependence on different beam parameters. The main results of these studies will be presented in the following sections, while EC related experimental observations at the LHC will be treated in the following chapter.

In all the simulations of the present chapter we have used the secondary emission model presented in Sec. 1.2, with the relevant parameters for the copper coating applied in the arc beam screen.

For the simulations at injection energy we have modeled the realistic chamber shape using the FD solver embedded in PyECLOUD (see Sec. 2.4) to obtain the beam field on a square grid fine enough to correctly sample the transverse beam profile. This was not possible for the 7 TeV cases, where the required grid size would have been computationally too demanding for the implemented FD solver. In these cases we decided to approximate the beam chamber with an ellipse tangent to the actual shape at the positions where multipacting is occurring and to use the analytic formula for the beam field (see Sec. 2.4). The values used for the semiaxes are: x_{chamb} = 22 mm, y_{chamb} = 17.3 mm for the dipole and x_{chamb} =y_{chamb} = 22 mm for the quadrupole.

4.1 DIPOLE MAGNETS

The EC buildup in the arc dipoles has been simulated both at injection energy (450 GeV) and at the design collision energy (7 TeV). The SEY parameter (see Sec. 1.2) has been scanned in order to simulate different conditioning states of the beam screen surface.

Figure 4.1 shows the dependence of the EC induced heat load on the SEY both for 50 ns and 25 ns bunch spacing. The multipacting thresholds (see Sec. 1.3) can be localized at SEY $\simeq$ 1.45 for the 25 ns beam and SEY $>$ 2.0 for the 50 ns beam. The difference between 450 GeV and 7 TeV is more evident in the seed accumulation regime (see Sec. 1.3) and is mainly due to the different seeding mechanism, since photoemission at high energy is much stronger compared to the residual gas ionization occurring at injection energy.

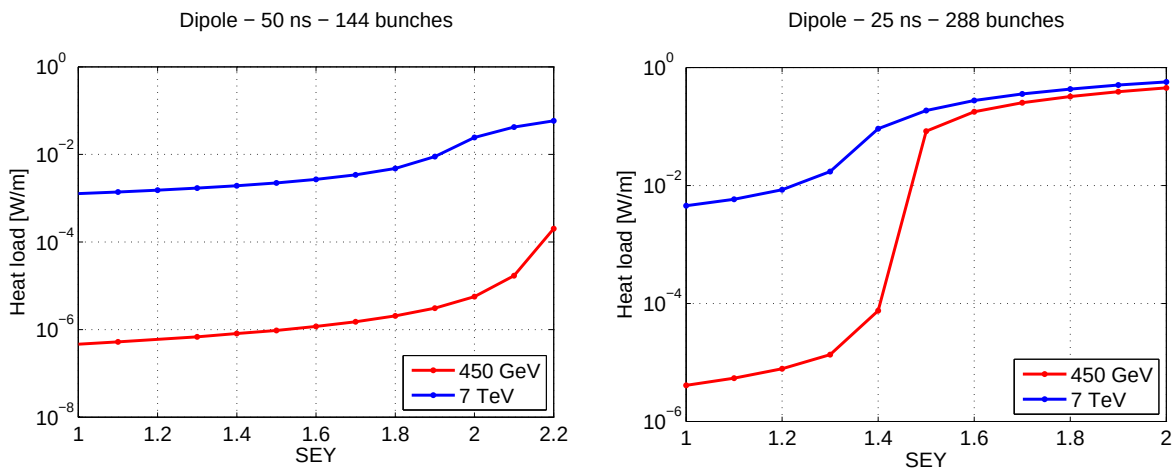

Figure 4.1: Heat load in the LHC arc dipoles as a function of the SEY parameter for a single bunch train.

The electron distribution in the x-y plane shows the vertical stripes which are typical for dipolar magnetic field and are a direct consequence of the electron trapping around the field lines and of the presence of regions with maximum multipacting because of the shape of the SEY curve (see Sec. 1.4).

Snapshots taken at different moments during and after the bunch passage are presented in Fig. 4.2. The electrons are mainly concentrated in two wide vertical stripes lateral to the beam and in a narrower stripe around the beam location. We can observe that the pinch of the cloud is faster for the electrons in this central stripe, due to the strongest kick from the beam, and the time of flight of this electrons is actually comparable to the bunch length. This means that a large fraction of these electrons reach the beam position while the bunch is still there, and therefore can have a strong impact for beam quality. Moreover the fact that this electrons closely interact with the beam makes the EC buildup in this region very sensitive to small variations of the beam parameters (see also Secs. 4.4, 4.5, and 4.6).

Figures 4.3, 4.4 and 4.5 show some further detail for the case of 25 ns bunch spacing. Looking at the evolution of the number of electrons per meter of beam chamber (Fig. 4.3), we notice that an increase in SEY translates both in a faster rise of the EC and in a larger saturation level. The main difference between injection and collision energy is the different number of seed electrons, which allows the EC to reach saturation earlier along the train at 7 TeV with respect to 450 GeV.

Figure 4.4 shows the distribution of the electron current to the wall as a function of the horizontal position. Since this quantity is often used for scrubbing dose estimations, electrons with energy lower than 20 eV are not taken into account in the flux estimation since they do not effectively contribute to the scrubbing process (see Sec. 1.2.1). We can notice that when the SEY decreases the central region tends to be depleted of electrons before the lateral ones. In the 7 TeV case we can clearly see the effects of the seeding from photoelectrons, namely a small peak in the left part, where the synchrotron radiation is directly impinging, and a flux of about 10^{-2} A/m^2 spread over the chamber, which is due to multipacting seeded by the reflected photons.

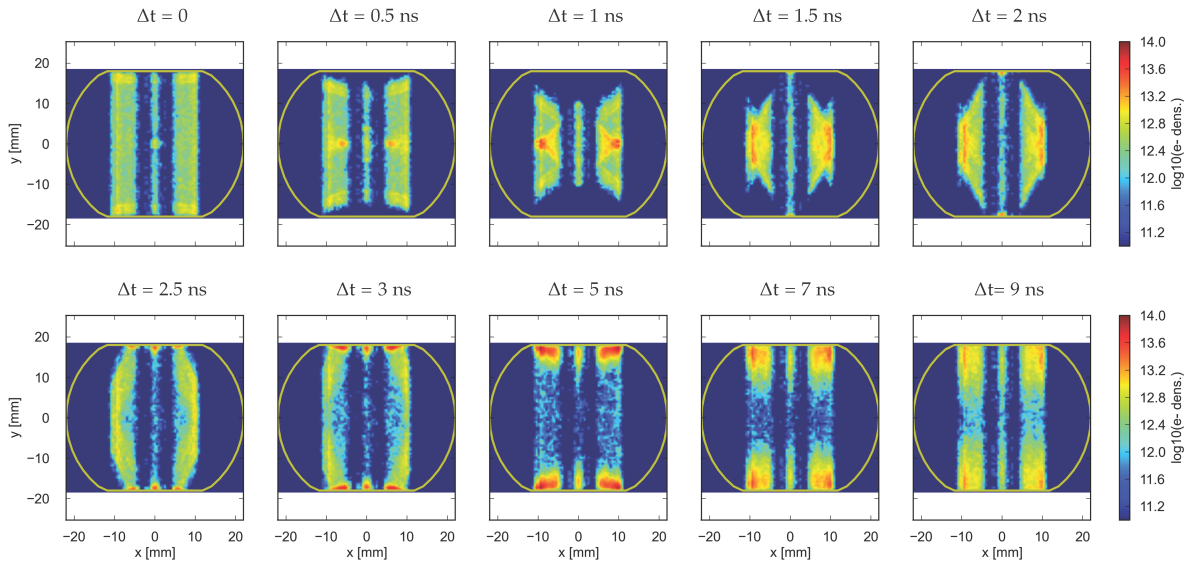

Figure 4.2: Different snapshots of the simulated EC pinch in the LHC arc dipoles, for a bunch passage in the EC saturation stage. The simulation is performed at injection energy, with 25 ns bunch spacing, for SEY = 1.6. $\Delta t = 0$ corresponds to the passage of the head of the bunch at the simulated section.

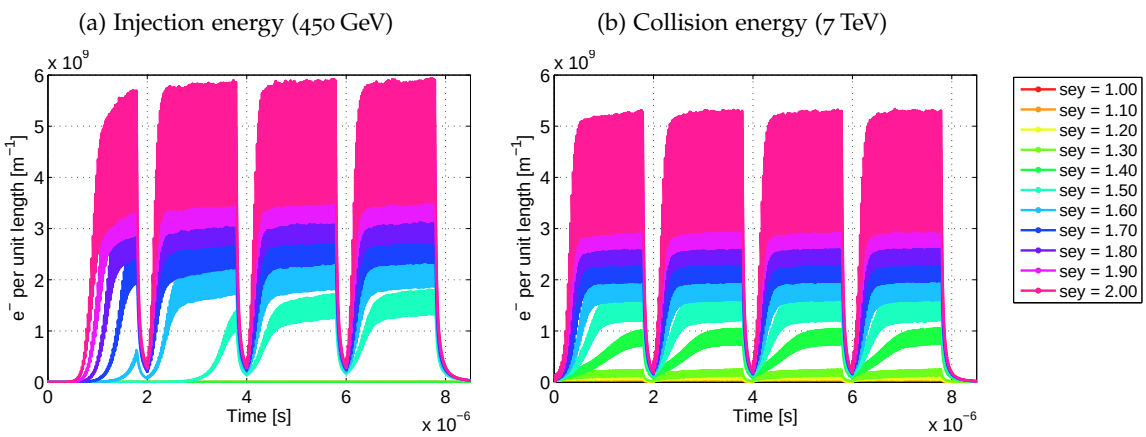

Figure 4.3: Evolution of the total number of electrons in the beam chamber of the LHC arc dipoles during the passage of a bunch train. Simulations for injection (a) and collision (b) energy, 25 ns bunch spacing.

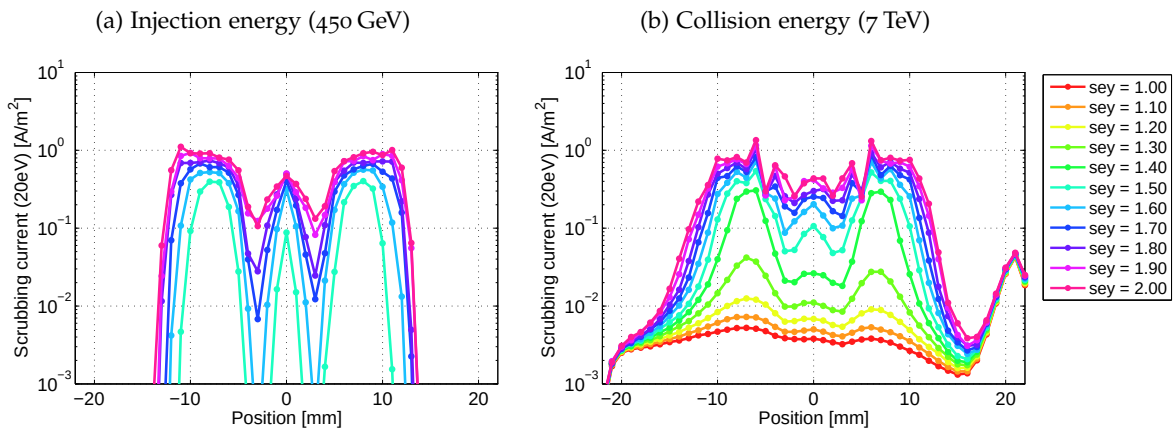

Figure 4.4: Horizontal distribution of the current of scrubbing electrons on the LHC arc dipole beam screen. Simulations for injection (a) and collision (b) energy, 25 ns bunch spacing. The buildup is simulated for a single bunch train and reascaled to the nominal number of bunches.

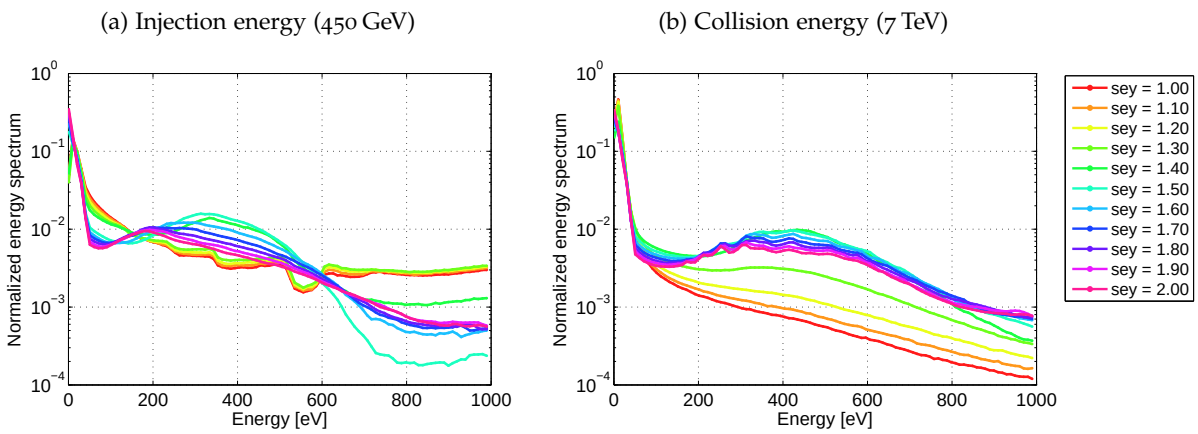

Figure 4.5: Normalized energy spectrum of the electrons impacting the wall in an arc dipole magnet. Simulations for injection (a) and collision (b) energy, 25 ns bunch spacing.

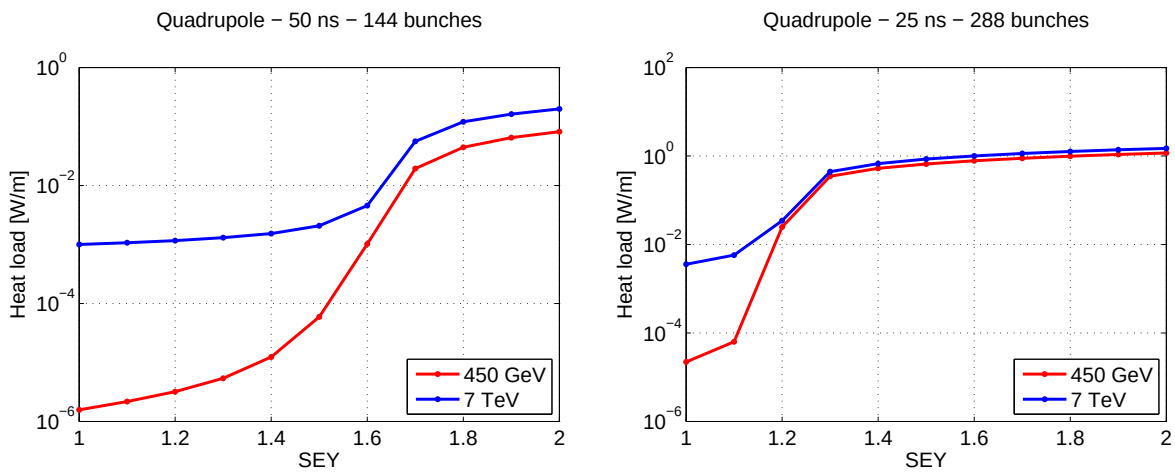

Figure 4.6: Heat load in the LHC arc quadrupoles as a function of the SEY parameter for a single bunch train.

Finally in Fig. 4.5 we present the energy spectrum of the impinging electrons. The 450 GeV and the 7 TeV case exhibit similar features, apart from a different behavior in the seed accumulation regime due to the different seeding mechanism. In both cases we can note a peak of low energy electrons, which are mainly secondaries that reach the wall without being accelerated by a bunch and a bump around 300 eV which is due to the electrons located in the regions where multipacting is occurring. These electrons receive from the beam the right acceleration to reach the wall with energies for which the SEY is larger than one.

4.2 QUADRUPOLE MAGNETS

As was done for the dipoles, we have simulated the EC buildup in the arc quadrupoles both at injection energy (450 GeV) and at the design collision energy (7 TeV) for different values of the SEY parameter.

Figure 4.6 shows the dependence on the SEY of the EC induced heat load both for 50 ns and 25 ns bunch spacing. We can localize the multipacting thresholds at SEY $\simeq$ 1.65 for the 50 ns beam and at SEY $\simeq$ 1.25 the 50 ns beam. In both cases the thresholds are much lower compared to the corresponding values for the dipole magnets. This is mainly due to the fact that the electrons can be trapped due to the magnetic field gradient and therefore the decay of the EC after the bunch passage is much slower. Again the difference between 450 GeV and 7 TeV is mainly due to the different seeding regime and is evident in the seed accumulation regime.

From the snapshots in Fig. 4.7 we can observe that the electron distribution in the x-y plane is mainly concentrated along the pole-to-pole lines and that the central density can reach quite high values during the bunch passage.

The evolution of the number of electrons per meter of beam chamber displayed in Fig. 4.8 shows that an increase of the SEY translates both in a faster rise of the EC and in a larger saturation level.

Differently from the case of the dipoles, we can notice that the number of electrons that accumulate in the beam pipe is almost twice larger in the 450 GeV case compared to 7 TeV.

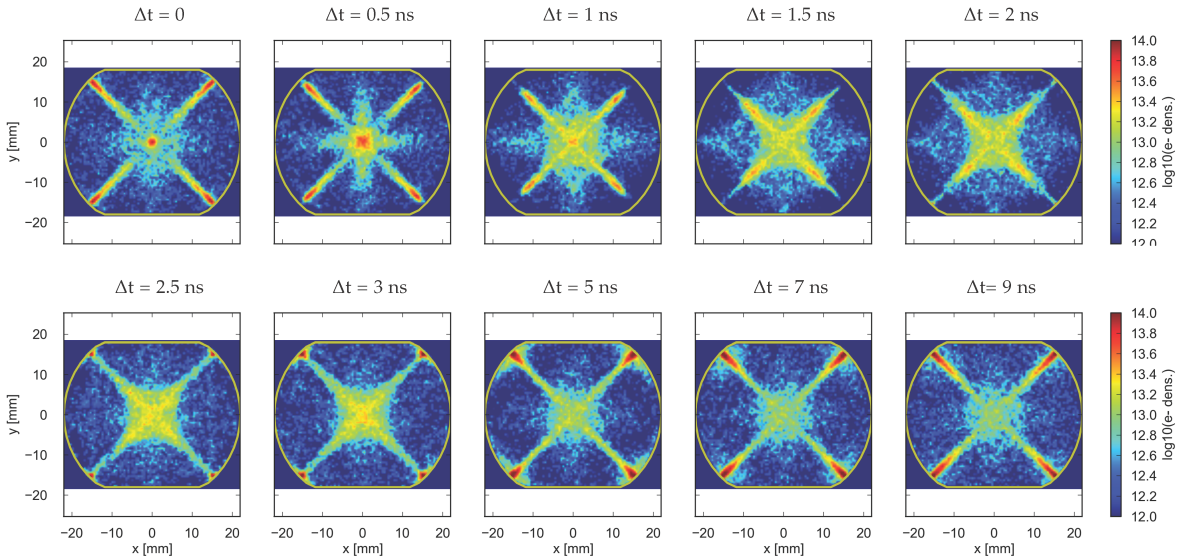

Figure 4.7: Different snapshots of the simulated EC pinch in the LHC arc quadrupoles for a bunch passage in the EC saturation stage. The simulation is performed at injection energy, with 25 ns bunch spacing, for SEY = 1.6. $\Delta t = 0$ corresponds to the passage of the head of the bunch at the simulated section.

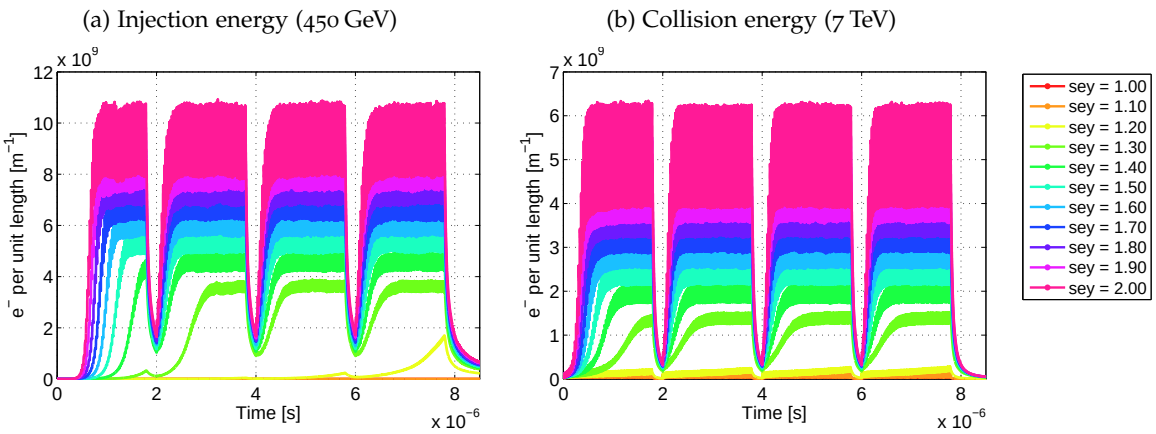

Figure 4.8: Evolution of the total number of electrons in the beam chamber of the LHC arc quadrupoles during the passage of a bunch train. Simulations for injection (a) and collision (b) energy, 25 ns bunch spacing.

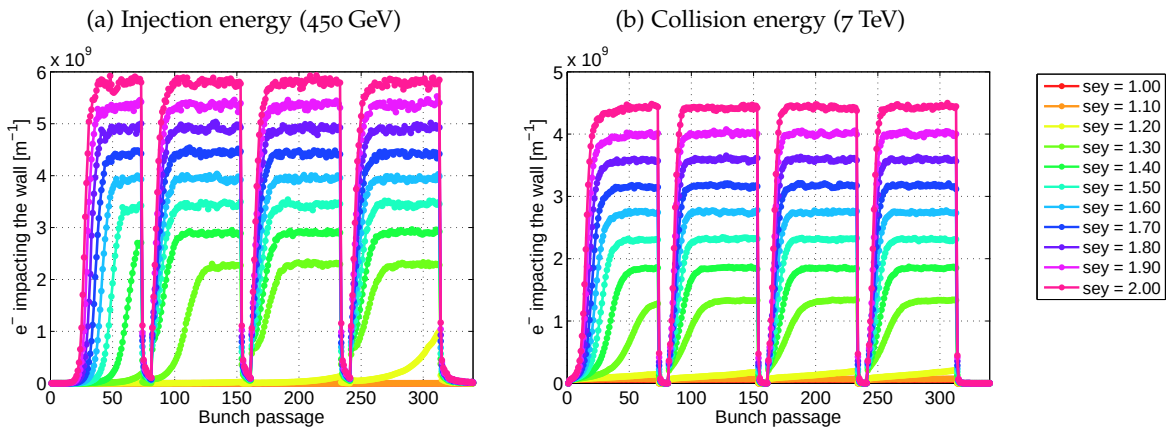

Figure 4.9: Evolution of the total number of electrons impacting on the chamber's wall of the LHC arc quadrupoles during the passage of a bunch train. Simulations for injection (a) and collision (b) energy, 25 ns bunch spacing.

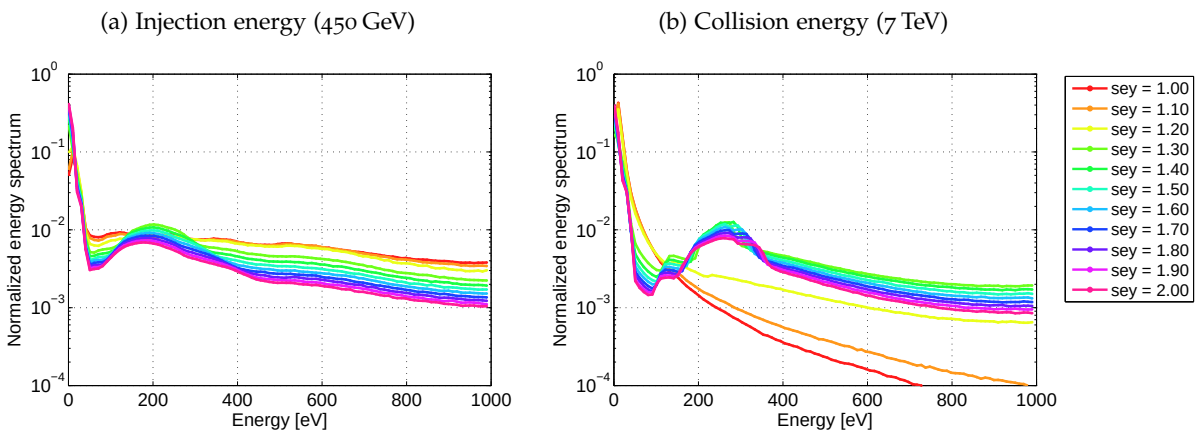

Figure 4.10: Normalized energy spectrum of the electrons impacting the wall in an arc quadrupole magnet. Simulations for injection (a) and collision (b) energy, 25 ns bunch spacing.

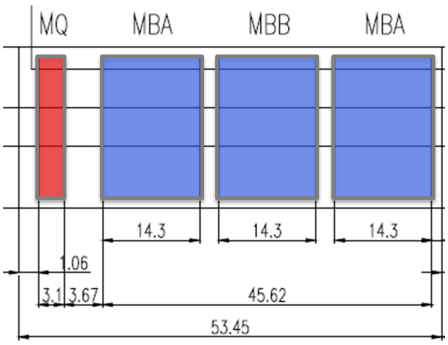

Figure 4.11: Structure of an half-cell of the LHC arc FODO lattice.

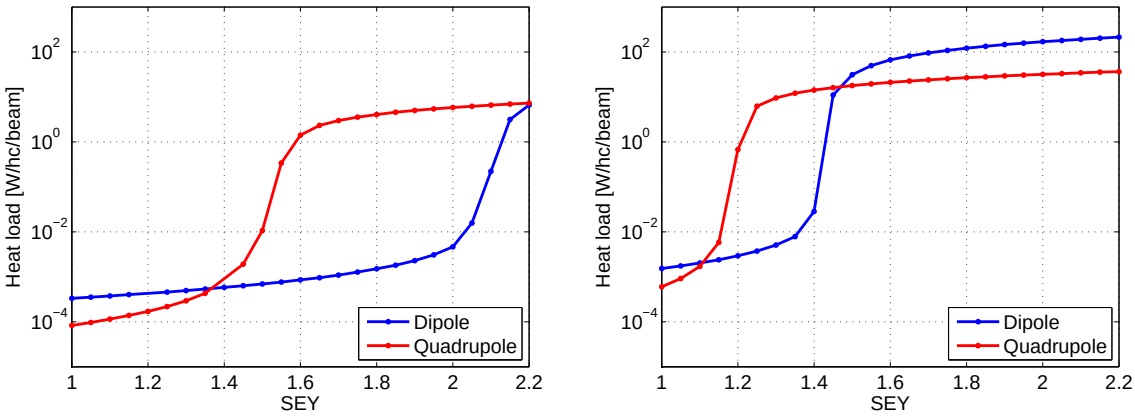

(a) 50 ns (b) 25 ns

Figure 4.12: Contribution of the dipole and the quadrupole magnets to the heat load in an LHC half cell, for 50 ns (a) and 25 ns (b) bunch spacing.

On the other hand, in Fig. 4.9, we observe that the number of electrons that impact the wall at each bunch passage does not show the same difference. This is due to the fact that at low energies there is a larger number of electrons which are just trapped by the magnetic field and do not contribute effectively neither to the electron flux to the wall nor to the heat load (see Fig. 4.6).

The energy spectra of the impacting electrons (see Fig. 4.10) are very similar to the dipole case. The most remarkable difference is that the peak due to the multipacting electrons is slightly narrower.

4.3 RELATIVE CONTRIBUTIONS TO HEAT LOADS

Figure 4.11 shows the structure of an half-cell of the LHC FODO lattice (see also Sec. 3.1). We can observe that the dipoles are in total about 15 times longer than the quadrupole.

In Fig. 4.12 we have rescaled the heat load computed for the two kinds of magnets (see Figs. 4.1 and 4.6) to the relevant lengths in order to obtain the respective contributions to the heat load measured in an arc half cell (the corresponding experimental data will be presented in the following chapter).

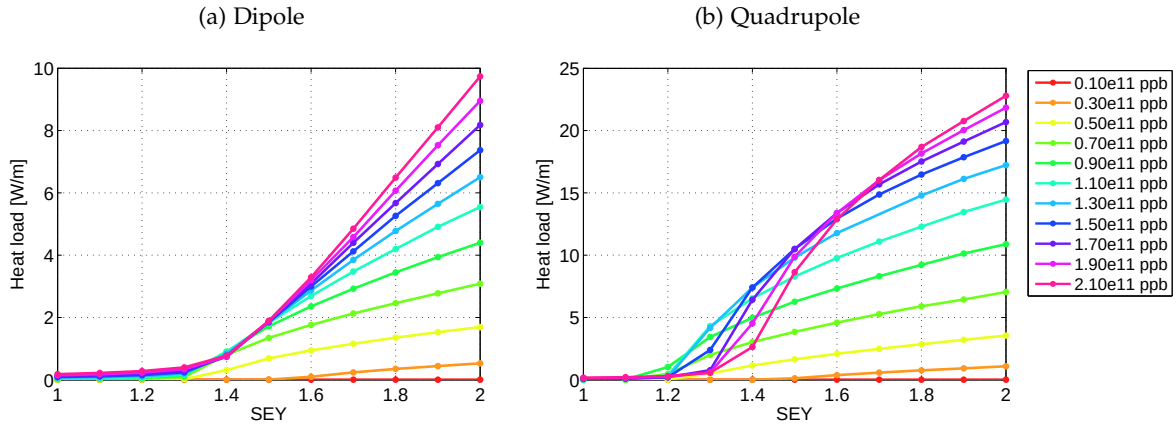

Figure 4.13: EC induced heat load as a function of the SEY, for the LHC arc dipole (a) and quadrupole (b) magnets. Simulations for collision energy, 25 ns bunch spacing, different bunch intensities.

We can notice that for high values of the SEY parameter (i. e. for SEY > 2.2 for 50 ns beams and for SEY > 1.4 for 25 ns beams) the dipoles are by far the dominating contribution. For lower values, due to the lower multipacting threshold, and despite the smaller integrated length, the quadrupole becomes the only non negligible contribution to the heat load.

4.4 EFFECT OF BUNCH INTENSITY

In the present section and in the two following the PyECLOUD simulation code will be applied to address the dependence of the EC buildup in the LHC arc dipoles and quadrupoles on the main parameters of the circulating beam. These studies can provide interesting information in order to mitigate EC effects while minimizing the impact on the machine performances, or to enhance the EC for efficient scrubbing purposes. These dependencies are also important to predict EC related issues in the framework of the High Luminosity Upgrade of the LHC (HL-LHC) [54] as well as for other future projects.

Figure 4.13 shows the dependence on the SEY parameter of the heat load due to EC, for different bunch intensities, both for the dipole and quadrupole magnets. The simulations do not show multipacting for the lowest intensity which has been considered, i. e. 0.1×10^{11} ppb, while EC appears already for 0.3×10^{11} ppb for relatively large values of the SEY. For larger intensities the multipacting threshold is about constant around SEY = 1.4 for the dipole while for the quadrupole it is between SEY = 1.1 and SEY = 1.3, slightly increasing for large bunch intensity values.

The heat load as a function of the bunch intensity, for different values of the SEY is presented in Fig. 4.14. For large values of the SEY the heat load is monotonically increasing with the bunch intensity. For smaller SEY values, the heat load is increasing only for small values of the bunch intensity, then it tends to stay constant for the dipole and even decreases for the quadrupole.

In the latter case, looking at the evolution along the bunch train of the total number of electrons in the beam chamber (Fig. 4.15), it is possible to recognize the seed accumulation regime for very small values of the bunch intensity, the multipacting regime for intermediate values and again only seed accumulation for large values. This can be understood looking

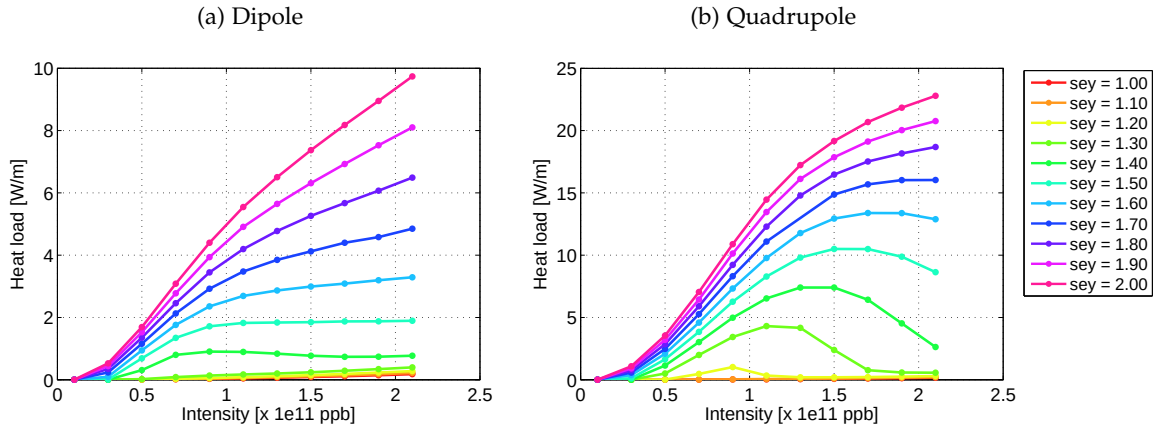

Figure 4.14: EC induced heat load as a function of the bunch intesity, for the LHC arc dipole (a) and quadrupole (b) magnets. Simulations for collision energy, 25 ns bunch spacing.

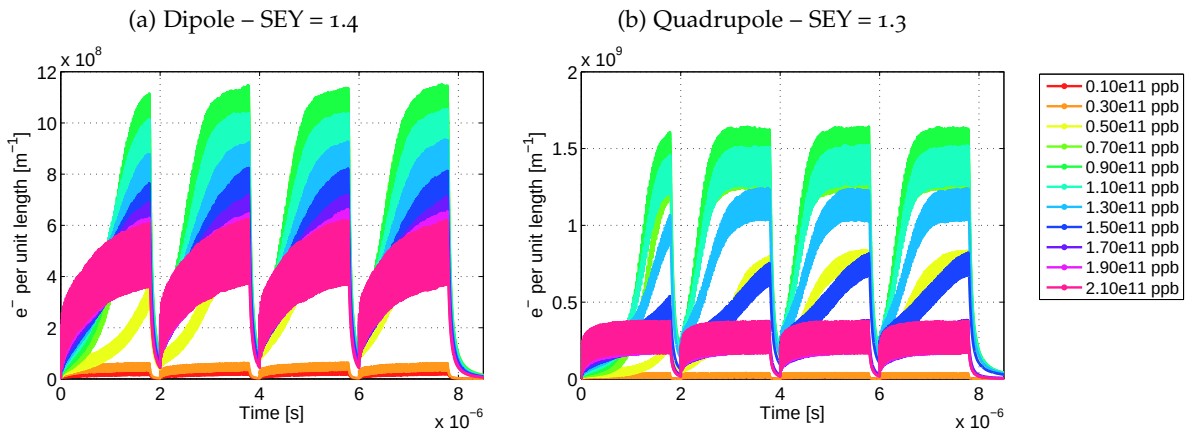

Figure 4.15: Evolution of the total number of electrons in the beam chamber of the LHC arc dipole (a) and quadrupole (b) magnets during the passage of a bunch train. Simulations for collision energy, 25 ns bunch spacing, different bunch intensities.

at the evolution of the energy spectra while increasing the bunch intensity, as depicted in Fig. 4.16. For low values of the SEY parameter, the energy range for which the SEY curve is larger than one is quite narrow (see Fig. 1.6). Since for larger bunch intensities the electrons receive a stronger kick from the beam, the spectrum tends to shift towards larger energies and fewer electrons hit the wall with energies that produce an efficient multipacting.

Changes of the bunch intensity can also influence the spacial distribution of the EC in the beam chamber. In Fig. 4.17 the impact on the electron stripes in the dipole magnet can be observed. For values of the SEY significantly larger than the multipacting threshold (see Fig. 4.17 b), the increase in bunch intensity mainly translates into a broadening of the chamber's region interested by EC, while the peak value stays practically unchanged. For SEY values closer to the threshold (see Fig. 4.17 a), a similar broadening is observed, and besides the increase of bunch intensity also leads to a depletion of the electron density in the central part of the chamber and to a moderate decrease on the density peak value.

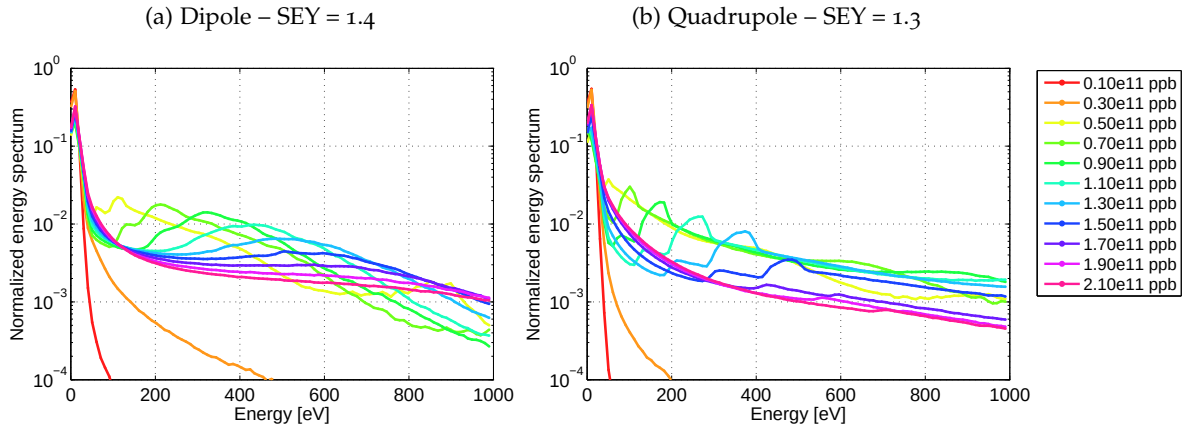

Figure 4.16: Normalized energy spectrum of the electrons impacting the wall in the LHC arc dipole (a) and quadrupole (b) magnets. Simulations for collision energy, 25 ns bunch spacing, different bunch intensities.

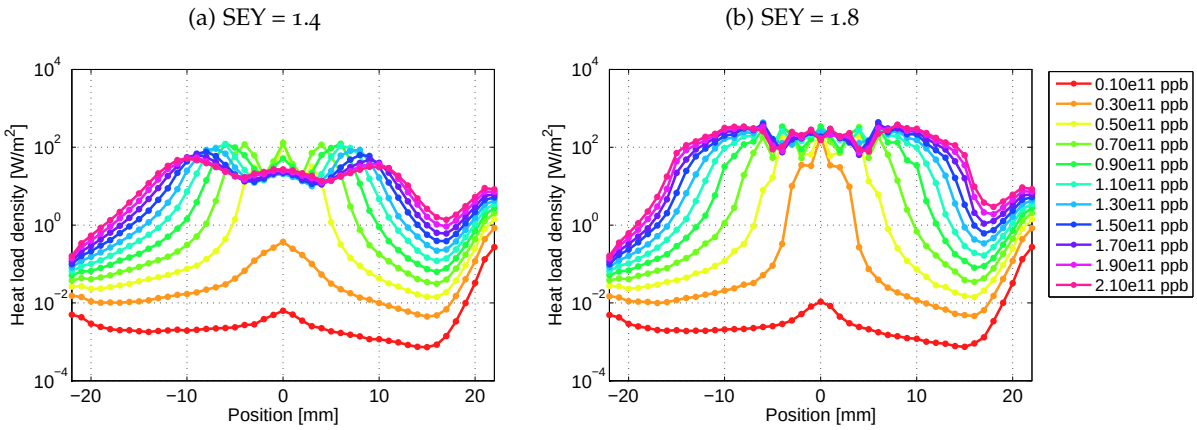

Figure 4.17: Horizontal distribution of the EC induced heat load on the wall of the LHC arc dipole chamber. Simulations for collision energy, 25 ns bunch spacing, different bunch intensities.

4.5 EFFECT OF BUNCH LENGTH IN DIPOLE MAGNETS

Concerning the dependence of the EC buildup on the bunch length, we were mainly interested in studying the impact on the main features of the multipacting process (i. e. on EC rise time and saturation level). For this purpose we decided to simulate a long uniform bunch train (640 bunches) and removed any beam dependent seeding and just started the buildup simulation with 10^8 e^-/m uniformly distributed in the transverse section of the vacuum chamber. Since one of the goals of the study was to gain information in order to understand the EC behavior observed in the initial part of the energy ramp (see Sec. 5.3.5), the dipolar magnetic field and the beam transverse size were set to the injection values.

Figure 4.18 (a) shows the EC induced heat load in an arc dipole as a function of the SEY for different values of the bunch length. We can notice that longer bunches have higher multipacting thresholds, due to the lower longitudinal peak densities. From Fig. 4.18 (b) we can observe that, for SEY = 1.4 (i. e. close to the multipacting threshold for the nominal beam parameters), there is no multipacting for bunches longer than 1.6 ns. For shorter bunches we observe that

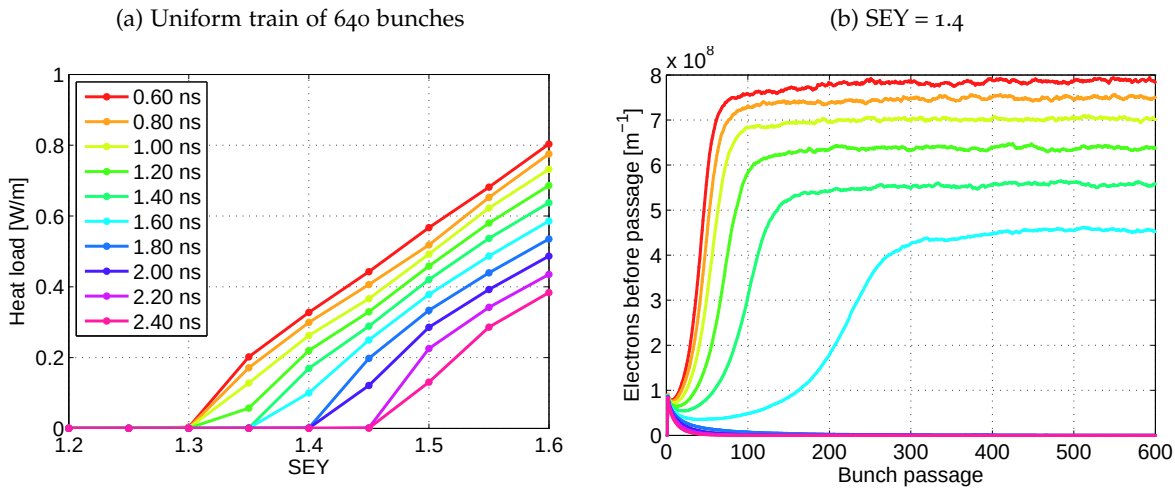

Figure 4.18: (a) EC induced heat load as a function of the SEY, for the LHC arc dipole magnets. Simulations for injection energy, 25 ns bunch spacing, different bunch intensities; No beam dependent seeding. (b) Evolution of the total number of electrons in the beam chamber; the distribution is sampled before each bunch passage.

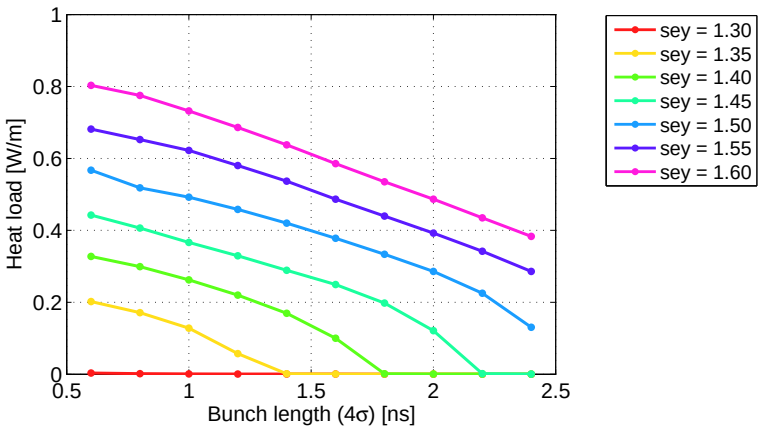

Figure 4.19: EC induced heat load as a function of the bunch length, for the LHC arc dipole magnets. Simulations for injection energy, 25 ns bunch spacing, different bunch intensities. No beam dependent seeding, uniform train of 640 bunches.

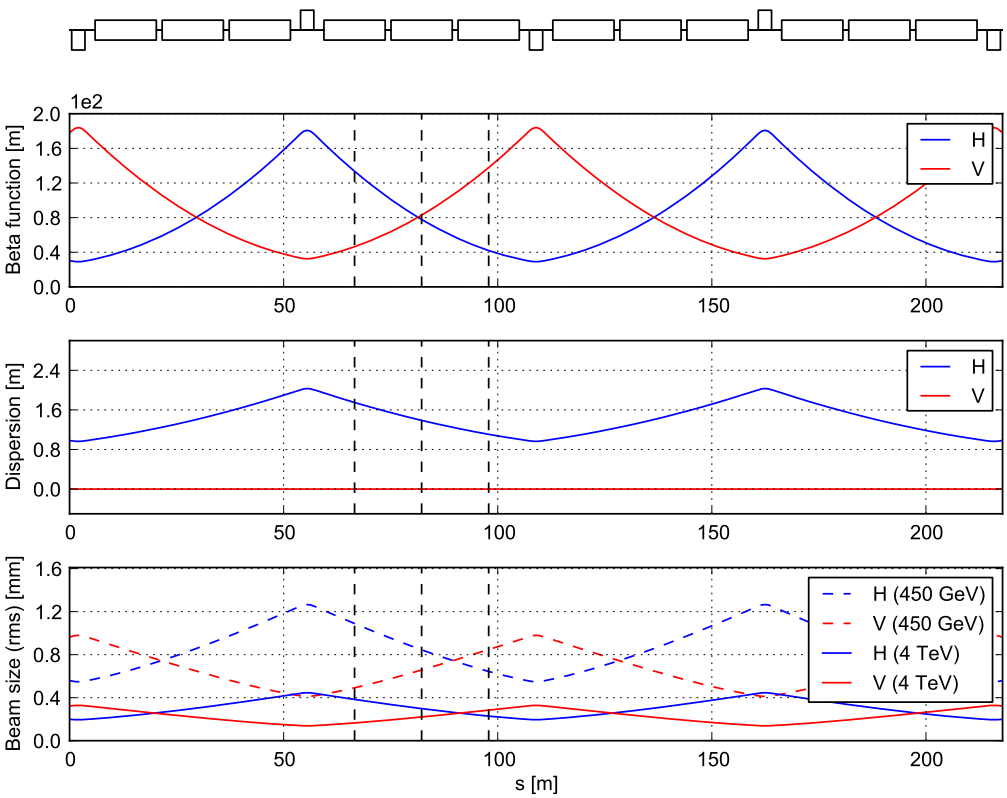

Figure 4.20: Beta functions, dispersion functions and beam transverse size along two cells of the LHC arc FODO lattice. The vertical dashed lines represent the sections for which PyECLOUD simulations have been run (from left to right: MB1, MB2 and MB3).

when the bunch length decreases, the rise time becomes faster and the number of electrons at saturation larger. The EC induced heat load as a function of the bunch length, for different SEYvalues, is shown in Fig. 4.19.

4.6 EFFECT OF TRANSVERSE SIZE VARIATION IN DIPOLE MAGNETS

The simulation studies presented in this section will address the effect of the transverse size variation on the EC buildup along different points of the arc dipoles (different beta functions) and on the energy ramp. The r.m.s. transverse size of the beam ($\sigma_{x,y}$) can be written as follows:

$$\sigma_{x,y} = \sqrt{\beta_{x,y}\frac{\varepsilon_{x,y}}{\beta_{rel}\gamma_{rel}} + \left(D_{x,y}\frac{\Delta p}{p}\right)^2} \tag{4.1}$$

where $\beta_{x,y}$ and $D_{x,y}$ are the optics beta and dispersion functions [53] in the horizontal and vertical plane, $\varepsilon_{x,y}$ are the normalized emittances, β_{rel} and γ_{rel} are the relativistic factors, $\Delta p/p$ is the r.m.s. longitudinal normalized momentum spread of the beam.

During the acceleration, assuming that the machine optics stays unchanged (generally true for the LHC) and that no emittance blow-up occurs (quite optimistic for the LHC [55]), since the term $\beta_{rel}\gamma_{rel}$ increases and $\Delta p/p$ decreases, a reduction of the beam size is observed.

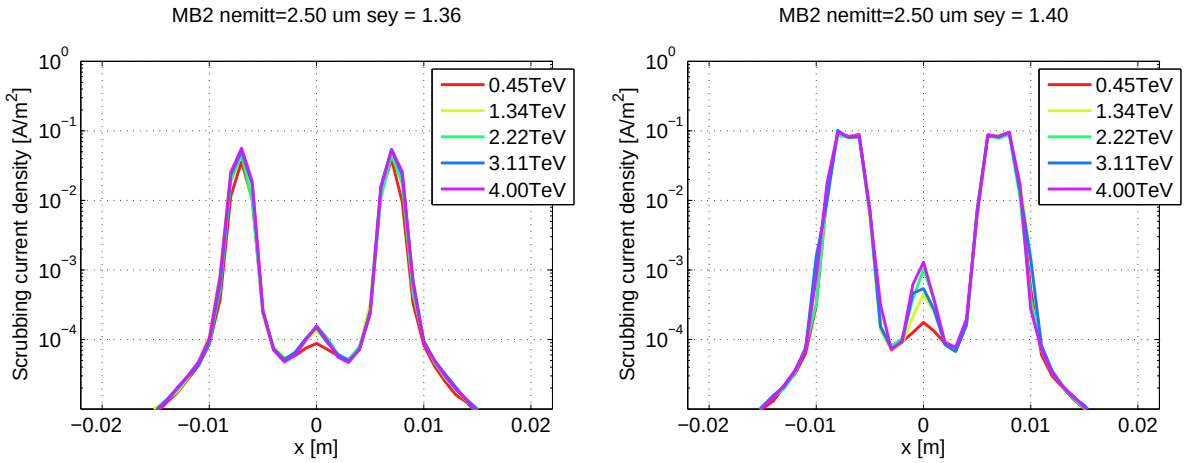

Figure 4.21: Horizontal distribution of the current of scrubbing electrons on the beam screen of the LHC arc dipole. Simulations for 25 ns bunch spacing, no beam dependent seeding, uniform train of 640 bunches. Beam transverse size and magnetic field corresponding to different beam energies.

Figure 4.20 shows the oscillations of the optics functions along the FODO lattice of the LHC arcs and the corresponding beam size at 450 GeV and 4 TeV, i. e. the largest collision energy reached by the LHC at present.

Since the size and the aspect ratio of the beam is changing along the FODO cell, we decided to simulate the EC buildup at three different sections of the cell, namely at the middle of the three dipoles, which are marked by vertical dashed lines in Fig. 4.20 and in the following will be denoted as MB1, MB2 and MB3 starting from the closest to the focusing quadrupole. For the beam size calculation we assumed $\varepsilon_{x,y} = 2.5\,\mu$m, $\Delta p/p = 4 \times 10^{-4}$ at 450 GeV and $\Delta p/p = 1.5 \times 10^{-4}$ at 4 TeV, which are typical values measured during the 2012 tests with 25 ns beams (see Sec. 5.3). In order to be as accurate as possible in the evaluation of the electric field of the beam we decided to use the elliptic approximation for the shape of the LHC beam screen and the corresponding analytic expression for the beam electric field.

As for the studies presented in the previous section we were mainly interested in studying the impact on the multipacting process (i. e. on EC rise time and saturation level) and therefore we decided to simulate a long uniform bunch train (640 bunches), we eliminated any beam dependent seeding and just started the buildup simulation with 10^8 e$^-$/m uniformly distributed in the transverse section of the vacuum chamber. The dipolar magnetic field is increased according to the beam energy.

We observed that the impact of the transverse beam size on the EC buildup is quite weak. On the EC distribution at saturation the only appreciable difference is in the central region of the beam chamber (see Fig. 4.21). This is quite intuitive since when changing the transverse beam size the change on the electric field due to the beam is concentrated in a region very close to the beam.

Figure 4.22 shows on the left side the EC induced heat load as a function of the SEY at the three simulated locations and on the right side the corresponding scrubbing current in the region $|x|<5$ mm. Previous studies [56] suggested that the effect of the transverse size is more visible for SEY values close to the multipacting threshold, so we decided to explore in detail this SEY region. The behavior of the EC is extremely similar at the three simulated

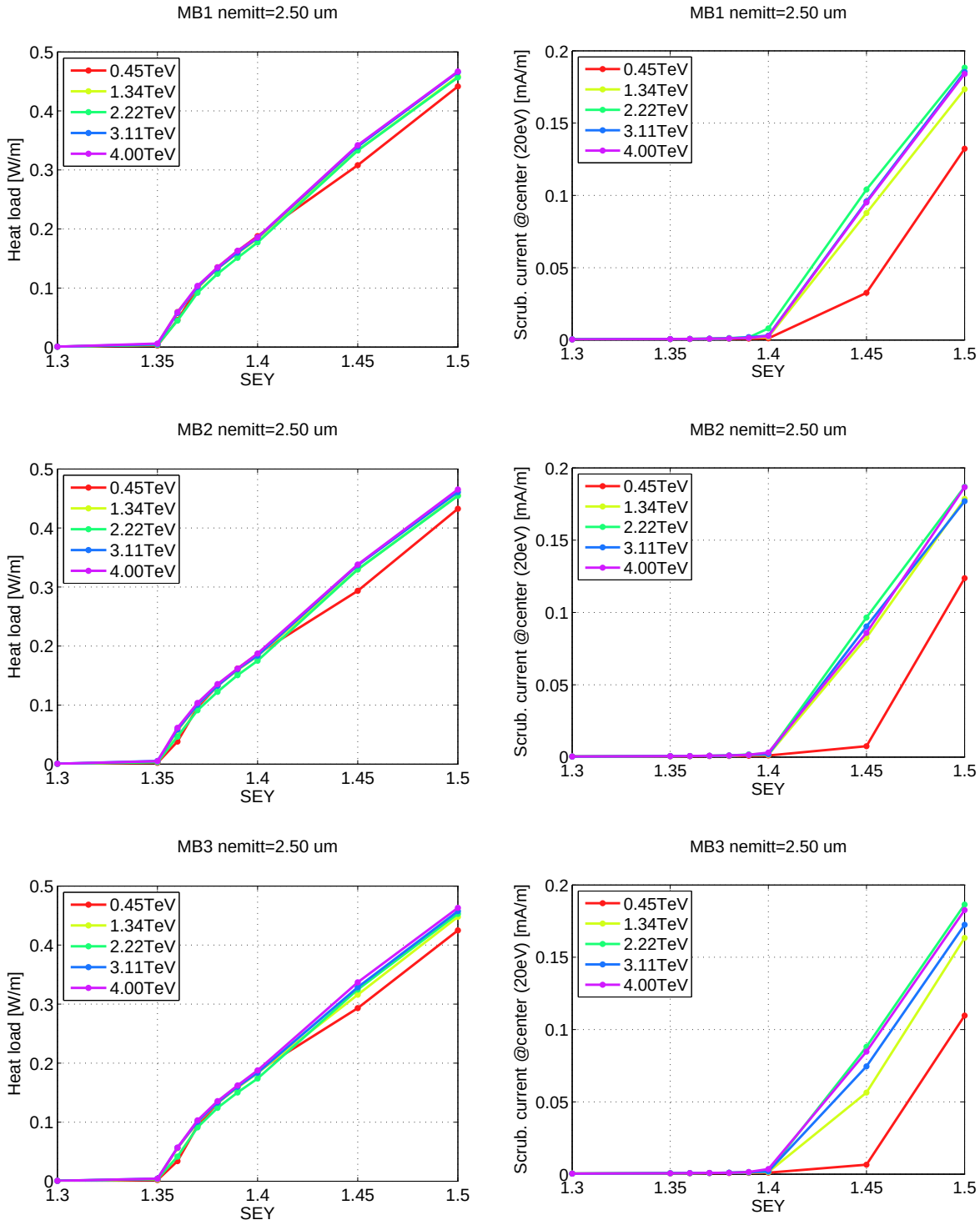

Figure 4.22: EC induced heat load (left) and scrubbing current around the beam location ($|x|<5$ mm – right) at the three simulated section of an LHC arc FODO cell. Simulations for 25 ns bunch spacing, no beam dependent seeding, uniform train of 640 bunches. Beam transverse size and magnetic field corresponding to different beam energies.

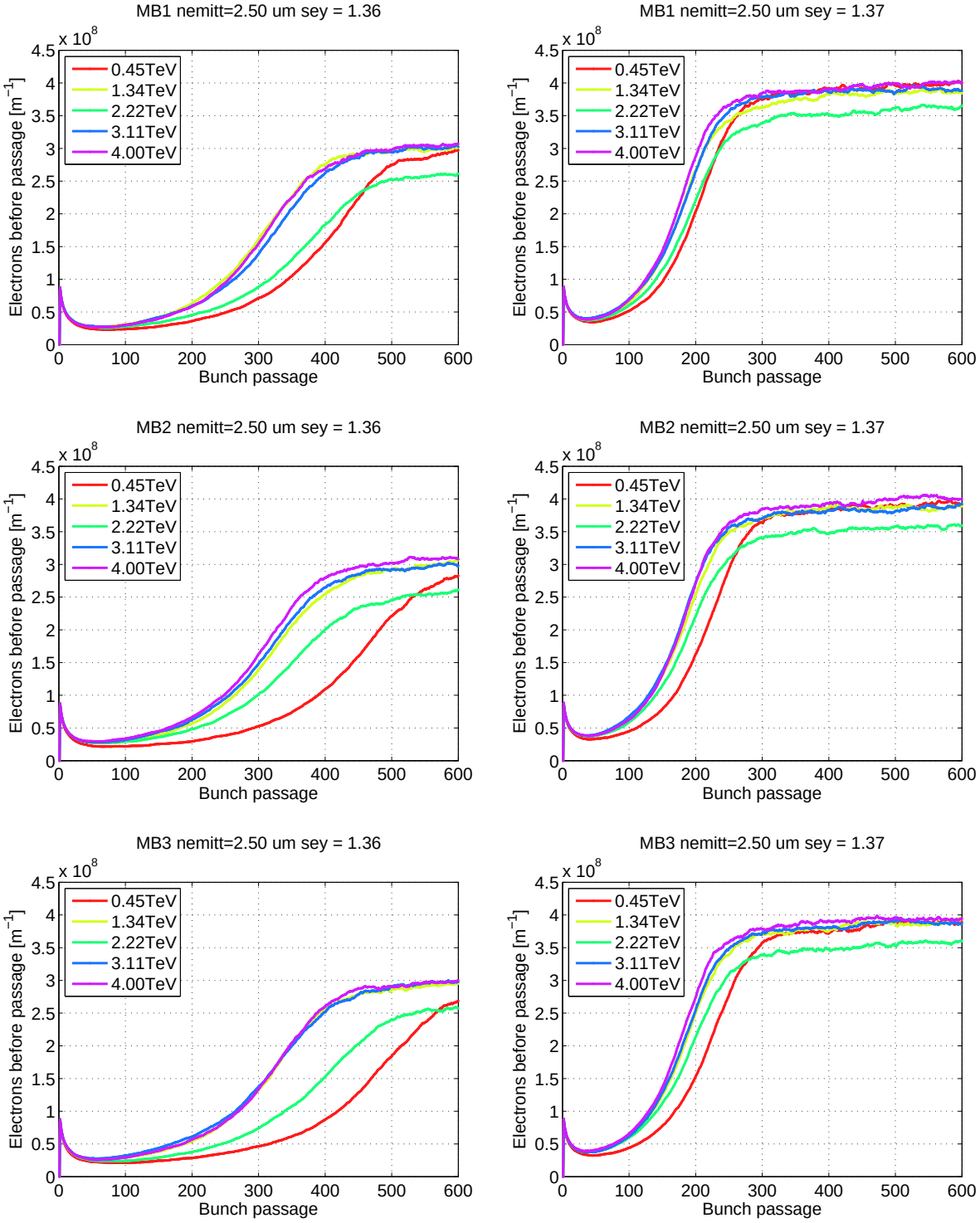

Figure 4.23: Evolution of the total number of electrons in the beam chamber of the LHC arc dipoles during the passage of a bunch train. Simulations for 25 ns bunch spacing, no beam dependent seeding, uniform train of 640 bunches. Beam transverse size and magnetic field corresponding to different beam energies.

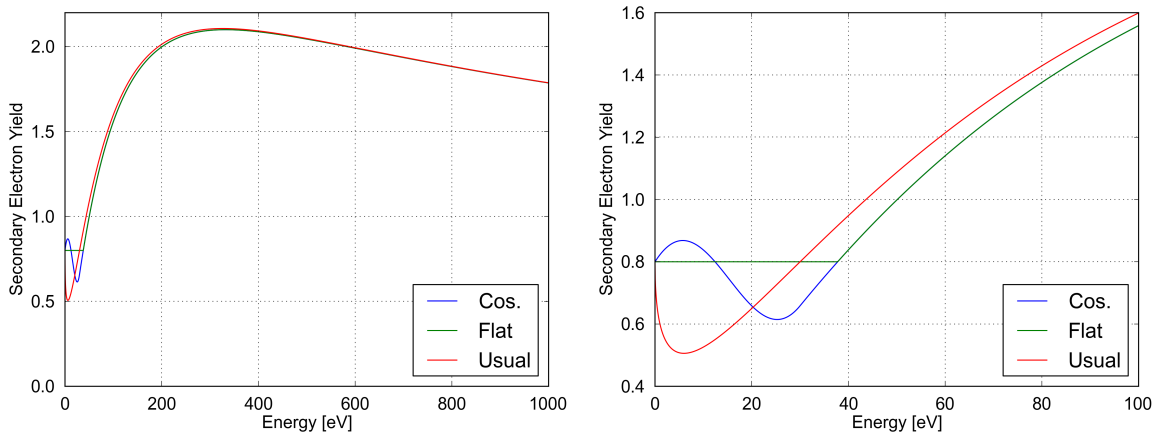

Figure 4.24: The different SEY models compared in simulations. On the right, zoom on the low energy part of the curve.

sections. A non negligible flux in the central region appears only for SEY values larger than the multipacting threshold and, on this quantity, a difference is visible between the injection energy (450 GeV) and the other simulated values. From the right side of the figure we observe that the effect of the beam transverse size on the total heat load is hardly visible. The small difference for the larger SEY values is explained by the behavior of the central region we just discussed before. Apart from this, the largest differences in the EC buildup can be spotted for the smallest SEY value for which multipacting is observed, namely SEY = 1.36, extremely close to the multipacting threshold. For this particular value, significant differences among the different energies can be observed both on the EC rise time and on the saturation level (see Fig. 4.23 left) but already for SEY = 1.37 the effect is much less evident (see Fig. 4.23 right).

4.7 IMPACT OF THE LOW ENERGY PART OF THE SEY CURVE

In the simulations presented in this thesis, we always modeled the Secondary Electron Emission using the approach presented in Sec. 1.2 which was proposed in [24] based on laboratory measurements. The largest uncertainties of this model are related to the low energy part of the SEY curve, i. e. the region 0 - 50 eV, which is particularly difficult to address both with measurements and with theoretical considerations [57, 58]. We decided to study with PyECLOUD simulations the impact that this a region of the SEY has on the EC buildup and in particular on the dependence of the EC induced heat load on the SEY parameter.

In the model presented in Sec. 1.2 the component of the SEY due to elastically reflected electrons is given by:

$$\delta_{refl}(E) = R_0 \left(\frac{\sqrt{E} - \sqrt{E + E_0}}{\sqrt{E} + \sqrt{E + E_0}} \right)^2 \tag{4.2}$$

In our simulations we typically choose $R_0 = 0.7$ and $E_0 = 150$ eV. Using this model for an SEY parameter of 2.1 we obtain the red curve in Fig. 4.24 which shows a minimum of the SEY slightly below 10 eV.

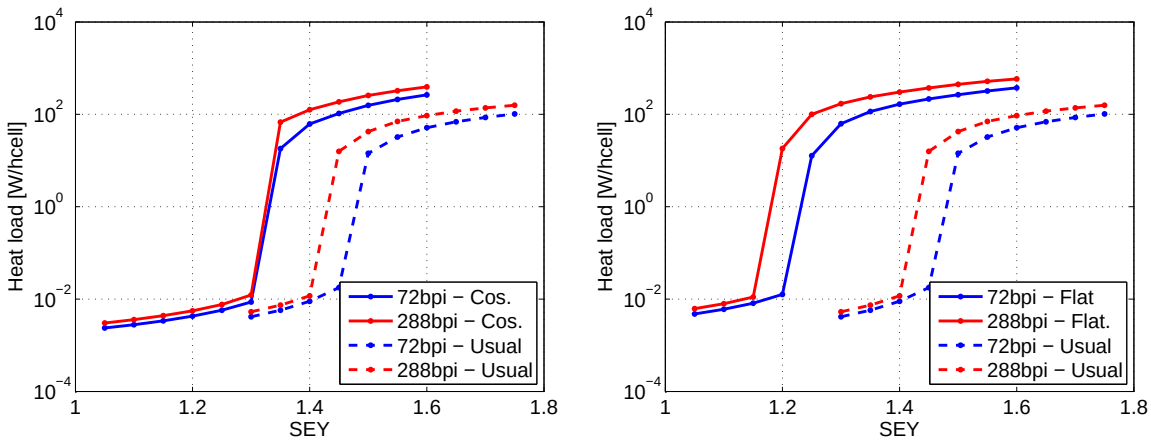

Figure 4.25: Heat load as a function of the SEY parameters for different SEY models and different filling patterns.

We decided to perform buildup simulations in two possible scenarios. In the first case, which will be referred as "Cos." model, we used the following expression of for $\delta_{refl}(E)$:

$$\delta_{refl}(E) = \begin{cases} R_0 \cos^2\left(\frac{\pi}{2}\frac{E}{E_0}\right) & \text{if } E < E_0 \\ 0 & \text{elsewere} \end{cases} \tag{4.3}$$

with $R_0 = 0.7$ and $E_0 = 10\,\text{eV}$. This gives, for an SEY parameter of 2.1, the blue curve in Fig. 4.24, where the minimum of the SEY is less pronounced and shifted towards higher energies, as it happens to be in some of the measurements shown in [58, 59]. In the second case we wanted to investigate the extreme case in which the minimum is not present at all. We used the following expression of for $\delta_{refl}(E)$:

$$\delta_{refl}(E) = \begin{cases} R_0 - \delta_{true}(E) & \text{if } \delta_{true}(E) < R_0 \text{ and } E < E_{max} \\ 0 & \text{elsewere} \end{cases} \tag{4.4}$$

which implies that $\delta(E) = R_0$ at low energy. Therefore this model, shown in green in Fig. 4.24, will be therefore referred as "Flat".

We performed simulations for an arc dipole magnet, at injection energy, with two different filling patterns, filling the LHC with trains of 72 bunches and 288 bunches per injection respectively, in both cases leaving the minimum possible gap of 925 ns between the injected trains.

The results of this buildup simulations, in terms of EC induced heat load as a function of the SEY are shown in Fig. 4.25. We can see that in both cases the change of the low energy part of the SEY curve has an important impact on the simulation results, both on the resulting heat load and on the obtained multipacting threshold. Moreover while the "Flat" model preserves the difference in multipacting threshold which is observed between the two filling patterns with the "Usual" model, such a feature is much less evident for the "Cos." model.

This simple study shows that the shape of the SEY curve at low energies can have an important impact on several estimates coming from EC buildup simulations like heat loads,

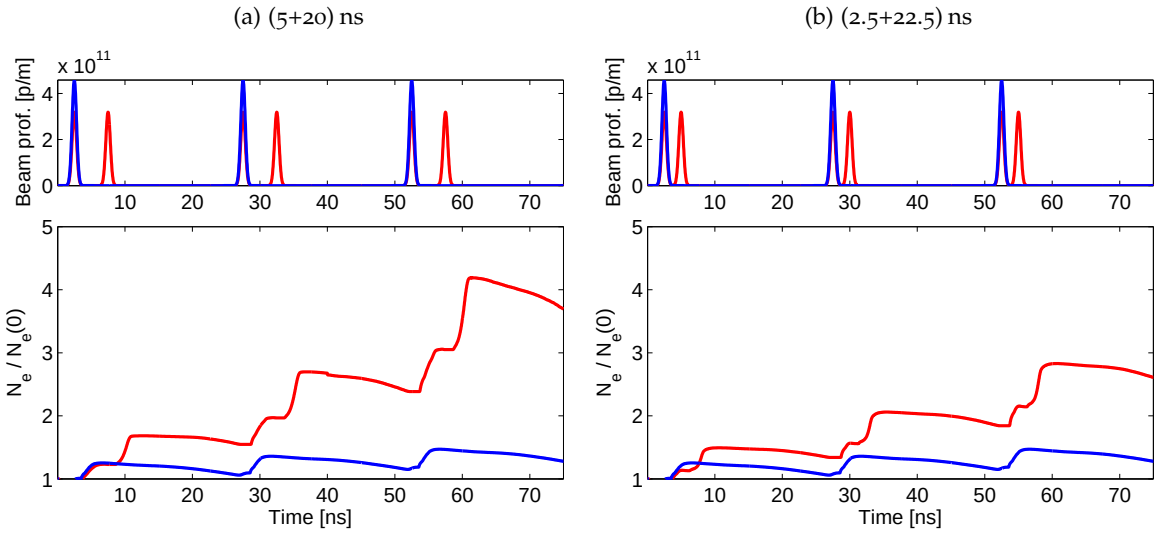

Figure 4.26: Longitudinal profile (top) and simulated evolution of the number of electrons in the beam chamber for few bunch passages during the buildup (bottom) for the doublet scrubbing beam (red) and for the standard 25 ns beam (blue).

multipacting thresholds, or scrubbing dose requirements. Important efforts are presently ongoing (e. g. at CERN and at INFN-LNF) in order to improve laboratory SEY measurement techniques for low energy impinging electrons and therefore reduce the related uncertainties in our EC models.

4.8 SIMULATION STUDIES FOR A DOUBLET SCRUBBING BEAM IN THE LHC

The possibility of using an hybrid bunch spacing to enhance the scrubbing efficiency, which has been proposed and tested at the SPS (as it will be discussed in more detail in Sec. 8.6), has been explored in simulations also for the LHC. Two possible scenarios were considered:

- (5+20) ns spacing, which could be produced by splitting at the injection of the beam from the PS to the SPS, as for SPS scrubbing (see Sec.. 8.6);
- (2.5+22.5) ns spacing, which could be produced by splitting at the injection of the beam from the SPS to the LHC using the same technique.

The beam profile and the buildup for few bunch passages (normalized to the initial density) is shown in Fig. 4.26 for the two options. The enhancement of the EC production is evident in both cases.

Figure 4.27 shows the computed scrubbing dose as a function of the SEY, comparing hybrid schemes with different bunch intensities against the nominal beam with 25 ns spacing. Both schemes present multipacting thresholds significantly smaller than the nominal beam, even for relatively low bunch intensity. Therefore both beams allow getting a consistent scrubbing dose in the SEY region where the standard 25 ns beam tends to become ineffective for scrubbing. The EC enhancement looks much stronger for the (5+20) ns scheme. The reason can be understood by looking again at Fig. 4.26: in the (5+20) ns scheme the electron generation stages following the passages of the two bunches of the doublet are very similar. This means

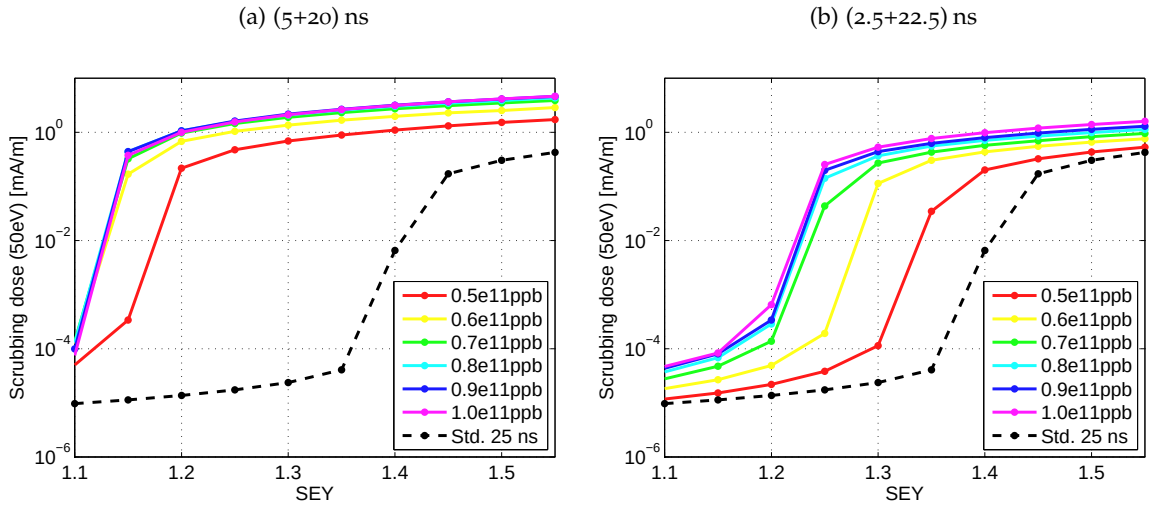

Figure 4.27: Scrubbing dose as a function of the SEY parameter for the two proposed scrubbing schemes. Simulations for a single bunch train at 450 GeV.

that most of the electrons kicked by the first bunch have enough time to reach the wall and effectively participate to the multipacting process, before the second bunch arrives and attracts them towards the center of the chamber. On the contrary in the (2.5+22.5) ns case, the passage of the second bunch happens before most of the electrons have reached the wall, which gives a much reduced enhancement compared to the other case.

Figure 4.28 shows some further details on the EC buildup for the case SEY = 1.45, i. e. close to the multipacting threshold for the nominal beam. The EC rise time (see Fig. 4.28 top) is quite fast and in most of the cases saturation is reached within the first half of the first batch as opposed to the two batches needed for the nominal beam. The saturation level is also larger for the doublet beam than for the standard 25 ns beam.

Looking at the horizontal distribution of the scrubbing current (see Fig. 4.28 middle) we find out that for the (5+20) ns scheme a bunch intensity of about 0.9 ppb is enough to condition the entire region which is interested by EC for the standard beam. This does not happen in the (2.5+22.5) ns case where the electron flux tends to be concentrated in a too narrow region.

Finally we need to verify that the enhancement of the electron flux is not given by low energy electrons which would not efficiently contribute to the scrubbing process 1.2.1. This check is made in Fig. 4.28 bottom, from which we can observe that, if the bunch population is large enough, the energy distribution of the impacting electrons is quite similar to that of the nominal beam.

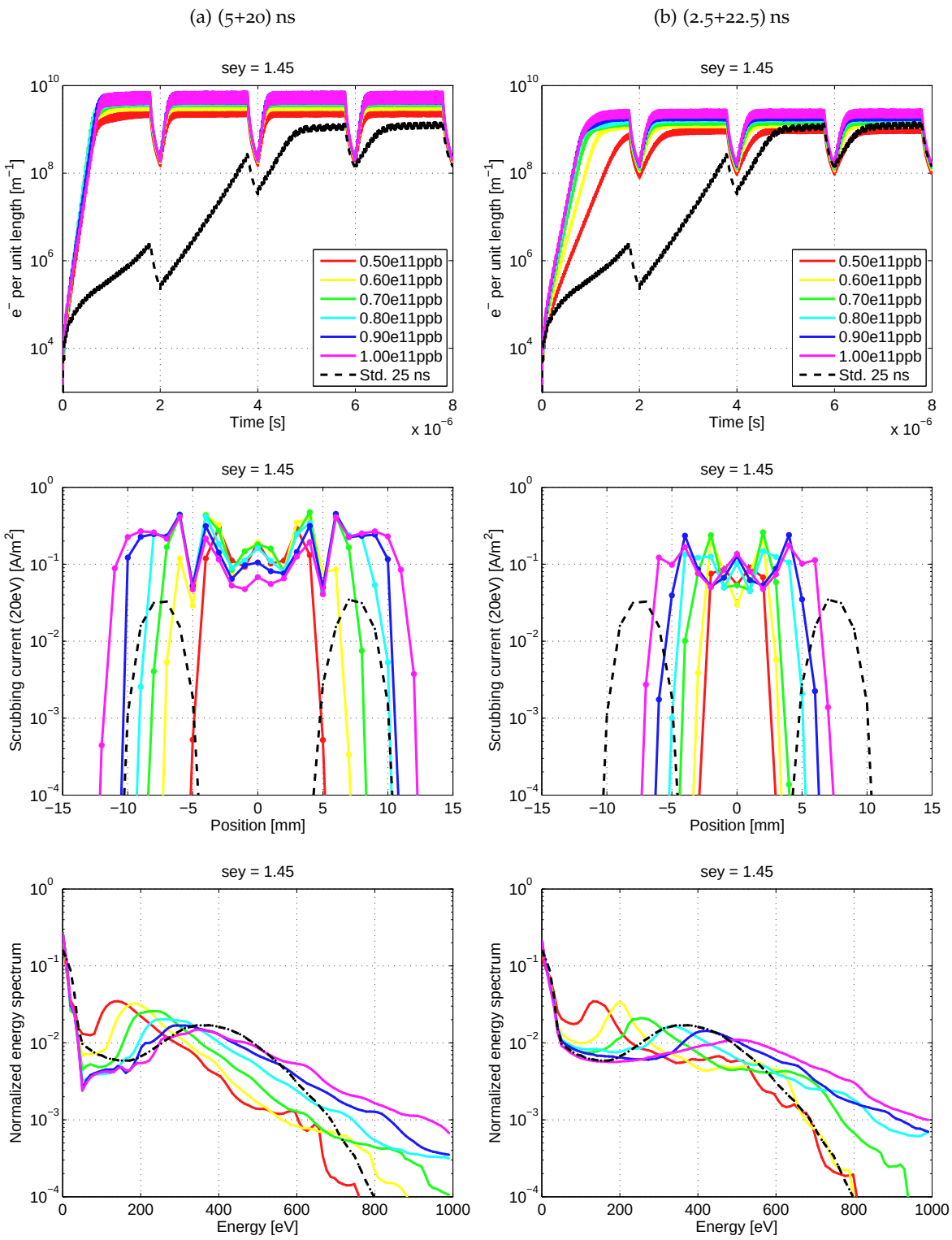

Figure 4.28: Evolution of the number of electrons in the beam chamber (top), horizontal distribution of the scrubbong current (middle), and energy spectrum (bottom) for the two proposed scrubbing schemes with different bunch intensity. Simulations for SEY = 1.45, i. e. close to the multipacting threshold for the standard 25 ns beam. The results for the standard 25 ns beam are shown for comparison by the dashed lines.

5

ELECTRON CLOUD OBSERVATIONS AND EXPERIMENTAL STUDIES AT THE LHC

EC effects were observed at the LHC during the first three years of beam operation (Run 1, 2010 – 2012), becoming more and more severe while moving to tighter bunch spacing [34, 48, 60–76]. EC effects with 50 ns beams could be successfully mitigated through beam induced scrubbing (see Sec. 1.2.1) and this bunch spacing could be used for most of the integrated luminosity production with 7–8 TeV Center of Mass (CoM) energy in 2011–12 [77].

After the 2013–14 machine shutdown (LS1) the LHC will be able to run at 13–14 TeV CoM energy and it will be necessary to move to the design bunch spacing of 25 ns in order to reach the design luminosity within the *pileup* limits required by the LHC experiments [78].

Up to now, the 25 ns beam has been used only for test purposes, and as expected from simulation studies (see Secs. 4.1 and 4.2), due to the smaller multipacting threshold, EC effects proved to be significantly more severe compared to the 50 ns case. Therefore, several experimental studies have been performed at the LHC with this bunch spacing in order to characterize the EC formation in the machine and its impact on the performances, crosscheck and possibly improve our models and simulation tools, and finally define possible mitigation strategies for the future.

These studies will be treated in the present chapter, after a brief recapitulation on the observations with 50 ns and larger bunch spacings.

5.1 EC OBSERVATIONS AND MITIGATION WITH BEAMS WITH 50 NS AND LARGER BUNCH SPACING

First operation with bunch trains injected from the SPS into the LHC was performed in 2010 with 150 ns bunch spacing. With this beam configuration no EC effects could be observed in the cryogenic arcs and in the portions of the straight sections where the two beams circulate in separate vacuum chambers. On the other hand vacuum pressure increases were observed in the common beam chambers close to the Interaction Points (IPs) where the presence of the two counter-rotating beams in the same chamber has an enhancing effect on the EC buildup [60]. This type of effects will be treated in Chapter 6. Nevertheless, after the installation of solenoids for EC suppression in the most critical of these regions, the LHC could run safely with this beam configuration.

Subsequently, at the end of October 2010, an attempt was made to switch to 50 ns spacing operation. After an initial physics fill with 108 nominal bunches (filling scheme with one pilot bunch and 9×12 bunches), important dynamic pressure rises were observed at injection when filling with trains of 24 bunches, also in sections where the two beam circulate in separate chambers, which prevented safe operation with this beam configuration. In fact, the first

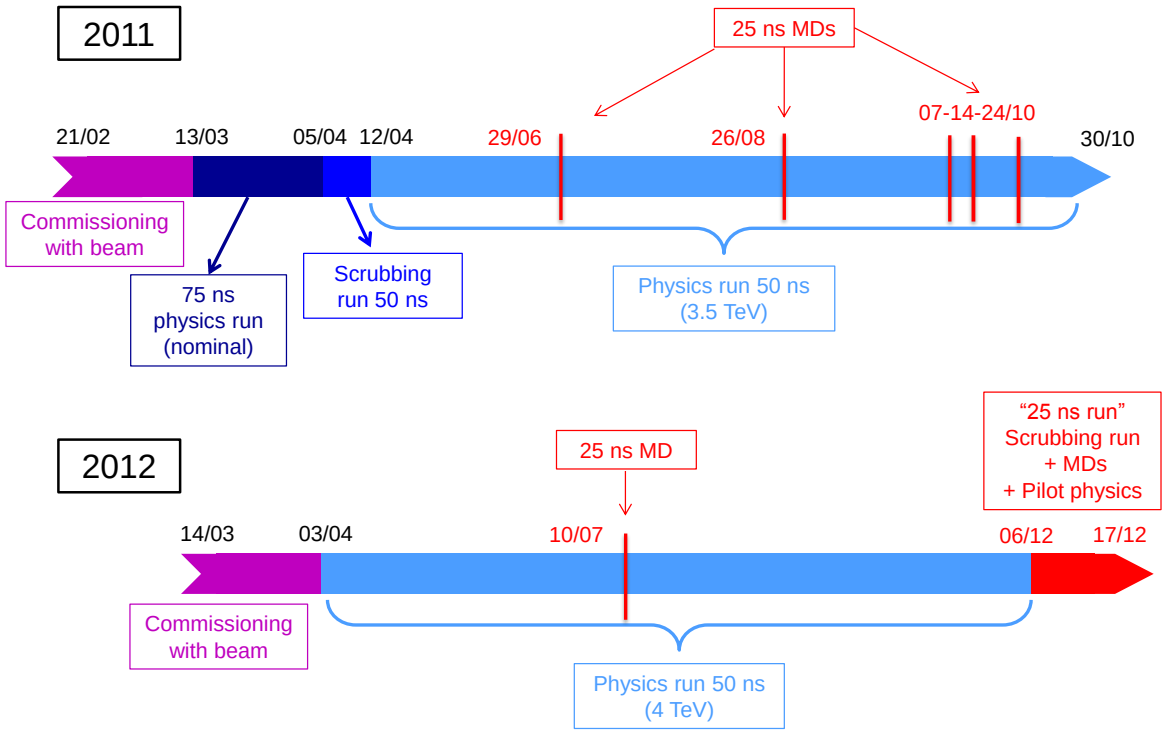

Figure 5.1: Summary of the bunch spacing used at the LHC in 2011 and 2012.

attempt of injection in batches of 24 even led to the closure of the safety vacuum valves in the Insertion Region (IR) 7 after the injection of 108 nominal bunches per beam, as the interlock level of 4×10^{-7} mbar was reached on two vacuum gauges.

After that, few Machine Development (MD) sessions were devoted to dedicated tests in order to understand the machine behavior with this bunch spacing. It was clear that when batches of 24 bunches with 50 ns spacing were injected into the LHC, an EC could build up in a large part of the LHC (including the cryogenic arcs), as evidenced not only by pressure rises but also by the heat load on the beam screens of the cryogenic magnets, and by coherent and incoherent effects on the beam, like transverse instabilities and emittance blowup, especially on the trailing bunches of the batches [60, 61].

At the end of 2010, tests with 75 ns spacing were also performed at the LHC in order to study a possible fallback strategy for 2011. These tests gave a clear indication that, probably also benefiting from the previous MD's scrubbing with 50 ns beams, the EC effects with 75 ns appeared significantly less pronounced than with 50 ns beams, such that this bunch spacing could be regarded as a relatively safe option [62].

The LHC operation was therefore resumed in 2011 directly with 75 ns beams (see Fig. 5.1). After the scrubbing in 2010 it was expected that up to 200-300 bunches could be injected and accelerated without major problems. This was confirmed during the start-up with beam. After about one month of operation, the LHC could successfully collide trains of 200 bunches distributed in batches of 24 bunches each.

Later on, the full week 5-12 April, 2011, was devoted to the scrubbing run with 50 ns beams, although three days were lost due to issues independent of the scrubbing program and the last day was devoted to tests of accelerating/colliding beams with 50 ns spacing (up to 246 bunches). The goal was to prepare the machine to switch to 50 ns physics operation and thus extend the luminosity reach for the 2011 run. Over the scrubbing run, the number of bunches injected into the LHC was gradually ramped up to a maximum of 1020 per beam (in batches of 36). Several stores at injection energy with different numbers of bunches took place. During the first days of scrubbing, pressure rise, heat load in the cryogenic arcs, coherent beam instabilities as well as emittance growth were observed. Nevertheless, the beams could be kept in the LHC at injection energy thanks to the fact that the heat load could be handled by the cooling capacity of the cryogenic system, the pressure rise was tolerable or, where needed, the interlock level on the pressure value was temporarily raised so as not to cause a beam dump, high chromaticity settings were used for damping the coherent instability, the incoherent emittance growth and the associated intensity loss, mainly affecting the last bunches of each batch, were sufficiently slow as not to trigger the Beam Loss Monitors (BLMs).

In these conditions, the EC produced by the circulating beams served the purpose of scrubbing the inner wall's surface of the LHC beam chambers. The strategy adopted to optimize the scrubbing process consisted of constantly topping the total beam intensity in the LHC with the injection of more trains, such that the vacuum activity, and therefore the EC in the room temperature straight sections, could be kept at a constant level. This was expected to efficiently reduce the SEY of the walls to a value eventually at the limit for a significant EC buildup (and below the threshold for beam instability at nominal intensity). After approximately 17 effective hours of beam scrubbing time – corresponding to about 72h of beam time – the pressure improved by an order of magnitude throughout the machine. At the end of the scrubbing run, a residual pressure rise was still observed in some cold-warm transitions and straight sections, while in the arcs the heat load on the beam screen practically disappeared. The effectiveness of the scrubbing process could also be monitored through RF stable phase measurements providing the beam energy loss per turn [67].

The success of the scrubbing run was proved by the subsequent smooth LHC physics operation with 50 ns spaced beams. Between mid-April and end-June the number of bunches collided in the LHC was steadily increased up to its maximum value of 1380 per beam, while the intensity per bunch and the transverse emittances remained constant at their nominal values (i.e., 1.15×10^{11} ppb and 2.5 μm). During this period some residual EC activity was still observable especially through transverse instability at injection energy, which could be cured by introducing Landau damping through the octupole magnets [35]. At the same time, the surface scrubbing naturally continued, as witnessed by an additional one-order-of-magnitude decrease of the dynamic pressure level around the machine. The switch to 50 ns beams with lower transverse emittances (1.5 μm) allowed the LHC peak luminosity to easily score an additional 50% increase, while not leading to any critical recrudescence of the EC. This could be expected, given the weak dependence of the EC formation on the beam transverse emittances (see Sec. 4.6). Finally, to push the peak luminosity further up, the intensity per bunch was adiabatically increased to approximately 1.5×10^{11} ppb over the final few months of the 2011 run. Again, no significant return of the EC was observed during this phase.

After three weeks commissioning with beam, the 2012 physics run of the LHC started in early March colliding beams with 50 ns bunch spacing. Owing to beam scrubbing from the 2011, especially that accumulated during MD sessions with 25 ns beams (which will be

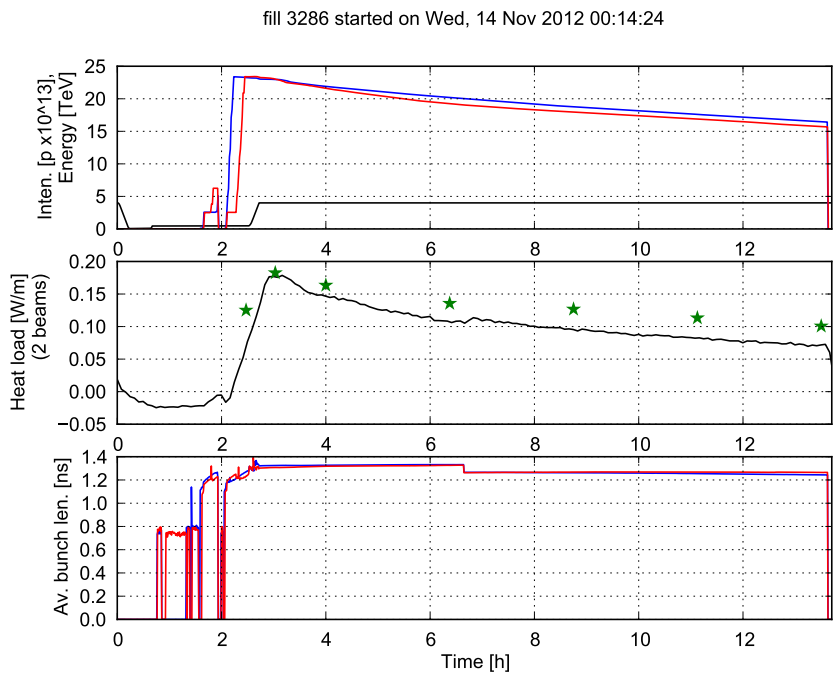

Figure 5.2: Top: beam energy (black) and total intensity for beam 1 (blue) and beam 2 (red) during a typical fill for luminosity production in 2012 with 50 ns bunch spacing; middle: measured heat load in the cryogenic arcs (black), and the corresponding estimation from beam screen impedance and synchrotron radiation (green stars); bottom: average bunch length for the two beams.

presented in Sec. 5.2), which provided a safe enough margin to guarantee EC free operation with 50 ns beams, the LHC quickly became productive for physics with 50 ns beams without suffering any major limitations from EC. The only exception is represented by EC effects observed in the common vacuum chambers, which will be treated in detail in the following chapter. The physics run successfully continued up till the 6 December 2012, with an intensity per bunch boosted to 1.6×10^{11} ppb within transverse emittances as low as 1.6 μm at injection. This could be achieved thanks to the careful optimization and tuning in the injectors and the implementation of the low gamma transition optics (Q20) in the SPS for the production of LHC beams [79, 80].

The fact that no significant EC was developing in the LHC arcs in 2012 is confirmed by heat load measurements. Figure 5.2 shows that the heat load measured during a typical physics fill with 50 ns beams is perfectly consistent with the estimation made including the contributions from the beam screen impedance and from synchrotron radiation, without any significant contribution from the EC. Moreover the heat loads measured in the Stand Alone Modules (SAMs) dipole and quadrupole magnets exhibited very similar values (see Fig. 5.3) again consistently with impedance and synchrotron radiation, which are practically independent of the local magnetic field.

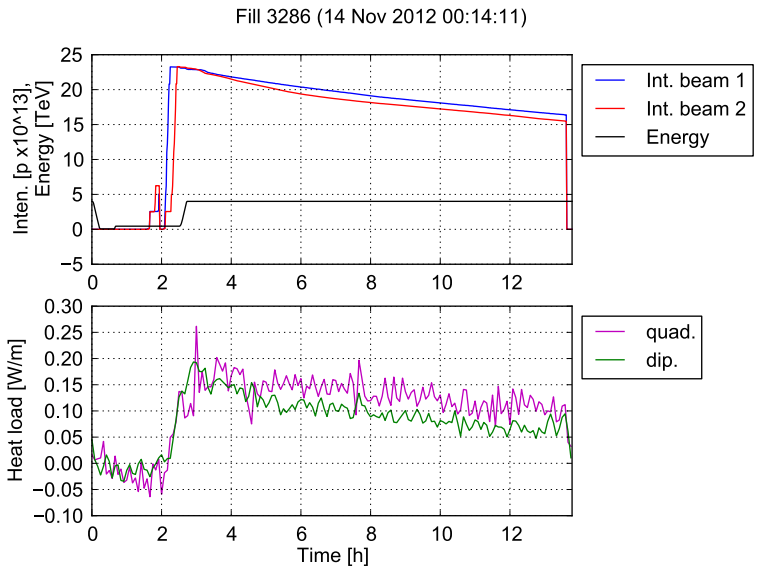

Figure 5.3: Heat load measured in the stand alone quadrupoles (Q5 and Q6 in IR 1 and 5) and dipoles (D3 in IR 4) during the fill already shown in Fig. 5.2

5.2 EC OBSERVATIONS AND STUDIES WITH BEAMS WITH 25 NS SPACING IN 2011

In 2011 beams with 25 ns spacing were injected into the LHC only during five MD sessions during which strong EC effects were observed all around the ring. A brief summary of the MDs will be given in the following, while a more detailed analysis of the EC observations will be presented in the next sections:

(a) **29 June 2011**: first injections of 25 ns beams into the LHC. The filling scheme consisted of nine batches of 24 bunches separated by increasing gaps (2.28, 5.13 and 29.93 μs). Pressure rise around the machine as well as heat loads in the arcs were observed. All the last bunches of each batch suffered losses and emittance growth [63];

(b) **26 August 2011**: first injections of a 48-bunch train into the LHC with 25 ns spacing. Two attempts were made to inject a 48-bunch train from the SPS, which led to beam dump triggered by large beam excursion and beam loss interlocks, respectively. The analysis of the "post mortem" data showed that in both cases a transverse instability occurred right after injection especially on the trailing bunches of the injected trains. These observations have been reported in [64] and a more detailed analysis will be presented in Sec. 5.2.3. This MD session had then to be interrupted because of a failure of the cryogenics caused by a thunderstorm;

(c) **7 October 2011**: injection tests and first ramp. In the first part of the MD, trains with 48-72-144-216-288 bunches from the SPS were injected into the LHC. Given the experience during the previous MD, the chromaticity Q' was set to around 15-20 units in both the horizontal and vertical planes in order to keep the beams stable. In the second part, only 60 bunches per beam were injected in trains of $12 + 2 \times 24$, were accelerated to 3.5 TeV and collided during approximately 5 h;

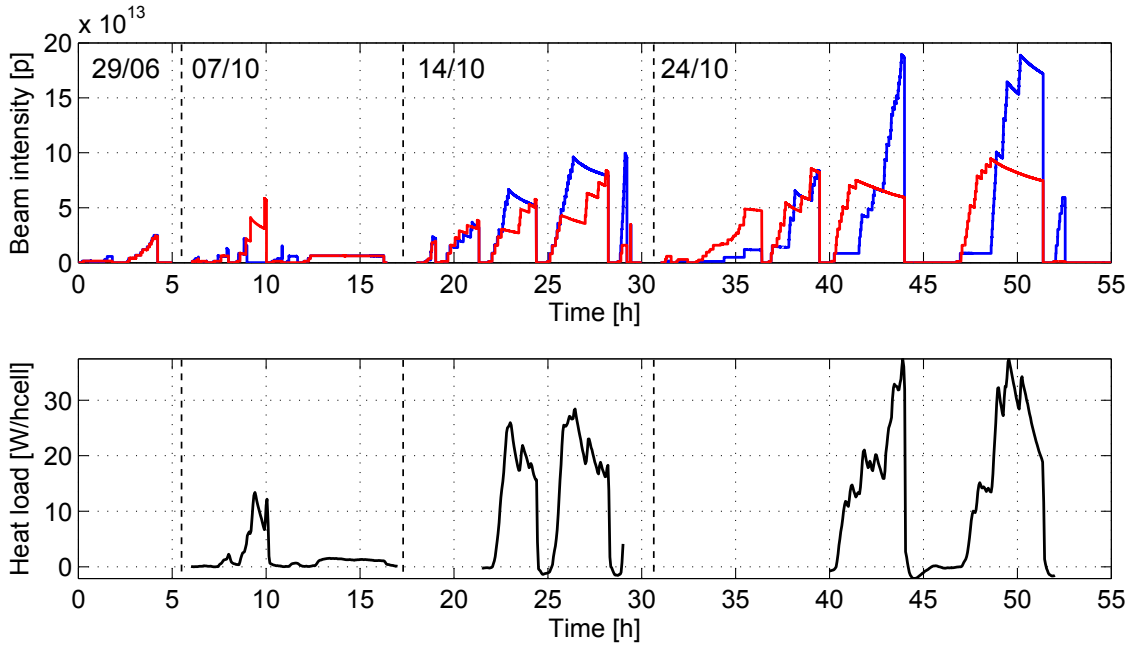

Figure 5.4: Beam intensity (top) for beam 1 (blue) and beam 2 (red) and heat load measure in the cryogenic arcs (bottom) in the MD sessions labeled as (a), (c), (d) and (e).

(d) **14 October 2011**: first long stores of 25 ns beams at injection energy in the LHC for scrubbing tests. During this session up to 1020 bunches per beam were injected in batches of 72. The chromaticity was kept high in both planes ($Q'_{x,y} \simeq 15$) in order to preserve the beam stability. First, a dedicated fill for pressure measurements was made, with batches injected at gradually reduced distances from 4 to 2 μs (in steps of 1 μs). Subsequently, the batch spacing was kept constant for each of the next three fills and it was set to 6.3, 3.6 and 1 μs. Strong emittance growth and slow losses affecting the last bunches of each train were observed throughout this MD session;

(e) **24–25 October 2011**: record number of bunches in the LHC. Four long fills took place for scrubbing purposes (average store time was approximately 4 h), with 25 ns beams injected into both rings in batches of 72 separated by 1 μs. In the third and fourth fills, 2100 bunches were injected for beam 1, while the number of bunches could not exceed 1020 for beam 2, due to a vacuum interlock on one of the LHC injection kickers (MKIs). Although the situation seemed to improve over the MD, slow losses and emittance growth kept affecting both beams. Before starting the fourth fill, the horizontal chromaticity Q'_x was lowered from 15 to 3 units and the horizontal damper gain was slightly increased. Probably due to that, some horizontal instabilities could be observed from the signal of the damper pick up during the fourth fill, but the overall performance did not appear degraded with respect to the previous fill. The MD ended with a 30 min. fill with only beam 1, during which batches of 72 bunches were injected into the LHC at different spacings in order to provide the stable pressure measurements needed for the modeling of the EC in the straight sections (for the method and main results of these studies see [81]).

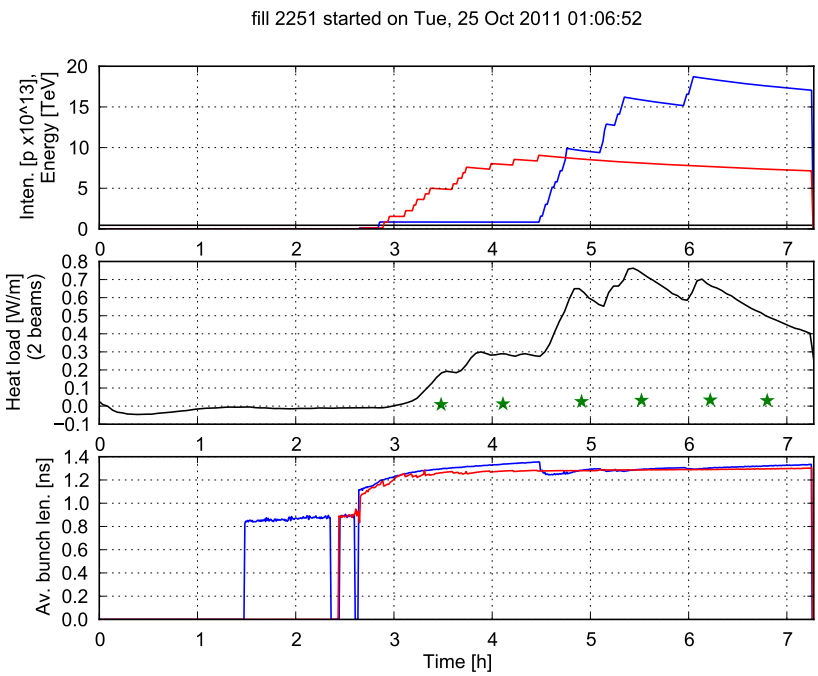

Figure 5.5: Top: beam energy (black) and total intensity for beam 1 (blue) and beam 2 (red) during a the last fill for scrubbing with 25 ns bunch spacing in 2011; middle: measured heat load in the cryogenic arcs (black), and the corresponding estimation from beam screen impedance and synchrotron radiation (green stars); bottom: average bunch length for the two beams.

For sake of compactness, we have chosen to concatenate the MD sessions (a), (c), (d) and (e) and represent them on a continuous time axis in Fig. 5.4, which will be systematically used throughout this section.

5.2.1 *Heat load measurements and reconstruction of the SEY evolution in the dipole chambers*

In all the occasions when long batches with 25 ns spacing were injected into the LHC a strong heat load could be detected on the arc beam screens (see Fig. 5.4). For example, in Fig. 5.5 we show the heat load detected during the last fill carried out for scrubbing test purposes during the MD session labeled with (e) in the previous section. We observe that in this case, as practically in all the other occasions when 25 ns beams were injected into the LHC, the estimation for the heat loads coming from the beam screen impedance and from synchrotron radiation are much smaller (in Fig.5.5 by a factor of about 15) than the measured value, which is an indication that a strong EC is developing in the beam chamber.

Heat load measurements, in combination with PyECLOUD simulations, have been used in order to reconstruct the evolution of the SEY of the arc beam screens following the method illustrated in Fig. 5.6. During the tests the beam quality was strongly degraded due to EC effects. For example, looking in Fig. 5.7 at the beam parameters during the fill of Fig. 5.6, we can clearly see important shortening and particle losses on the trailing bunches of the batches, especially for those which have spent more time in the ring. The EC buildup and consequently also its effects are strongly dependent on the beam structure, therefore, in order to compare the simulation results with the heat load measured in the machine at a certain

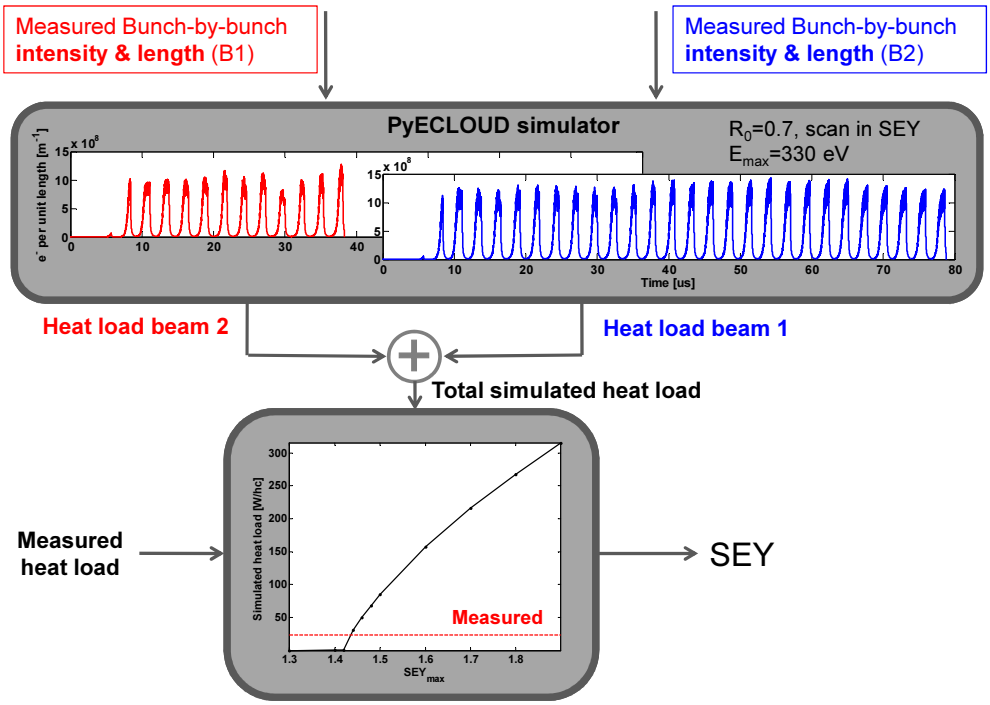

Figure 5.6: Illustration of the method we used to reconstruct the SEY of the LHC arc beam screens based on heat load measurements from the cryogenic system.

time, we downloaded from the LHC Logging Database the beam parameters measured at the same time and used them to setup realistic EC simulations in PyECLOUD. This allowed us to obtain, for both beams, the estimated heat load as a function of the SEY of the chamber, which could be compared against the measured value in order to estimate the SEY. To do so we needed to assume that: 1) the SEY model presented in Sec. 1.2 with R = 0.7 and E_{max} = 330 eV can be applied to the LHC beam screen; 2) the beam screens of the two beams have the same SEY parameter; 3) the heat load in the arc FODO lattice is dominated by the dipole magnets.

The estimation has been carried out both for fills with 50 ns beams (from early 2011, when EC induced heat load could still be detected) and for the 25 ns tests. The results are shown in Fig. 5.8.

For the 50 ns spacing the goal was to estimate the evolution of the SEY during the 2011 scrubbing run with 50 ns beams. For this purpose we used the heat load data from the first LHC fill with 1020 bunches per beam (9 April 2011) and those from the physics fill 1704 of 13 April 2011 (recorded during the ramp with 228 nominal bunches per beam). The SEY was estimated to be 2.28 at the last injection of the first analyzed fill and it had decreased to 2.18 during the ramp of the fill 1704 (first two points in Fig. 5.8). This is compatible with the known build up thresholds of 2.2 at 450 GeV and 2.1 at 3.5 TeV for 50 ns beams [68].

More heat load observations in the arcs have been made with 25 ns beams. Measurements in some reference cells from the first LHC MD with 25 ns beams MD session (a) (29 June 2011) can be found in Ref. [63] while Fig. 5.4 shows the heat load data, averaged over the eight sectors, collected during the MD sessions (c), (d) and (e). We can notice that the heat load

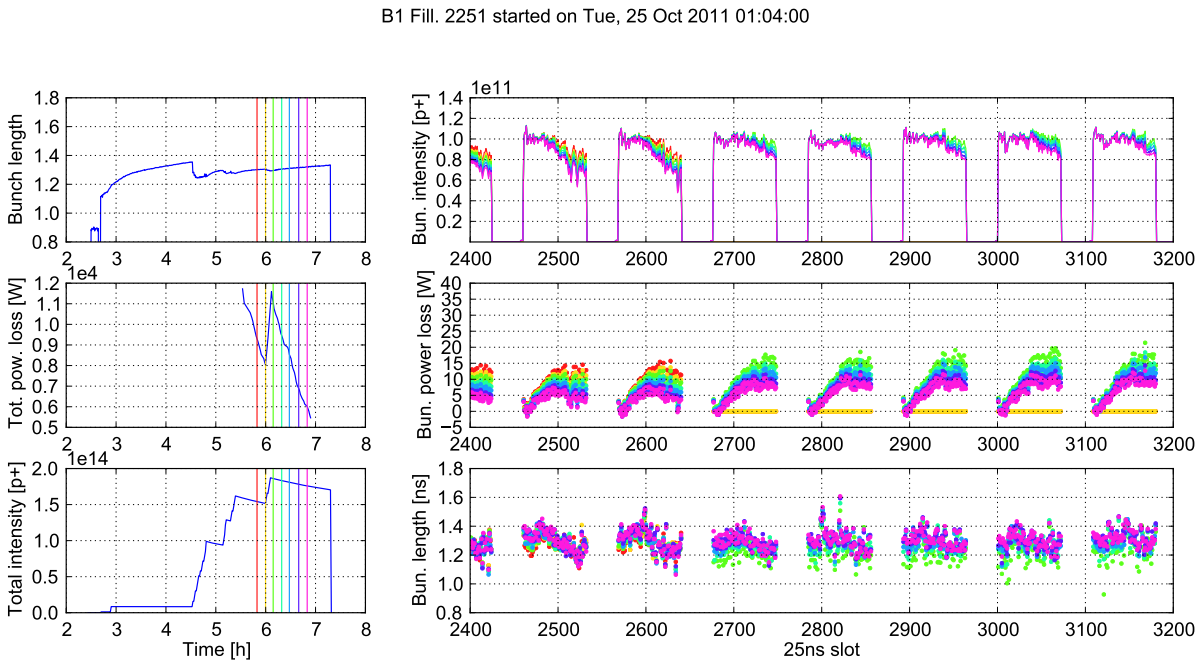

Figure 5.7: Measurements on beam 1 during the last scrubbing fill during the 25 ns MD in 2011. Left, from top to bottom: average bunch length; total power loss from stable phase shift measurement; total beam intensity. Right, from top to bottom: bunch intensities; bunch by bunch power loss from stable phase measurements; bunch lengths. The different traces correspond to different moments indicated by vertical bars in the left plots.

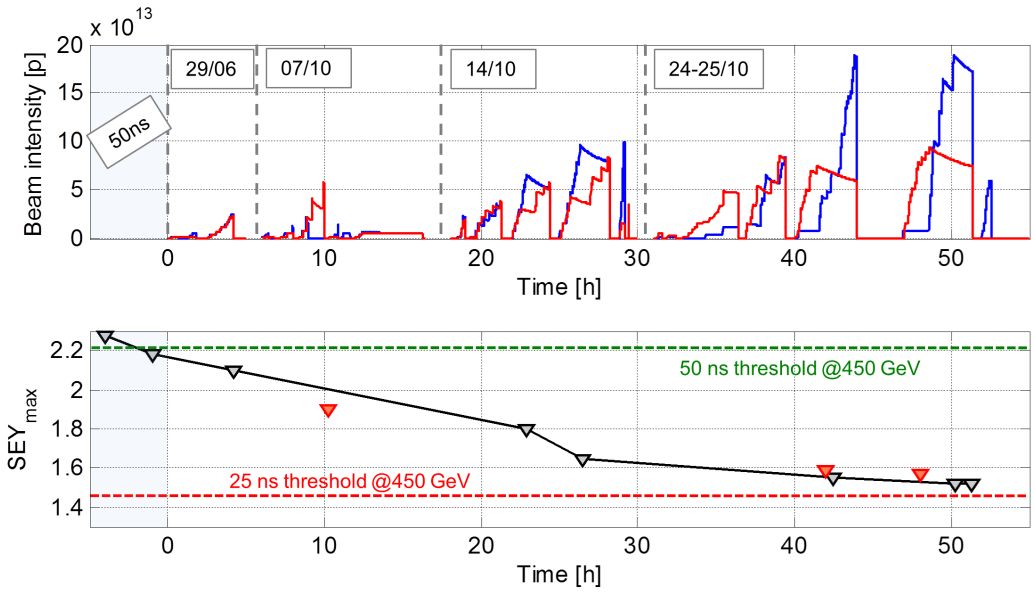

Figure 5.8: Estimated evolution of the SEY on the inner surface of the beam screen in the arc dipoles. The first two points correspond to the measurements done with the 50 ns bunch spacing during and after the scrubbing run with 50 ns beams. The other points correspond to measurements taken during the 25 ns MDs. The three points marked in red correspond to situations in which the total heat load could be only (or mainly) attributed to beam 2.

peaked to values of nearly 50 W/half-cell (i.e. approximately an average of 0.5 W/m/beam) during the last fill with 2100 bunches for beam 1 and 1020 bunches for beam 2. A decay of the measured heat load between injections, and in any case after the last injection, is also clearly visible in the examined cases and it is due to both the weakening of the EC activity from scrubbing and the intensity loss.

Each point in Fig. 5.8 corresponds to a moment in which we have applied the procedure described before in order to reconstruct the SEY of the beam screen. The three points marked in red correspond to situations in which the total heat load could be only (or mainly) attributed to beam 2. This gives the opportunity of making a separated estimation for the beam screen of beam 2 alone.

From this curve we can see that the SEY was about 2.28 at the beginning of the scrubbing run and then it had already decrased to 2.1 by the time the first 25 ns beams were first injected into the LHC. According to the evaluation from the last two measurement points chosen during the same store, the SEY had decreased to 1.52 at the end of the last MD with 25 ns beams in 2011. Looking at the last three black points, it is clear that, while a little scrubbing effect is still observed between the second to last and the last 25 ns store, no significant decrease of the SEY can be detected over the last two points belonging to the same store. This suggests that, although the EC had not yet disappeared from the arcs, the SEY already entered a region in which the electron doses required to continue the scrubbing can be only accumulated over much longer times. The decay of the heat load after the last injection cannot be attributed to scrubbing, but only to beam loss.

The three measurement points with the contribution of beam 2 alone show that, while it seems plausible that at the beginning of the 25 ns MDs the beam screen of beam 2 was more quickly scrubbed than that of beam 1, the conditioning status of the two screens has become later equalized. The last two points for beam 2 can be hardly distinguished from the values obtained from the total heat load.

5.2.2 *Beam observations: bunch by bunch energy loss*

Another quantity that could be used to monitor the EC activity, and therefore the scrubbing process in the LHC, is the beam energy loss per turn, which can be inferred from stable phase measurements from the Radio Frequency (RF) system. The measurement procedure developed by the RF team is quite complex, since the phase shift signal is very low (∼0.5 deg) and several effects (e. g. the reflections from the cables going from the underground cavern to the surface) have to be corrected [67, 71, 74].

This type of measurements was already applied in 2010 with 50 and 75 ns beams, and then again during the scrubbing run with 50 ns beams in 2011 to qualify the efficiency of the scrubbing process [67]. However, in these cases it was always based on the global shift of the stable phase averaged over the whole beam. The method was then further refined during the 25 ns MDs in 2011, when the stable phase shift could be measured in a bunch resolved mode. The measurement does not provide the absolute RF phase seen by each bunch but only the relative bunch-to-bunch phase differences since a phase reference is not available. Since we are interested in the energy loss due to the EC we take as a reference the short bunch train of 12 bunches always injected at the head of the beam for safety reasons, for which the EC induced energy loss is expected to be negligible [74].

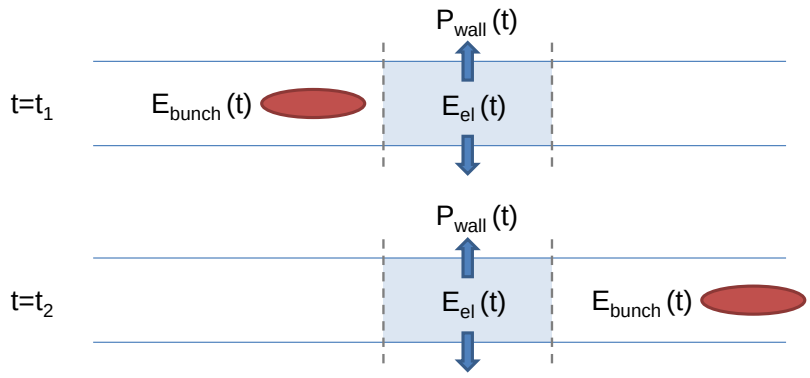

Figure 5.9: Illustration of the energy balance used to determine the bunch energy loss from PyECLOUD buildup simulations.

Figure 5.7 shows energy loss measurements taken during the last scrubbing fill of the MD session (e). The signature of the EC buildup can be easily recognized on the measurement: the bunches at the head of the train, which see less electrons in the beam chamber, are practically not affected, then the electron density, and therefore the energy loss grows along the first portion of the train, and finally saturation can be observed at the tail. From Fig. 5.7 we can also recognize the impact of particle losses on the measured energy loss, and therefore on the EC buildup.

Despite the fact that PyECLOUD uses a rigid beam model (where no effect of the electrons on the beam are taken into account), the energy loss of each bunch due to the interaction with the EC can be estimated from the buildup simulations using a simple energy balance, which is sketched in Fig. 5.9. We consider a slice of the beam chamber (the one in which we are simulating the EC buildup) and a certain bunch of the train. We want to estimate the energy lost by the bunch while traversing the EC in the slice. We take an instant t_1 before the bunch has entered the slice and an instant t_2 after the bunch has left the slice. The only energy lost by the system (bunch + electrons) is the one deposited by the electrons on the chamber's wall. Therefore we can write:

$$[E_{bun}(t_2) + E_{el}(t_2)] - [E_{bun}(t_1) + E_{el}(t_1)] = \int_{t_1}^{t_2} P_{wall}(t)dt \tag{5.1}$$

where E_{bun} is the energy of the bunch, and E_{el} is the total energy of the EC (it includes both the kinetic and the electrostatic energy of the electrons, even if the second one has always been found to be negligible) and P_{wall} is the power deposited by the electrons on the wall. Just by rearranging the terms we obtain the energy loss of the bunch:

$$\Delta E_{bun} = [E_{bun}(t_1) - E_{bun}(t_2)] = [E_{el}(t_2) - E_{el}(t_1)] + \int_{t_1}^{t_2} P_{wall}(t)dt \tag{5.2}$$

We applied this method to the scrubbing fill of Fig. 5.7. The best agreement was found for SEY=1.6 (quite consistent with the value estimated from the heat load – see Fig. 5.8). The comparison between measured data and simulation results is shown in Fig. 5.10. The agreement between the experimental data and the simulations is excellent in the regions with saturated EC while it is clear that the data tend to indicate a faster build up of the EC in the machine with respect to the one predicted by simulations. This becomes especially evident if

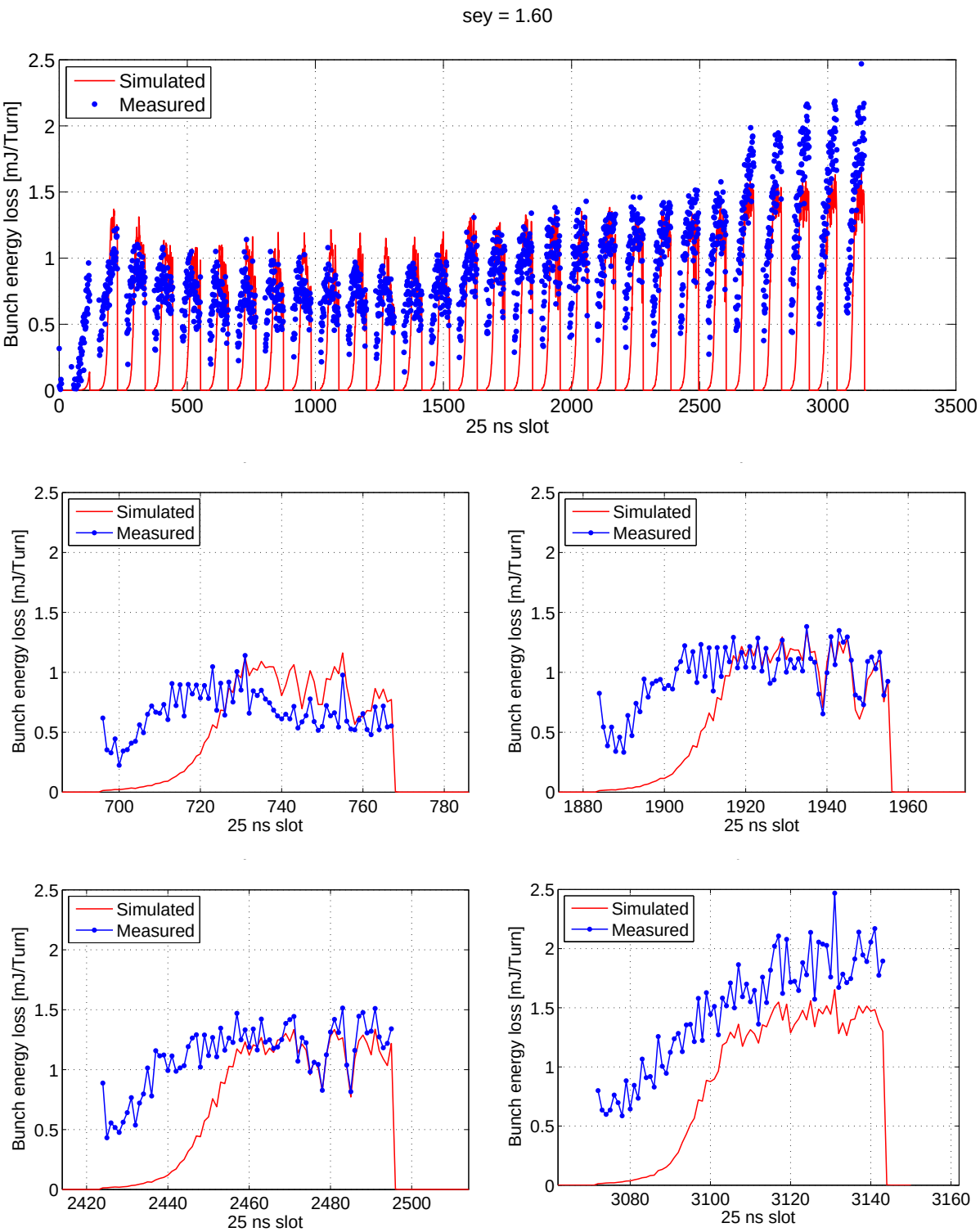

Figure 5.10: Simulated and measured energy loss for beam 1 after the last injection of the last scrubbing fill during the 25 ns MD in 2011.

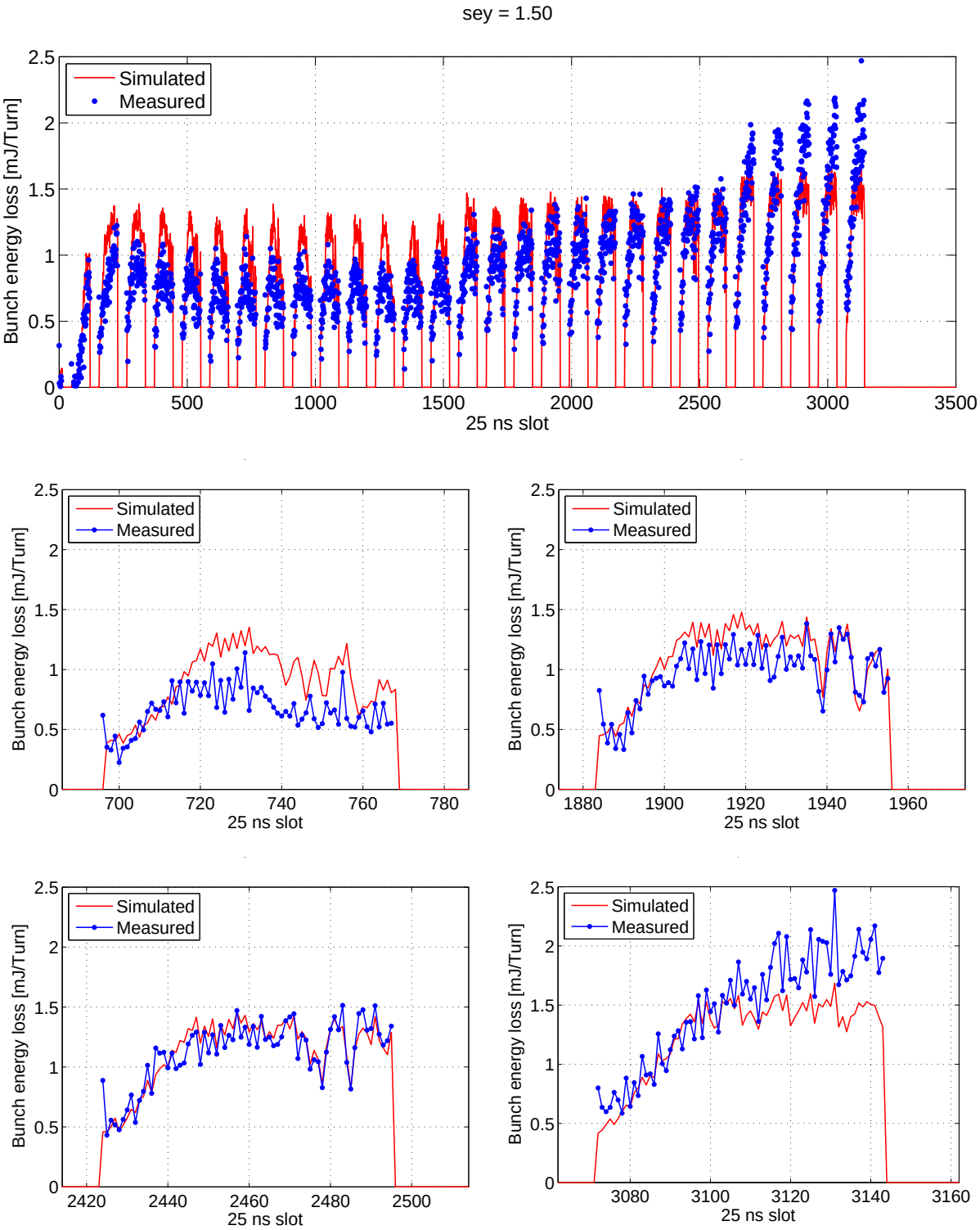

Figure 5.11: Simulated and measured energy loss for beam 1 after the last injection of the last scrubbing fill during the 25 ns MD in 2011 – 10% uncaptured beam is added to the beam profile in the simulation.

we zoom only on single batches extracted from the full train and we look into the details of the bunch-by-bunch trend (lower plots in Fig. 5.10).

The reason of the discrepancy could be either too low electron seeding in the simulation (residual gas ionization underestimated) or too fast decay of the EC between subsequent batches. Therefore we attempted to enhance the "memory effect" between batches in the simulations, by adding to the beam profile a coasting beam having total intensity equal to 10% of the circulating bunches, representing the uncaptured particles in the accelerator. In this case the best agreement has been found for SEY=1.5. From the results presented in Fig. 5.11 we can notice that now the buildup phase is correctly reproduced by the simulation, while the good agreement found already without uncaptured beam in the saturation phase is preserved.

It is worth underlining that the uncaptured beam is only one possible factor that could slow down the EC decay. For example, other possibilities could be a larger value of R_0 in the SEY model or a different shape of the SEY curve in the low energy region, as it has been briefly discussed in Sec. 4.7.

5.2.3 *Beam observations: transverse instabilities*

As mentioned in Sec. 5.2, the first attempt to inject bunch trains of 48 bunches spaced by 25 ns into the LHC with the an intensity of about 1.0×10^{11} ppb was made during the MD session we labeled with (b) on August 26, 2011. Shorter bunch trains of 12 and 24 bunches with the same bunch spacing had been successfully injected earlier in the same session as well as in session (a).

The first injection of 48 bunches with the transverse damper switched on resulted into a beam dump after 1000 turns due to a beam excursion interlock. The following injection of 48 bunches without transverse damper was aborted already after around 500 turns due to a beam loss interlock. In both cases, chromaticity was set to the values usually used during operation ($Q'_{x,y} \approx 2$).

Data of the damper pick-ups for about 73 turns are stored for both beams in the post mortem system after a beam dump. Each data set (channel) represents one of the allowed 3564 bunch positions along the ring. Figure 5.12 shows the turn-by-turn oscillation of each of the 48 bunches around the closed orbit in both planes for the two injections just before the respective beam dump. The oscillation amplitude is very small for the first 25 bunches, especially when the damper is switched on (see Fig. 5.12 - left). In this case the last bunches of the bunch train reach peak values of around 1 mm in the horizontal plane and up to 6 mm in the vertical plane, thus the instability is mainly observed in the vertical plane. Without damper, the last bunches of the train exhibit oscillations of up to 3 mm amplitude in both planes with a clear "coupled bunch" pattern.

The frequency spectrum without damper is dominated by coupled bunch modes up to 1 MHz in the horizontal plane and up to 2 MHz in the vertical plane. With damper on, instabilities in both planes are damped up to a frequency of about 15 MHz [64].

The observed pattern along the bunch train, as well as the similarities with transverse instabilities observed at the first tests with 25 ns beams at the SPS [82] suggested that these instabilities could be caused by the EC in the dipole magnets.

Therefore we decided to try to reproduce these observations by combining PyECLOUD and HEADTAIL [83] simulations in order to crosscheck our models and codes [72]. As first step the EC buildup in the LHC dipoles is simulated with PyECLOUD for an r.m.s. bunch length

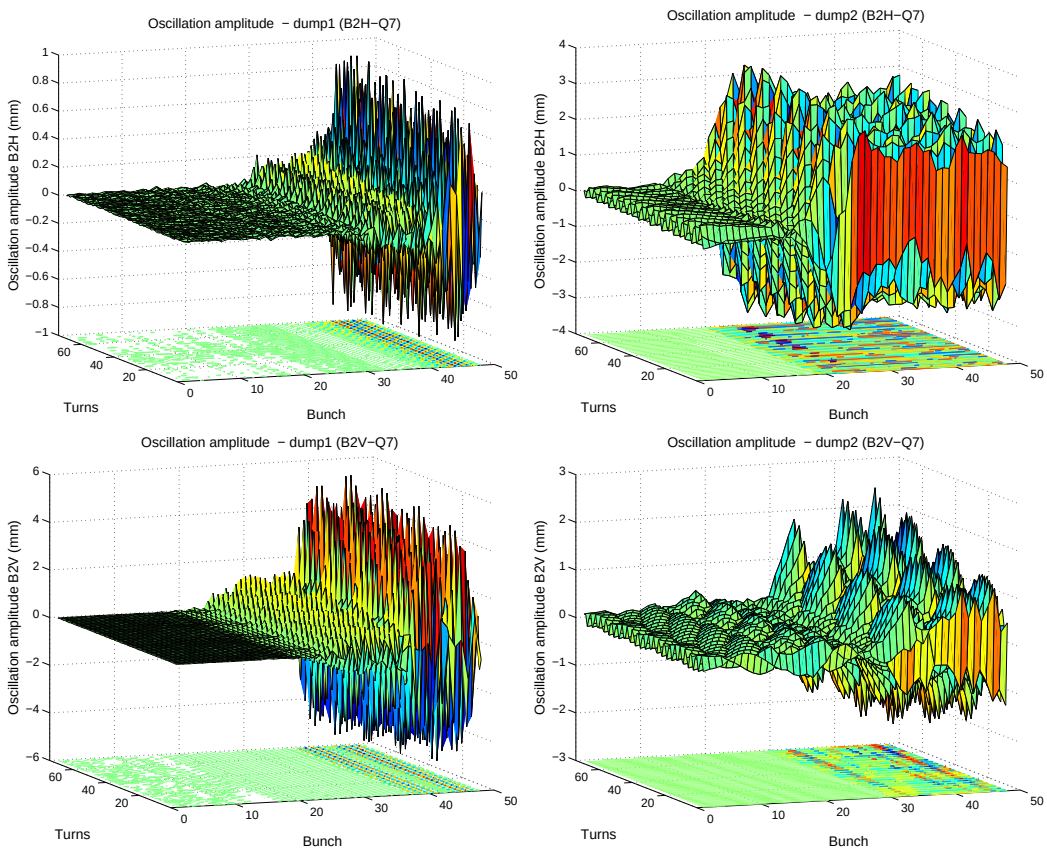

Figure 5.12: Transverse oscillations measured with the pick-ups of the transverse feedback for 73 turns close before the beam dump, for the first case with transverse damper (left) and the second case without transverse damper (right) in the horizontal (top) and vertical plane (bottom).

of 12 cm, equal bunch intensities of $N = 1.0 \times 10^{11}$ protons per bunch (ppb) along the train[1] and SEY=2.1, i. e. the value estimated on the previous MD with 25 ns beams (see Sec. 5.2.1). The simulation was initialized with a uniform distribution using the same number of primary electrons as in the simulations for determining the evolution of the SEY as discussed in Sec. 5.2.1. The importance of the number of primary electrons and their spatial distribution for the onset of the EC instability is discussed in more detail in [72]. The electron distribution is sampled right before each of the 48 bunch passages and these snapshots are used as input for a set of 48 HEADTAIL simulations, to simulate the interaction of each bunch with the EC.

Such distributions look very similar to those presented in Sec. 4.2, with the accumulation of electrons in two stripes, as typically obtained for the buildup with 25 ns bunch spacing in the LHC beam screen when the electrons move in a strong dipolar magnetic field. In HEADTAIL the EC is modeled by thin slices lumped at several accelerator sections and the electron motion is frozen in the horizontal plane in order to account for the effect of the dipole magnetic field. At each EC section the electron proton interaction is computed consecutively for longitudinal bunch slices. After a complete bunch passage the EC is reset to the initial distribution for the next interaction section. Figure 5.13 shows the evolution of the transverse emittance for a few selected bunches in the middle of the bunch train obtained with HEADTAIL for the

1 It was not possible to retrieve the actual bunch-by-bunch intensity variation from the data logging during the injection tests due to the short time of circulating beam before the dump.

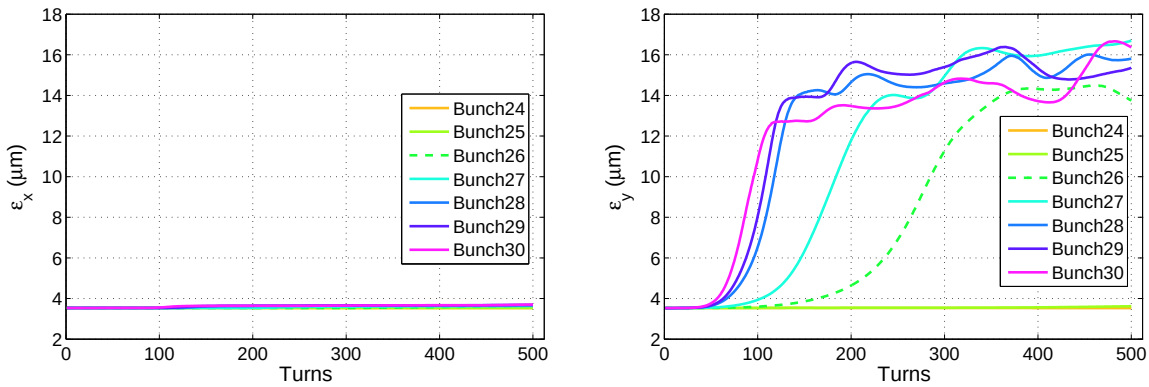

Figure 5.13: Evolution of the horizontal (top) and vertical (bottom) emittance along 500 turns for a few selected bunches in the center of the bunch train.

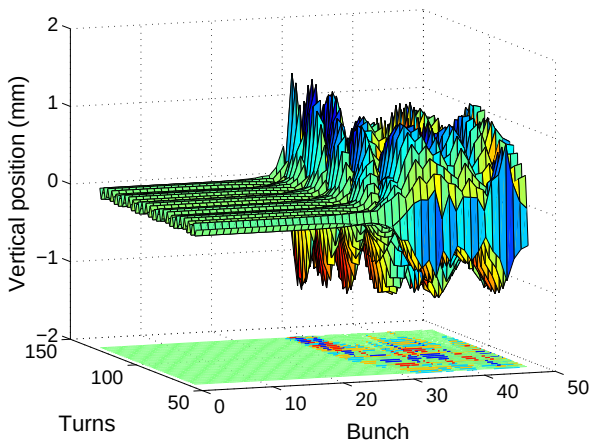

Figure 5.14: Bunch-by-bunch oscillations in the vertical plane as obtained with HEADTAIL. For better comparison, only 70 turns during the instability (from turn 50 to turn 120) are shown.

simulation of 500 turns at the LHC injection plateau using the initial electron distribution as described above.

No instability or coherent excitation of the horizontal bunch motion is observed, as was expected since the EC is located in dipole regions. On the other hand the EC drives a single bunch instability in the vertical plane. This instability can be observed in the form of an exponential emittance growth, as in the case studied here, for all bunches after bunch number 25. Figure 5.14 shows the bunch-by-bunch oscillations in the vertical plane during the instability (from turn 50 to turn 120) as obtained from HEADTAIL.

The simulation is in good agreement with the experimental observations during the first injection of 48 bunches in August with the transverse damper on, where the second half of the bunch train is unstable mainly in the vertical plane (see Fig. 5.12), as the damper is suppressing horizontal coupled bunch instabilities. Horizontal instabilities are not observed in the simulation, since the coupling between bunches is not taken into account but each bunch is treated by an independent HEADTAIL simulation.

Further studies were devoted to assess which part of the EC distribution is mainly responsible for driving the beam unstable. Figure 5.15 shows an example for a bunch in the middle

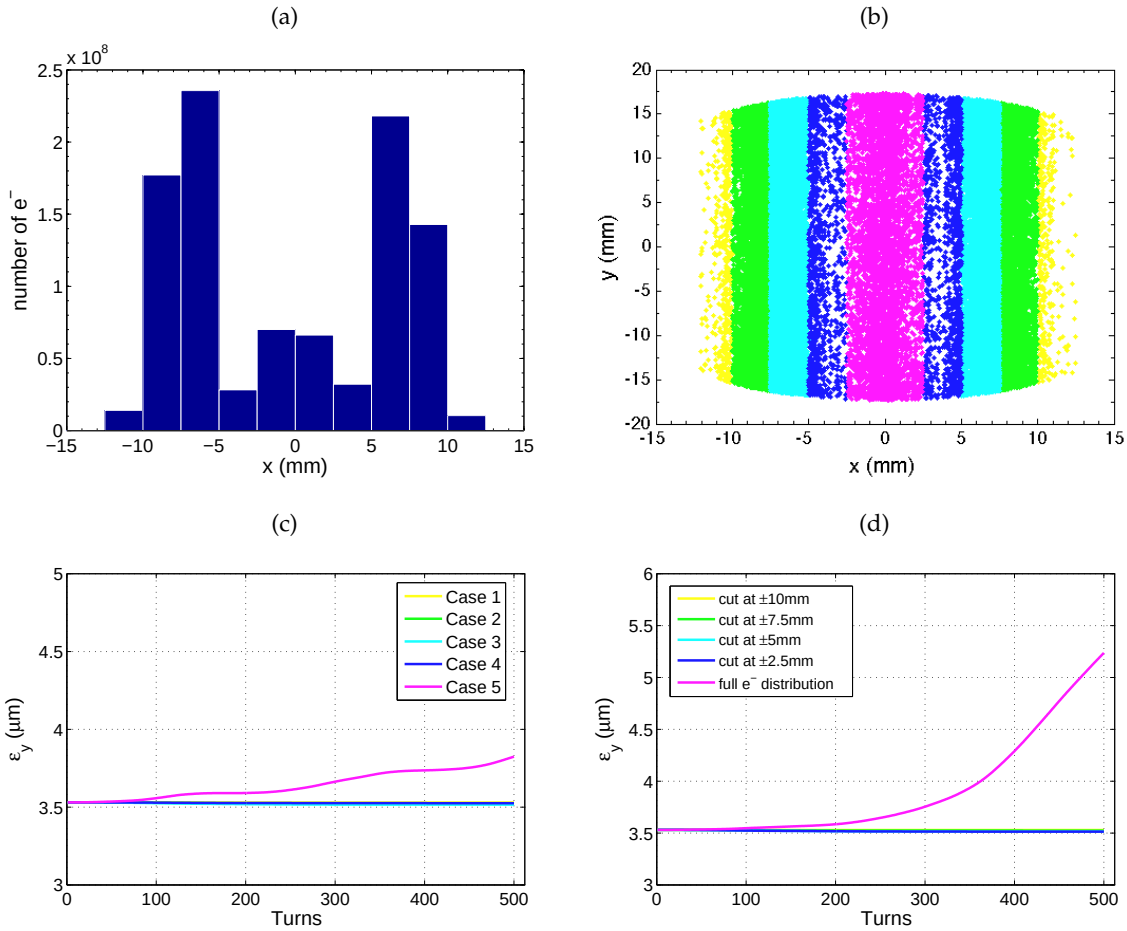

Figure 5.15: (a) Histogram of the horizontal electron distribution; (b) transverse electron distribution divided into colored regions; (c) evolution of the vertical emittance for the interaction with the electrons of the respective colored area; (d) evolution of the vertical emittance for different horizontal cuts of the electron distribution.

of the train, which encounters an electron density which is just above the instability threshold. Fig. 5.15 (a) shows a histogram of the horizontal electron distribution before the bunch arrival as obtained from the PyECLOUD simulation and used as input for the HEADTAIL simulation. Most of the electrons are concentrated in the two stripes far away from the beam (the 3σ beam envelope covers roughly the two central bins). Fig. 5.15 (b) shows for the same case the actual positions of the macro-electrons in the transverse plane provided by the PyECLOUD simulation. The macro-particle distribution is divided here into five regions as indicated by the color code (corresponding to the bins in the histogram). In order to study the contribution from these five regions to the vertical instability, each of these regions is considered independently and used as input for individual HEADTAIL simulations. The evolution of the vertical emittance for these five cases is shown for 500 turns in Fig. 5.15 (c). In the case studied here, only the central part of the electron distribution is able to drive the beam unstable. Conversely, Fig. 5.15 (d) shows the vertical emittance evolution in case all electrons enclosed by the respective colored areas have been removed, i.e. cutting the electron distribution at the inner borders of the colored regions. The instability appears only when the electrons in the central part of

the distribution are taken into account. It follows that for the typical EC distributions encountered in the simulations of the LHC dipole regions, it is mainly the central electron density that determines the onset of the instability. Therefore the instability threshold can be inferred roughly from the central electron density. Only in cases where the central electron density is *very* small compared to the density in the stripes this approximation may not hold.

It should be noted that the instability thresholds found in this study, using the non uniform distribution provided by buildup simulations, are consistent with thresholds previously found in HEADTAIL simulations assuming a uniform electron distribution before the bunch passage, which is around $1 \times 10^{12}\, e^-/\mathrm{m}^3$ [34].

Further sensitivity studies focusing on the dependence of these results on the number of primary electrons and on their distribution in the beam chamber can be found in [72].

5.2.4 *Beam observations: transverse emittance growth and particle losses*

While the 50 ns beam proved to be stabilized in the LHC by the EC mitigation achieved with the scrubbing run, the 25 ns beam has exhibited clear signs of transverse instability and emittance growth throughout all the dedicated MD sessions in 2011. Despite a clearly improving trend from one fill to the next one, these signs have not completely disappeared. During the first tests on 29 June, when only batches of 24 bunches were injected from the SPS, the beam could be kept inside the machine because the level of EC reached along each batch was enough to cause significant emittance growth, but no coherent instability and fast beam loss [63]. Then, as described in the previous section, when, on the following MD session, batches of 48 bunches were for the first time transferred from the SPS to the LHC, the beam was twice dumped after few hundreds of turns, due to the excitation of a transverse instability leading to unacceptable losses. During the successive MD sessions, this problem was circumvented by injecting the beam into the LHC with high chromaticity settings.

Values of $Q'_{x,y}$ around 15 were chosen, as they had been found to be sufficiently stabilizing in HEADTAIL simulations [34]. Using these settings, the beam could be kept inside the LHC, albeit with degraded transverse emittances, as shown in Fig. 5.16. Since the Beam Synchrotron Radiation Telescope (BSRT) needs about 2 sec to measure the emittances of each bunch, each of the snapshots in the figure does not represent an instantaneous photograph of the beam at a certain time, but results from a sweep over the bunches that can last as much as several minutes. Although the batch spacing was decreased from 2 μs during the measurement of 14 October to the 1 μs of the last MD session, the vertical emittance blow up exhibits signs of improvement. No significant further change is observed then in the vertical plane between the measurements taken in the last two fills (consistently with the slight scrubbing effect between them as inferred from the heat load measurements). The situation looks more complicated in the horizontal plane. Here a deterioration can be noticed from the 14 October measurement to the 24 October one. It is interesting that the situation appears improved for the 25 October measurement, when the LHC was run with lowered horizontal chromaticity settings. This fact may suggest that by lowering chromaticity we have moved from a regime of strong incoherent emittance growth driven by EC and high chromaticity to a new one, in which the beam suffers a fast instability, but later evolves with a better lifetime. In any case, as a general consideration, a clear weakening of the EC effect from 14 to 25 October is witnessed by the improved quality of the first two–three batches. The first two seem to be hardly affected by emittance growth in both transverse planes by the time of the last 25 ns fill.

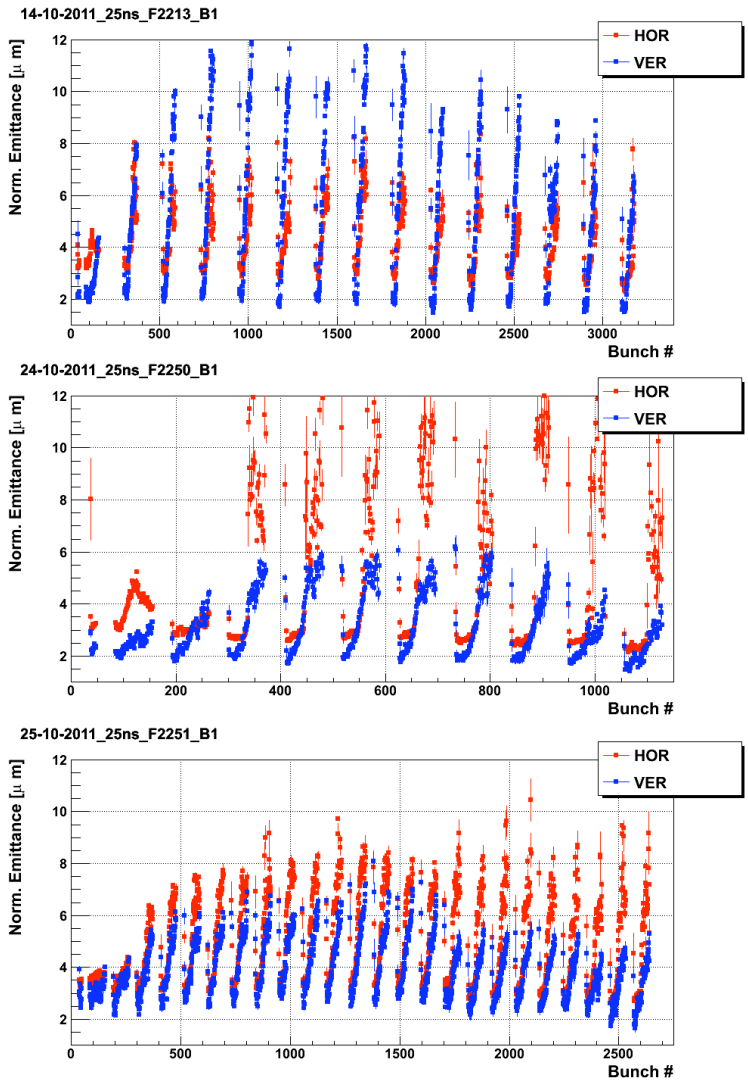

Figure 5.16: Snapshots of the horizontal and vertical emittance measurements for beam 1 during the last fill of the MD session (d) and the scrubbing fills of MD session (e).

Other beam observables that can be used to study EC and scrubbing effects are the bunch-by-bunch particle losses and lifetimes. Losses mainly affecting the bunches at the tails of the injected batches are systematically visible in all the 25 ns fills in 2011, but an improvement has been noticed over time. The bunch-by-bunch intensities evolution during the MD session (e) is shown in Fig. 5.17 (a), a zoom over the first three batches in shown in Fig. 5.17 (b) and the corresponding instantaneous bunch lifetimes are shown in Fig. 5.17 (c). A steady improvement in the loss pattern can be observed.

During the first fill the first batch exhibited hardly visible signs of losses after a store of approximately 2.5 h. A large fraction of the second and third batch suffered fast losses, which reduce the bunch intensity of the second half of the batch to 30% of their initial values within the first hour. During the second fill the losses on the first batch have almost entirely disappeared, while in the second batch they only become visible in our color scale after about 2 h. Some bunches at the end of the third batch are still affected by fast losses, like in the

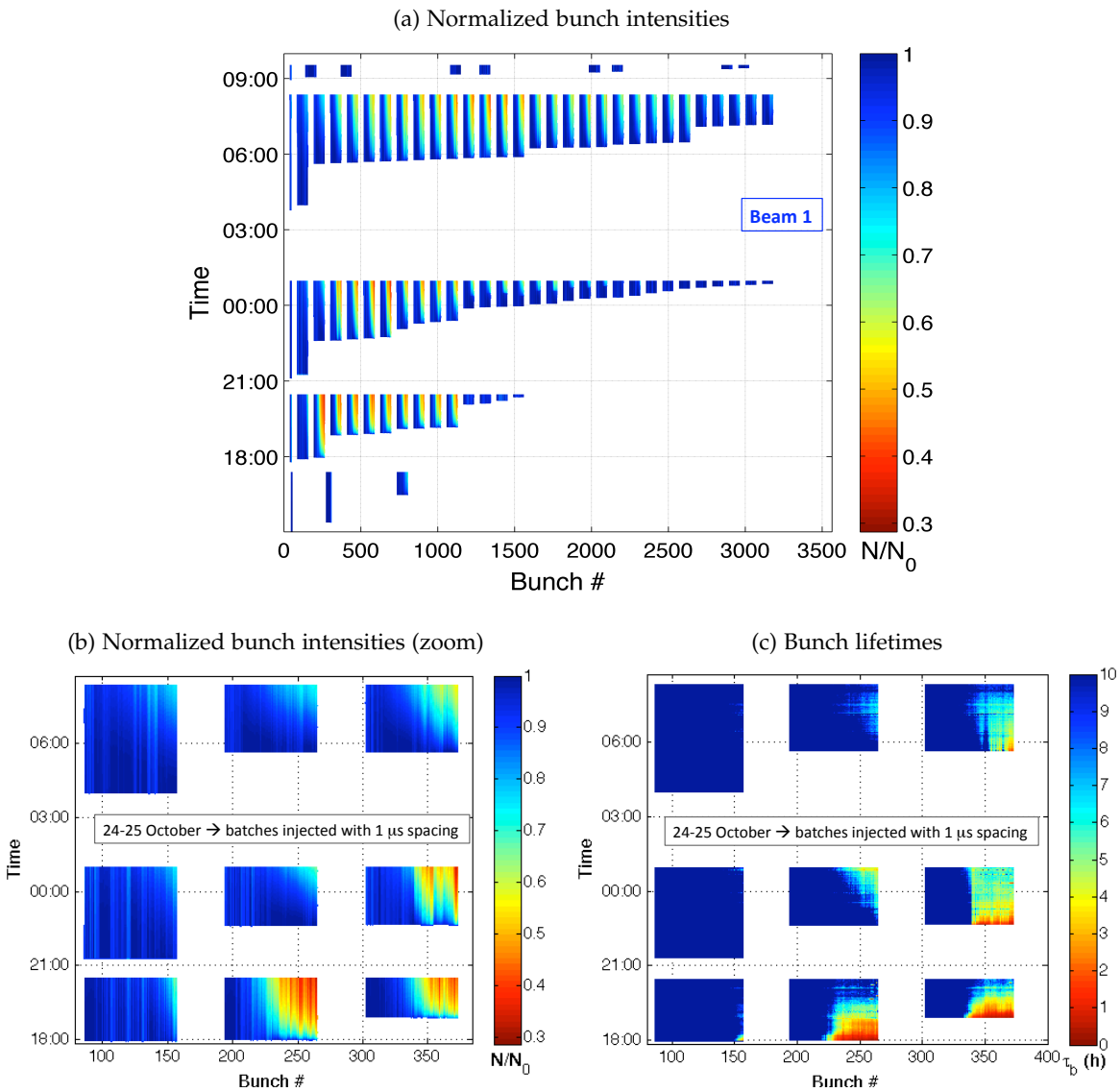

Figure 5.17: Bunch intensity measurements during the MD session (e): (a) evuolution of the normalized bunch intensities; (b) zoom over the first three batches; (c) Instantaneous bunch lifetime for the first three batches.

previous fill. During the third fill the situation seems improved, because the losses on the third batch have become slower.

Looking into the bunch-by-bunch lifetimes (essentially the derivatives of the previous plots), we also notice the existence of two different loss regimes. During the first fill, losses seem to always occur very quickly and then the bunch-by-bunch lifetimes improve as the bunches have already lost a significant fraction of their intensities. On the other hand, during the second fill we can already observe that the second batch is not affected by fast losses anymore, as it rather tends to lose at a later stage and has a deteriorating lifetime. This could be interpreted as the signature of an incoherent effect, which gently pushes the protons towards the large amplitudes and the losses only occur when these particles are then scraped at the machine aperture restrictions. The third batch is still entirely in the fast loss regime. During the third fill, the bunches at the end of the second batch exhibit a deteriorating lifetime, followed by a phase of recovery. This could indicate that the mechanism underlying the incoherent effect has weakened with respect to the previous fill and protons stop being drained into a halo after the first hour of operation. The third batch is divided between an intermediate part of few bunches, which suffers from degrading lifetime (weak EC), and the very last bunches that are still affected by fast losses.

Hence, we can assume that by the time of the last long fill on 25 October, the SEY has reached a value such that the EC in the arcs fully saturates only at the end of the third batch (with a batch spacing of 1 μs). This is further confirmed by the very last fill of 25 October, aimed at collecting stable pressure measurements for the estimation of the SEY in the uncoated regions. During this fill, batches with variable spacing from 4 to 1 μs were injected into the LHC and, despite the pressure rise associated with each injection, no evident sign of quality degradation was observed on the beam (see Fig. 5.17 (a), fill starting at 9:00).

5.3 EC OBSERVATIONS AND STUDIES WITH BEAMS WITH 25 NS SPACING IN 2012

In 2012, the first injection of beams with 25 ns spacing in the LHC took place on 10 July and was mainly devoted to injection setup. This gave the occasion to get a first qualification of the conditioning state of the machine after the 2011-12 End of Year Technical Stop (EYTS) and a long period of operation with 50 ns beams during which no EC effect could be observed in the LHC arcs. An overview of the EC observation during these tests will be presented in Sec. 5.3.1.

In September one of the MKIs in the IR 8 was exchanged due to RF heating issues. Due to lack of conditioning, the new kicker showed an important dynamic pressure rise even with 50 ns beams with consequent risk of breakdown when pulsing the kicker to inject beam [84]. As expected, during a rapid test on 10 October, the situation was found to be even more severe with 25 ns beams, precluding a safe injection of a large number of bunches with 25 ns spacing into the LHC. It was therefore decided to move all further tests with 25 ns beam to the end of the 2012 run in order to profit from parasitic slow conditioning of the MKI from the physics fills with 50 ns beams and minimize the impact on the physics program of a possible damage to the kicker.

Finally the "25 ns Run" took place in December 2012. An overview of this period is presented in Fig. 5.18 where the different stages of the tests have been color coded and described. At the beginning few hours were devoted to finalizing the setup of the injection and of the transverse feedback, then the LHC could move to a 3.5 days Scrubbing Run with 25 ns beams

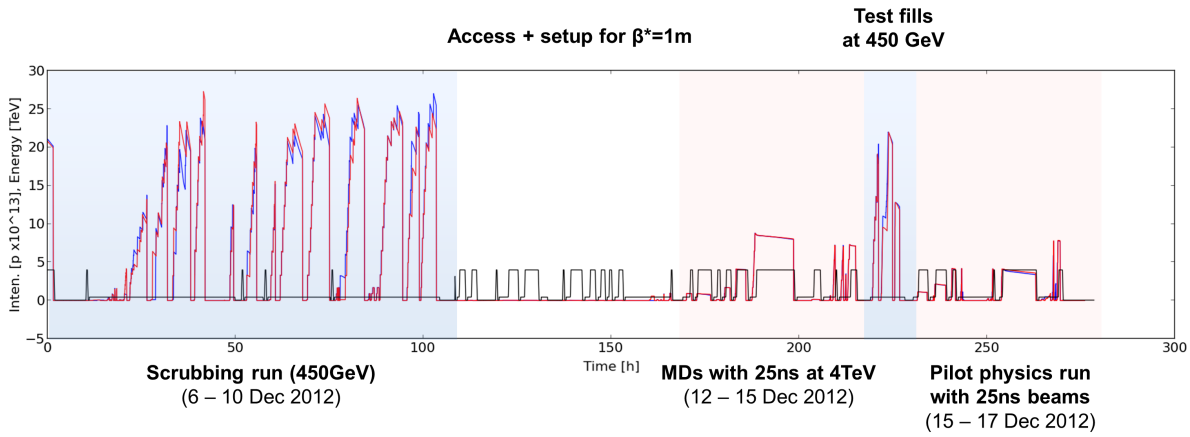

Figure 5.18: Beam energy and total beam intensity – in blue for beam 1 and in red for beam 2 – during the LHC 25 ns run in 2012.

at injection energy. EC related observations during this period will be discussed in Secs. 5.3.2, 5.3.3, and 5.3.4. Later on, after a stop of the operation with beam due to urgent interventions, the machine setup took place to allow safe operation with larger beam size at the main IPs ($\beta^* = 1$ m) in order to be less sensitive to larger transverse beam size (inherent for 25 ns beams with respect to 50 ns due to the production mechanism in the injectors – see Sec. 3.2) and to have more margin with respect to EC induced transverse emittance blowup. The operation with high intensity beams could be restarted on 12 December with MDs during which long bunch trains with with 25 ns spacing were accelerated for the first time to 4 TeV, for machine studies concerning mainly EC and beam-beam effects. This allowed studying the impact of the beam energy on EC effects as we will describe in Secs. 5.3.5 and 5.3.6. These MDs were followed by three fills where the beam was kept at injection energy in order to qualify the conditioning state of the machine after the high energy tests (see Sec. 5.3.7). Thanks to the scrubbing accumulated in the previous phase, a pilot physics run with 25 ns beams could take place right before the 2012-13 EYTS (15-17 December), when it was possible to accelerate and put in collision up to 800 bunches in order to allow the LHC experiments to perform tests with this spacing. The EC activity in the ring was monitored also during this period, the main observations will be presented in Secs. 5.3.5 and 5.3.6.

5.3.1 *Injection tests*

During the 25 ns injection tests performed on 10 July, trains of 72, 144, 216 and finally 288 bunches were successfully injected for Beam 1 while for Beam 2, only trains of 72 and 144 bunches could be injected due to risk of sparking in the MKIs.

After the first successful injection of 72 bunches it was immediately evident that the rings were in a worse conditioning state compared to the last MD with 25 ns beams in 2011.

Figure 5.19 compares the evolution of the bunch intensity in the first hour after the injection of each train for the last scrubbing fill with 25 ns beams in 2011 and for the injection tests of July 2012. In the latter case, it is possible to notice important particle losses even on the first injected batch of 72 bunches, which were not observed at the end of 2011. The losses on the longer injected trains are even more severe, with a large part of the bunches losing more than

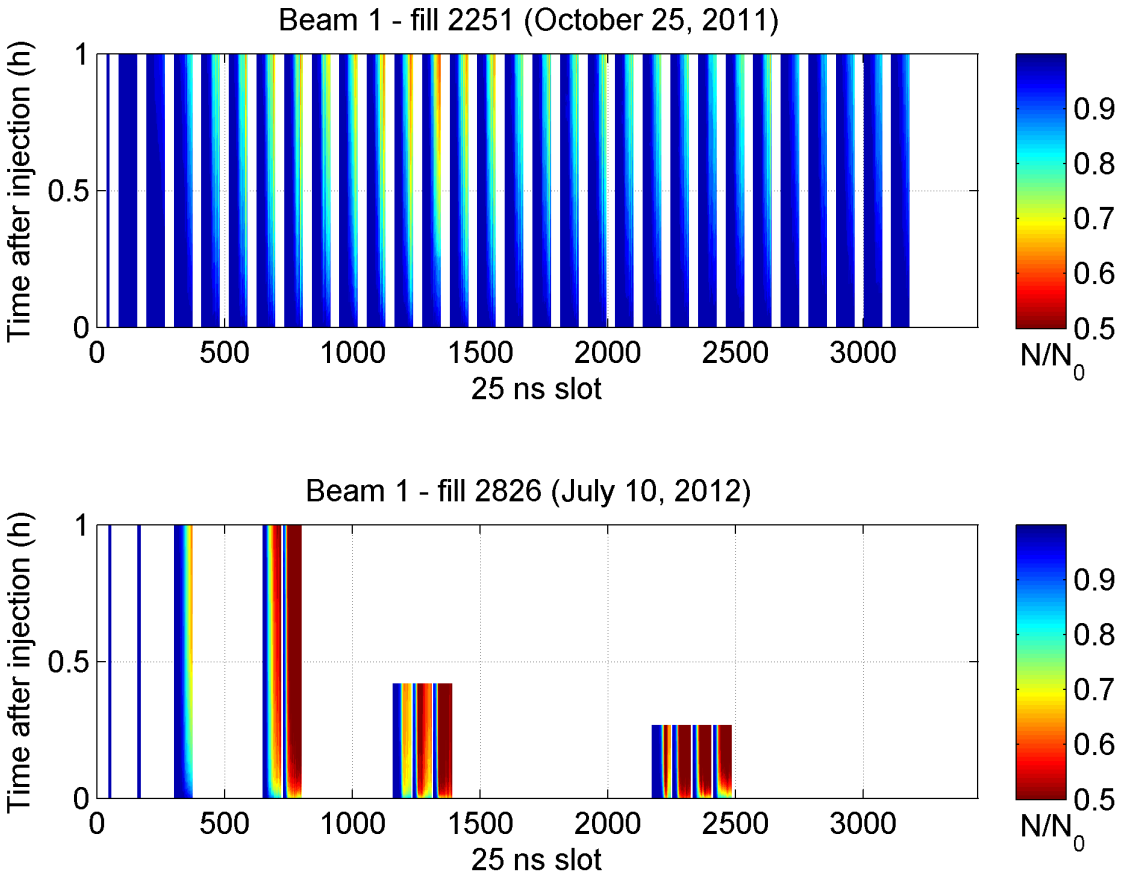

Figure 5.19: Evolution of the bunch by bunch intensity (normalized to the injected values) in the first hour after injection. Comparison between the last scrubbing fill with 25 ns in 2011 and the injection test of 10 July 2012.

half of the intensity in the first few minutes after the injection. These bunches also showed important bunch length reduction and transverse emittance blowup [73].

Indications of severe EC effects came also from the bunch by bunch energy loss measurements, where peaks up to 30 W/bunch could be recorded (see Fig.5.20) again larger than what was observed at the end of 2011 (compare with Fig. 5.7).

Applying the method presented in Sec. 5.2.1 to the heat load measured during the injection tests, it could be indeed inferred that the SEY in the arc dipoles had an initial value of about 1.65 and then quickly returned to 1.55 by the end of the MD. The deterioration with respect to the last value determined from heat load data in 2011 confirmed that, although the arcs were not opened to air during the EYTS 2011-2012, a deconditioning of the inner surface of the beam screen occurred. However, it is encouraging that a value of SEY of about 1.55 could be quickly recovered within less than one hour store of 712 bunches for Beam 1 and 344 bunches for Beam 2, as opposed to the almost 20 hours needed in 2011 to obtain a similar decrease in SEY with a larger beam filling fraction.

The injection tests were carried out with high chromaticity settings ($Q'_{x,y} = 15$) in order to fight EC induced transverse instability. Towards the end of the MD, it was attempted to lower chromaticity to $Q'_{x,y} = 5$, only for Beam 2, and repeat the injections with increasing numbers of batches. After successfully injecting a train of 72 bunches (in spite of a horizontal instability,

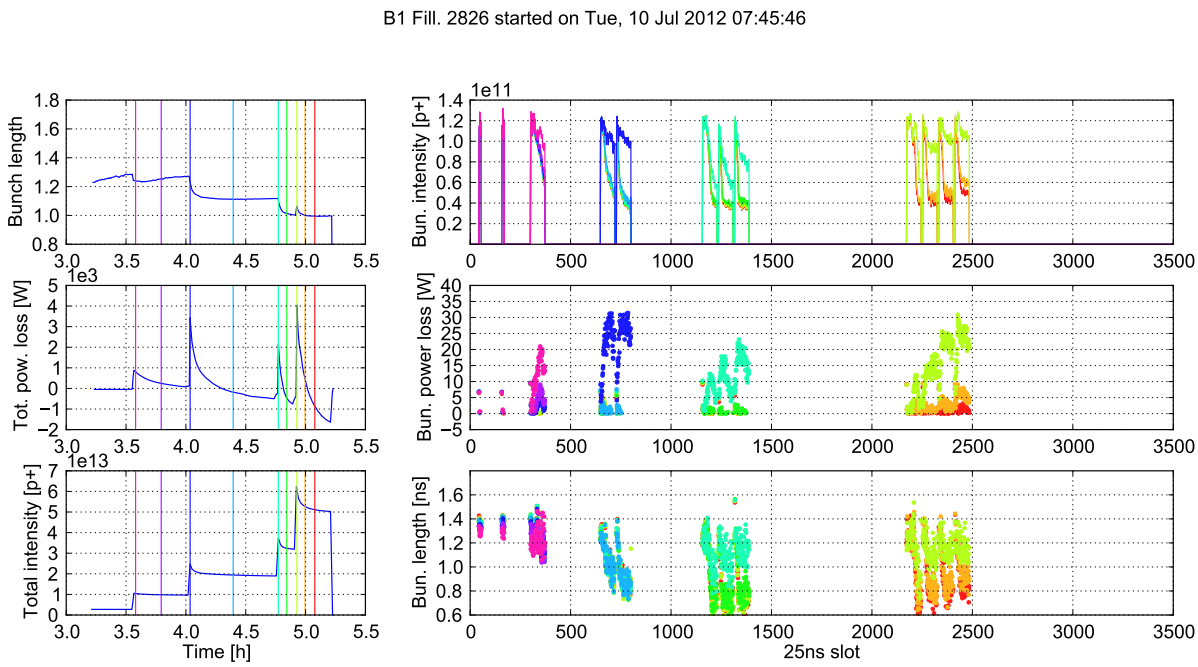

Figure 5.20: Measurements on beam 1 during the injection tests with 25 ns of 10 July 2012. Left, from top to bottom: average bunch length; total power loss from stable phase shift measurement; beam energy. Right, from top to bottom: bunch intensities; bunch by bunch power loss from stable phase measurements; bunch lengths. The different traces correspond to different times indicated by vertical bars in the left plots.

which could be controlled by the transverse damper), the injection of 144 bunches triggered the beam dump within 700 turns due to a fast EC induced instability.

5.3.2 *The scrubbing run with 25 ns beams: goals and strategy*

The scrubbing run with 25 ns beams at injection energy, which took place in the period 6-10 December, aimed to reach the following goals:

(a) Further reduce the SEY over the whole machine by storage of 25 ns beams at 450 GeV, while monitoring EC observables and beam quality evolution;

(b) Collect additional information on the evolution of the SEY as a function of the accumulated electron dose (especially in the low SEY region) and compare machine data with existing models. This is an essential step to validate and improve models, and establish strategies for the post-LS1 era;

(c) Enable LHC to be eventually ramped to 4 TeV with a few hundreds of bunches of 25 ns beams for EC studies and for other studies with 25 ns beams (e.g. beam-beam, UFO) without significant EC perturbations;

(d) Learn about other possible differences in 25 ns vs. 50 ns operation (e.g., equipment heating, beam longitudinal and transverse stability, UFO rates);

(e) Enable a pilot physics run with 25 ns beams at 4 TeV.

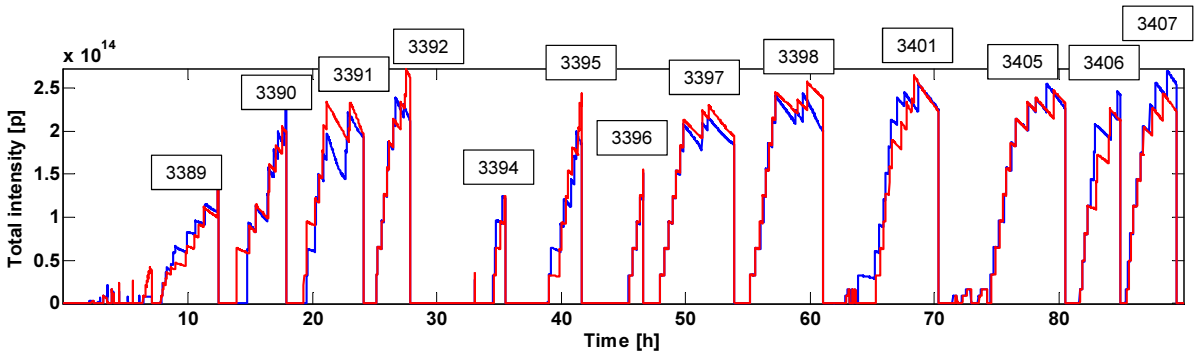

Figure 5.21: Total beam intensity in the two rings of the LHC (blue for beam 1 and red for beam 2) during the 2012 scrubbing run. For all the scrubbing fills the LHC fill number is also reported.

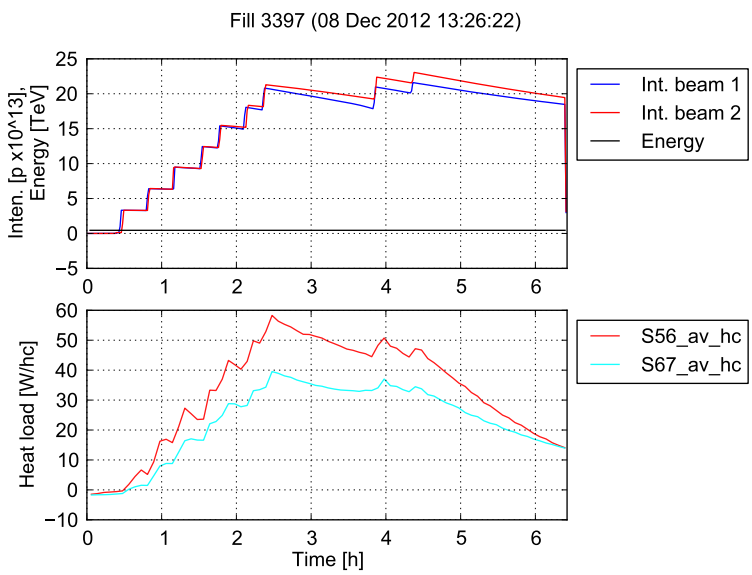

Figure 5.22: Total beam intensity and heat load in two of the LHC arcs during a typical scrubbing fill.

The operation during the scrubbing run was rather smooth and no fundamental showstoppers were found. Thanks to the excellent machine availability, a significant scrubbing flux could be maintained all along the scrubbing period. During the initial stages, the overall efficiency was determined by the vacuum pressure in the MKI region. Later on, when higher intensities were injected into the LHC, cryogenics slowed down the injection process requiring 10 – 15′ between successive injections from the SPS. This was mainly due to the limited cooling power for some of the stand-alone modules, while no limitation in the arcs appeared at this time (for some more details on issues not directly related to EC and detected on the different machine elements see [73]).

After the first half day of operation mainly devoted to finalize the set up of injection and of the transverse damper, there was only one fill with trains of 72 bunches, during which the quality of the beams could be seen to improve significantly from injection to injection (see Sec. 5.3.3). From the second fill onwards, it was decided to switch to trains of 288 bunches per injection, since PyECLOUD simulations showed that this was desirable in order to keep an

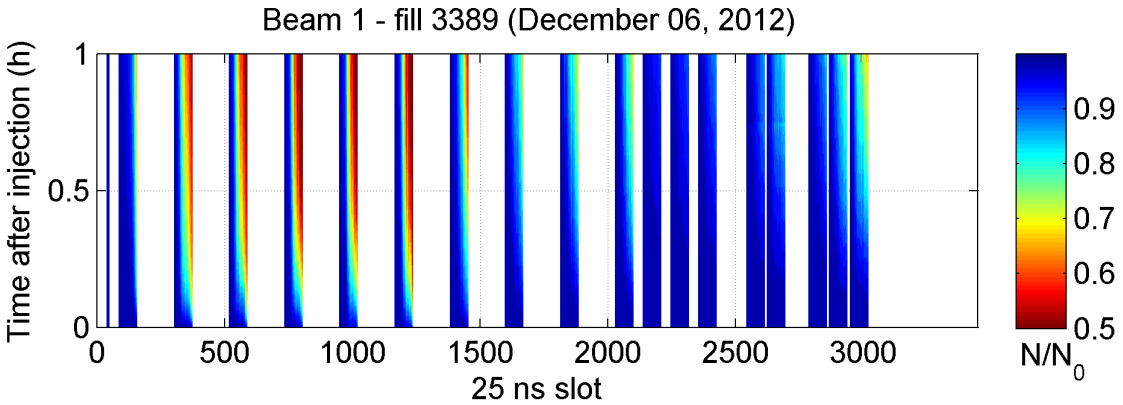

Figure 5.23: Evolution of the bunch by bunch intensity (normalized to the injected values) in the first hour after injection for the first scrubbing fill performed on 6 December 2012.

efficient scrubbing in the arc dipole magnets when entering a "low SEY" regime [73], as was confirmed by a later test conducted on 15 December (see Sec. 5.3.7). Within the first 24 hours of scrubbing, the number of injected bunches reached the maximum in both rings (2748) and a record intensity of 2.7×10^{11} ppb was stored for Beam 2. Several stores with full machine took then place over the scrubbing period, as visible in Fig. 5.21.

The heat load measured on the beam screens of the cryogenic arcs was monitored in order to decide when it was more efficient to dump the beams and refill the machine. Figure 5.22 shows the heat load measured in two of the LHC arcs during a typical scrubbing fill. We can notice that at the end of the fill, despite the drop of the total beam intensity was not dramatic, the heat load, and therefore the scrubbing dose, had decayed by a factor of 5 compared to the peak value reached during the same fill. This was mainly due to the beam degradation. It was therefore more efficient to interrupt the scrubbing store by dumping the beams and refill the LHC with new beams from the SPS.

5.3.3 *The scrubbing run with 25 ns beams: beam observations*

At the beginning of the first scrubbing fill the machine was found to be again in a worse conditioning state with respect to the last MD with 25 ns beams in 2011. High chromaticity settings ($Q'_{x,y} \simeq 10$) had to be used and large gaps had to be left between the injected trains of 72 bunches in order to control EC induced instabilities. On the other hand a rapid improvement could be observed throughout the fill itself since the chromaticity could be decreased in steps ($Q'_{x,y} \simeq 10$ for the first three injections of 72 bunches, $Q'_{x,y} \simeq 8$ for the following three and $Q'_{x,y} \simeq 6$ for the rest), the beam lifetime was evidently improving (see Fig. 5.23) and the gaps between the injected trains could be reduced. From Fig. 5.24 (top) we can see that the reduction of the EC activity is visible also on the bunch by bunch energy loss, which peaked to 30 W/bunch right after the 7th to the 10th injection (measurements right after injection are not available for trains injected earlier in the machine), while it reaches only about 20 W/bunch for later injections.

During the following scrubbing fills, all performed with 288 bunches per injection from the SPS and with $Q'_{x,y} \simeq 6$, the conditioning process seemed to be much slower. In Fig. 5.25 we compute for each scrubbing fill the average losses over the first 30 minutes, of the last 72

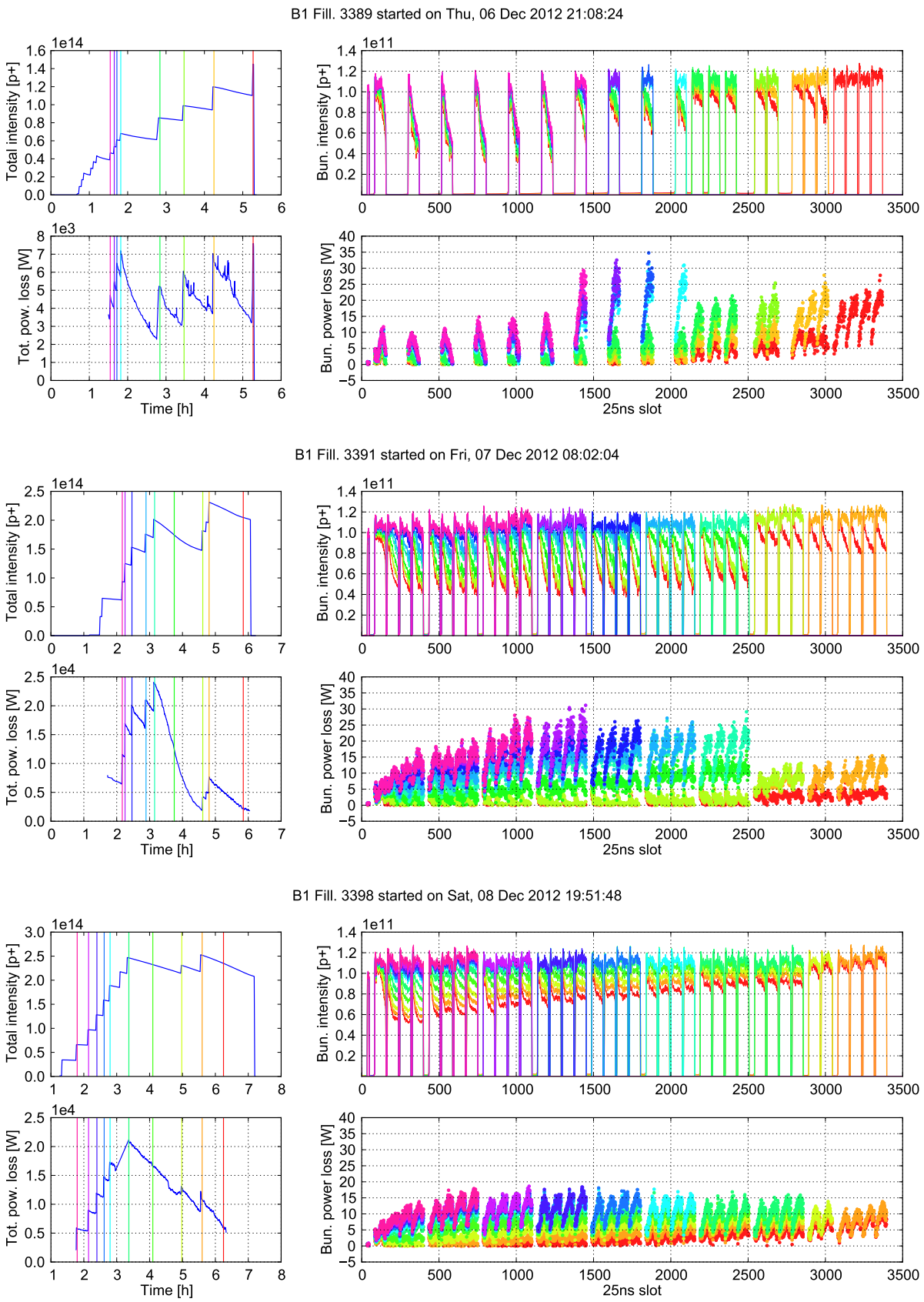

Figure 5.24: Intensity and energy loss measurements during three different fills of the 2012 scrubbing run. The different traces in the right plots correspond to different times indicated by vertical bars in the left plots.

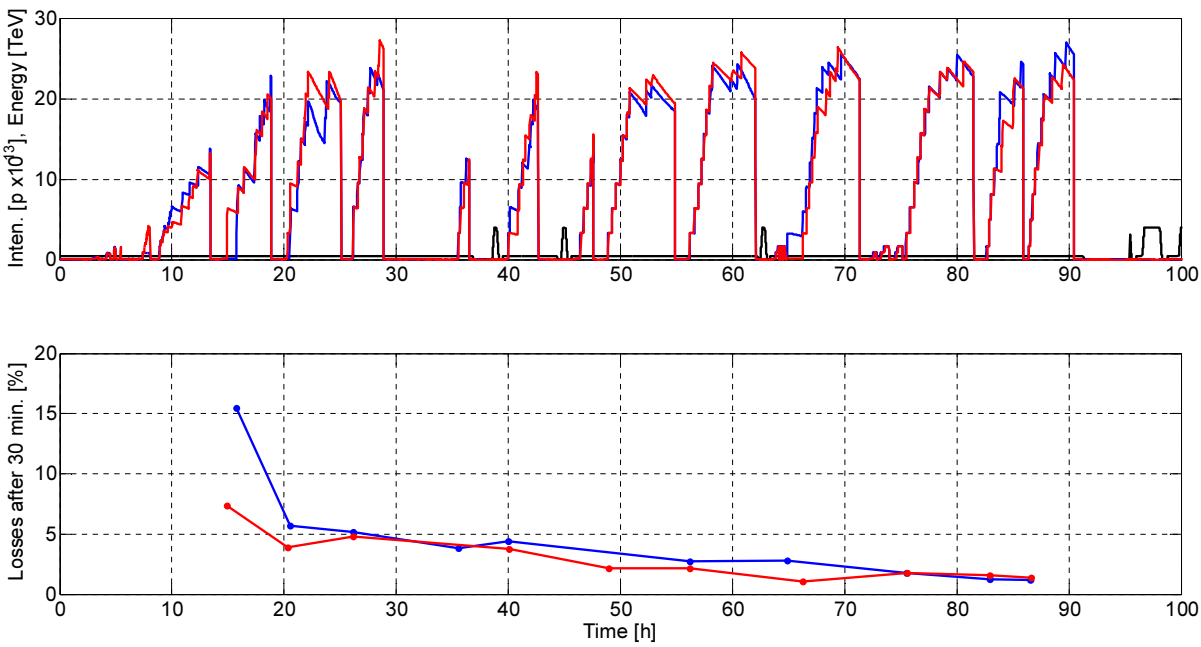

Figure 5.25: Top: total beam intensity evolution during the 2012 scrubbing run. Bottom: average losses over the first 30 minutes for the last 72 bunches of the first three injected trains.

bunches (most sensitive to EC) of the first three injected trains (since these injections were always performed in very similar conditions). It is evident that after a first stage when a fast improvement was observed, a second phase followed, in which much larger electron doses were required to observe an effect on the beam quality.

Figure 5.26 shows the bunch by bunch intensity evolution in the first hour after injection for four different fills throughout the scrubbing run. As it was occurring in the later stage of the 2011 scrubbing tests (see Sec. 5.2.4), the losses did not occur right at injection but several minutes later and are likely to be driven by a slow transverse emittance blowup induced by the EC. From fill to fill we could observe how the losses were becoming less severe and appeared later and later along the fill. This means that the emittance blowup was getting less strong, which is an indication that the electron density acting on the beam was getting lower.

The reduction of the EC activity is visible also on the bunch-by-bunch energy loss as shown in Fig. 5.24. Here we can observe that the peak energy loss decreased by a factor two by the end of the second day of scrubbing.

Nevertheless, EC effects could not be fully suppressed by the end of the 3.5 days scrubbing run and beam energy loss, slow particle losses and emittance blow-up driven by EC were still observable at the end of the scrubbing period.

Apart from the very first injections, the scrubbing run was not hampered by transverse instabilities. Actually during several scrubbing fills a strong emittance blowup was observed right after injection exclusively on the first injected bunch train, but this effect could be suppressed by increasing the strength of the octupole magnets. These observations and possible mechanisms which could explain them are reviewed in [35].

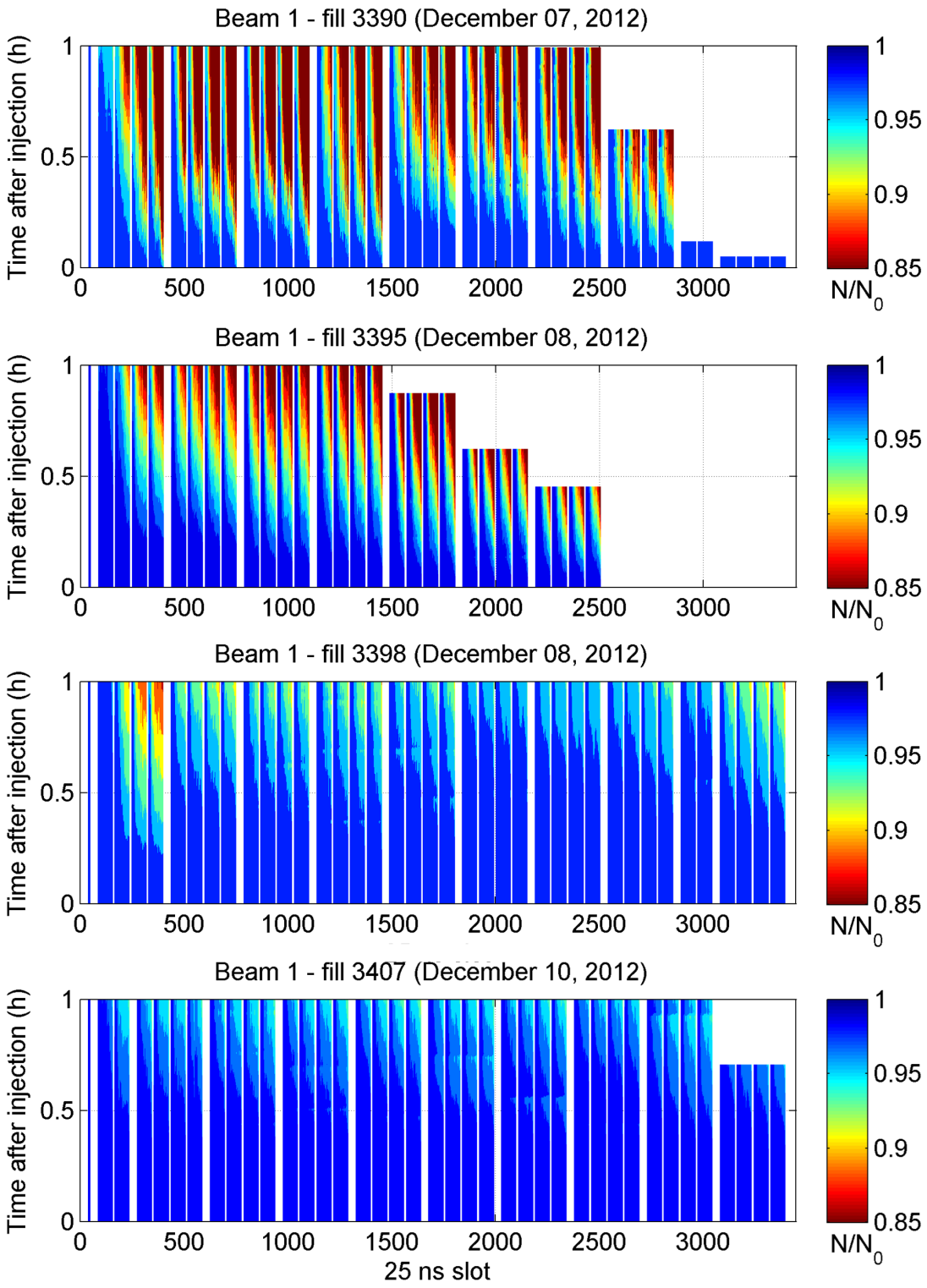

Figure 5.26: Evolution of the bunch by bunch intensity (normalized to the injected values) in the first hour after injection, for four scrubbing fills taken at different moments of the 2012 scrubbing run.

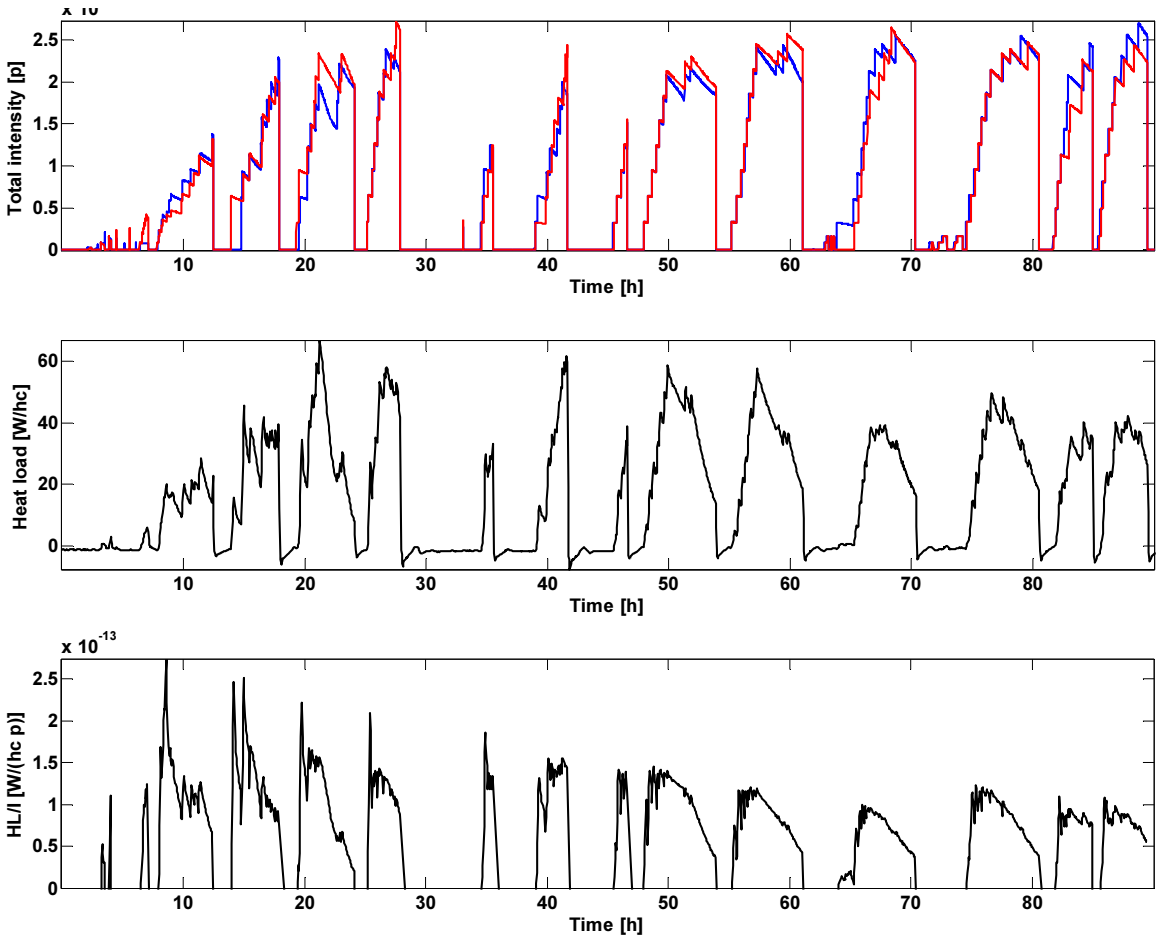

Figure 5.27: Beam intensity (top) for beam 1 (blue) and beam 2 (red), heat load measured in the cryogenic arc S56 (middle) and their ratio (bottom) during the 2012 scrubbing run with 25 ns beams.

5.3.4 *The scrubbing run with 25 ns beams: heat load evolution*

During the 2012 scrubbing run the heat load data have been monitored on line and recorded for the beam screens of all the cryogenic sections. Figure 5.27 shows the average heat load measured in one of the LHC arcs (S56) all along the scrubbing run (middle) and also the same normalized to the total beam intensity in the two rings (bottom). From the latter plot quite large values can be observed during the first fills, consistently with the strong EC effects which were observed at this stage on the beams (see Sec. 5.3.3). A clearly improving trend can be observed especially in the first half of the scrubbing run, while it is difficult to spot any further scrubbing over the last few fills. In Fig. 5.28 we compare the heat load measured during the last scrubbing fill with the estimated beam induced heating due to synchrotron radiation and to the impedance of the beam screen, confirming that a strong contribution due to EC was still observable at that stage. In synthesis, the heat load measurements in the arcs confirm the picture obtained from beam quality observations.

Applying the method presented in Sec. 5.2.1 to the data collected during the first scrubbing fill an SEY value of about 1.55 can be inferred, consistently with what was estimated at the end of the injection tests in July (see Sec. 5.3.1). This shows that we were approaching the

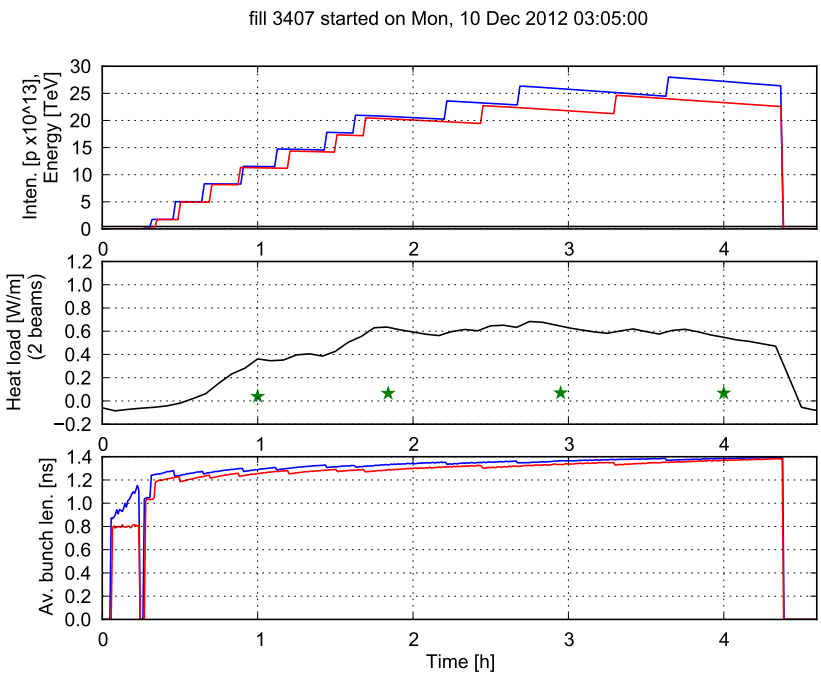

Figure 5.28: Top: total intensity for beam 1 (blue) and beam 2 (red) during the last fill of the 2012 scrubbing run; middle: measured heat load in the cryogenic arcs (black), and the corresponding estimation from beam screen impedance and synchrotron radiation (green stars); bottom: average bunch length for the two beams.

region of SEY values in which the quadrupoles, due to the significantly lower multipacting threshold with respect to the dipoles, also give a significant contribution to the heat load measured in each half cell (see Sec. 4.3).

Unfortunately the beam screen cooling circuit extends over a full half cell, hence a magnet by magnet measurement of the heat load was not available. In order to disentangle the contributions from dipoles and quadrupoles we decided to use the information coming from the heat load measurements in the SAMs in the straight sections, which are magnets equipped with a dedicated cryostat for which heat load detection is available. In particular we considered the matching quadrupoles Q5 on both sides of the IRs 1 and 5 (see also Sec. 6.1) and the separation dipoles D3 of the IR 4. The measured heat load for these magnets, normalized to the respective length, are shown in Fig. 5.29, for one of the first and one of the last fills of the scrubbing run. As expected from simulations, the quadrupoles show a much larger specific heat load compared to the dipoles.

In Fig. 5.30 we rescale the values of Fig. 5.29 to the lengths of the magnets in a regular LHC arc half-cell (green and purple curves) in order to estimate the respective contributions to the total heat load. The total heat load estimated by this procedure is shown by the continuous black curve and is quite consistent with the average value measured in the LHC arcs (dashed black line).

An important feature to be noticed is that the heat load in the dipoles looks much more sensitive to beam degradation. In particular for the last fill of the scrubbing (Fig. 5.30 left) we see that the dipole contribution is larger than the one from the quadrupoles at the beginning of the fill, when the beam parameters are close to nominal, while the two become roughly

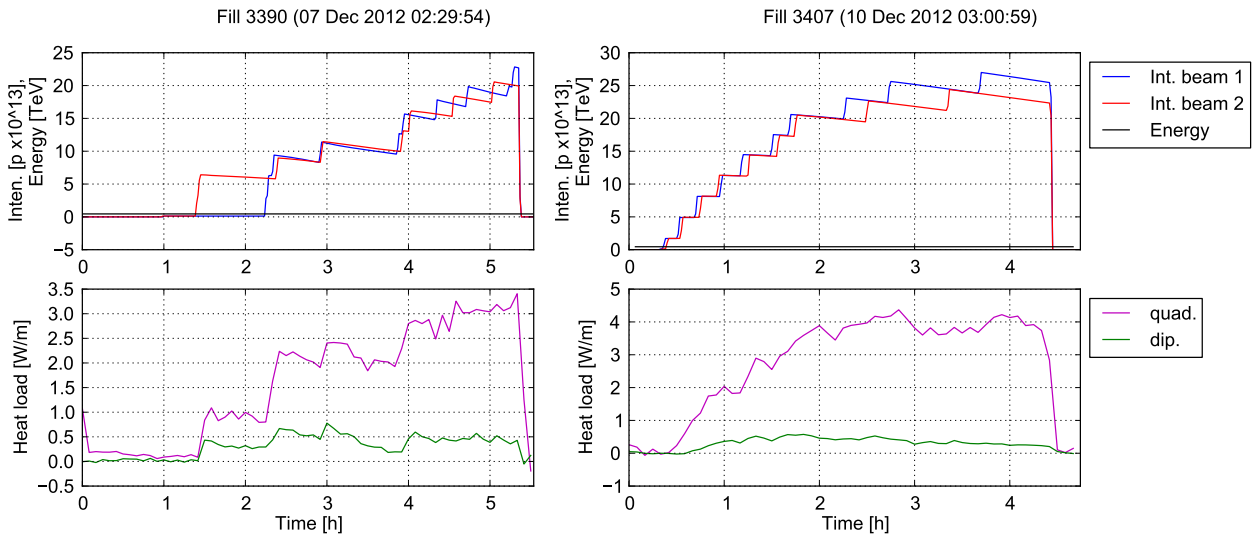

Figure 5.29: Heat load measured in the matching quadrupoles Q5 on both sides of the IRs 1 and 5 (purple, average among the four magnets) and in the separation dipoles D3 of the IR 4 (green, average between the two magnets).

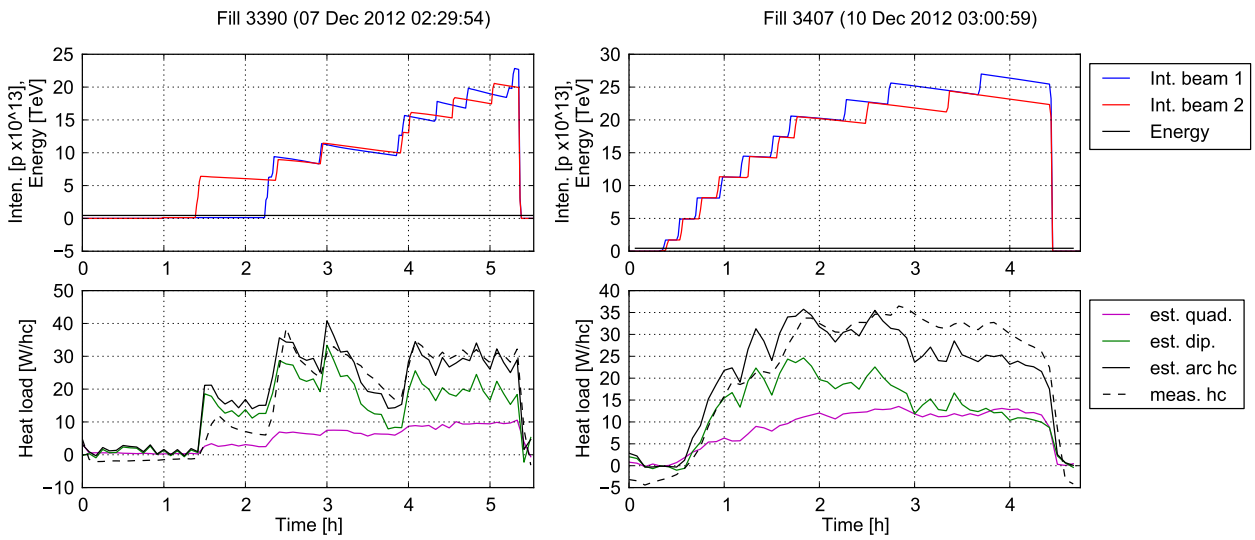

Figure 5.30: Curves in Fig. 5.29 rescaled to the lengths of the magnets in a regular LHC arc half-cell (purple and green), their sum (black continuous) and measured heat loads in the LHC arcs (black dashed).

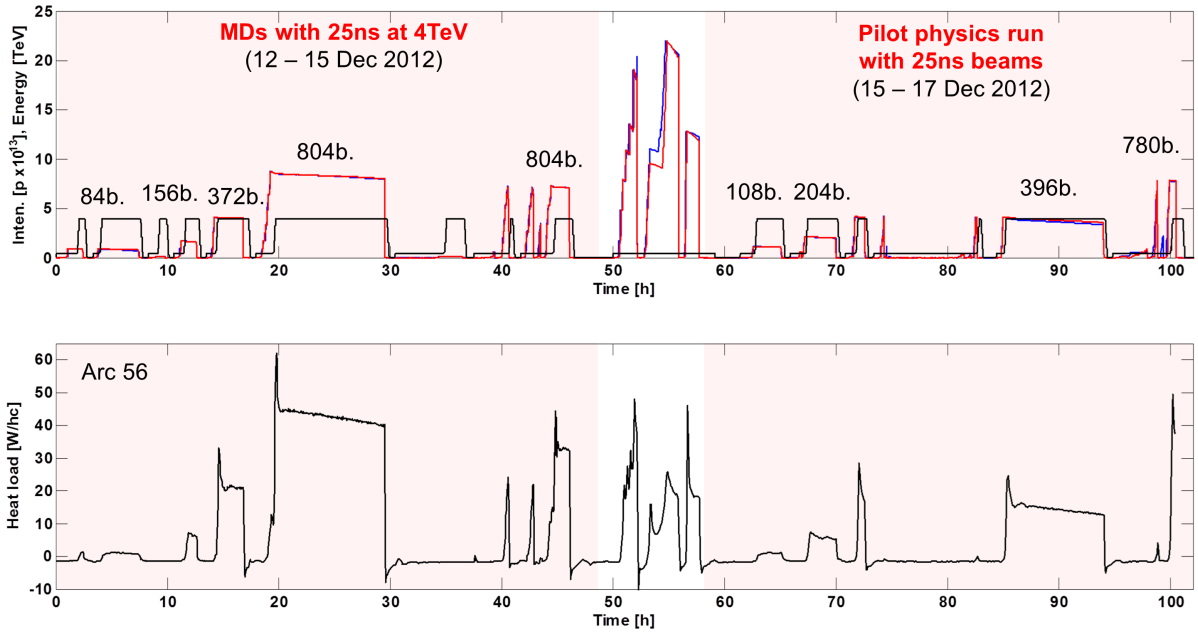

Figure 5.31: Experiments with 25 ns beams at 4 TeV. Top: total beam intensities (in blue for beam 1 and in red for beam 2 , the number of bunches is indicated by the labels) and energy. Bottom: heat load measured in the arc S56.

equal at the end of the fill, when transverse blowup and particles losses had already occurred on many bunches of the beam. This is because the SEY in the dipoles is very close to the multipacting threshold and therefore small changes in the beam parameters can have a strong impact on the EC buildup.

This regime is not very suitable for an efficient scrubbing because most of the beam in the ring is not efficiently contributing to the scrubbing of the dipoles (60% of the ring) but is still producing heat load in the quadrupoles, especially in the SAM ones, which were limiting the injection speed due to the limited cooling power. A better option at this point would be to employ a different beam configuration, for example the one presented in Sec. 4.8, which has a lower multipacting threshold and allows having an electron dose more uniformly distributed along the ring. In any case, online monitoring of heat loads and bunch-by-bunch stable phase measurements are desirable to steer the scrubbing process and dump the beams as soon as they become insufficient at producing electron dose.

5.3.5 *Heat load and beam energy loss during the energy ramp*

Despite not being sufficient to fully suppress the EC at injection energy, the conditioning accumulated during the 2012 scrubbing run was sufficient to allow ramping for the first time beams with 25 ns beams, in trains of 48, 72, or 96 bunches, up to 4 TeV. Several fills at 4 TeV (see Fig. 5.31) were performed for MD purposes in the period 12-15 December 2012 and for a pilot physics run in the period 15-17 December, when the four LHC experiments could collect data from p-p collisions with 25 ns bunch spacing.

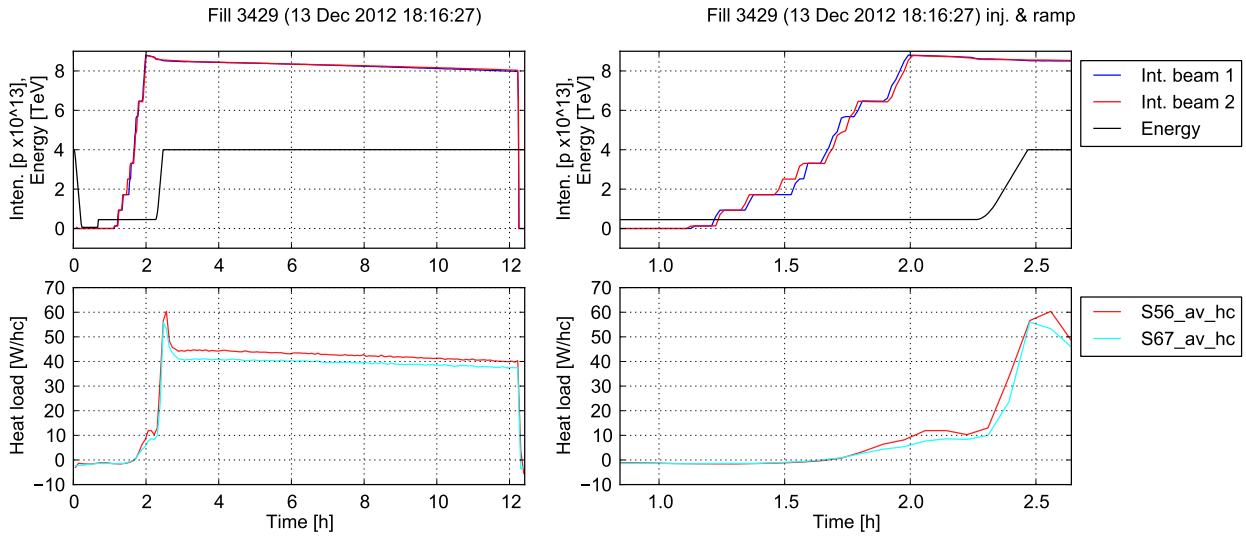

Figure 5.32: Heat load measured in the arcs S56 and S67 during the MD fill 3429. Entire fill time (left) and detail of the injection and energy ramp (right).

While the MDs were conducted with the standard 25 ns production scheme from the injectors (bunch intensity of about 1.2×10^{11} ppb, transverse emittances of about 2.5 μm, in batches of 72 bunches), for the pilot physics run, in order to provide the experiments with the highest possible luminosity with 25 ns beams, it was decided to use low emittance beams from the injectors, produced with the Batch Compression Merging and Splittings (BCMS) production scheme [85] (bunch intensity of about 1.0×10^{11} ppb, transverse emittances of about 1.4 μm, in batches of 48 bunches, up to two batches per train from the SPS).

For reasons related to machine protection, both for the MDs and for the pilot physics run the number of bunches had to be gradually increased in subsequent fills reaching in both cases a maximum of about 800 bunches.

Figure 5.31 shows the overview on the total intensity and energy of the two beams together with the heat load measured in one of the LHC arcs during these tests.

Figure 5.32 shows the heat load measured in two of the LHC arcs during the MD fill 3429 in which the largest total intensity with 25 ns at 4 TeV was achieved (804 bunches with about 1.15×10^{11} ppb – the beams were not colliding). Most of the results presented in this section will refer to this fill, but practically all the other show very similar features. As in all the other tests with 25 ns beams, the heat load exceeds by a large factor the value expected just from the synchrotron radiation and the beam screen impedance contributions [86]. A strong enhancement of the heat load can be observed between injection energy (450 GeV) and top energy (4 TeV).

The rapid increase of the heat load during the ramp required to increase the flow of helium on the beam screens at the start of the ramp. This transient is not correctly accounted by the heat load measurement, causing an artificial peak in the heat load evolution plots. Partially due to this effect, and partially because of the slow time response of the cryogenic system to the fast heat load changes, we could not use these measurement to resolve the behavior of the EC induced heat load on the energy ramp. Instead, this could be achieved by observing the beam energy loss from the stable phase measurements, which is about equivalent to the arc

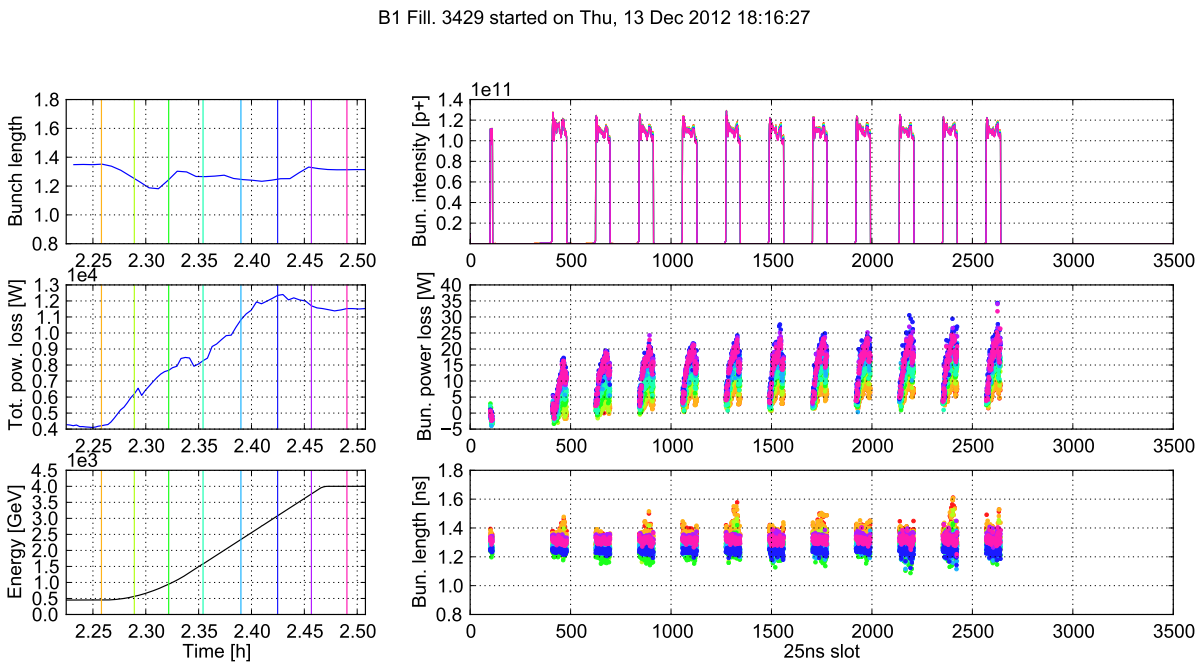

Figure 5.33: Measurements on beam 1 during the energy ramp of the MD fill 3429. Left, from top to bottom: average bunch length; total power loss from stable phase shift measurements; beam energy. Right, from top to bottom: bunch intensities; bunch by bunch power loss from stable phase measurements; bunch lengths. The different traces correspond to different times indicated by vertical bars in the left plots.

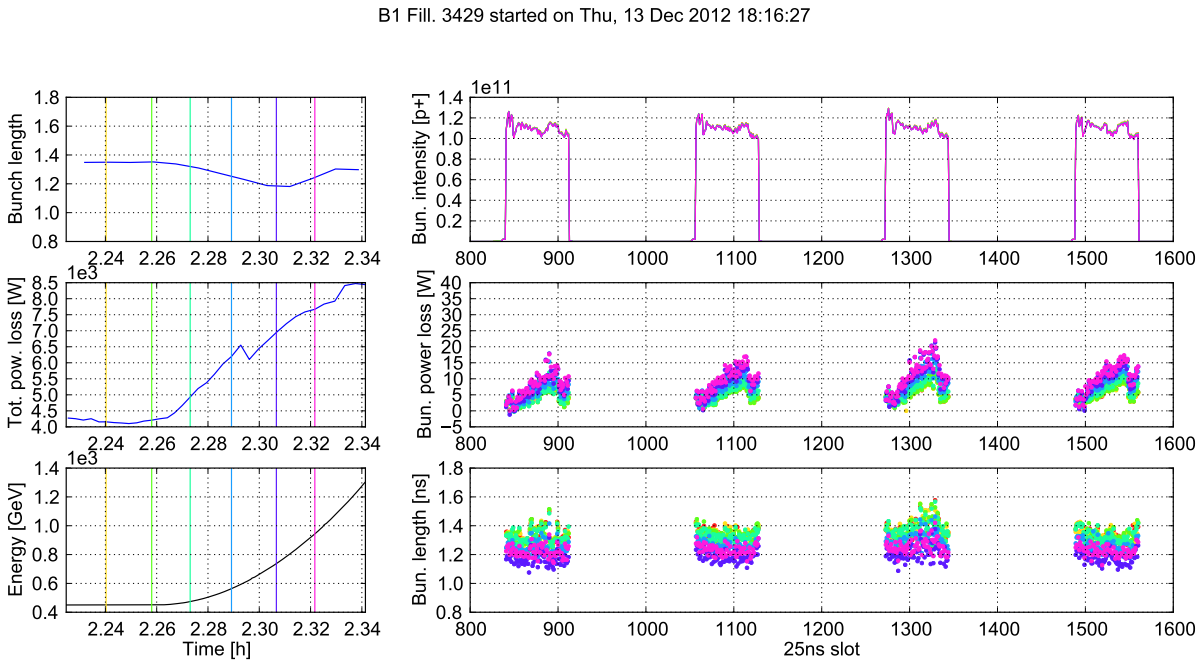

Figure 5.34: Same as in Fig. 5.33, zoom over the first part of the energy ramp, and on the central portion of the beam.

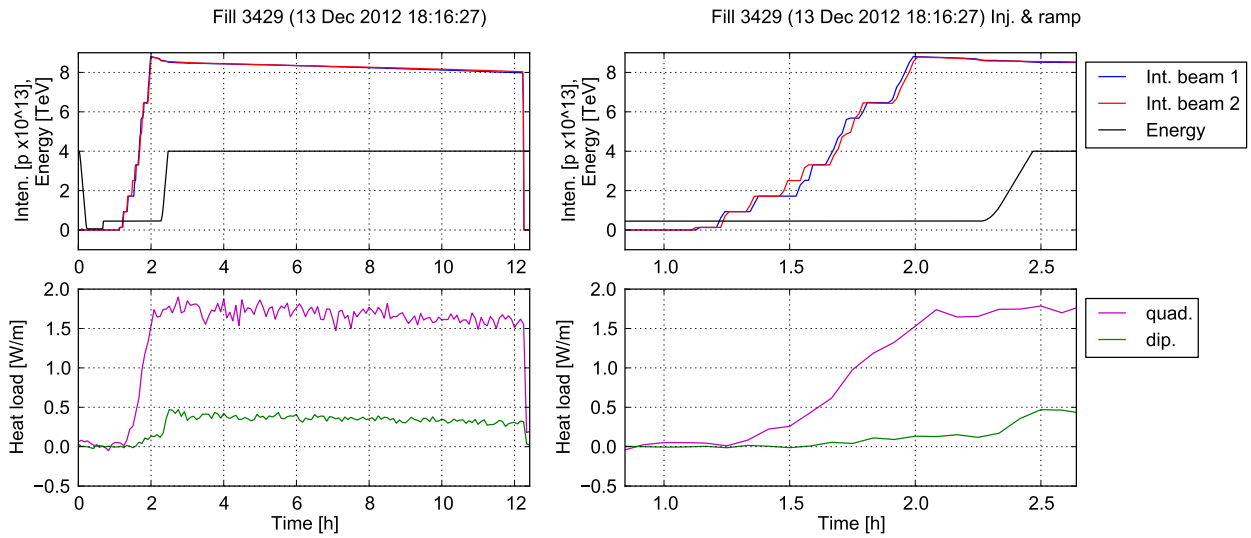

Figure 5.35: Heat load measured in the matching quadrupoles Q5 on both sides of the IRs 1 and 5 (purple, average among the four magnets) and in the separation dipoles D3 of the IR 4 (green, average between the two magnets).

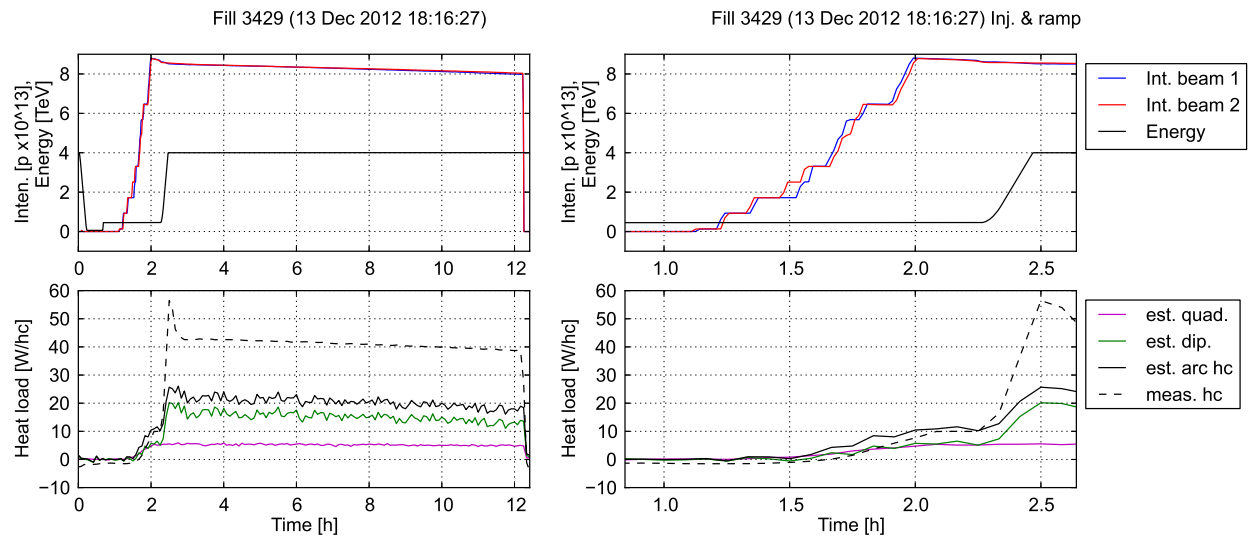

Figure 5.36: Curves in Fig. 5.35 rescaled to the lengths of the magnets in a regular LHC arc half-cell (purple and green), their sum (black continuous) and measured heat loads in the LHC arcs (black dashed).

heat load measurement (since this represents about 80% of the total beam energy loss [74]) but has a better time resolution and also allows disentangling the contributions from the two beams.

Figure 5.33 shows that the enhancement of the energy loss is much less pronounced on the first bunches of the circulating batches (as expected for EC effects) and happens practically uniformly along the ramp. Since an increase in energy loss is observed even in the very first part of the energy ramp (as shown in Fig. 5.34), the increase in primary electrons due to photoemission along the arc dipoles (see Sec. 1.1) cannot be the only mechanism driving the observed enhancement, since it should become non negligible only when the beam energy reaches about 2 TeV. Most likely the impact on the EC buildup other mechanisms like bunch length and transverse beam size reduction (see Secs. 4.5 and 4.6) is also non negligible, especially in the dipole magnets where the SEY at the moment of the experiment was very close to the multipacting threshold estimated for the injection energy. We cannot exclude that even more involved mechanisms like a dependence of the SEY on the magnetic field applied on the beam screen (never fully investigated with laboratory measurements) and synchrotron radiation from the edges of the magnets play a role in the observed behavior [76, 87].

Like for the scrubbing run, in order to gain some information on the EC builbup in the different magnets of the lattice, we analyzed the heat load in the SAMs. The observations on the matching quadrupoles Q5 on both sides of the IRs 1 and 5 and the on separation dipoles D3 at the IR 4 are presented for the fill 3429 in Fig. 5.35. As found for the stores at injection energy during the scrubbing run, the quadrupole magnets show a larger heat load compared to the dipoles all along the fill. Moreover the two families of magnets show completely different behaviors during the energy ramp, since while the heat load in the quadrupoles looks practically independent on the beam energy, an increase of about a factor four is observed on the heat load in the dipoles. As already stated before, this is not surprising since the SEY in the dipoles at the moment of the experiment was close to the multipacting threshold and therefore the EC buildup in these devices is more sensitive to the changes on beam parameters, primary electrons etc. which occur during the energy ramp. In Fig. 5.36 we rescale the values of Fig. 5.35 to the lengths of the magnets in a regular LHC arc half-cell (green and purple curves). The total heat load estimated by this procedure (continuous black curve) is quite consistent with the average value measured in the LHC arcs (dashed black line) at injection energy but the two curves differ by about a factor two at 4 TeV. This suggests that there is a difference between the EC buildup in the SAM dipoles and in the arc dipoles, which could be due to the fact that primary electrons production from synchrotron radiation is much stronger in the arcs than in the straight sections where the SAM dipoles are installed.

5.3.6 *EC observations during the high energy stores*

From Figs. 5.31, 5.32, 5.35, and 5.36 we can observe that, despite the strong EC activity, no important reduction of the heat load was observed in the arcs nor in the SAMs during the high energy stores with 25 ns beams, as confirmed also by energy loss measurements (see Fig. 5.37). Indeed, the relatively small drop which is observed is mostly explained with the slow beam losses occurring during the store and not by beam induced scrubbing.

Figure 5.38 shows the heat load measured at the beginning of each 4 TeV store as a function of the total intensity in the two rings. The blue line corresponds to the MD fills performed with the standard production scheme from the injectors while the purple line corresponds

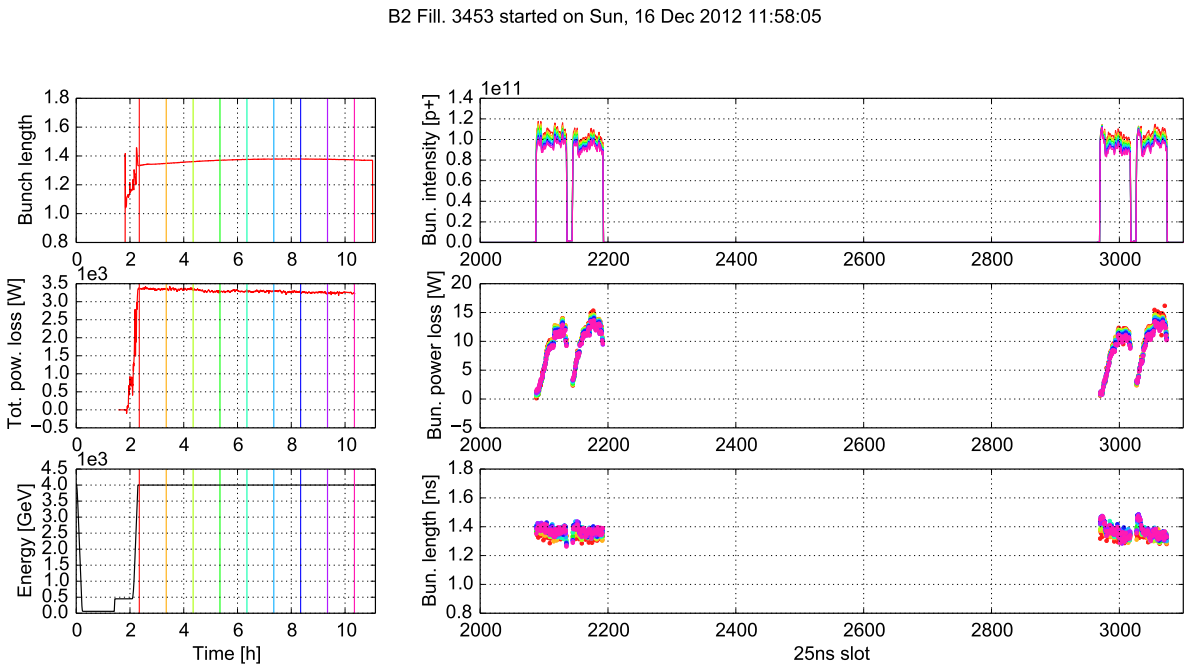

Figure 5.37: Measurements on beam 2 during the physics fill 3453. Left, from top to bottom: average bunch length; total power loss from stable phase shift measurements; total beam intensity. Right, from top to bottom: bunch intensities; bunch by bunch power loss from stable phase measurements; bunch lengths. The different traces correspond to different times indicated by vertical bars in the left plots.

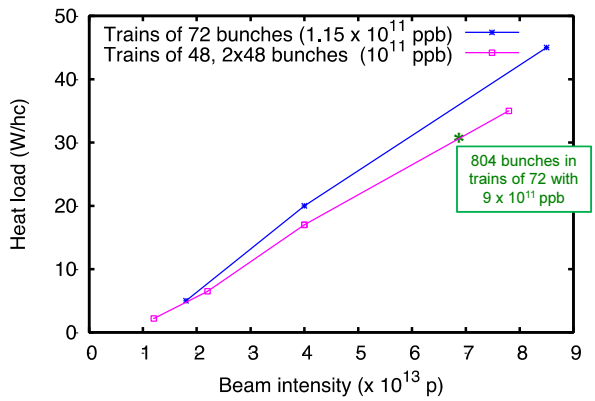

Figure 5.38: Heat load measured at the beginning of each 4 TeV store as a function of the total intensity in the two rings. The blue line corresponds to the MD fills performed with the standard production scheme from the injectors while the purple line corresponds the physics fills performed with the BCMS production scheme in the injectors. An MD fill performed with the standard beam but lower bunch population is also included.

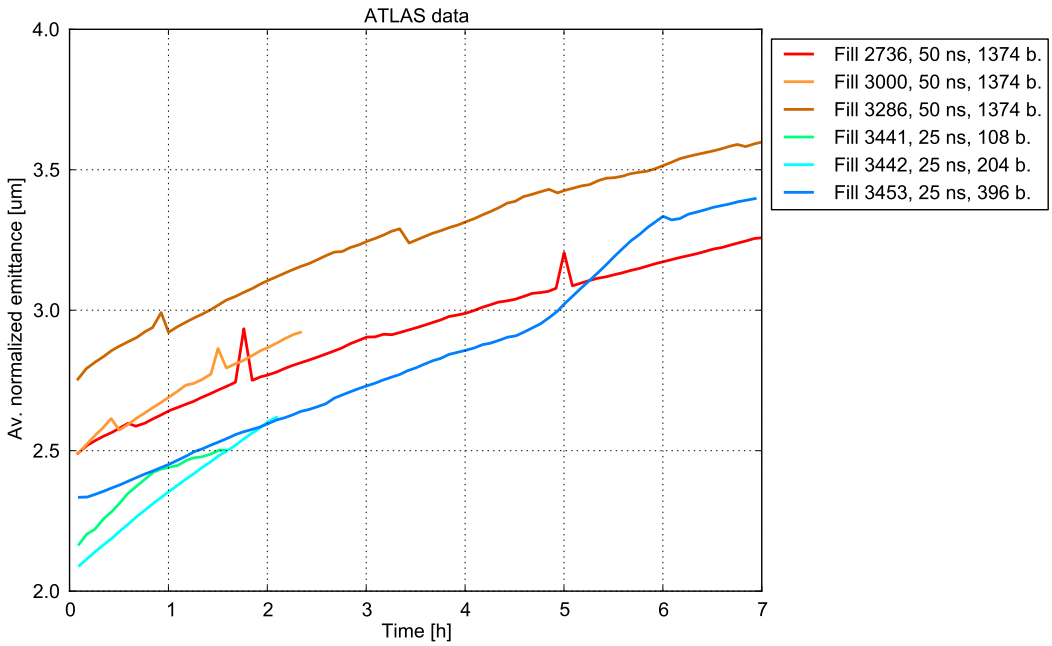

Figure 5.39: Average transverse emittance estimated from luminosity at the ATLAS experiment for three typical fills with 50 ns beams in 2012 and for the three successful fills of the 25 ns pilot physics run. (The change in trend towards the end of the fill 3453 is due to spurious excitation coming from the abort gap cleaning).

to the physics fills performed with the BCMS production scheme in the injectors. We can observe that for the fills performed with the same bunch intensity and the same number of bunches per batch, the heat load shows practically a linear dependence on the total intensity, i. e. on the number of bunches, which confirms that no important scrubbing is observed from one fill to the next one.

Despite the strong EC activity observed during the high energy stores, there were no signs of important beam degradation that could be ascribed to EC effects. This is not completely surprising, since the at higher energies the beam tends to become less sensitive to transverse kicks due to the larger longitudinal momentum (increased "beam rigidity").

Figure 5.39 shows the evolution of the average transverse emittance, estimated from the luminosity measured by the ATLAS experiment, during the three successful fills of the 25 ns pilot physics run and during three typical fills performed in 2012 with 50 ns beams. The transverse emittance blowup observed with 25 ns beams looks very similar to the one observed with 50 ns, for which, as we showed in Sec 5.1, no EC buildup was occurring in the LHC arcs. This suggests that also in the 25 ns cases the blowup during collision is driven by other mechanisms more than by EC. This is also confirmed by bunch by bunch emittance measurements. Figure 5.40 shows the emittances estimated from the luminosity at different moments of the physics fill performed with 204 bunches with 25 ns spacing. We can observe that, despite the strong EC activity observed from heat load and energy loss measurements, the emittances do not show any signature of degradation due to EC, since all bunches along the train, despite seeing very different EC densities, show practically the same emittance blowup.

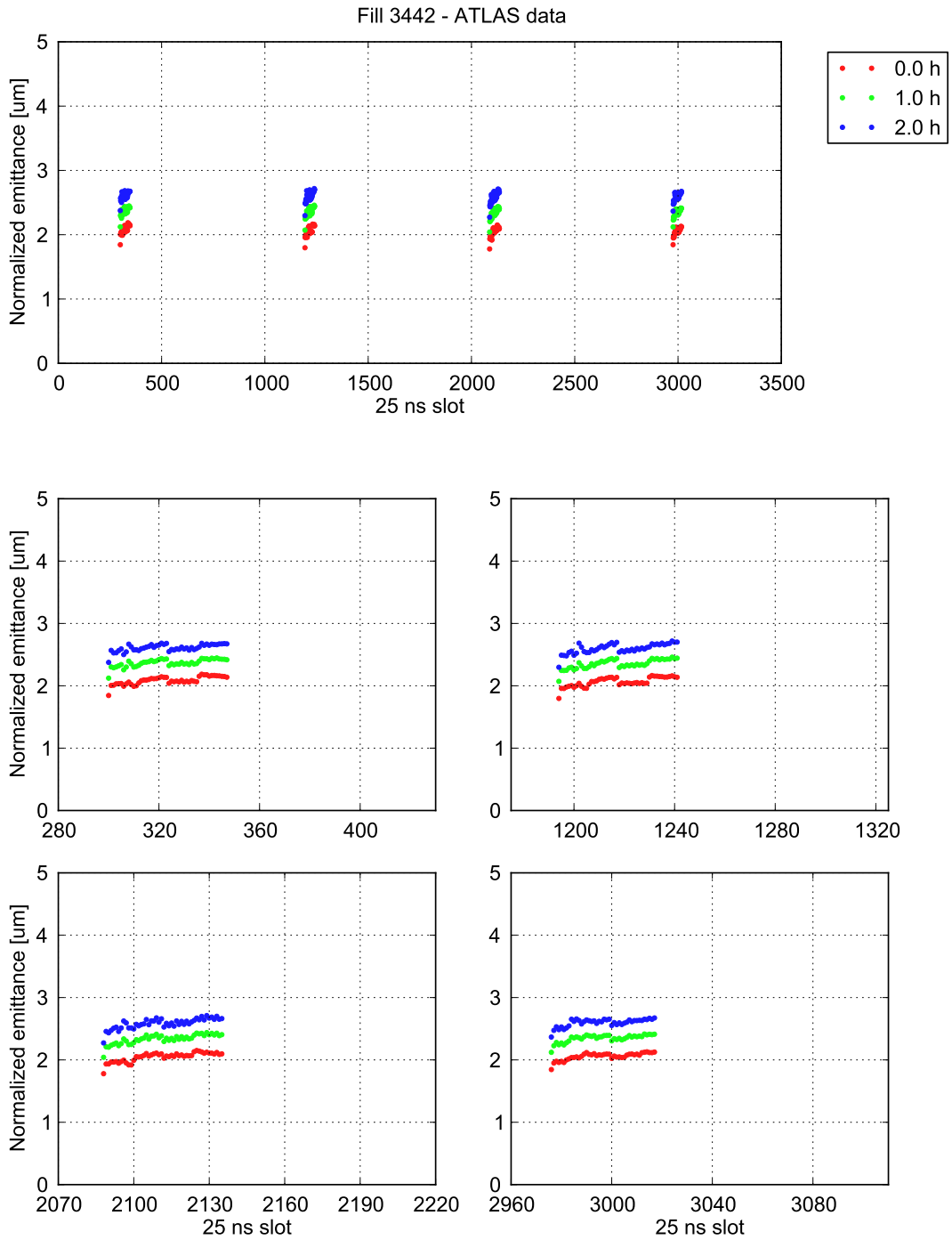

Figure 5.40: Bunch-by-bunch transverse emittances estimated from luminosity at the ATLAS experiment during the fill 3442 (the fill with 204 bunches in Fig. 5.31). Different traces correspond to different moments during the store, t = 0 is the moment when "stable beams" is declared.

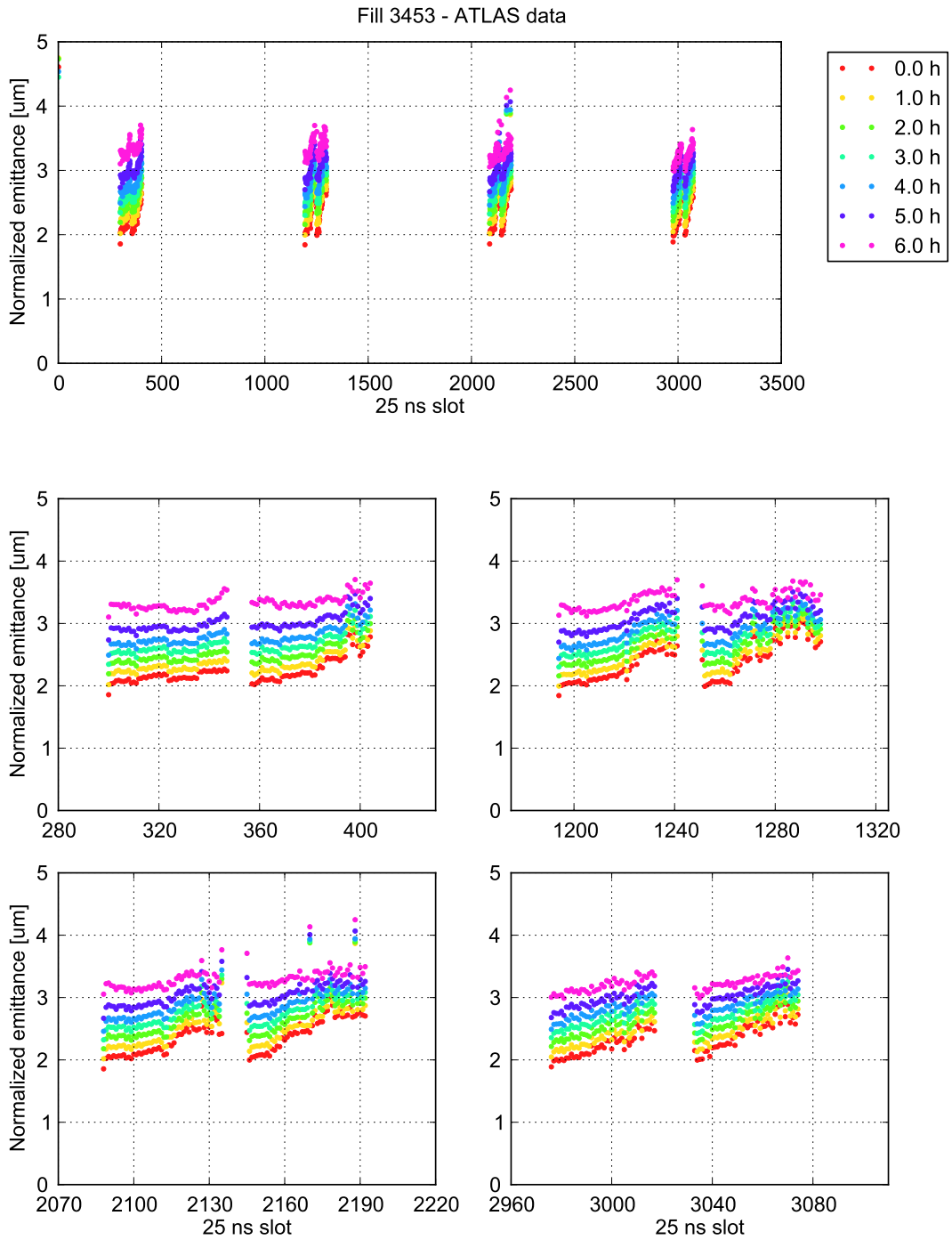

Figure 5.41: Bunch-by-bunch transverse emittances estimated from luminosity at the ATLAS experiment during the fill 3453 (the fill with 396 bunches in Fig. 5.31). Different traces correspond to different moments during the store, t = 0 is the moment when "stable beams" is declared.

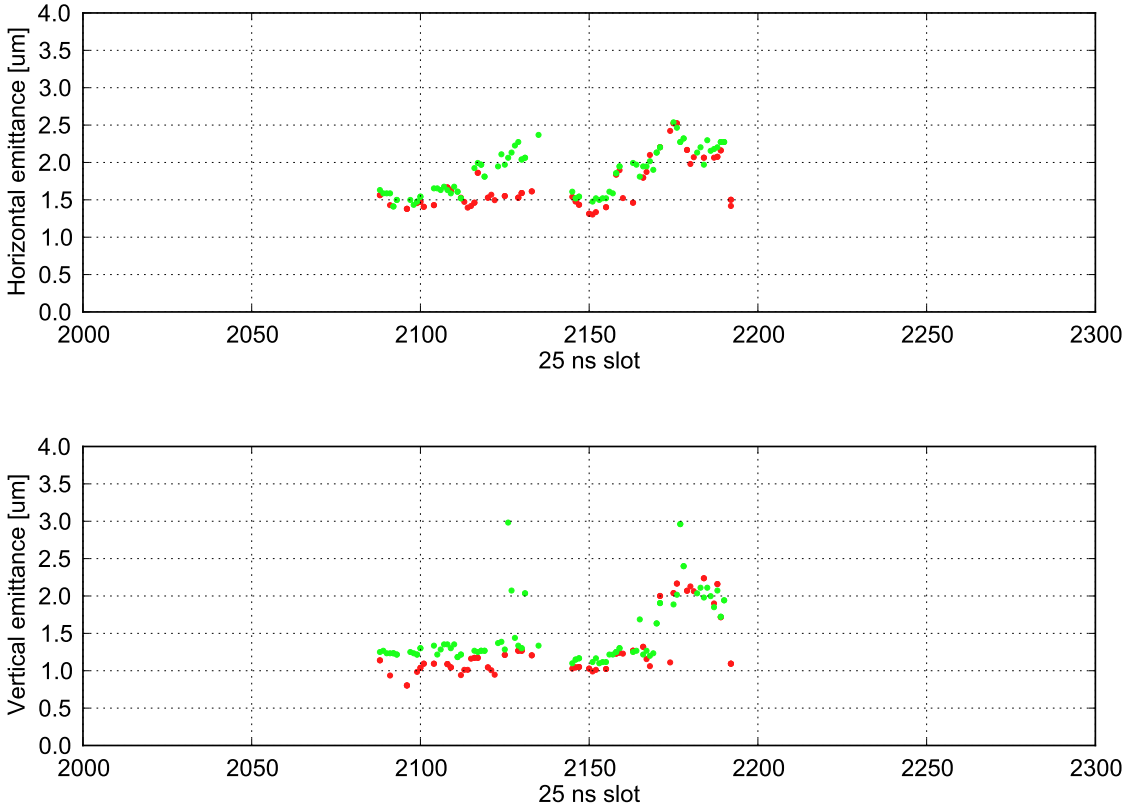

Figure 5.42: Bunch-by-bunch transverse measured by the BSRT before (red) and after (green) the energy ramp of the fill 3453 (the fill with 396 bunches in Fig. 5.31).

The case of the physics fill 3453 (the fill with 396 bunches in Fig. 5.31) performed with longer trains with 25 ns spacing is even more interesting. In this case, from Fig. 5.41 we can notice the typical EC signature on the transverse emittances along the train already on the first trace, which was taken right after the beams were brought in collision. Actually, using transverse emittance measurements from the BSRT, we could verify that the blowup had occurred mainly at injection energy (see Fig. 5.42). During the high energy stores (when beams were colliding in all the IPs) we notice a completely different behavior (see Fig. 5.41). The transverse blow up is stronger for the bunches at the head of the bunch trains, even if they experience a much weaker interaction with the EC, as confirmed by bunch by bunch energy loss measurements in Fig. 5.37. This again goes in the direction that the transverse blowup observed at high energy is driven by other mechanisms than EC.

5.3.7 *Test fills at injection energy after high energy stores*

Between the MD period with 25 ns beams at 4 TeV and the pilot physics run with 25 ns beams, three test fills at injection energy were performed in order to qualify the conditioning state of the machine after the high energy stores and investigate the dependence on the filling pattern of the EC buildup in the LHC arcs. In particular (see also Fig. 5.43):

- **Fill 3437** was performed with the same filling pattern employed during the scrubbing run, i. e. with 288 bunches per injection from the SPS;

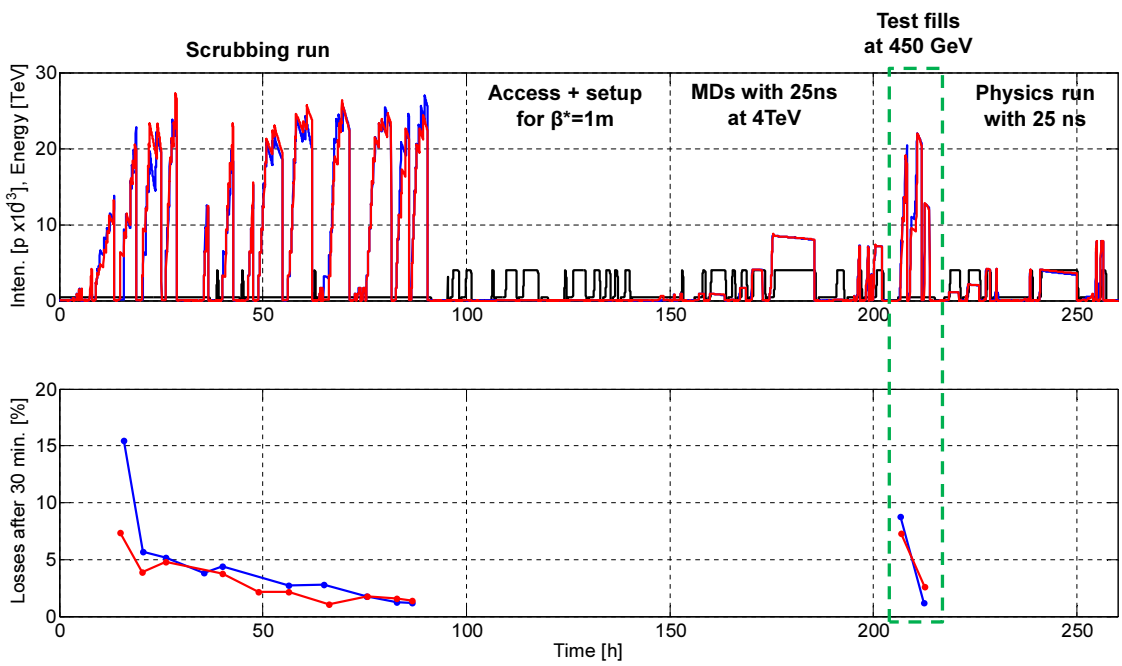

Figure 5.43: Top: total beam intensity evolution during the 25 ns run in 2012. Bottom: average losses over the first 30 minutes of the last 72 bunches of the first three injected trains (these injections were always performed in very similar conditions).

- **Fill 3438** was performed with the same filling pattern employed during 2011 scrubbing tests (72 bunches per injection from the SPS;
- **Fill 3439** was performed with the same filling pattern employed during the scrubbing run, i. e. with 288 bunches per injection from the SPS, but the injection process had to be stopped before the LHC rings were completely filled.

Quite surprisingly, despite the high doses accumulated during the previous high energy stores, the beam quality during the fill 3437 was found to be much worse compared to the end of the scrubbing run (all machine settings were very similar). From Fig. 5.43 we observe that the losses on the last 72 bunches of the first three injected trains (the same figure of merit used in Sec. 5.3.3) were found to be significantly increased. On the other hand a quick recovery was observed between the fill 3437 and the fill 3439 (see also bunch-by-bunch detail in Fig. 5.44) confirming, as already known from the SPS experience, that to recover a lost conditioning state requires a much smaller dose compared to what was needed to achieve the same performance for the first time (at least when the beam screen surface is not exposed to air).

The fill 3438 was dedicated to crosscheck the dependence of the EC buildup on the filling pattern, in particular by filling the ring with trains of 72 bunches spaced by 925 ns gaps. In Fig. 5.45 we compare heat load measurements performed during the fills 3438 and 3439 (which was performed with 288 bunches per injection). Using the same approach as in Sec.5.3.4 we rescale the heat load measures in the SAMs to the length of the magnets in the arc FODO lattice. In order to compare similar total beam intensity, we can consider the measurements at t =1.2 h in the left plot and at t =0.8 h in the right one. We observe that while the filling pattern has a quite modest impact on the heat load in the quadrupoles, it has a strong

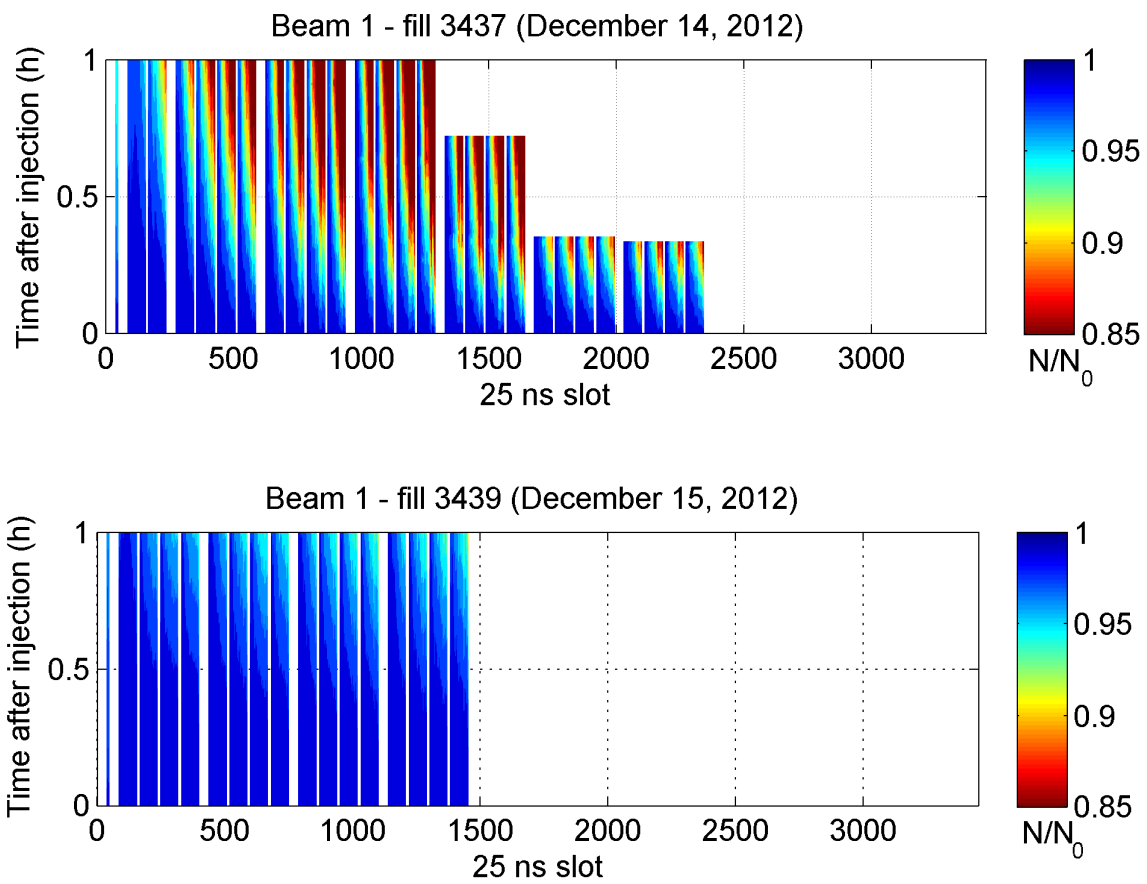

Figure 5.44: Evolution of the bunch by bunch intensity (normalized to the injected values) in the first hour after injection, for the two test fills performed wit 288 bunches per injection.

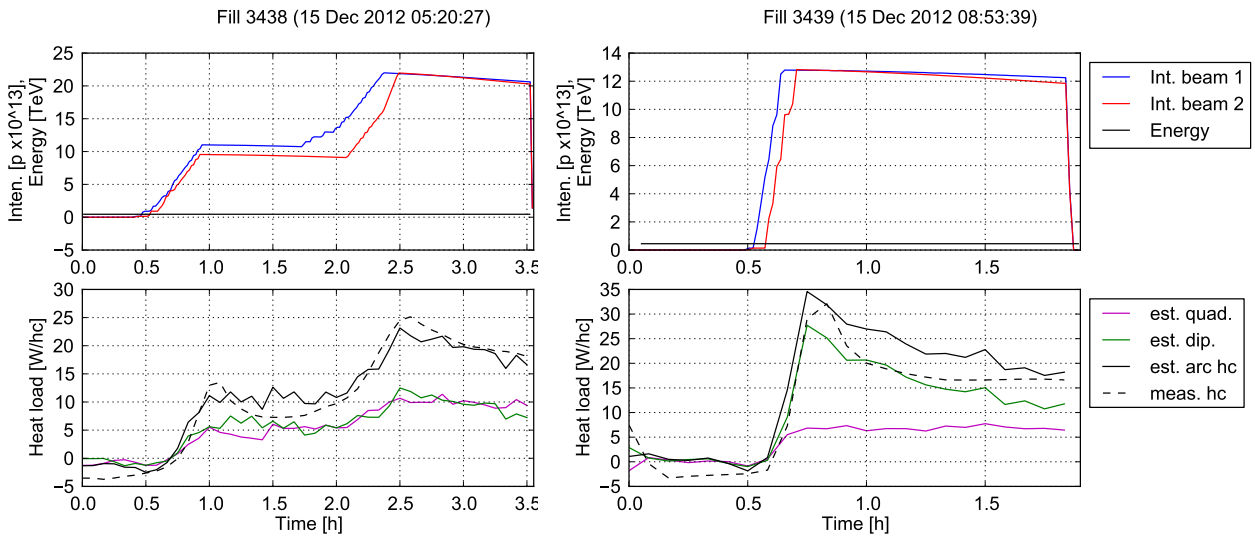

Figure 5.45: Heat load measured in the matching quadrupoles Q5 on both sides of the IRs 1 and 5 (purple, average among the four magnets) and in the separation dipoles D3 of the IR 4 (green, average between the two magnets), rescaled to the lengths of the magnets in a regular LHC arc half-cell (purple and green), their sum (black continuous) and measured heat loads in the LHC arcs (black dashed).

effect on the measurement in the dipoles. This is again a consequence of the fact that the SEY of the dipoles beam screen is close to the multipacting threshold (a similar behavior has been observed in simulations as seen in Sec.4.7 or in [73]).

6

ELECTRON CLOUD EFFECTS IN COMMON CHAMBERS

Several observations showed that EC effects in the LHC are particularly severe in the regions where the two beams circulate in the same chamber, i. e. around the four experiments. In fact common beam chambers not equipped with low SEY coatings or solenoids were the only regions where EC effects could be observed already in 2010 with beams with 150 ns spacing and could still be observed during the operation with 50 ns beams in 2012, despite the conditioning accumulated during physics operation and during the scrubbing tests with 25 ns beams.

After a brief introduction on the layout and optics in these regions, we will present some of the EC studies we conducted for LHC devices equipped with common chambers.

6.1 THE LHC INSERTION REGIONS

The LHC experiments are hosted in the Insertion Regions (IRs) 1, 2, 5 and 8 [52].

IR 1 and IR 5 house the high luminosity experiments (ATLAS and CMS respectively) and are identical in terms of hardware and optics (except for the crossing-angle scheme: the crossing angle in IR1 is in the vertical plane and in IR5 in the horizontal plane). These IRs are comprised of the following sections, given in order from the IP (see Fig. 6.1):

- A 31 m long superconducting **low-β triplet assembly** (Q1-Q2-Q3 in Fig. 6.1) operated at a temperature of 1.9 K and providing a nominal gradient of 205 T/m.
- A pair of **separation/recombination dipoles** separated by approximately 88 m. The D1 dipole located next to the triplet magnets has a common chamber and consists of six 3.4 m long conventional warm magnet modules yielding a nominal field of 1.38 T. The

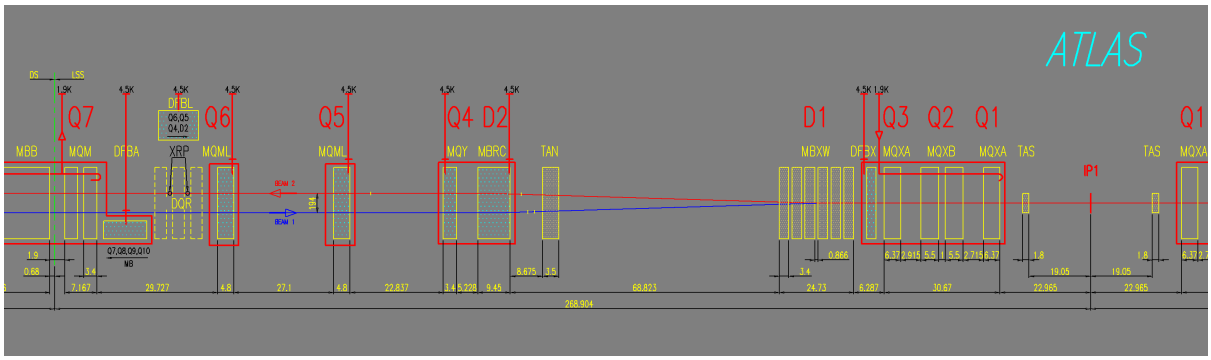

Figure 6.1: Layout of the Insertion Region 1 (IR1), right side.

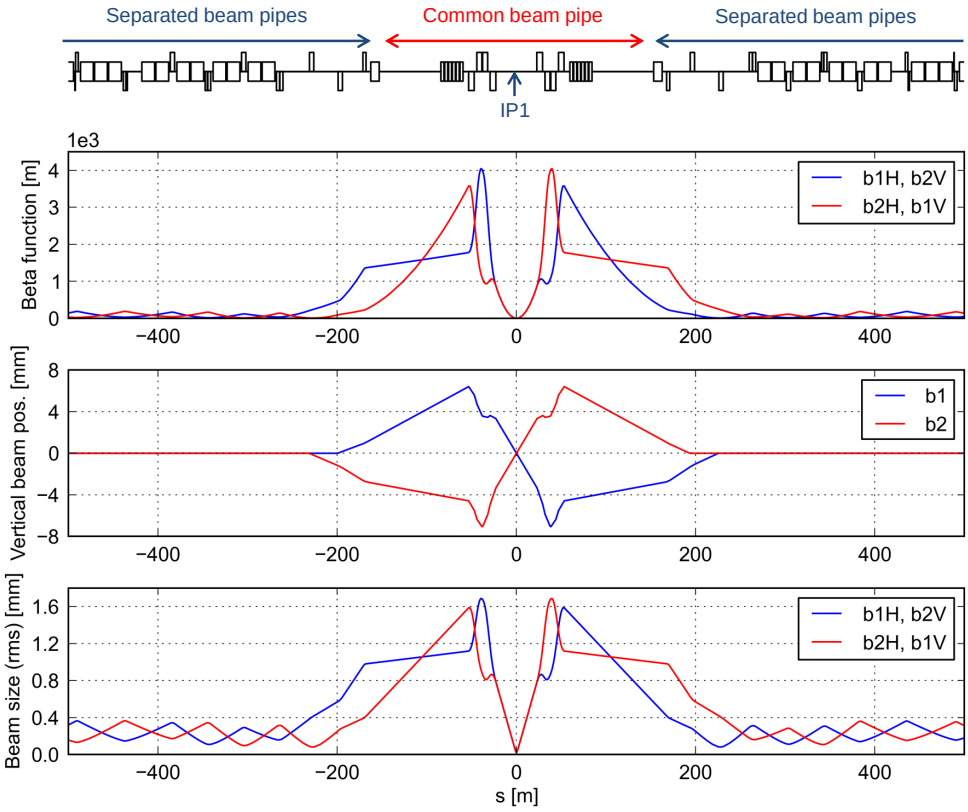

Figure 6.2: Beam optics at the Insertion Region 1 (IR1).

following D2 dipole is a 9.45 m long, double bore, superconducting dipole magnet operating at a cryogenic temperature of 4.5 K with a nominal field of 3.8 T.

- Four **matching quadrupole magnets**. The first quadrupole following the separation dipole magnets, Q4, is a wide-aperture magnet operating at a cryogenic temperature of 4.5 K and yielding a nominal gradient of 160 T/m. The remaining three quadrupole magnets are normal-aperture quadrupole magnets operating at a cryogenic temperature of 1.9 K with a nominal gradient of 200 T/m.

The small β-function values at the IP ($\beta^* = 0.55$ m in the design) are generated using the matching quadrupoles and the triplet quadrupole assemblies. Figure 6.2 shows the beta functions, the beam trajectories in the crossing plane and the beam sizes (for typical 2012 beam parameters). The two beams share the same vacuum chamber in a region including the experiments, the low-beta triplet magnets, the D1 dipole magnets, and part of the drift space between D1 and D2. The warm parts of this region are equipped with low SEY coating, while the cold magnets have stainless steel beam screens with colaminated copper and therefore are subject to EC effects.

The machine layout at IR2 and IR8 is quite similar to the case of IR1 and IR5, the main differences being the presence of a superconducting D1 magnet, and of the beam injection equipment (septum - MSIs, kicker - MKIs, stopper - TDI).

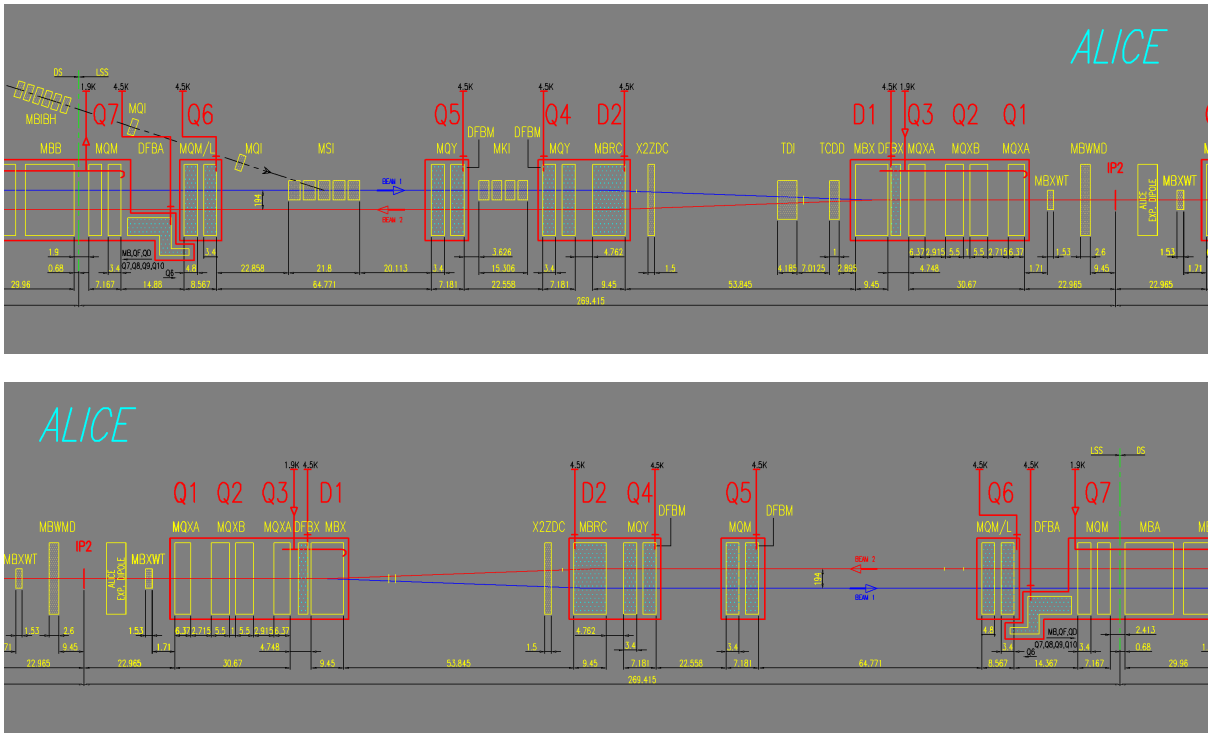

Figure 6.3: Layout of the Insertion Region 2 (IR2).

6.2 THE INNER TRIPLETS

The inner triples are the focusing elements closest to the experiment and are essential to obtain the small beta functions required at the IP. Each triplet is made of four superconducting quadrupole modules as shown in Fig. 6.4. In the following we will always refer to the triplet on the right side of IP1, but, due to symmetry considerations, the results will be valid also for the one of the left side as well as for the triplets in IR5 [88]. In IR2 and IR8, the cooling circuit of the inner triplet beam screen extends also to the D1 separation/recombination superconducting dipole (also equipped with a common chamber). For this reason the D1 dipole of the IR2 has been also included in our study.

In these magnets the two beams circulate in the same bore and, due to the crossing scheme they are displaced with respect to each other and with respect to the axis of the chamber. The position and transverse profiles of the two beams in the different modules is show in Fig. 6.5. Thanks to the smaller beam sizes and displacements the Q1 quadrupole can have a smaller beam screen.

Figure 6.4 (bottom) shows also the bunch pattern in the triplets at an instant in which two bunches are colliding at the IP (the bunch spacing is 25 ns, i. e. the distance between following bunches is about 7.5 m). There are only specific locations, which are called "long range encounter" positions, in which bunches of the two beams pass at the same time. At all the other positions there is a certain time delay between the bunch passages from two beams.

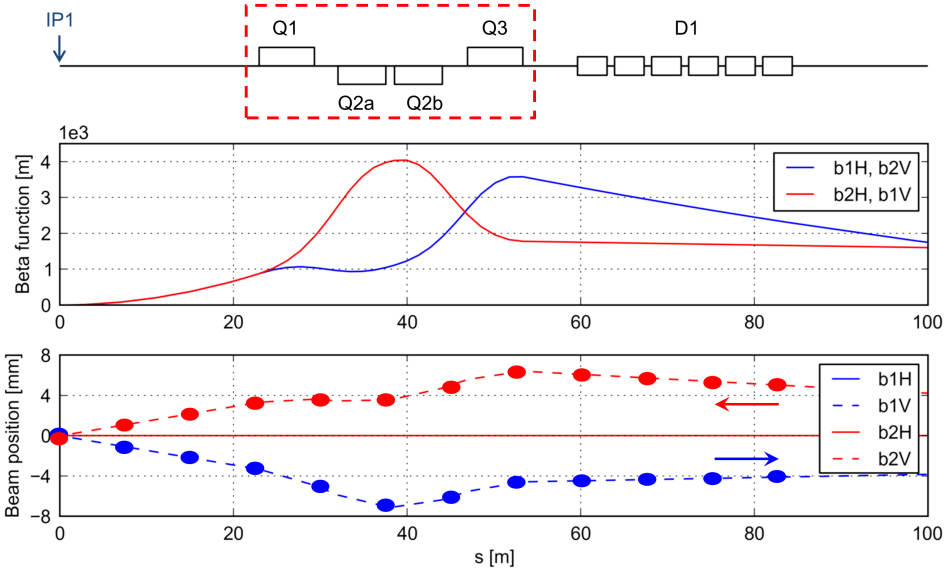

Figure 6.4: Machine layout on the right side of the IR1. The inner triplet is within a red dashed box in the sketch at the top. The two graphs beneath represent Beam 1 and Beam 2 beta functions and orbits with respect to the chamber axis when the two beams are in collision.

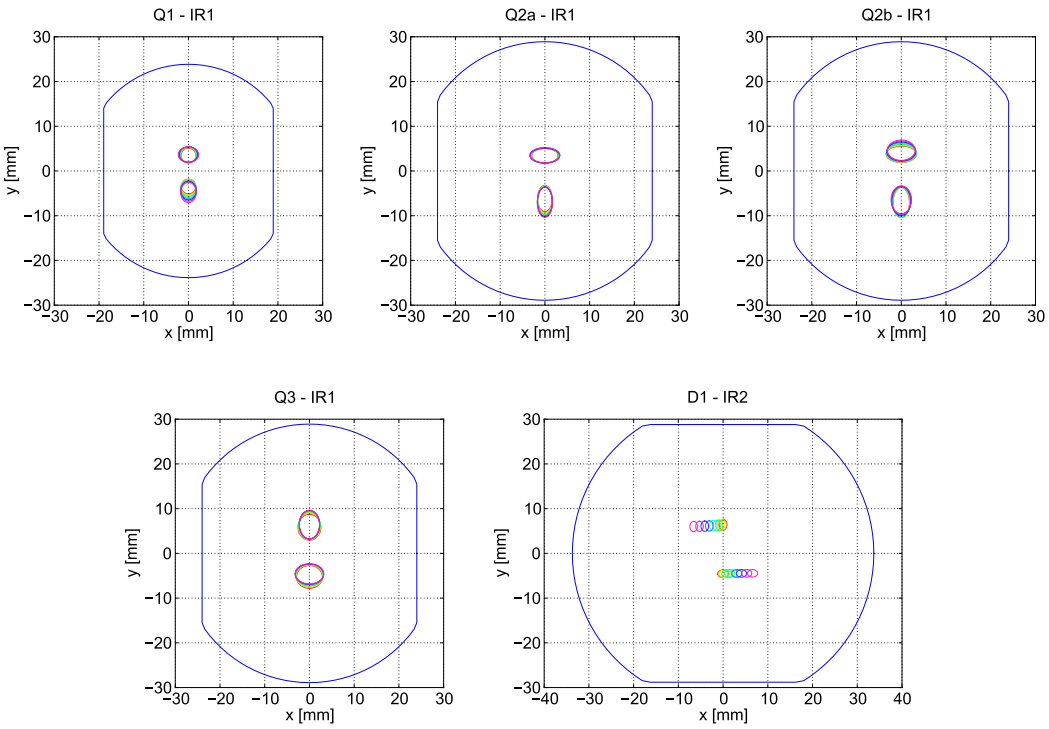

Figure 6.5: Beam screens of the four modules of the inner triplet in IR1 and of the D1 dipole in in IR2, with the transverse envelopes of the two beams (2σ).

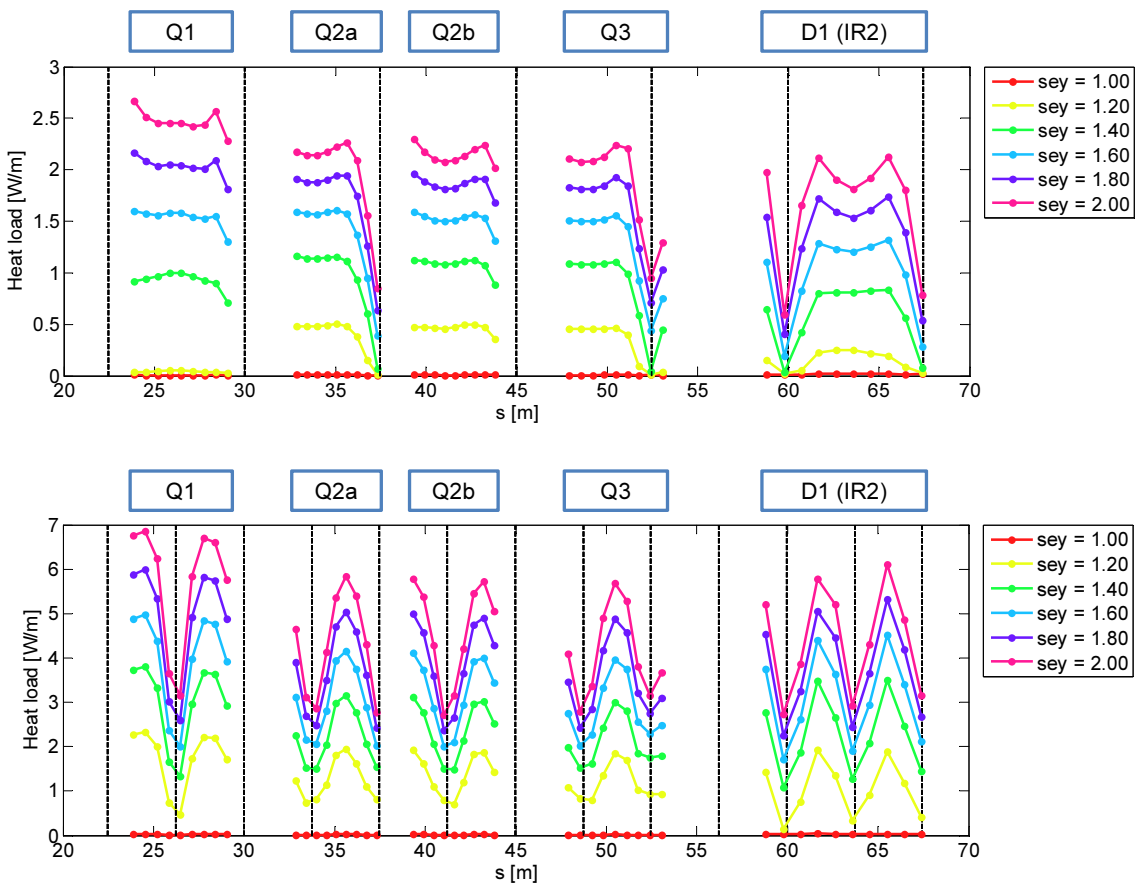

Figure 6.6: Simulated EC heat load all along the four modules of the inner triplet on the right side of IR1 and along the D1 dipole on the right side of IR2. Results are shown for 288 bunches of 50 ns beams (top) and 576 bunches of 25 ns beams (bottom).

6.2.1 *PyECLOUD simulation studies*

The inner triplets represented a quite challenging scenario for EC buildup simulations. The presence of two beams arbitrarily delayed with respect to each other, with different transverse positions and shape required the introduction of important upgrades in PyECLOUD. Moreover, since PyECLOUD is a 2D code and the beam properties (delay, position, size) are changing along the triplet, it was necessary to launch separate simulations for different slices ($\sim$ 10 per module) of the triplet.

Both the 25 ns and the 50 ns beams had to be simulated in order to compare against heat load data collected in 2012, and different SEY values had to be scanned since the conditioning state of the beam screen was unknown. This resulted in quite an important simulation load, requiring several hundreds of CPUs for several days and hundreds of Gigabytes of simulation data storage space.

We considered typical beam parameters used in operation in 2012, i. e. beam energy equal to 4 TeV and bunch intensities 1.6×10^{11} ppb for the 50 ns beam and 1.15×10^{11} ppb for the 25 ns beam. The buildup simulations at the different locations of the triplet were carried out

for values of the SEY ranging between 1.0 and 2.0, so that the heat load on beam screen could be determined all along the device for all these cases.

The outcome of this simulation campaign has been summarized in Fig. 6.6, in which we can see the expected EC induced heat load at the different longitudinal positions of the considered triplet for different values of the SEY. The heat load along the D1 dipole in IR2 is also reported for comparison. The case of 288 bunches with 50 ns spacing is shown in the top plot, while the bottom one represents the expected heat load from 576 bunches with 25 ns spacing. Dashed black lines are used for highlighting the positions of the long range encounters, where the heat load decreases because of the lower electron production with larger bunch spacing (despite the larger equivalent intensity per bunch). It is also evident that Q1, which has a smaller aperture (see Fig. 6.5) shows a stronger heat load. The D1 dipole presents a qualitative behavior and heat load values very similar to the quadrupole modules.

Figures 6.7, 6.8, and 6.9 show some more details about the EC buildup in the Q3 quadrupole module. The typical build up profile is shown in Fig. 6.7 for a specific example with 25 ns beams and the SEY parameter equal to 1.2. Here Beam 2 is chosen as a reference and Beam 1 is shifted with respect to it by different amounts such as to simulate all possible different longitudinal positions within Q3 (as labeled). It is evident from this plot that at most Q3 locations the presence of two beams in the chamber is instrumental to the build up of a highly populated EC. Only at few locations, corresponding to the longitudinal positions of the long range encounters in Q3, the difference between two beams and one beam becomes less evident.

Figure 6.8 shows the local heat load at each section of the Q3 module as a function of the SEY. The dashed curves show the heat load obtained from simulations where only one circulating beam is considered (the simulation with only beam 1 is shown in blue and the one with only beam 2 in red).

In the case of the 50 ns spacing (see Fig. 6.8 - left) we can observe that the simulated section which is closer to a long rang encounter (i. e. $s = 52.4$ m) shows the same multipacting threshold (SEY $\simeq 1.4$) as for a single circulating beam (despite the larger equivalent intensity per bunch). Other sections, instead, show significantly lower thresholds, due to the EC enhancement due to the shorter effective bunch spacing.

Although being still present, this behavior due to the different effective spacings is much less evident in the case of the 25 ns beam, for which a low multipacting threshold (SEY $\simeq 1.1$) is observed already for a single beam (qualitatively we can say that in this case there is not much room for EC enhancement since a single 25 ns beam already induces a strong multipacting).

Figure 6.9 shows different snapshots of the EC density in the Q3 module. The electron distribution is very similar to the one obtained in the case of the arc quadrupoles (see Sec. 4.2), concentrated along the pole to pole directions, although both beams cross the chamber off axis. On the other hand it is possible to notice that the electron "pinch" is indeed asymmetric, due to transverse displacement of the beams.

Finally, in Fig. 6.10, we compare the average heat load density obtained for the five simulated modules and for the two simulated bunch spacings. The average contribution per bunch passage is very similar for the two spacings, as opposed to what is observed in the arc dipole and quadrupole magnets (see Secs. 4.1 and 4.2). The 50 ns anyhow shows a slightly larger multipacting threshold. Moreover, also in these pictures, it is possible to notice that the

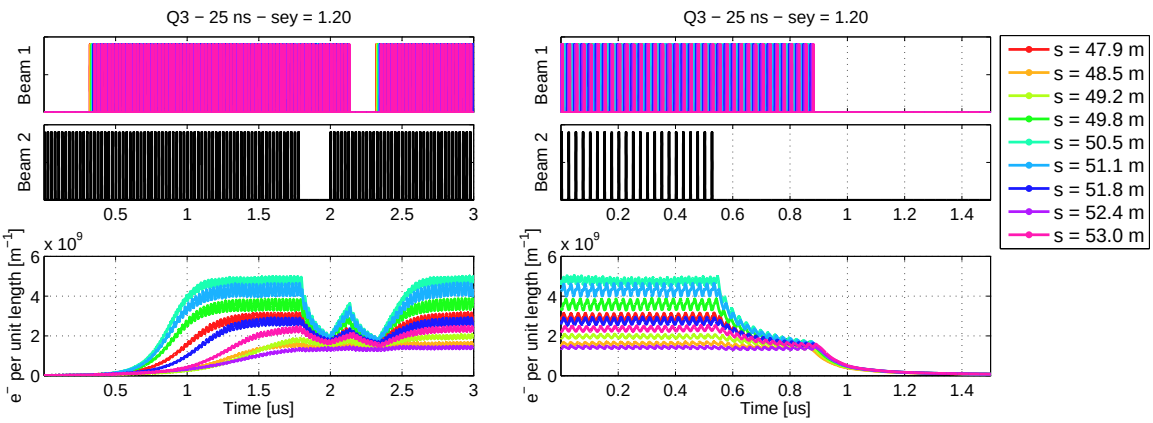

Figure 6.7: Simulated build up of the electron cloud in the Q3 module for a 25 ns beam and SEY = 1.2. evolution of the electron density during the passage of the first (left) and last (right) bunch train of the two beams.

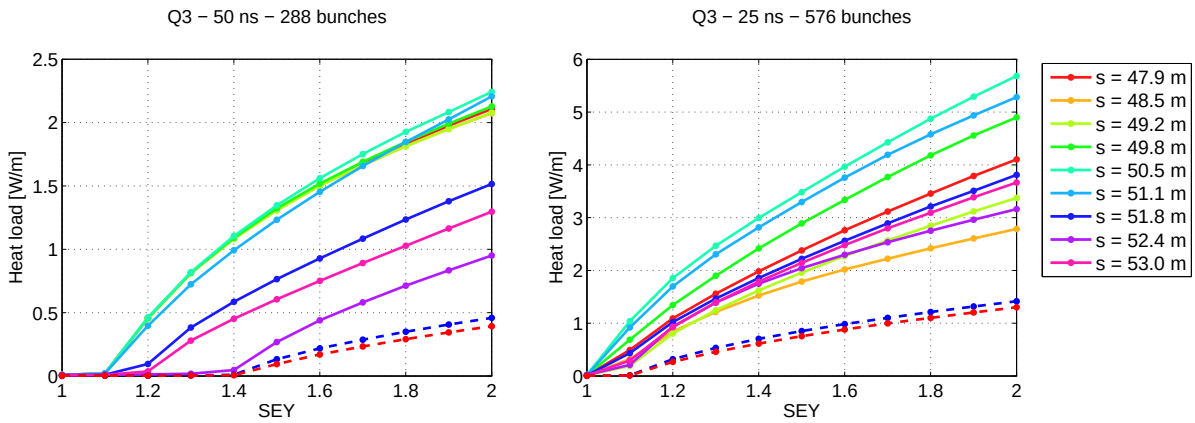

Figure 6.8: Heat load as a function of the SEY at different sections of the Q3 module.

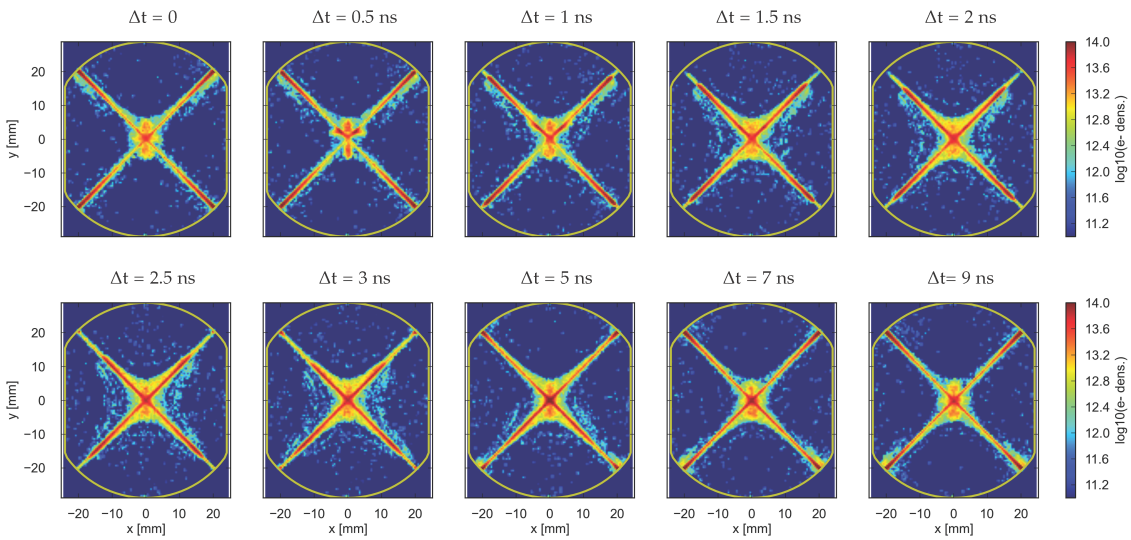

Figure 6.9: Different snapshots of the simulated EC pinch in the Q3 module for a bunch passage in the EC saturation stage. $\Delta t = 0$ corresponds to the passage of the head of the bunch.

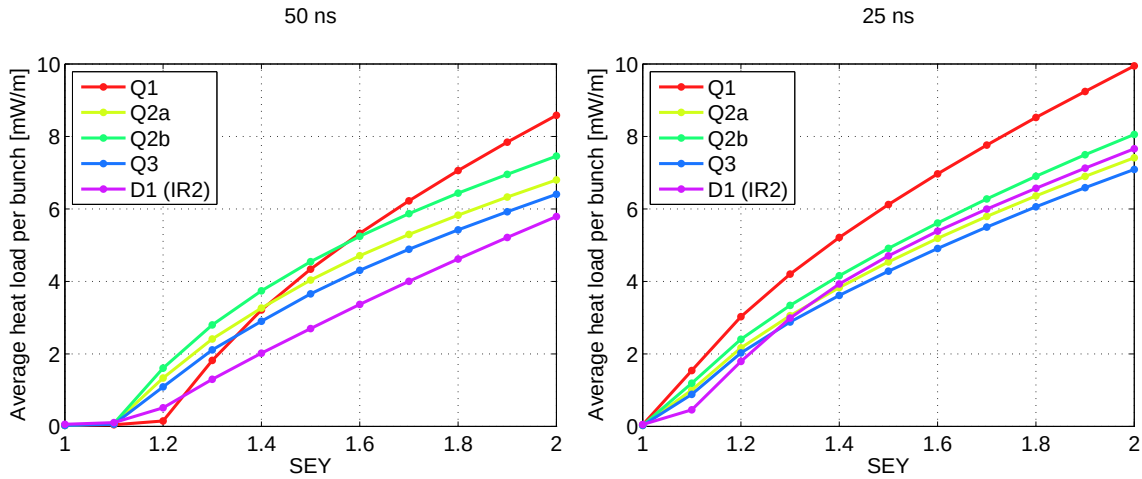

Figure 6.10: Average heat load density per bunch for the five simulated modules.

Q1 module has a different behavior compared to the other quadrupole modules, due to the smaller size of the beam screen.

6.2.2 *Machine observations*

Figure 6.11 shows the heat load evolution in the eight inner triplets during a typical physics fill with 50 ns spacing in 2012. We can observe that all the devices have a quite similar behavior. The heat load starts increasing at the end injection phase, stays about constant during the energy ramp and the beta squeeze and then slowly drops due to the beam intensity losses during the luminosity store. With this bunch spacing, the heat load per unit length is much stronger (more than 10 times) than the one observed in double bore magnets (e. g. in the matching quadrupoles) [88].

The heat load in the inner triplets showed a very similar behavior also during the tests with 25 ns beams at the end of the 2012 run (when a strong heat load was observed also in double bore magnets - see Sec. 5.3 and [88]).

In the inner triplets, the heat load contribution from synchrotron radiation is negligible due to the low emission in quadrupoles and the photon absorption from upstream aperture variations [20]. Besides, the measured heat load in the triplets does not exhibit any strong dependence on the beam energy which would be expected if the synchrotron radiation heating had been a significant contributor. The heat load due to the beam screen longitudinal impedance has been estimated to be 20 times smaller than the measured value. As a result, the measured heat load can be practically entirely attributed to the EC.

In Fig. 6.12 we compare against the simulation values (from the study presented in Sec. 6.2.1), the heat load measured during a fill with 50 ns beams at 4 TeV, a fill with 25 ns beams at 4 TeV (carried out with trains of 72 bunches, see Fig. 5.33, and a fill with 25 ns beams at 450 GeV (this data have been actually compared against the corresponding simulations at 4 TeV, this should be still valid since the dependence of the heat load on the beam energy has been observed to be very weak in these magnets). We observe that in all cases the measured heat load is compatible with values of SEY between 1.2 and 1.3.

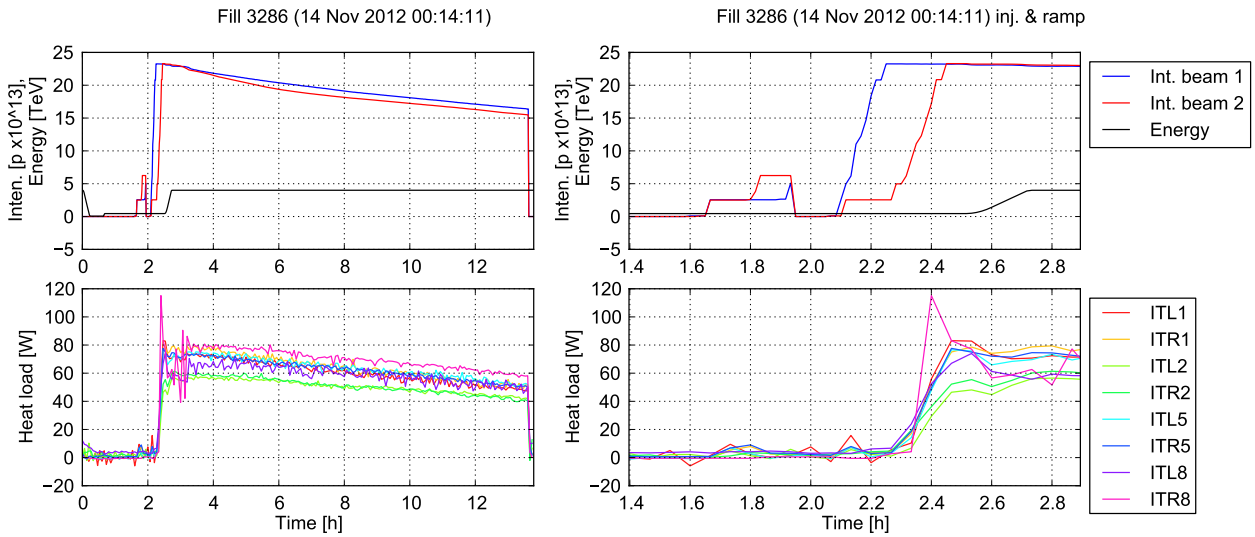

Figure 6.11: Heat load measured in the inner triplets during a typical physics fill with 50 ns spacing in 2012. Entire fill time (left) and detail of the injection and energy ramp (right).

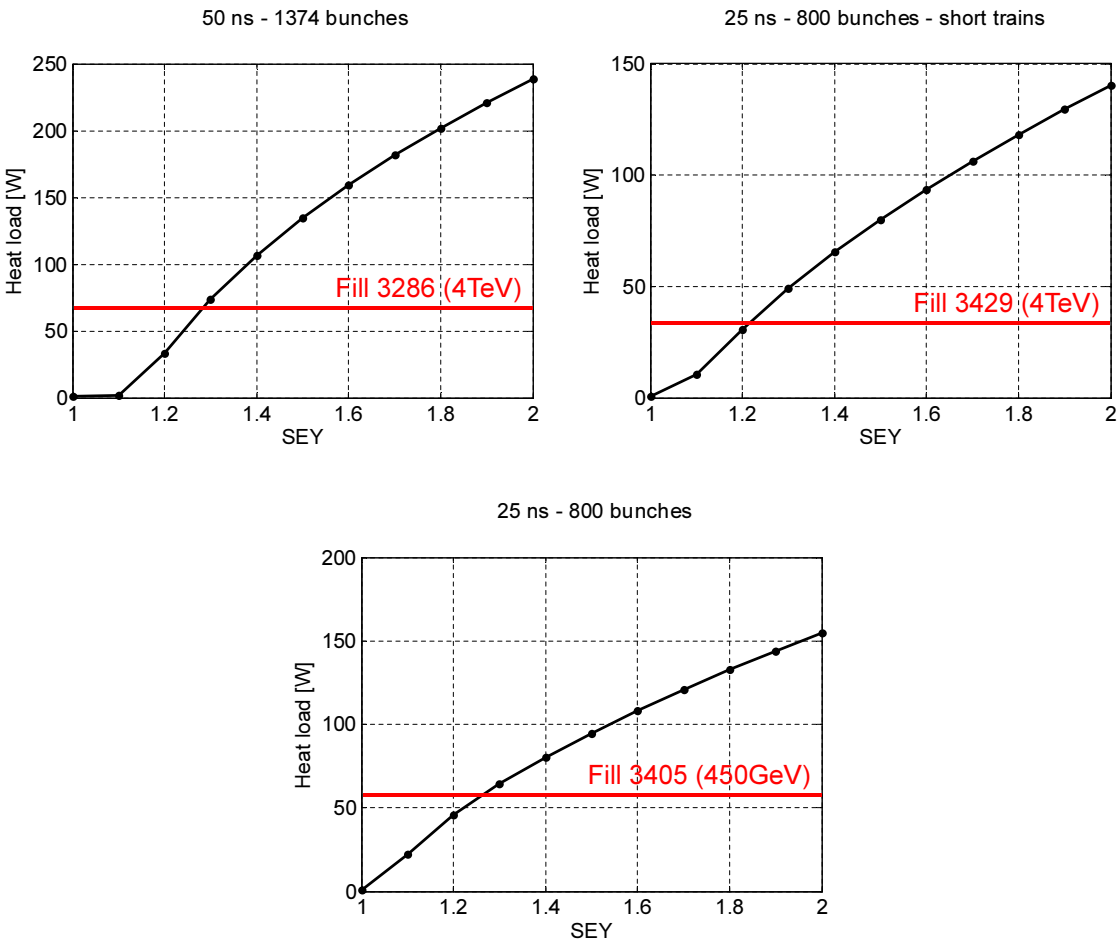

Figure 6.12: Comparison between simulated electron cloud heat load in the beam screen of the inner triplet (black curves) and measured values (red lines)

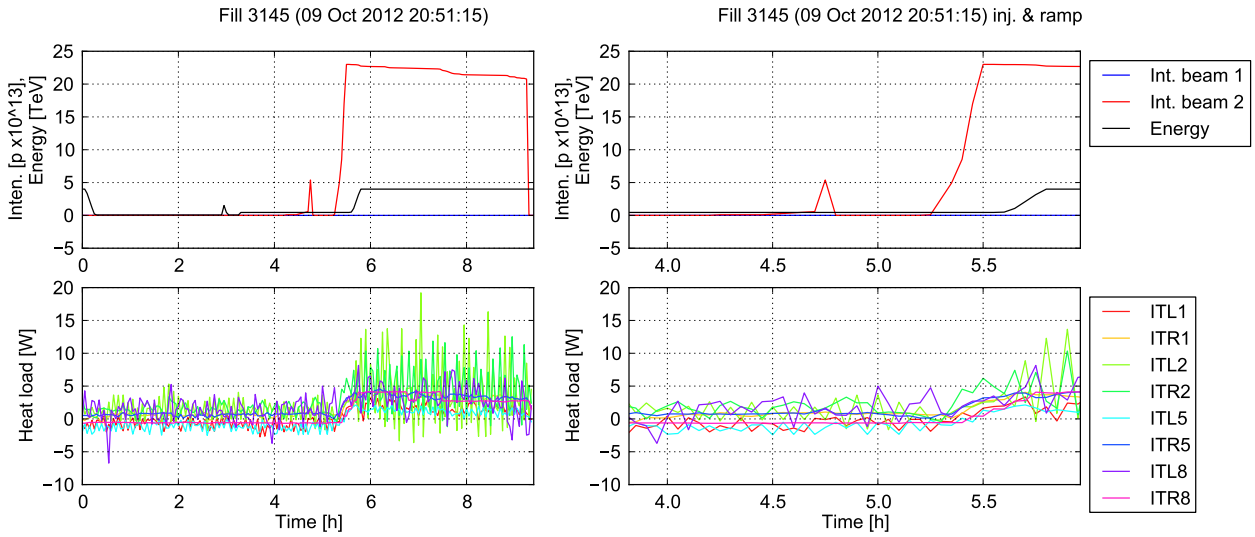

Figure 6.13: Heat load measured in the inner triplets with only beam 2 circulating in the LHC (50 ns spacing). Entire fill time (left) and detail of the injection and energy ramp (right).

According to this estimate no heat load from EC should be observed when only one beam with 50 ns spacing is circulating in the machine (see Fig. 6.8). This was confirmed by a fill dedicated to machine studies during which only beam 2 was circulating. On this occasion, as shown in Fig. 6.13, a much smaller heat load value was measured, perfectly consistent with the only impedance contribution of a single beam.

6.2.3 *Simulation studies for the High Luminosity Upgrade*

The High Luminosity LHC (HL-LHC) project has the goal of extending by a factor of ten the integrated luminosity reach of the LHC aiming at accumulating 3000 fB^{-1} by 2035 [54]. This will be made possible by several upgrades foreseen both on the LHC and on its injector chain. In particular the bunch intensity will be increased to 2.2×10^{11} ppb, and the inner triplets of the high luminosity IPs will be replaced with completely redesigned devices in order to allow reaching a much lower beta function at the IP (i. e. $\beta^* = 0.15$ m).

In this framework it is necessary to estimate the EC induced heat load for the HL-LHC beam parameters both for the present inner triplets, which will still be installed in IR2 and IR8 and for the newly designed triplet assemblies to be installed in IR1 and IR5, in order to assess the required cooling capacities and give specifications for suitable mitigation strategies like low-SEY coatings or clearing electrodes.

Projection for the present triplets in IR2 and IR8

In order to understand how the heat load in the present triplet scales with respect to the bunch intensity we simulated EC buildup at two sections, both far from the long range encounter, one within the Q1 module and one in the Q2 module of the present triplets. The simulations were carried out for 25 ns bunch spacing and for different bunch intensities. The results are summarized in Fig. 6.14.

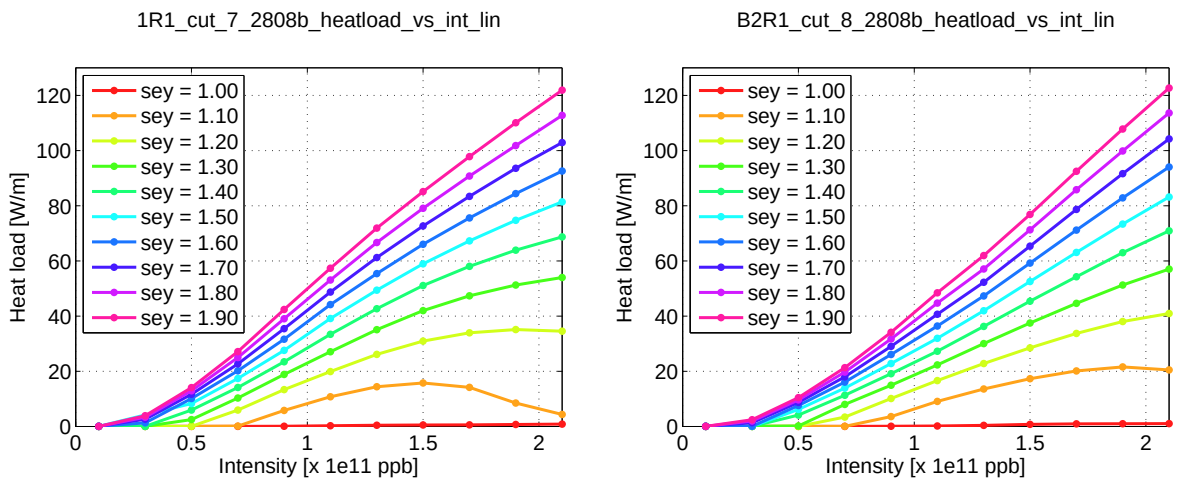

Figure 6.14: Dependence of the heat load on the bunch intensity at two sections, both far from the long range encounter, one within the Q1 module (left) and one in the Q2 module (right).

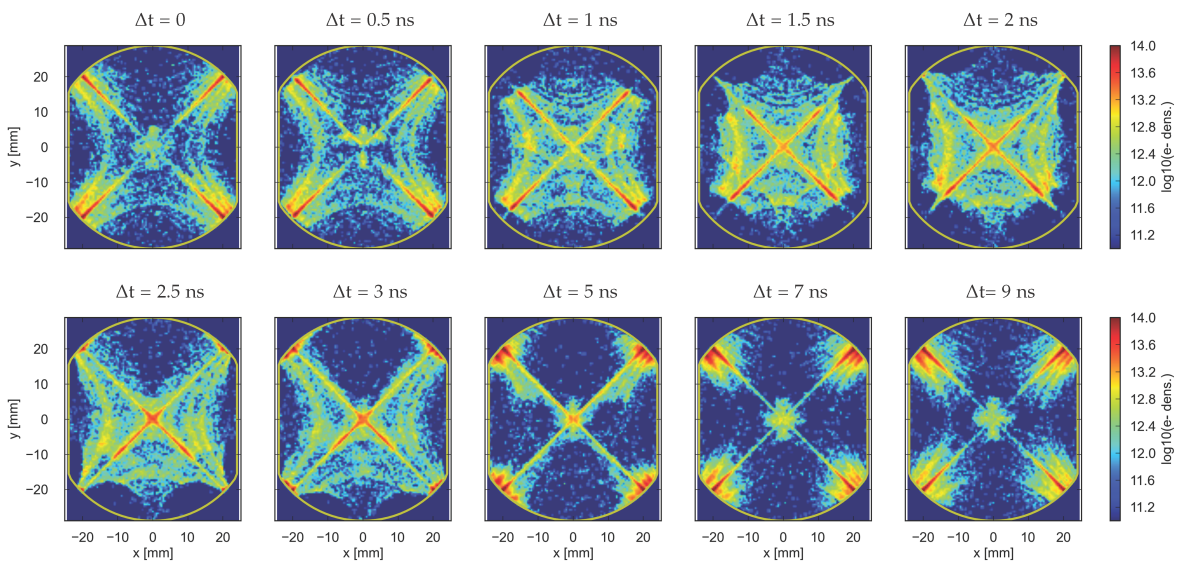

Figure 6.15: Different snapshots of the simulated EC pinch in one of the Q2 modules of the present triplet assembly with the HL-LHC beam parameters for a bunch passage in the EC saturation stage. $\Delta t = 0$ corresponds to the passage of the head of the bunch.

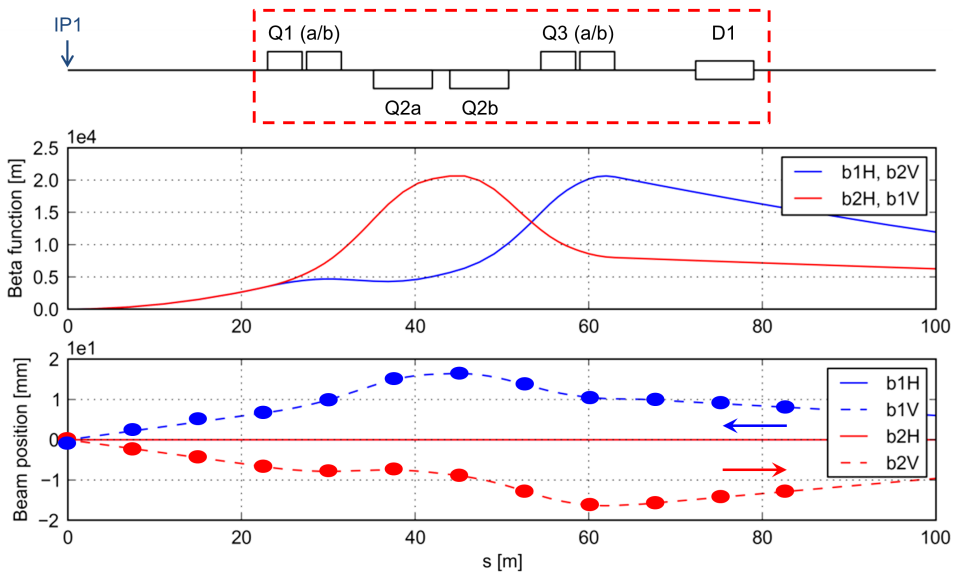

Figure 6.16: HL-LHC machine layout on the right side of the IR1. The inner triplet and the D1 dipole are within a red dashed box in the sketch at the top. The two graphs beneath represent Beam 1 and Beam 2 beta functions and orbits with respect to the chamber axis when the two beams are in collision.

The two sections show very similar behaviors, a non negligible heat load is observed already for bunch intensities lower than nominal and, for SEY larger than 1.2 (like the value estimated for the present triplets during 2012 operation - see Sec. 6.2.2) the heat load grows monotonically with the bunch intensity, and the increase from the nominal intensity to the HL-LHC value is more then a factor of two.

Figure 6.15 shows different snapshots of the EC density observed for the HL-LHC bunch intensity. Comparing against Fig. 6.9 we observe that for this high intensity value, multipacting interests a wider region of the beam chamber.

The new inner triplet design for IR1 and IR5

The newly designed layout and optics for the inner triplets in IR1 and IR5 are shown in Fig. 6.16. The new triplet assembly is longer than the one presently installed in the LHC and is made of six modules having a significantly larger aperture (see Fig. 6.17), in order to allow for larger beta function inside the triplet itself and therefore for a smaller beam size at the IP. The D1 dipole is superconducting, shares the beam screen cooling circuit with the triplet assembly, and has therefore been included in our simulation study.

All the modules are equipped with an octagonal beam screen (see Fig. 6.17). As in the present triplet the Q1 module has a smaller aperture compared to the other modules.

For these devices we have repeated the simulation study presented in Sec. 6.2.1. Figure 6.18 shows the heat load profile along the triplet assembly. The qualitative behavior is very similar to that observed for the present triplets. The heat load is weaker around the long range encounters positions, the Q1 modules shows larger values compared to the other modules due to the smaller aperture, while the D1 shows values comparable to those of the quadrupole modules.

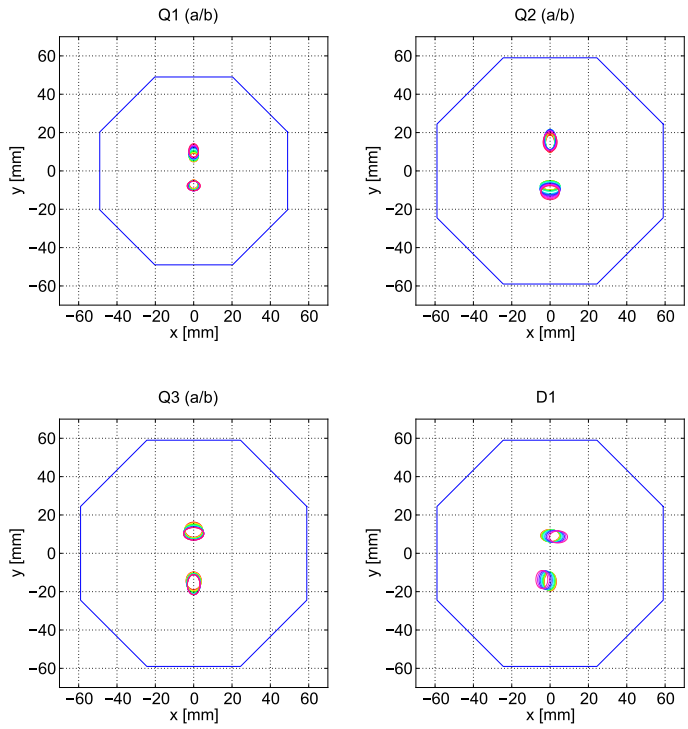

Figure 6.17: Beam screens of the different modules of the inner triplet and the D1 dipole for the HL-LHC upgrade with the transverse envelopes of the two beams (2σ).

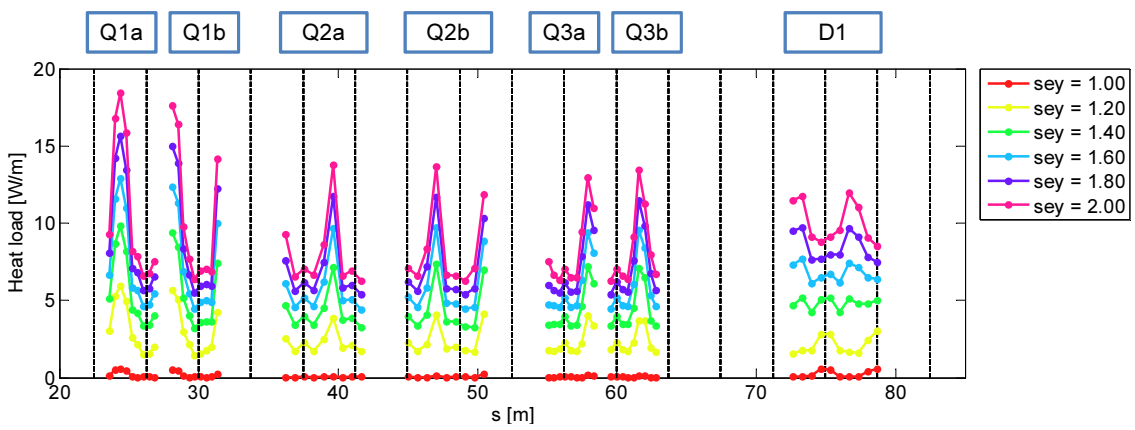

Figure 6.18: Simulated EC heat load all along the seven modules of the HL-LHC inner triplet on the right side of IR1. Results are shown 576 bunches of 25 ns beams.

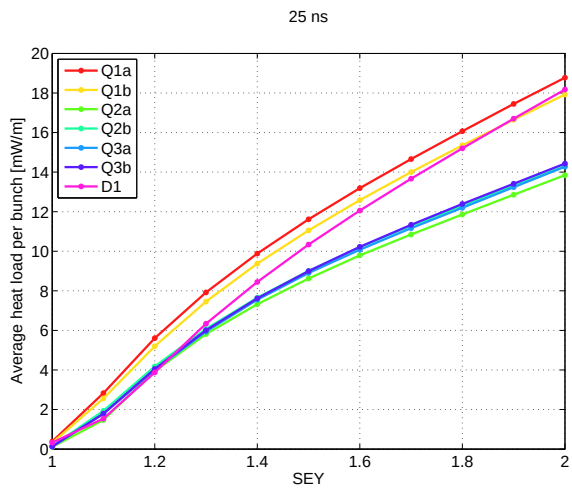

Figure 6.19: Average heat load density per bunch for the seven simulated modules of the HL-LHC triplet.

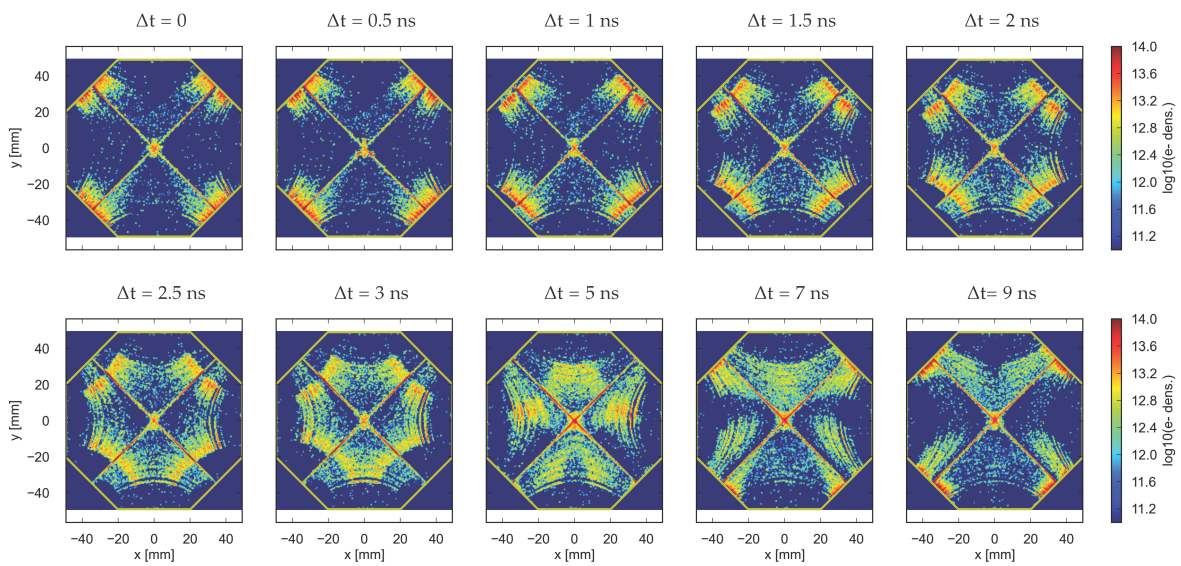

Figure 6.20: Different snapshots of the simulated EC pinch in one of the Q1 modules of the HL-LHC triplet assembly, for a bunch passage in the EC saturation stage. $\Delta t = 0$ corresponds to the passage of the head of the bunch.

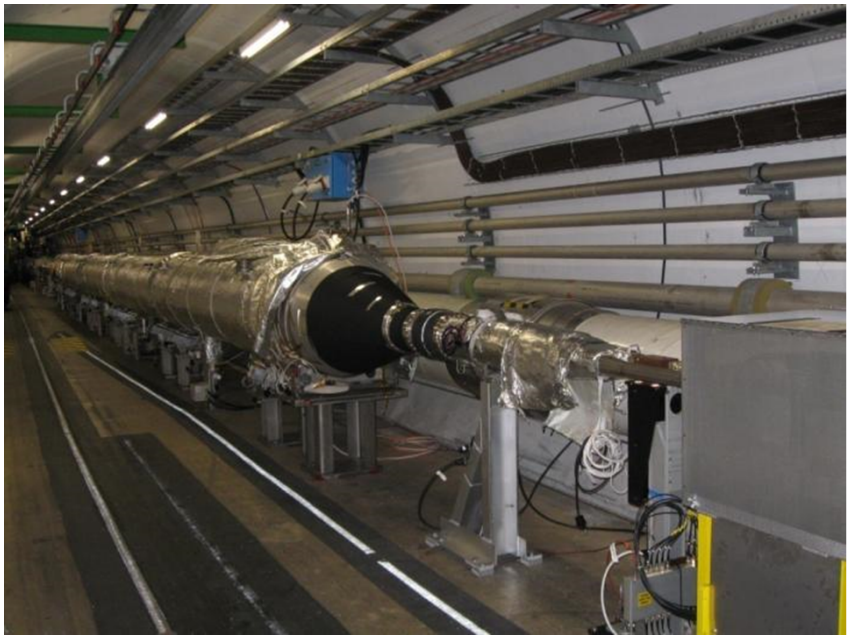

Figure 6.21: The 800 mm common chamber in IR2.

Figure 6.19 shows the average heat load density in each module as a function of the SEY. We can observe that the values are quite similar and that the multipacting threshold is very low in all the modules. This poses quite stringent requirements on the foreseen low SEY coating since, for a full suppression of the EC, SEY values lower than 1.1 are necessary.

Figure 6.15 shows different snapshots of the EC density observed for HL-LHC inner triplets. Comparing against Fig. 6.9 we observe that multipacting interests a wider region of the beam chamber, but still concentrated around the magnet pole regions.

6.3 THE 800 MM COMMON CHAMBER IN IR2

Common vacuum chambers having 800 mm diameter are installed on both sides of the ALICE experiment in the Long Straight Section 2 (LSS2) of the LHC, between the D1 and the D2 separation/recombination dipoles (see Fig. 6.21).

During 2011 operation with 50 ns bunch spacing an important pressure rise was noticed in these chambers with a significant impact on the background observed by the ALICE experiment.

The analysis of the pressure data has shown that a severe pressure increase is observed only when the two rings of the LHC are completely filled. Fig. 6.22 shows the pressure evolution during a proton-proton physics fill (with 50 ns spacing) in which the injection from the SPS of the last two trains of 144 bunches was delayed by about one hour. It can be noticed that the pressure rise appears already at the injection energy (450 GeV), but only after the last two injections have taken place.

PyECLOUD simulations have been run in order to investigate if the EC formation in these chambers could explain this peculiar behavior. The presence of both counter-rotating beams in the chamber had to be taken into account since it determines different “hybrid" bunch

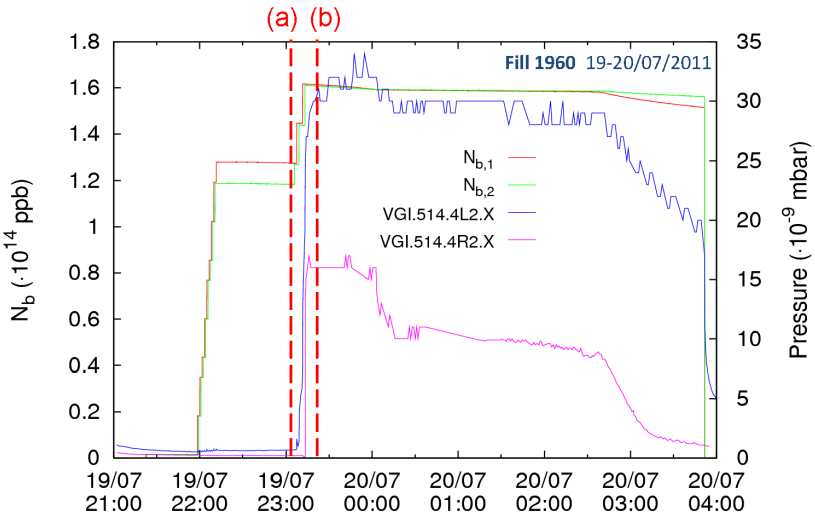

Figure 6.22: Pressure evolution in the 800 mm chambers near the ALICE experiment of the LHC during a proton physics fill. The total beam intensity is the two rings is also included.

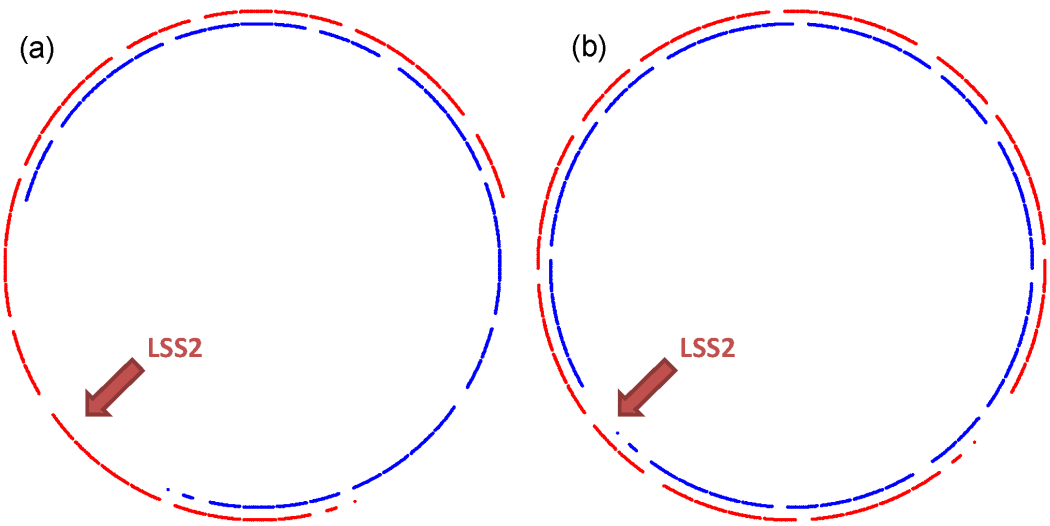

Figure 6.23: Filling pattern of the two beams in the LHC before (a) and after (b) the injections of the last two trains. Beam 1 (blue) is rotating clockwise, beam 2 (red) counterclockwise. The position the straight section 2 (ALICE) is highlighted.

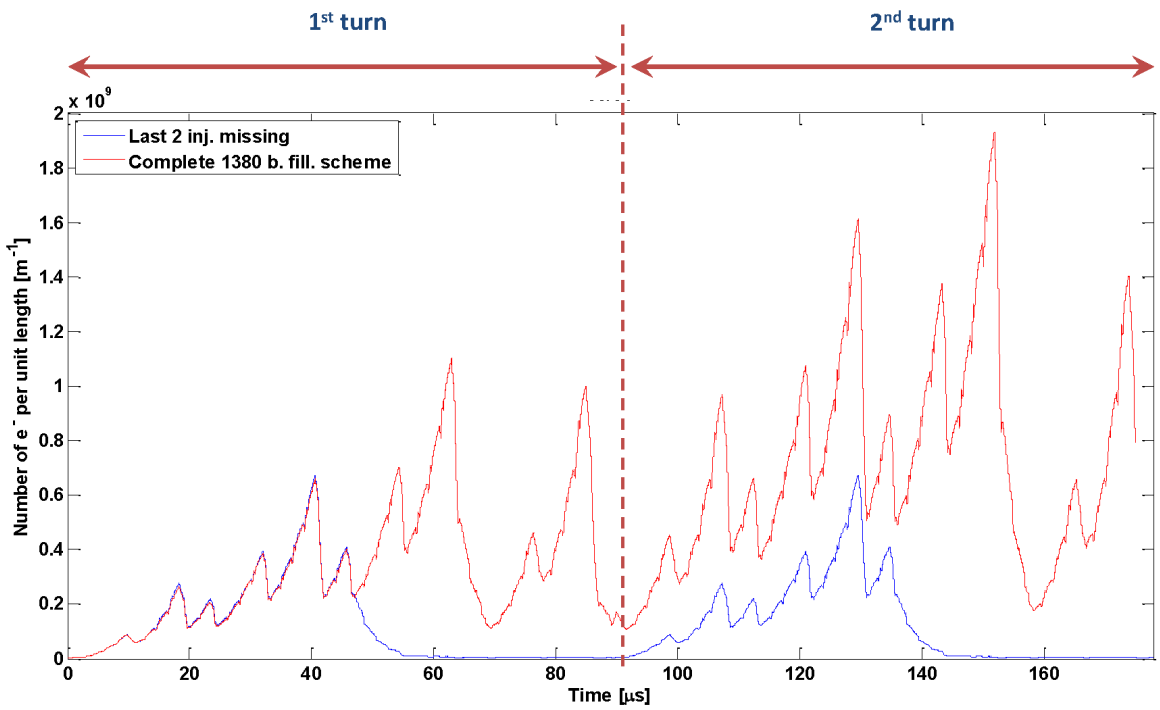

Figure 6.24: PyECLOUD simulation of the electron cloud build-up in the 800 mm common chambers for the filling patterns in Fig. 6.23.

spacings at the different sections of the ∼30 m long vacuum chambers when both beams are circulating in the LHC [89].

In particular the two beam configurations in Fig. 6.23 have been simulated, which correspond to the beam patterns in the two rings at the moments indicated by (a) and (b) in Fig. 6.22. The results at a section far from the long range encounters are shown in Fig. 6.24.

It can be noticed that, in the configuration of Fig. 6.23 (a), both beams present a gap of about one quarter of the length of the ring. Probably due to the large radius of the chamber, the EC can develop only when both beams are passing in the chamber, while a decay of the number of electrons is observed when only one beam is passing. The gap is long enough to allow a complete reset of the EC between subsequent turns.

On the other hand, after the injection of the last two trains from the SPS, the layout of the beam in the two rings looks like the one in Fig. 6.23 (b) where no large gap is present in any of the two beams. As a consequence a complete decay of the EC between subsequent turns is not possible anymore. In fact, a memory effect is observed between turns with a strong enhancement of the EC activity and, as consequence, of the electron stimulated gas desorption leading to the observed pressure rise.

Part III

ELECTRON CLOUD STUDIES FOR THE LHC INJECTORS

7

ELECTRON CLOUD STUDIES FOR THE CERN PROTON SYNCHROTRON

EC effects have been observed at the CERN Proton Synchrotron (PS) during the last stages of the cycle of the production of the LHC type beams. The first observations date back to 2001 when a distortion of the baseline was observed on electrostatic pickup signals both in the PS ring and in the transfer line towards the SPS [90]. In 2006 transverse instabilities immediately before extraction were observed for short bunches [91], and in 2007 an EC test setup with two shielded pickups was installed in one of the straight section of the ring and direct measurements could confirm the presence of EC in the vacuum chamber [92]. It is quite likely that EC is developing also in the main magnets, which constitute about 70% of the total length of the PS, but there is no direct confirmation since dedicated diagnostics will only become available after the 2013-2014 machine shutdown [92].

Despite these considerations, EC in the PS presently does not represent a limitation for the production of the LHC type beams. For example, in 2012 bunch by bunch transverse emittance measurements were performed in the SPS on LHC type beams with 25 ns spacing, for bunch intensities up to around 1.45×10^{11} ppb, and no EC signature was observed on the emittance pattern coming from the PS.

The reason for the absence of any visible degradation is that the beam does not interact with the EC for a sufficiently long time, since the structure of the beam becomes prone to the production of the EC only few tens of milliseconds before the extraction (see Figs. 7.1 and 7.2). This happens when the last bunch splitting is performed, giving the final pattern with 72 bunches and 25 ns spacing. As schematically shown in Fig. 7.2, the last bunch splitting starts $\sim$57 ms before the extraction, with the ramp-up of the 40 MHz (h_{RF}=84) RF voltage, and it is completed less than 10 ms before extraction, after the end of the ramp-down of the 20 MHz RF system voltage. At this point the bunches are still about 14 ns long and need to be shortened to fit the 5 ns buckets in the SPS. This is done in two stages, namely: 1) an adiabatic shortening in which the RF voltage is increased in 5 ms from 40 kV to 100 kV achieving bunch lengths of about 11 ns and 2) a non adiabatic “bunch rotation" performed by pulsing the RF voltage up to 300 kV (and using also a second harmonic RF system at 80 MHz) in order to finally reduce the bunch length to values of about 4 ns.

Already in 2001, an experiment was performed removing the bunch rotation and “storing" the 11 ns long bunches for few tens of milliseconds. A strong horizontal instability was observed, which could be possibly ascribed to EC [90].

Within the LHC Injectors Upgrade (LIU) project it is necessary to assess whether the EC instability, or incoherent effect, could degrade the beam quality on the timescale of the nominal cycle for the high intensity and high brightness beams foreseen for the upgrade. Therefore

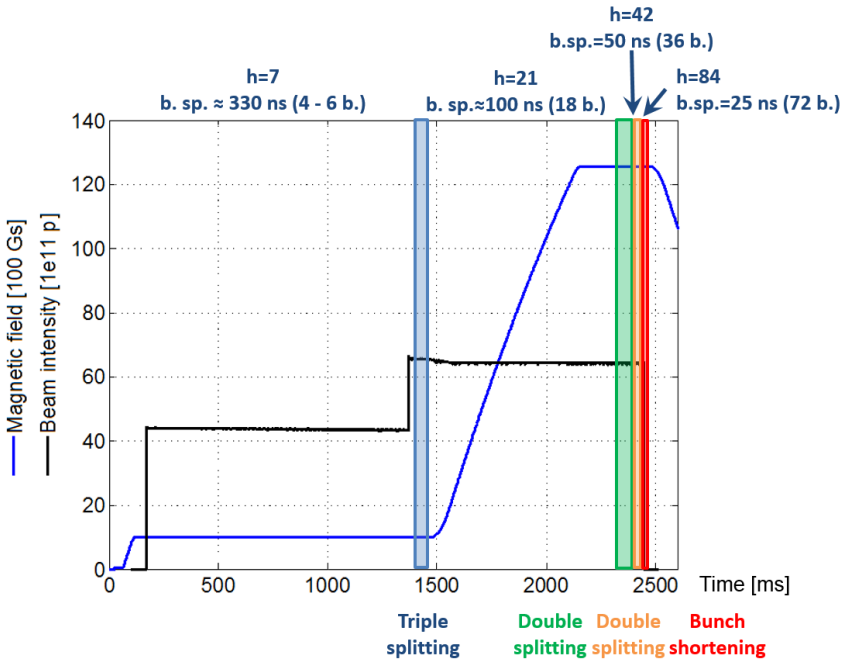

Figure 7.1: The machine cycle for the production of the LHC-type beam with 25 ns spacing in the PS. The employed harmonic number and the different RF manipulations are highlighted.

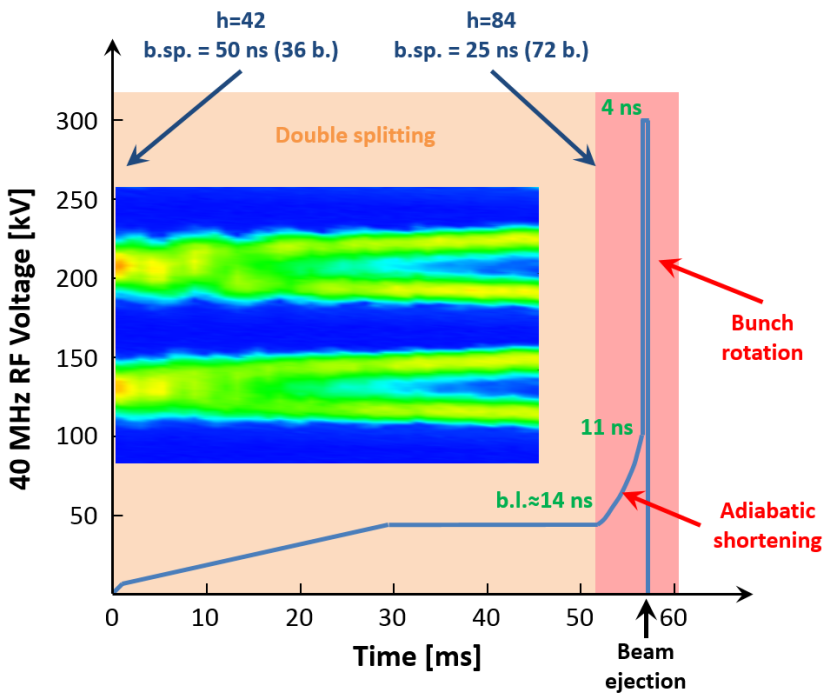

Figure 7.2: RF voltage program (40 MHz) during the last stages of the cycle for the production of the LHC type beams. The total (4σ) bunch length is reported in green. In the inset the evolution of the longitudinal profile of two bunches during the last bunch splitting (from 50 ns to 25 ns bunch spacing).

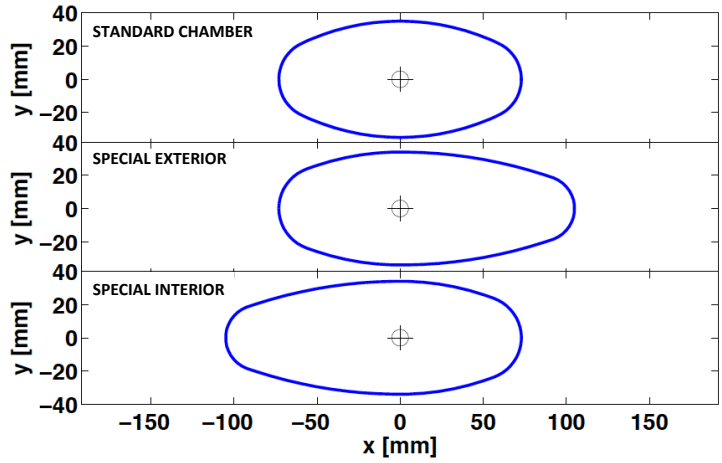

Figure 7.3: Geometry of the three PS chambers analyzed in the EC parameter studies. From top to bottom: the standard chamber (width 146 mm, height 70 mm), the special exterior chamber (width 178 mm, height 68 mm) and the special interior chamber (width 178 mm, height 68 mm).

several studies are being carried out in order to develop a reliable EC model of the PS vacuum chambers, identify possible future limitations and find suitable countermeasures.

In this framework, during the 2013-2014 machine shutdown, one of the main magnets of the machine will be equipped for EC detection [93]. To support the design of the new detector as well as to improve our general understanding on EC effects in the PS, the possibility of simulating combined function magnets has been implemented in the EC build up code PyECLOUD and is presently being used for the characterization of the different chambers (see Sec. 7.1).

To have first crosschecks of our models and simulation codes several measurements with different beam conditions have been collected with the shielded pickups installed in one of the straight sections in the PS (see Sec. 7.2 and [50]). In 2012 several machine study sessions were also devoted to 1) further investigate the instability developing on the "stored" 25 ns beam (see Sec. 7.3 and [94]) and 2) investigate the possibility of modifying the 40 MHz RF voltage program in order to mitigate the EC without affecting the beam quality (see Sec. 7.4 and [94]).

7.1 PYECLOUD SIMULATION STUDIES

An intensive simulation campaign has been conducted in 2013 in order to characterize the main PS chambers (and different magnetic field configurations) in terms of EC formation [95]. In this study, the relevant ranges of bunch length and population were covered, i.e. $[4, 16]$ ns and $[10^{11}, 2.6 \times 10^{11}]$, respectively. The bunch length range simply corresponds to the values really covered during the last part of the cycle of the LHC 25 ns beam production, namely after the last bunch splitting at 26 GeV/c up until extraction (see Fig. 7.2). The bunch population range has been chosen as to reasonably include values that can be reached nowadays and extend to the future LIU values. The main goal of these simulation scans was to determine SEY thresholds all around the PS machine in different operating conditions.

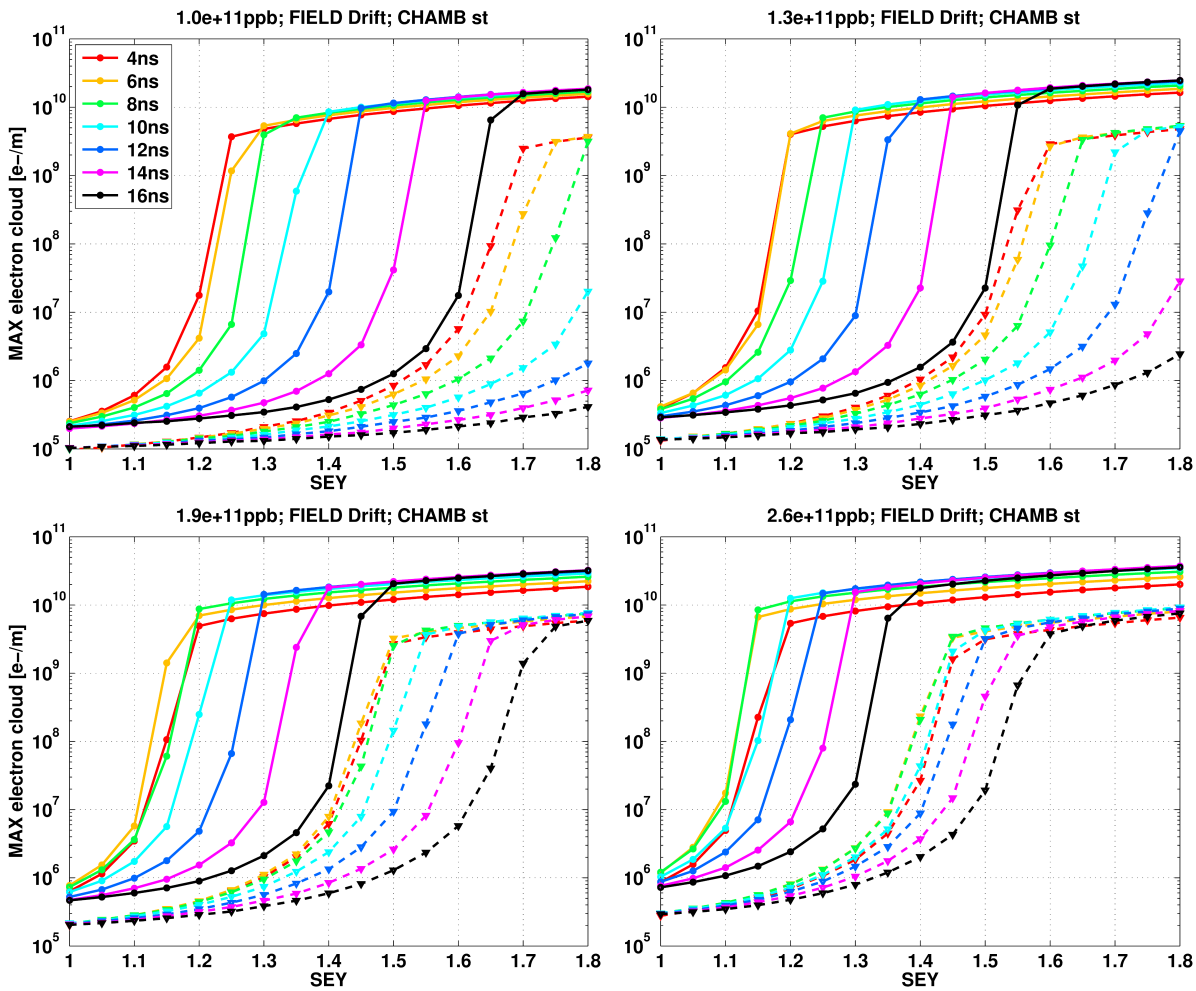

Figure 7.4: PyECLOUD simulations for a PS standard chamber in a field free region. EC line density as a function of the SEY for different bunch lengths (as labeled), for different values of bunch population (1.0, 1.3, 1.9 and 2.6×10^{11} ppb, from top left to bottom right, for two possible bunch spacings (25 ns solid lines and 50 ns dashed lines).

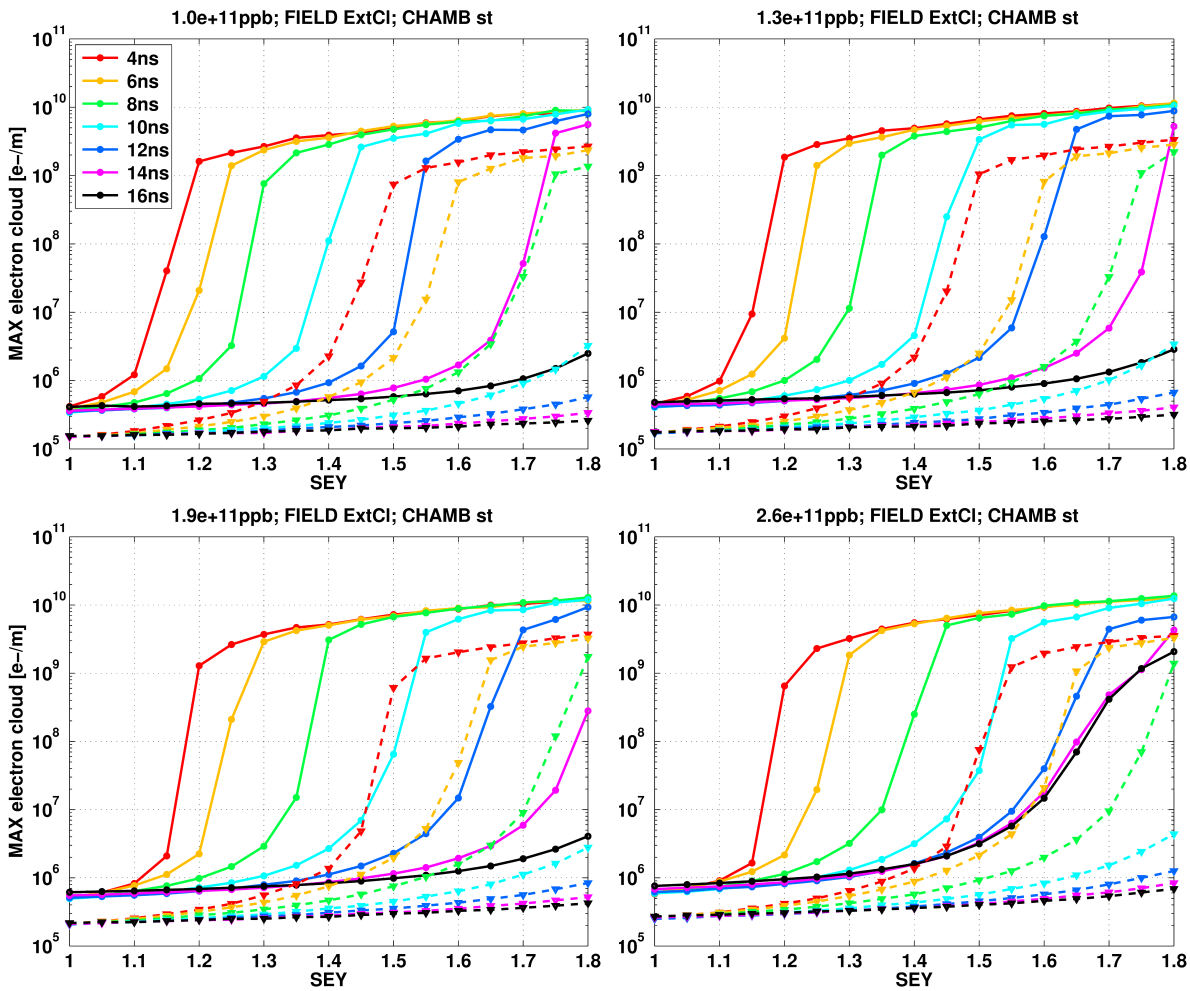

Figure 7.5: PyECLOUD simulations for a PS standard chamber in a combined function magnet. EC line density as a function of the SEY for different bunch lengths (as labeled), for different values of bunch population (1.0, 1.3, 1.9 and 2.6×10^{11} ppb, from top left to bottom right, for two possible bunch spacings (25 ns solid lines and 50 ns dashed lines).

Three PS chambers were considered in the analysis, i. e. those show in Fig. 7.3. For each chamber five possible magnetic field configurations have then been considered to cover all possible combinations observed in the PS straight sections and combined function magnets.

In Figs. 7.4 and 7.5 we show the simulation results for the PS standard chamber which is the most common in the PS ring.

In particular Fig. 7.4 shows the maximum EC linear density along the buildup as a function of SEY parameter, bunch length, bunch intensity and bunch spacing, for the situation in which the standard chamber is installed in field free region. Solid curves represent the results obtained for the 25 ns bunch spacing, the dashed ones those for 50 ns. We can observe that the multipacting threshold decreases when the bunch length decreases as well as when the bunch intensity increases.

Figure 7.5 shows the same results for a standard chamber installed in a combined function magnet (field configuration corresponding to the extraction energy of 26 GeV). Again shorter bunches correspond to lower multipacting thresholds while the increase of the bunch intensity has a significant impact only for relatively long bunches. Comparing Fig. 7.5 against Fig. 7.4, we see that, especially for longer bunches, the field free region shows significantly lower thresholds compared to the magnet case.

7.2 SHIELDED PICKUP MEASUREMENTS

EC build up data were recorded for 25 ns and 50 ns beams using the shielded pickup installed in the Straight Section 98 of the PS ring (standard chamber profile). The bunch intensities were scanned in the ranges indicated in Table 7.1. The trigger for the data acquisition was set at extraction, when in normal conditions each bunch of the beam has been already fully rotated (4 ns bunch length). However, specifically for these measurements, the bunch length at this time for a fixed bunch intensity was also set to 6.5 ns or 15 ns by simply adjusting or fully removing, respectively, the final step of the fast bunch rotation. This allowed studying the dependence of the EC build up not only on the bunch intensity but also on the bunch length.

Several measurements of EC build up were taken with 50 and 25 ns beams and the results of the bunch intensity scan are displayed in Fig. 7.6. Each plot shows the EC signal over a time

	50 ns	**25 ns**
Beam energy (GeV/c)	26	
Bunch intensity ($\times 10^{11}$ ppb)	0.82-1.95	0.83-1.33
Bunch length (ns)	$15 \rightarrow 12 \rightarrow 4$	
Number of bunches	36	72
Transv. norm. emittances (μm)	1-2	2-3

Table 7.1: Relevant beam parameters in the PS during the flat top RF gymnastics for the two bunch spacings of 50 and 25 ns.

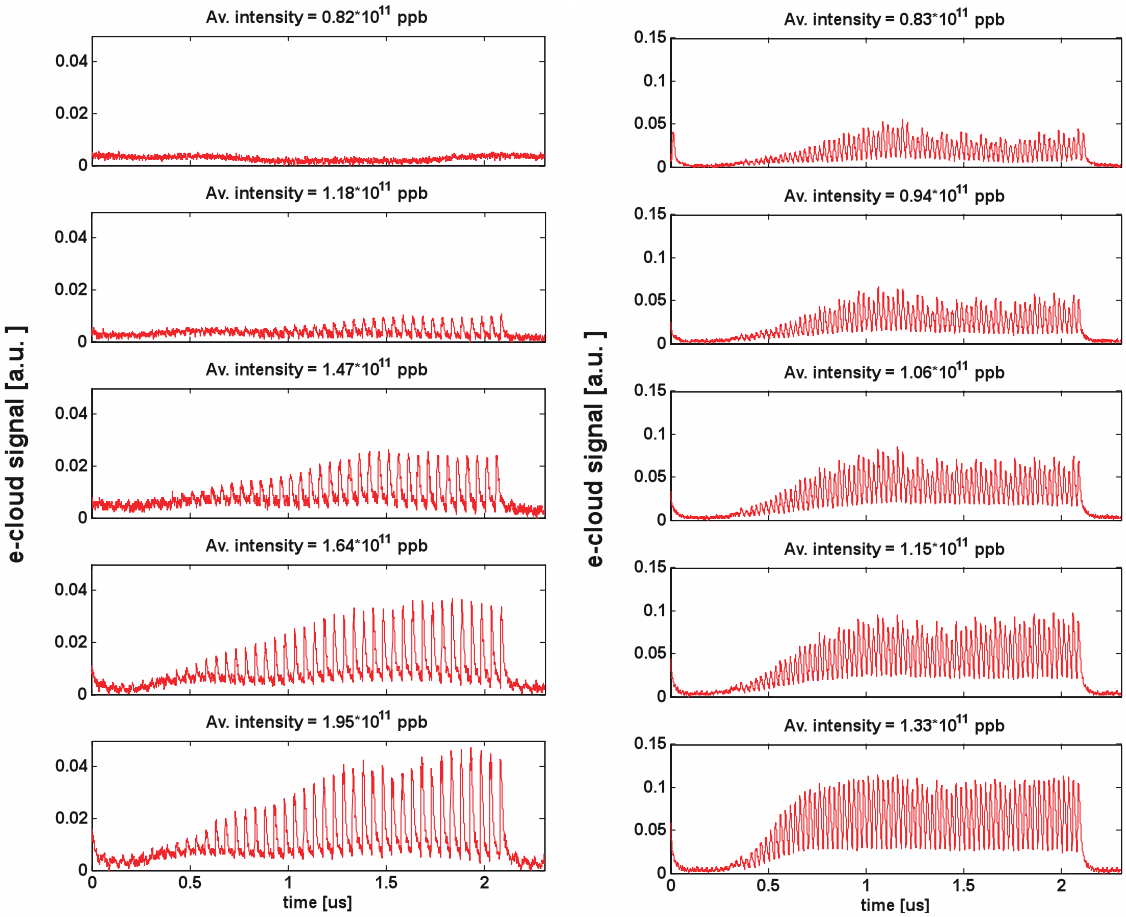

Figure 7.6: EC build up during passage of a 50ns bunch train with 4ns bunch length (left) and during passage of a 25ns bunch train with 4ns bunch length (right). The sometimes visible saw-tooth behaviour follows a bunch-by-bunch intensity modulation present during the measurements.

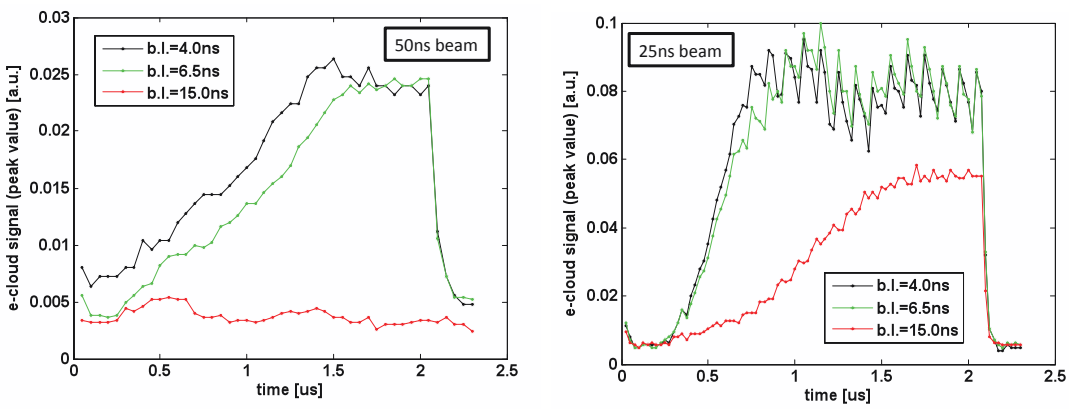

Figure 7.7: Envelope of the build up during passage of a 50 ns (left) and 25 ns (right) bunch train with 1.5×10^{11} ppb.

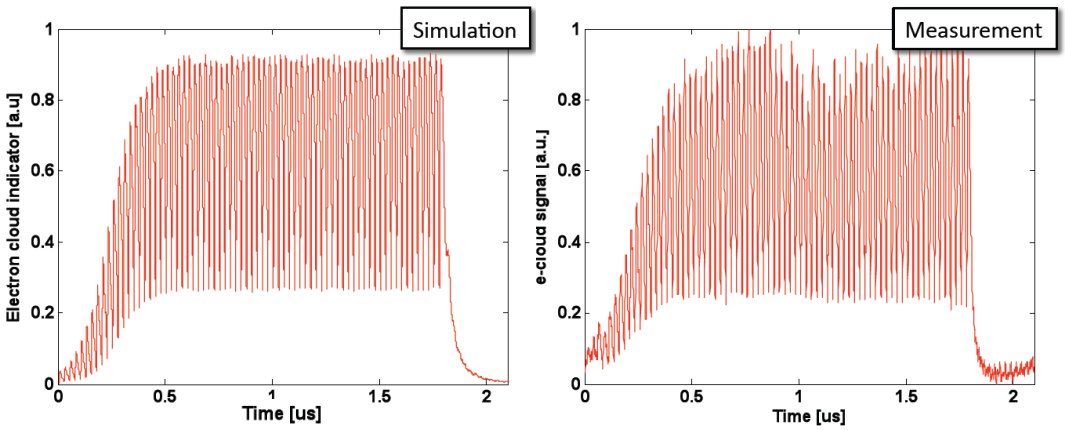

Figure 7.8: E-cloud build up simulation (left) and measurement (right) for a 25ns beam with 1.33×10^{11} ppb and 4 ns long.

window slightly longer than one PS revolution time (2.1 μs with 1.8 μs length of the 36-bunch or 72-bunch train plus 300ns gap). The bunch intensity was varied over a broad range.

The threshold for EC formation with 50 ns beams lies at about 10^{11} ppb and the measured signal increases monotonically with the bunch intensity, as expected from the simulation study (see Fig. 7.4).

The shielded pick up is installed inside a C-magnet, which was kept off during the MD sessions because the orbit perturbation it introduces would have required a specific correction. The scans with 25 ns beams covered a smaller intensity range, as labeled in Fig. 7.6, right column. Here we can see that the threshold for EC formation is below 8×10^{10} ppb for 25 ns spaced beams and then again the EC signal increases with the bunch intensity.

The scans in bunch length for a fixed bunch intensity of 1.5×10^{11} ppb are plotted in Fig. 7.7 for both 50 ns (left) and 25 ns beams (right). From the left plot it is clear that, while the difference between the build up with bunches of 4 and 6.5 ns is small, there is no sign of EC with 15 ns long bunches. This suggests that 50ns beams might see the EC only in the very last phase of the beam production, i.e. during and after the fast bunch rotation. For 25 ns beams, while the difference between the EC build up with bunches of 4 and 6.5 ns is negligible, the EC is lower, yet still significant, with 15 ns long bunches.

7.2.1 *Comparison against simulation*

We have compared the MD data with those from EC build up simulations. The output of the code that should be compared with the measured signal is the electron flux to the wall.

In a first approximation, we do not consider the holes in the vacuum chamber, which are expected to cause only a minor perturbation in a field-free region. In general, the simulated electron flux to the wall vanishes during the bunch passage, because initially all the electrons are drawn to the center of the vacuum chamber by the passing bunch (e.g. during the first $\sim$2 ns of a 4 ns long bunch) and they are gradually released only during the falling edge of the bunch, when they may reach the walls again. The fact that the measured signal does not exhibit this feature makes plausible a low pass filtering of the signal (inherent to the measurement technique or due to electronics and/or cables) with a corner frequency in the range of some hundreds of MHz.

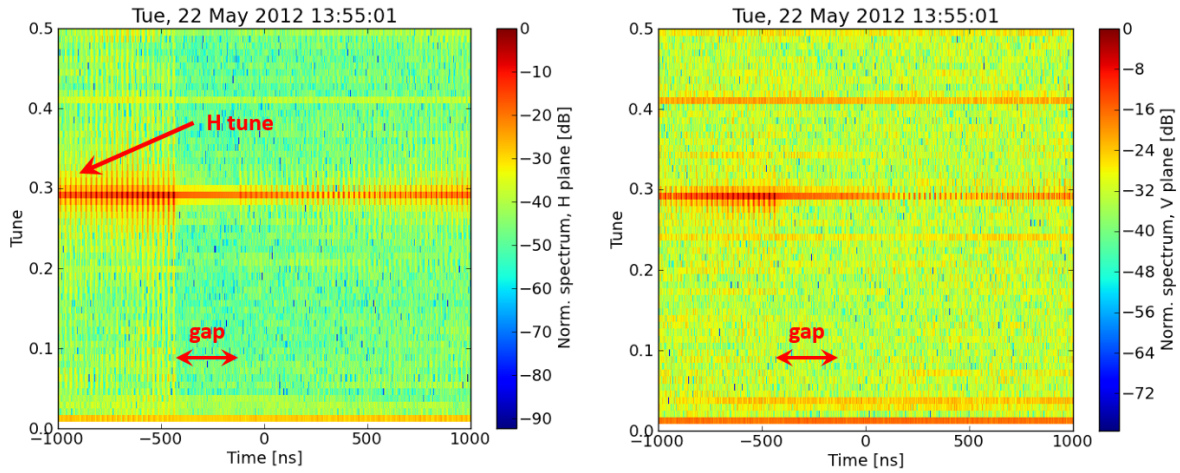

Figure 7.9: Amplitude spectrum of the collected transverse position data (120 turns). The gap of 12 empty RF buckets is highlighted.

Figure 7.8 shows measured and simulated signal, where the simulated signal, obtained with $\delta_{\max} = 1.6$ and $R_0 = 0.5$, was low pass filtered with a corner frequency of 200 MHz. The impressive resemblance between the two suggests that our EC model correctly describes the phenomenon and the rationale applied for the data analysis is promising.

7.3 TRANSVERSE INSTABILITIES

During 2012-13 MD sessions, several bunch by bunch position measurements were acquired on a modified cycle, in which the bunch rotation was removed and replaced by a 30 ms long flat top. In this cycle, the beam could be stored long enough after the adiabatic shortening (h_{RF}=84, V_{RF}=100 kV) to observe the beam become transversely unstable (even for quite low intensities $\sim 6 \times 10^{10}$ ppb).

The oscillation in the horizontal plane was much stronger than in the vertical plane. Actually, the spectral content of the vertical motion was concentrated around the horizontal tune, suggesting that the unstable motion observed also in the vertical plane is due to x-y coupling (see Fig. 7.9).

It could be noticed that the different bunches of the train have different behaviors, as shown in Fig. 7.10 (left). The rise time of the instability is almost the same for the bunches in the second half of the train and then it becomes longer for bunches towards the head. The first 10-15 bunches actually look stable during the 30 ms store. This kind of behavior is consistent with the evolution of the electron density along the train in a typical EC build up.

Moreover, the intra-train pattern revealed a clear coupled motion between bunches, whose mode number appeared to become larger when including bunches close to the train head, as shown in Fig. 7.10 (right). Spectral analysis performed on the same data shows a slightly negative detuning on the unstable bunches and a clear phase relation between the oscillations of the different bunches confirming the coupled bunch nature of the instability (see Fig. 7.11).

All these features look compatible with an EC driven instability, although also other mechanisms (e.g. impedances) might need to be investigated. More information about these studies can be found in [96].

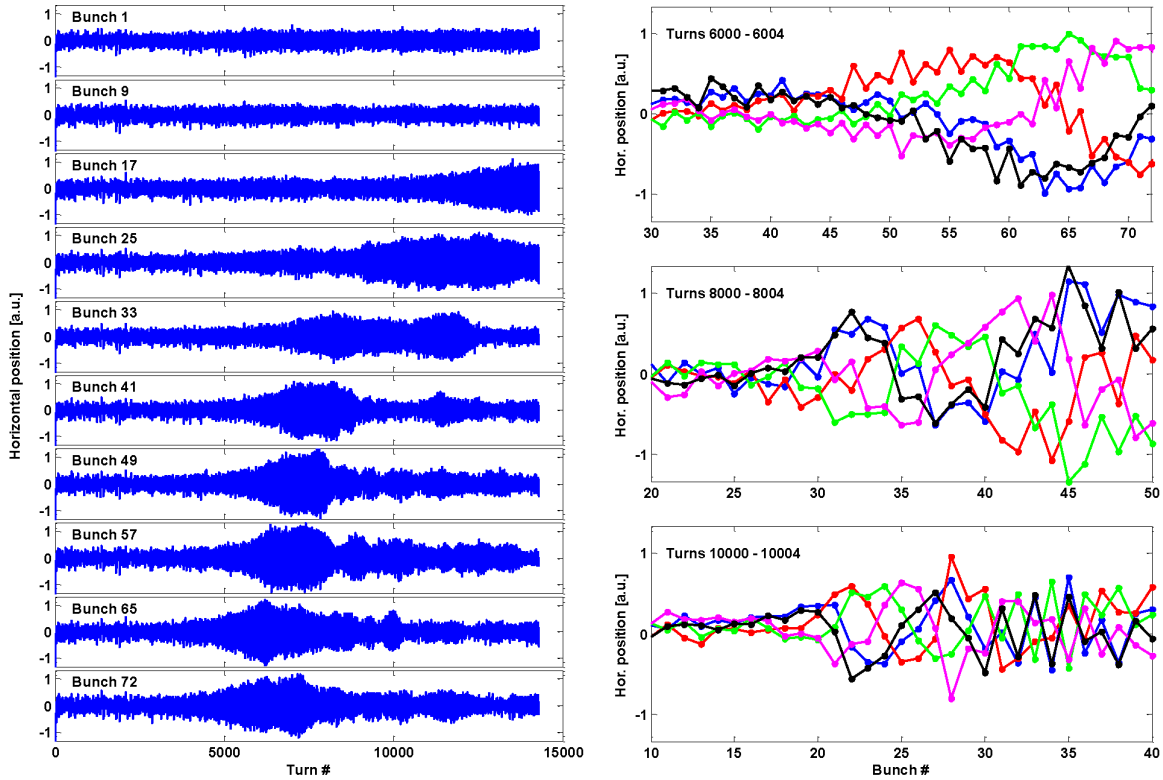

Figure 7.10: Left: Evolution of the horizontal centroid position for selected bunches along the bunch train ($t = 0$ roughly corresponds to the beginning of the bunch shortening). Right: bunch by bunch position for five consecutive turns, at different moments during the store (the horizontal scale is chosen in order to better visualize the unstable bunches).

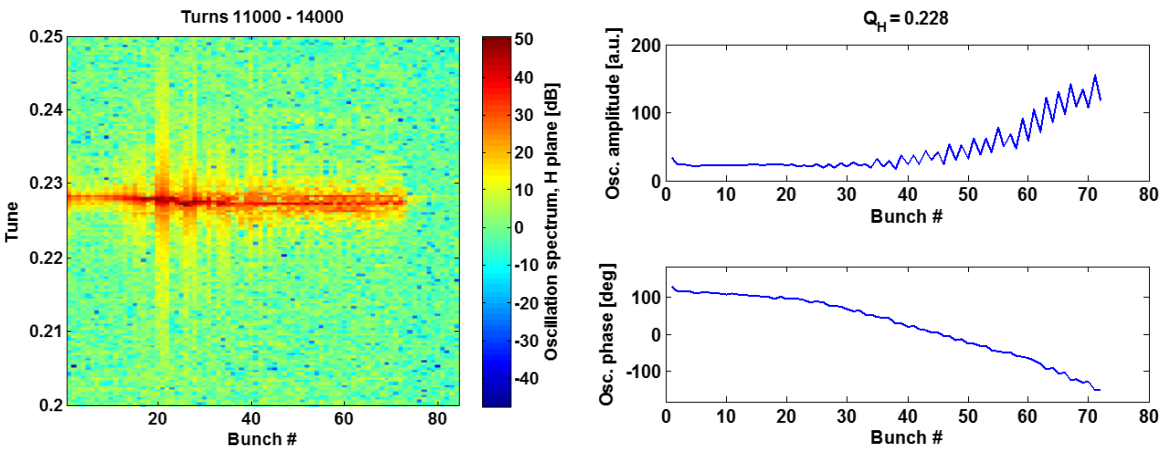

Figure 7.11: Left: Bunch by bunch amplitude spectrum corresponding to the position data in Fig. 7.10. Right: Relative amplitude and phase of the different bunches at the horizontal tune line.

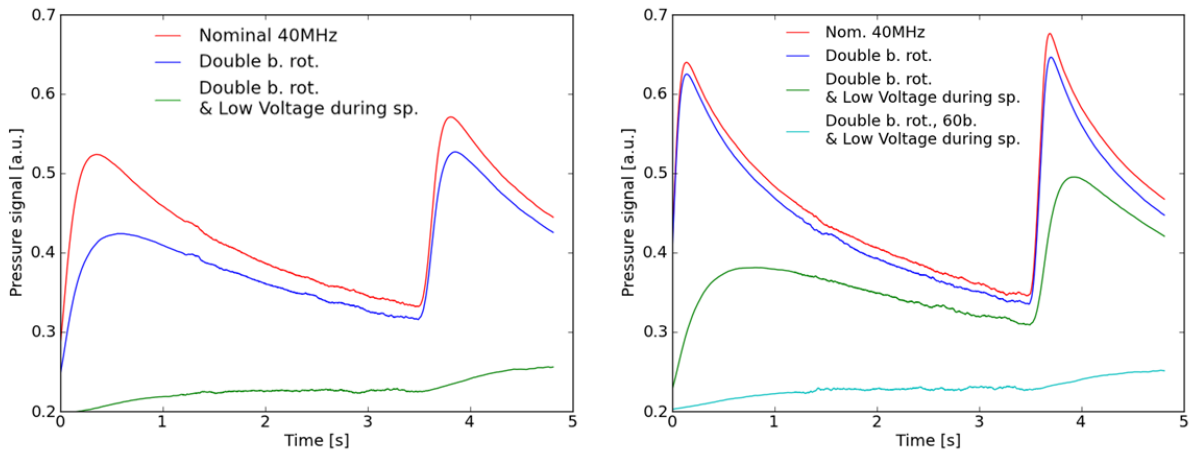

Figure 7.12: Pressure measured with two consecutive LHC type cycles (the beam is extracted at t=0 and t=3.6 s) for different RF manipulations. Comparison between two different bunch intensities: $\sim 1.25 \times 10^{11}$ ppb on the left and $\sim 1.45 \times 10^{11}$ ppb on the right.

In 2012 a new transverse feedback was commissioned in the PS [97], which could be also tested on the instability described before with very encouraging results. Since the feedback cannot be operated in Continuous Wave mode, it could not suppress the instability altogether along the whole 30 ms store. On the other hand, the instability onset could be successfully delayed by about 10 ms, which could provide an important margin when compared to the timescales of the bunch shortening in the nominal cycle.

7.4 LOW EC RF VOLTAGE PROGRAM

Simulations and measurements have shown that the EC build up in the PS is very sensitive to bunch length variations. Therefore, two modifications were introduced in the RF voltage program in order to minimize the interaction of the beam with the EC: 1) the adiabatic bunch shortening was replaced with a bunch pre-rotation [98], which allows to shorten the bunch length from 14 ns to 11 ns in a much shorter time, i.e. ~600 μs; 2) the 40 MHz RF voltage during the bunch splitting was reduced by 10%. Beam profile measurements confirmed that these modifications did not introduce any important degradation of the beam quality at the extraction from the PS.

For the tests the signal from a pressure gauge located in a straight section of the ring was used as a "time integrated" EC indicator. The effects of the modifications on the voltage program on the pressure signal are shown in Fig. 7.12 for a bunch intensity of 1.25×10^{11} ppb (on the left) and 1.45×10^{11} ppb (on the right).

It can be noticed that the strongest reduction of the pressure rise comes from the relatively small reduction of the voltage (and therefore slightly longer bunches) during the splitting, while the introduction of the double bunch rotation has a non negligible effect only for the lower intensity. Moreover the combination of the two strategies gives an almost complete EC suppression for the lower intensity, while a significant pressure rise is still observed for the higher one. In this last case, the EC could be almost completely suppressed only by reducing the number of bunches from 72 to 60, and hence increasing the empty gap in the ring from 300 ns to 600 ns. This is due to the fact that, especially when the bunches are longer

(which implies a longer EC risetime), the "memory effect" between subsequent turns plays an important role in the EC formation. Therefore a smaller number of bunches, and hence an increased gap in the ring, can give an important mitigation for the EC. This means that alternative RF schemes based on batch compression, which are presently considered for the production of higher brightness LHC type beams [85], should also be less critical in terms of EC effects thanks to the reduced number of bunches. More information about these studies can be found in [96].

8

ELECTRON CLOUD STUDIES FOR THE CERN SUPER PROTON SYNCHRONTRON (SPS)

EC effects have been identified as a possible performance limitation for the SPS since LHC type beams were injected into the machine for the first time in the early years of 2000. At that time a severe pressure rise was observed all around the machine together with transverse beam instabilities (which could be suppressed by increasing chromaticity), important losses and emittance blow-up on the trailing bunches of the train. These observations triggered several machine studies in order to understand the performance limitations coming from EC effects and prepare suitable mitigation strategies [29, 30, 38, 82, 99–133].

Since 2002, a scrubbing run with 25 ns beams was carried out almost every year of operation in order to condition (*scrub*) the inner surfaces of the beam pipes and therefore mitigate the EC effect. Thanks to the conditioning achieved with these scrubbing runs, during the 2012 run the SPS could deliver to the LHC beams with 50 ns spacing (bunch intensities up to $1.6 \cdot 10^{11}$ ppb) and with 25 ns spacing (nominal bunch intensity of $\sim 1.2 \cdot 10^{11}$ ppb) without any visible beam degradation coming from EC.

Within the LHC Injectors Upgrade (LIU) project it is necessary to assess up to which extent EC effects could limit the production of the high intensity and high brightness beams foreseen by the upgrade. One of the main open questions is if a mitigation strategy based only on beam induced scrubbing can be sufficiently effective and efficient or a more aggressive (and expensive) solution, i. e. the coating with amorphous carbon of a large part of the SPS beam chambers, needs to be implemented.

These questions have been addressed with both simulation and experimental activities. PyECLOUD simulations have been employed to study how the EC in the different components of the SPS behaves for increasing bunch intensity (see Sec. 8.1). Then the experiments conducted during several MD sessions in 2012 had the two main purposes of assessing the present performance limitations of the SPS with respect to EC effects and of collecting measurements on dedicated EC detectors installed in the ring in order to crosscheck and improve our simulation model (see Secs. 8.2, 8.3, 8.4 and 8.5). Finally, both simulation and experimental studies have been devoted to define and test a beam structure optimized for scrubbing purposes (see Sec. 8.6).

8.1 PYECLOUD SIMULATION STUDIES

The dependence of the EC buildup on the beam intensity has been studied with PyECLOUD simulations for the main dipole magnets and for the beam chambers in the long straight sections of the ring (these components constitute more than 70% of the total length of the accelerator). The main results of these studies are summarized in Figs. 8.1, 8.2, 8.3 and 8.4.

(a) MBA dipole chamber

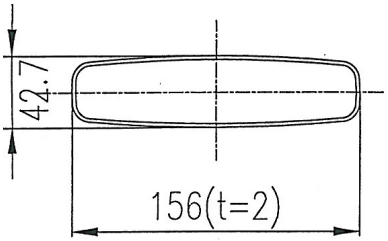

(b) Injection energy (26 GeV)

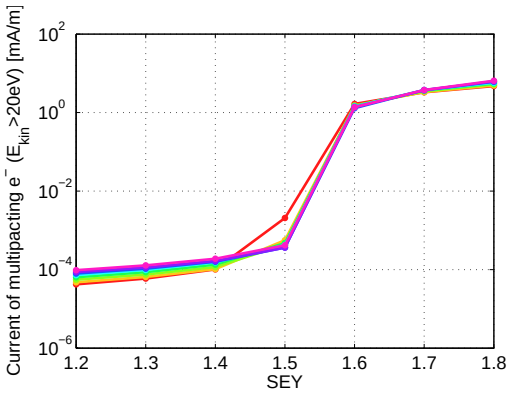

(c) Extraction energy (450 GeV)

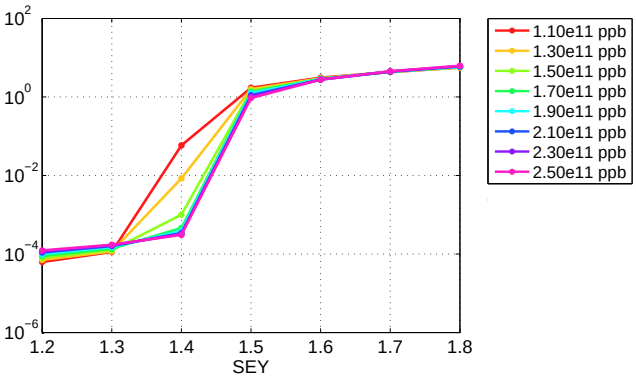

(d) Injection energy (26 GeV)

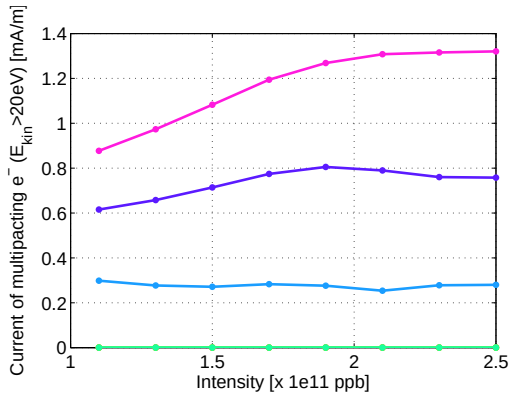

(e) Extraction energy (450 GeV)

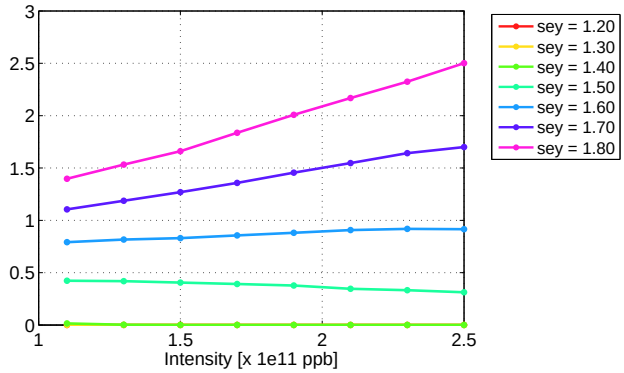

(f) Injection energy (26 GeV) - SEY = 1.6

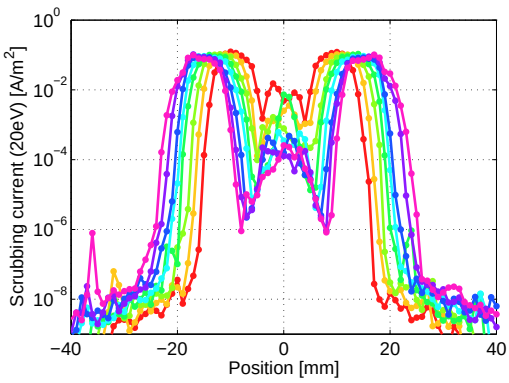

(g) Extraction energy (450 GeV) - SEY = 1.6

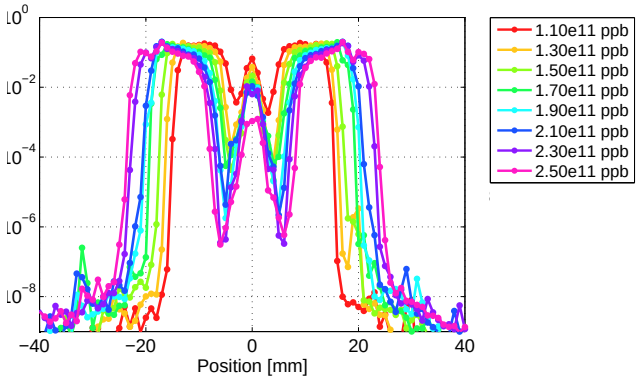

Figure 8.1: Transverse profile of the beam chamber installed in the MBA type magnets of the SPS (a) and results of the corresponding PyECLOUD simulations (b-g) at injection (left) and extraction (right) energy: Current of multipacting electrons as a function of the SEY (b,c), current of multipacting electrons as a function of the bunch intensity (d,e), scrubbing current density for an SEY value slightly larger than the multipacting threshold (f,g).

(a) MBB dipole chamber

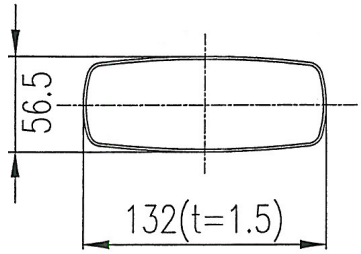

(b) Injection energy (26 GeV)

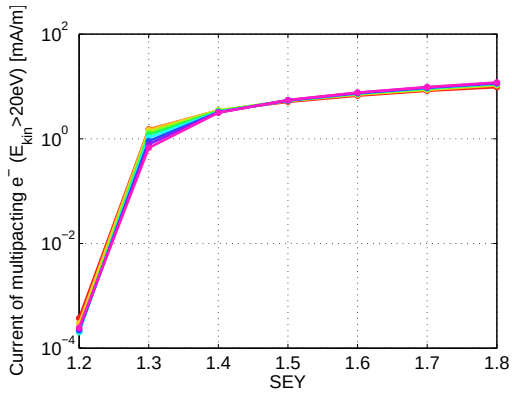

(c) Extraction energy (450 GeV)

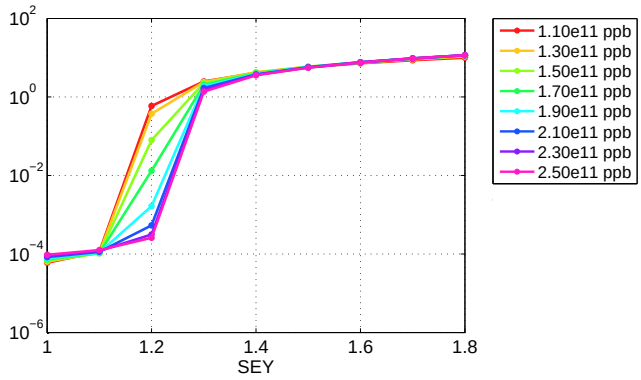

(d) Injection energy (26 GeV)

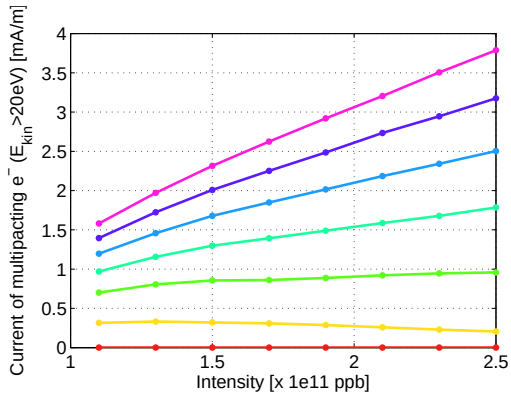

(e) Extraction energy (450 GeV)

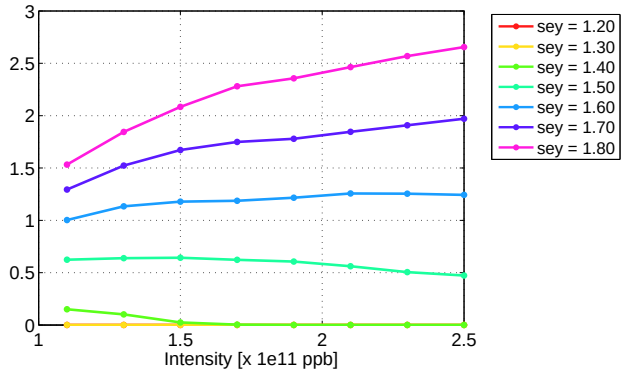

(f) Injection energy (26 GeV) - SEY = 1.3

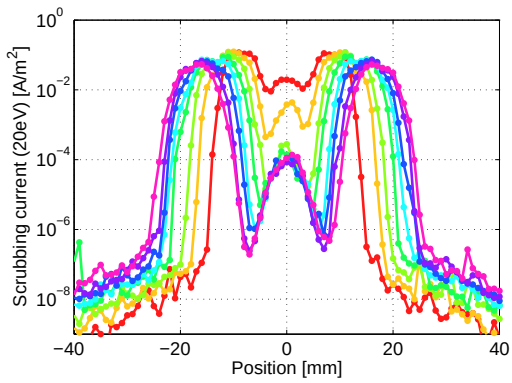

(g) Extraction energy (450 GeV) - SEY = 1.3

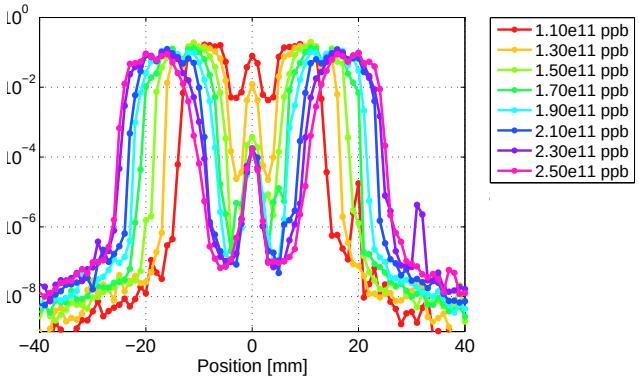

Figure 8.2: Transverse profile of the beam chamber installed in the MBB type magnets of the SPS (a) and results of the corresponding PyECLOUD simulations (b-g) at injection (left) and extraction (right) energy: Current of multipacting electrons as a function of the SEY (b,c), current of multipacting electrons as a function of the bunch intensity (d,e), scrubbing current density for an SEY value slightly larger than the multipacting threshold (f,g).

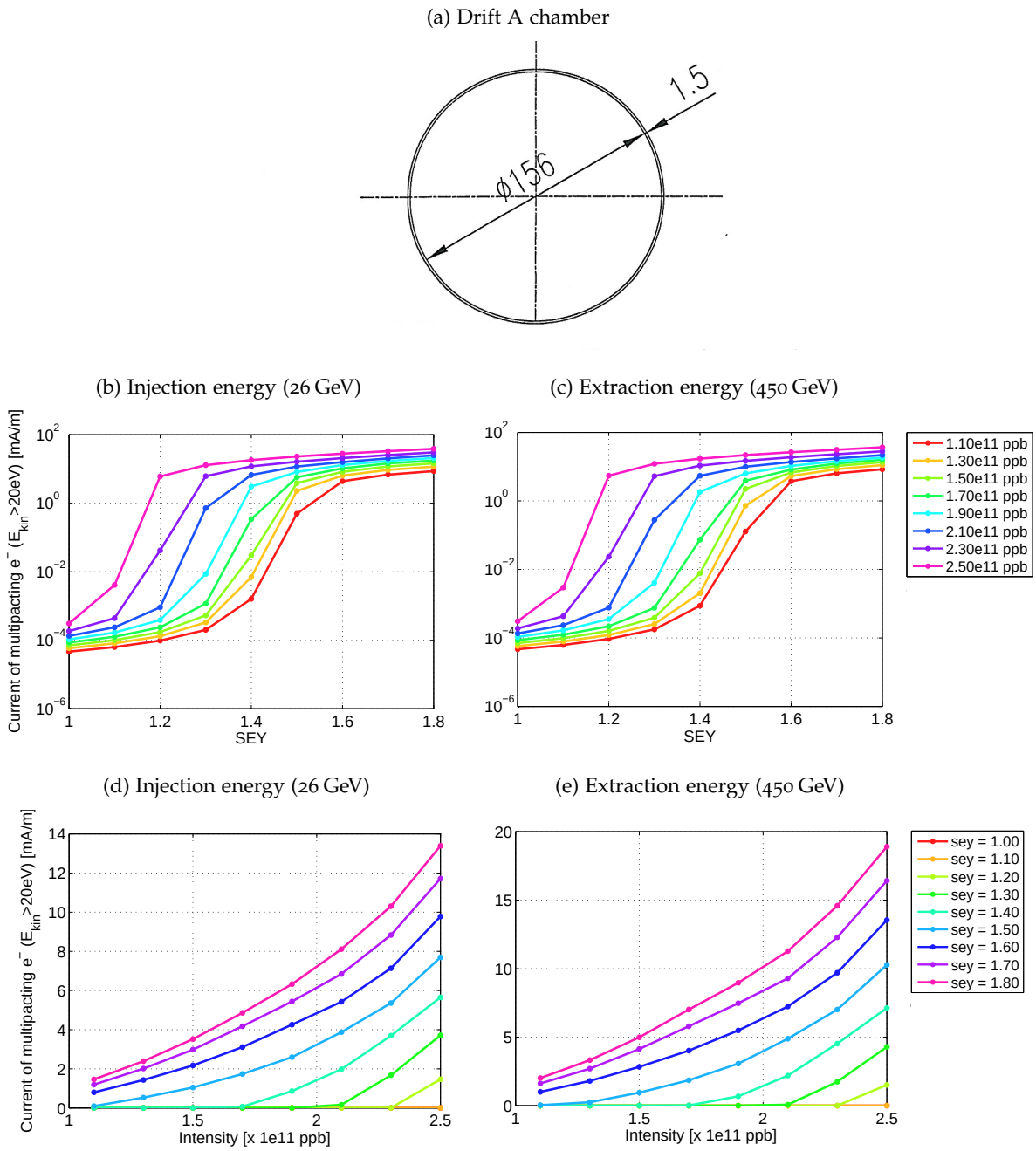

Figure 8.3: Transverse profile of the the driftA type chamber (field free) of the SPS (a) and results of the corresponding PyECLOUD simulations (b-e) at injection (left) and extraction (right) energy: Current of multipacting electrons as a function of the SEY (b,c), current of multipacting electrons as a function of the bunch intensity (d,e).

(a) Drift B chamber

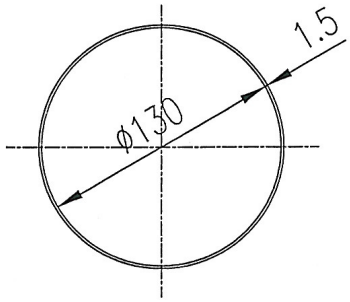

(b) Injection energy (26 GeV)

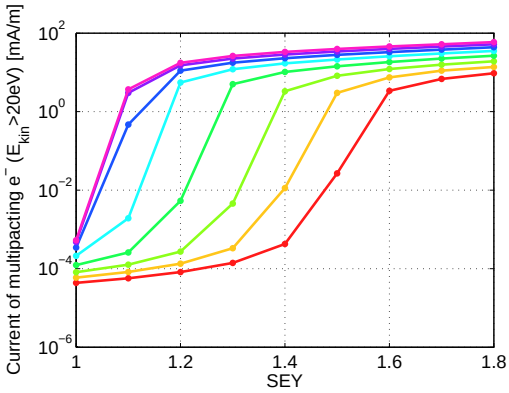

(c) Extraction energy (450 GeV)

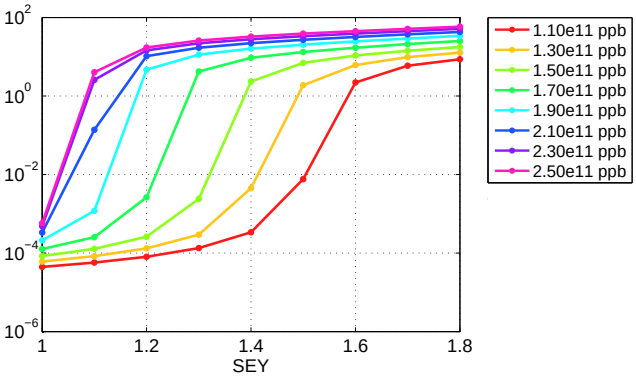

(d) Injection energy (26 GeV)

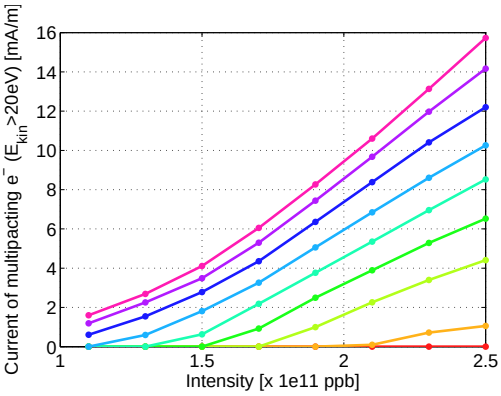

(e) Extraction energy (450 GeV)

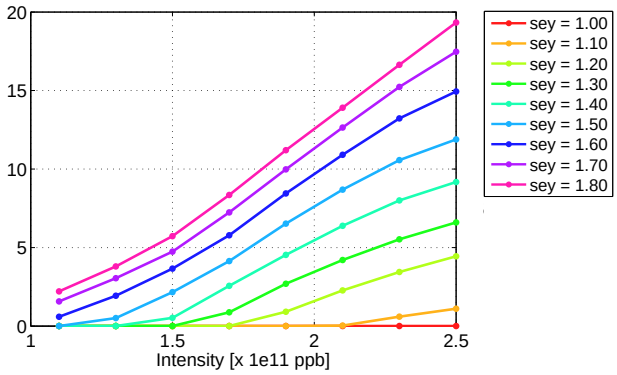

Figure 8.4: Transverse profile of the the driftB type chamber (field free) of the SPS (a) and results of the corresponding PyECLOUD simulations (b-e) at injection (left) and extraction (right) energy: Current of multipacting electrons as a function of the SEY (b,c), current of multipacting electrons as a function of the bunch intensity (d,e).

For all components the EC buildup has been simulated at injection and extraction energies (26 GeV and 450 GeV respectively) for the nominal bunch pattern made of four batches of 72 bunches with 25 ns spacing, with 225 ns gaps between consecutive batches[1]. The bunch length has been set to 2.7 ns and 1.4 ns respectively at injection and at extraction.

Figures 8.1 and 8.2 show the simulation results for the two types of dipole magnets in the SPS, called respectively MBA and MBB. The difference between the two is mainly in the beam chamber's shape (compare Figs. 8.1 (a) and 8.2 (a)) while the provided magnetic field is very similar, i. e. 0.1 T at injection and 2 T at extraction. Comparing Fig. 8.1 (b-c) against 8.2 (b-c) we observe that, for all the considered beam conditions, the MBA shows larger multipacting thresholds compared to the MBB. In both cases the threshold slightly decreases when moving from 26 GeV to 450 GeV, mainly due to the smaller bunch length. For both the devices, the threshold is practically constant in the explored bunch intensity range at 26 GeV and is slightly increasing with the bunch intensity at 450 GeV. The behavior of the electron flux on the walls as a function of the bunch intensity depends on the SEY value of the chamber (see Figs. 8.1 (d-e) and 8.2 (d-e)). For larger SEY values the EC tends to become stronger for larger bunch intensity, while for lower SEY values the flux stays about constant or, in some cases, even slightly decreases when the bunch intensity increases. Finally, from Figs. 8.1 (f-g) and 8.2 (f-g)) we can observe that, like in the case of the LHC dipole magnets (see Sec 4.1), the electron flux tends to cover a wider region of the beam chamber.

Figures 8.3 and 8.4 show the simulation results for the two kinds of circular chambers installed in the SPS straight sections. For both of them the dependence of the EC on the beam energy (and hence on the bunch length) is much weaker than for the dipoles. On the other hand, they feature a much stronger dependence on the bunch intensity. In these cases the multipacting threshold is significantly decreasing for larger bunch intensities (see Figs. 8.3 (b-c) and 8.4) (b-c)) and the electron flux is monotonically increasing as a function of the the bunch intensity for all the simulated SEY values.

8.2 EXPERIMENTAL STUDIES: AN OVERVIEW

In 2012, several machine studies have been devoted to gaining a deeper understanding on the EC effects occurring in the SPS with 25 ns beams. These studies had four main purposes:

1. Qualify the present conditioning state of the SPS ring (especially of the arcs) with respect to EC;
2. Collect experimental data for the validation of EC models and simulation codes;
3. Test possible methods for the enhancement of the scrubbing efficiency;
4. Validate the amorphous carbon coating for the EC mitigation (not covered in this thesis, see [29] for details).

The collected measurements will also be used as a reference to understand the amount of conditioning lost during the long shut-down 2013-2014 (LS1) and how much scrubbing will be needed to recover the achieved performance.

1 PyECLOUD simulations have been also carried out for cases with 50 ns bunch spacing. The corresponding results can be found in [134].

At the beginning of the 2012 run four and a half days of operation (26-30 March) were entirely devoted to specific studies aiming at qualifying the EC around the SPS and collecting direct information on the beam induced scrubbing. Subsequently, these studies have been followed up in several MD sessions during the 2012-13 Run.

Four SPS cycles have been used for these studies, two with the nominal SPS optics ("Q26") and two with the low gamma transition optics ("Q20") [79]. The four cycles in detail are:

- Long flat bottom (FB) cycle ($\sim 21\,s$ at 26 GeV) with nominal optics (Q26);
- Long flat bottom (FB) cycle ($\sim 21\,s$ at 26 GeV) with Q20 optics;
- Standard LHC filling cycle ($\sim 11\,s$ at 26 GeV + ramp to 450 GeV) with nominal optics (Q26);
- Standard LHC filling cycle ($\sim 11\,s$ at 26 GeV + ramp to 450 GeV) with Q20 optics.

Since most of the studies described in the following were conducted with the SPS nominal optics (Q26), in the next sections the Q26 optics will be assumed by default, unless it is differently specified.

During all the EC study sessions, the following equipment was used to constantly monitor EC and beam parameters (as specified in brackets):

- Beam Current Transformer (BCT) (total beam intensity);
- Fast Beam Current Transformer (FBCT) (bunch-by-bunch intensity);
- Mountain Range and RF measurements (longitudinal bunch profiles);
- LHC type BPMs (bunch-by-bunch transverse position);
- High bandwidth pickup (intra-bunch resolved transverse motion);
- Wire scanners (horizontal and vertical emittance);
- Penning gauges (pressure data recorded with 1 Hz sampling rate in fast acquisition mode or stored every three minutes by default);
- Strip detectors, also called Electron Cloud Monitors (ECMs) (EC);
- Shielded pickup EC detectors (EC).

It is worth emphasizing that direct EC measurements (e.g. strip detectors and shielded pick-ups), although being very useful to study the EC build-up under controlled conditions, have to be considered as local measurements, which do not give a direct information on the EC developing in the other sections of the accelerator. The reason is, on one hand, that the chambers in this devices have not undergone the same scrubbing history and, on the other hand, that the EC build up can also be different due to the special geometry of the monitors themselves (to be taken into account also when comparing against calculations or simulations). As a consequence, to characterize the state of the entire machine with respect to the EC, it is necessary to rely on beam quality measurements (looking at effects on the beam parameters which can be related to the EC) and on the pressure measurements around the machine. These are indeed EC indirect observables whose correlation with the EC can be however nontrivial. For example, the measurement of the dynamic pressure rise on the different gauges can be interpreted

as an estimation of the EC activity in the different parts of the machine only if we assume that the pressure rise is mainly caused by beam induced multipacting. Similarly, the typical evolution of the 25 ns beam can be also considered a measure of the integrated EC present in the SPS only if we are in a regime such that the incoherent mechanisms determining the beam lifetime and emittance growth are solely due to EC.

8.3 EXPERIMENTAL STUDIES: BEAM OBSERVATIONS

The main parameters of the 25 ns LHC beams used during the scrubbing and EC studies in 2012 are summarized in Table 8.1. In particular, the PS was able to deliver batches of 72 bunches of the *nominal* LHC beam with around 1.3×10^{11} ppb with tranvserse emittances below 3 μm, up to *ultimate* beam intensity of 1.8×10^{11} ppb with less than 4 μm in both planes. The corresponding intensities and emittance measurements in the SPS will be discussed in more detail in the following.

Table 8.1: Achieved beam parameters during the 2012 run

25 ns "nominal intensity"	SPS injection	SPS extraction
Intensity (ppb)	1.3×10^{11}	1.2×10^{11}
Horizontal emittance ε_x (μm)	~ 2.4	~ 2.6
Vertical emittance ε_y (μm)	~ 2.4	~ 2.6
Number of bunches	288	288
25 ns "ultimate intensity"	**SPS flat bottom (at 8 s)**	**SPS flat top**
Intensity (ppb)	1.8×10^{11}	-
Horizontal emittance ε_x (μm)	~ 5.0	-
Vertical emittance ε_y (μm)	~ 4.5	-
Number of bunches	216	-

8.3.1 Nominal *25 ns LHC beam in the SPS*

The transverse emittance of the nominal LHC beam with 1.25×10^{11} ppb extracted from the PS was preserved in the SPS within the accuracy of the wire scanner measurements. As summarized in Table 8.1, the emittances measured in the SPS were below 3 μm in both planes at the end of the long flat bottom cycle, as well as at the end of the accelerating cycle (at the 450 GeV flat top) with an intensity of around 1.2×10^{11} ppb. All beam quality measurements discussed in this section were performed using the nominal SPS optics for LHC beams (Q26) in order to allow for direct comparison with previous results. Detailed studies with the new low gamma transition optics (Q20) were subject of separate MD studies.

Before discussing in more detail the results of beam quality measurements in the 2012 experiments, it is worth recalling briefly previous beam observations and measurements per-

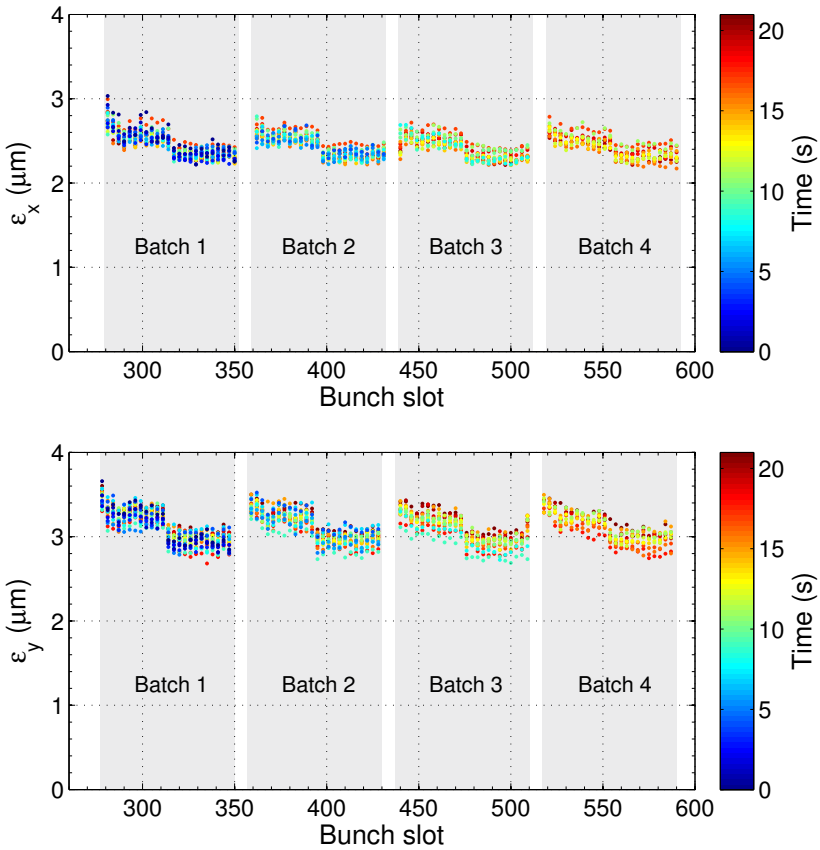

Figure 8.5: Bunch-by-bunch emittance measurements in the horizontal (top) and the vertical plane (bottom) on the SPS long flat bottom cycle, measured with BWS.416(H) and BWS.519(V) respectively. Each point corresponds to an average of 3 measurements of an individual bunch at a given time in the cycle as indicated by the color-code.

formed in early experiments with 25 ns beam in the SPS. Back in the years 1999-2003 EC effects strongly affected the beam quality and the achievable beam brightness, as observed in the form of emittance growth along the batch in both planes (up to a factor four emittance growth), losses affecting the tail of the batch and a positive detuning along the bunch train ($\Delta Q \approx 0.02$). At that time strong instabilities were observed in both planes, which were partially cured by running with high chromaticity ($\xi_x, \xi_y > 0.5$). Detailed summaries of these observations can be found in [101] and [82].

During the 2012 scrubbing run, a new (optional) operation mode of gated bunch-by-bunch emittance measurements of the SPS wire scanners BWS.519 and BWS.416 was successfully setup and tested. This allowed for a detailed qualification of the 25 ns LHC beam in the SPS in later MD sessions. Figure 8.5 shows the result of bunch-by-bunch emittance measurements along the long flat bottom where the color-code indicates the acquisition time in the cycle. Since the total number of acquisitions per measurement is limited by the memory of the wire-scanner front-end to about 120 bunches, a sample of every third bunch was recorded. Note that all four batches in the SPS exhibit very similar behaviour of the emittance evolution along the bunch train. It is worth pointing out that the measured emittances in the first half of each batch in the SPS are slightly larger compared to the second half. This structure can only be explained by differences of the beam characteristics already at or due to their injection into

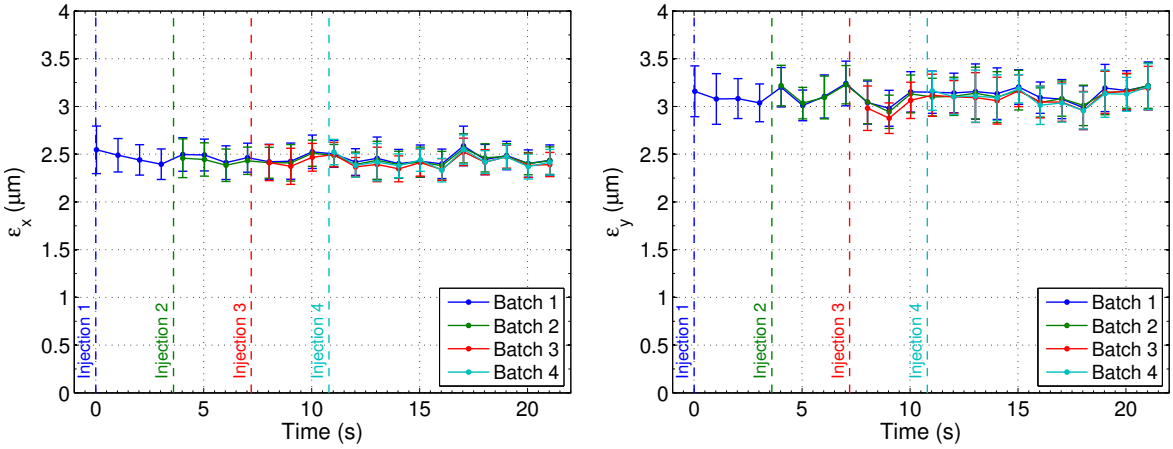

Figure 8.6: Bunch-by-bunch emittance measurements in the horizontal (left) and the vertical plane (right) plotted as average per batch versus time along the SPS long flat bottom cycle. The error bars indicate the r.m.s. spread within the batch over three measurements.

the PS[2]. Indeed it is found that these bunches with smaller transverse emittance exhibit also smaller intensity. This confirms the capability of resolving bunch-by-bunch emittance variations using the SPS wire scanners on the one hand, and on the other hand demonstrates that in 2012 the 25 ns LHC beam does not suffer from electron cloud effects at nominal intensity (1.15×10^{11} ppb) in the SPS. At the same time no significant emittance growth is observed on the 20 s long flat bottom. Figure 8.6 shows the evolution of the average transverse emittances per batch as function of time along the cycle using the same data set as above. The error bars correspond to the spread of measured emittances within the corresponding batch as determined from the bunch-by-bunch measurement and does not include any systematic errors. Within these error bars, the transverse beam size is conserved on the long flat bottom. It is interesting to note that the obtained average emittances of the four batches seem strongly correlated. This can be explained by systematic effects on the background noise which affects the bunch-by-bunch emittance measurement of all four batches in the same way. The relatively large noise level in the bunch-by-bunch mode is presently one of the main limitations of this new acquisition mode of the SPS wire scanners.

As mentioned already, experiments in the years 1999-2000 clearly showed a positive tune-shift along the bunch train in both planes, which was ascribed to the interaction of the beam with the electron cloud. Similar measurements have been performed in 2012, using the bunch-by-bunch turn-by-turn capability of the LHC-BPM in the SPS. Figure 8.7 shows the vertical betatron tunes for the 288 bunches of the four batches as determined by a refined Fourier analysis of 150 turns. In order to minimize decoherence, the vertical chromaticity was adjusted to small positive values ($\xi_y \approx 0.05$) and the gain of the vertical damper was significantly reduced before exciting the beam with the tune-kicker. Compared to the observations in past experiments, the tune-shift found in the 2012 measurements is about a factor five smaller and

2 The 72 bunches of each SPS batch are produced by multiple longitudinal splitting of six bunches in the PS [135]. These six bunches are extracted from two consecutive PSB cycles, which deliver single bunches from four and two booster rings respectively. Thus, the first $4 \times 12 = 48$ bunches of each SPS batch are treated equally on the PS flat bottom and any difference in their emittance (and intensity) could be attributed to intensity differences between the PSB rings.

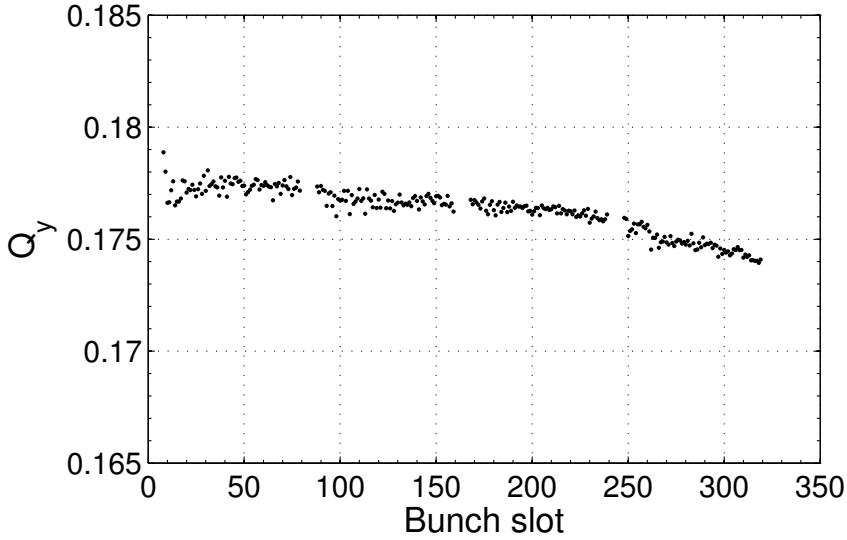

Figure 8.7: Vertical betatron tune for each of the 288 bunches of the four batches as determined from the Fourier analysis of 150 turns from bunch-by-bunch turn-by-turn data from the LHC-BPM in the SPS.

more importantly is negative along the bunch train. This negative tune-shift is probably due to the resistive wall impedance of the SPS and cannot be related to electron cloud effects.

A large positive vertical chromaticity ($\xi_y > 0.5$) was needed in the past in order to avoid fast instabilities in the vertical plane when one or more batches of 25 ns beams were injected into the SPS. A scan of the vertical chromaticity was performed in 2012 in order to see if this fast instability can still be observed. Figure 8.8 shows the total intensity along the cycle for different settings of vertical chromaticity for 288 bunches of around 1.2×10^{11} ppb. Incoherent effects for large chromaticity significantly reduce the beam life-time. The best life-time is obtained for $0.1 \leq \xi_y \leq 0.3$. For these settings no coherent instabilities were observed, thus confirming again that the nominal LHC beam is presently not suffering from electron cloud effects on the long flat bottom (for 20 s) at 26 GeV. Instabilities observed for lower chromaticity settings could be related to EC effects or simply to the machine impedance and thus further experimental studies are needed.

8.3.2 Ultimate *25 ns LHC beam in the SPS - on the flat bottom*

The 25 ns beam with *ultimate* intensity (around 1.8×10^{11} ppb) was injected on the long flat bottom cycle only for a few hours during the 2012 scrubbing run due to limitations coming from the heating of the non-serigraphed MKE kicker and the strong dynamic pressure rise (vacuum spikes). Although the bunch-by-bunch mode of wirescanners could not be used, a few emittance measurements with the usual acquisition mode were performed close to injection and at around 8 s in the cycle with 2 batches. In both cases the emittance measured in the SPS was between 4.5 μm and 5 μm, while the PS measurements at flat top (before bunch rotation) gave emittances between 3.5 μm and 4 μm. Further studies using the bunch-by-bunch capability of the wirescanners and 4 batches in the SPS are needed for understanding if EC effects are presently a limitation for 25 ns beams with the *ultimate* beam intensity in the SPS.

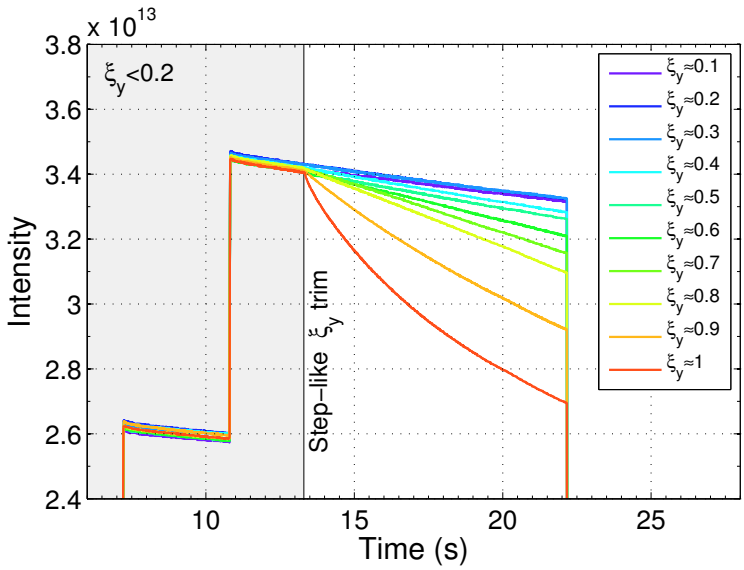

Figure 8.8: Total intensity along the cycle when changing the vertical chromaticity at around 13 s in the cycle from $\xi_y < 0.2$ to the values indicated by the color code.

In addition, it was not attempted to accelerate this high intensity beam during the scrubbing run due to power limitations of the RF system presently installed in the SPS [136].

8.3.3 *Test with large bunch intensity and Q20 optics*

In the second half of 2012, a series of machine studies were devoted to 25 ns beams with the Q20 optics. Rather than performing a direct comparison with the previously discussed measurements in the Q26 optics, the focus was put on increasing the beam intensity and on acceleration to 450 GeV/c. The aim was to identify performance limitations and the achievable beam parameters at extraction to the LHC in the present conditioning state of the SPS. Therefore the studies concerned two main aspects. Firstly, optimization of the RF settings for achieving longitudinal beam stability up to flat top. Secondly, careful monitoring of the transverse emittances using the wirescanners in bunch-by-bunch mode in order to identify possible beam degradation due to coherent and incoherent EC or any other intensity effects. As expected from the measurements with the Q26 optics, no indication for emittance blow-up or beam instabilities was observed for four batches of the 25 ns beam with nominal intensity ($\approx 1.20 \times 10^{11}$ p/b at injection) in the Q20 optics and typical chromaticity settings, despite the dynamic pressure rise usually observed in the presence of LHC beams with 25 ns bunch spacing (on the order of a few 10^{-8} mbar). Even for slightly higher intensity, i.e. $\approx 1.30 \times 10^{11}$ p/b at injection, no beam degradation due to EC effects could be observed when measuring the bunch-by-bunch emittance of the four batches of 72 bunches after ramping to top energy as shown in Fig. 8.9 (left). However, when increasing the intensity of the injected beam to about $\approx 1.40 \times 10^{11}$ p/b, emittance blow-up of the trailing bunches of the fourth and sometimes also of the third batch could be observed at flat top, as shown in Fig. 8.9 (right). Emittance measurements at the end of the flat bottom showed that this blow-up happens already at

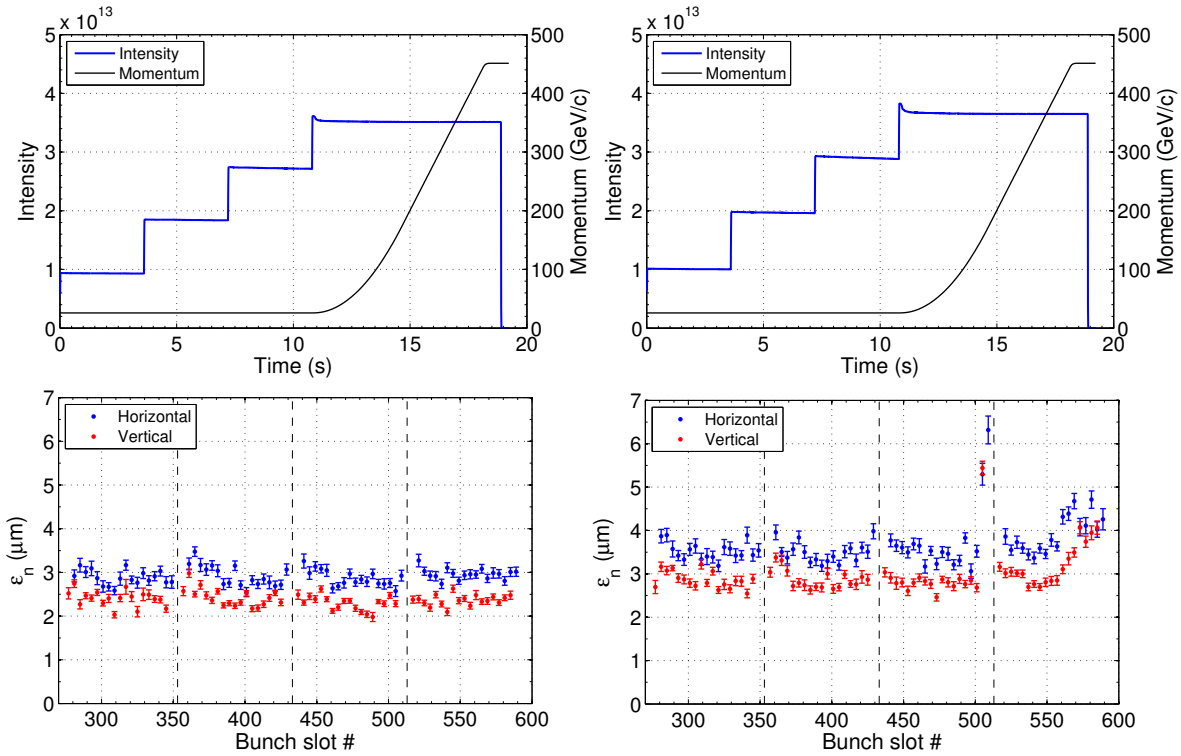

Figure 8.9: Typical example for the total beam intensity along the cycle for the 25 ns beam with four batches of 72 bunches (top) and the corresponding bunch-by-bunch transverse emittances measured at flat top (bottom) in the Q20 optics using the wirescanners BWS.416H and BWS.519V. The error bars are deduced from the fit parameter uncertainty. The plots show measurements for two different intensities corresponding to $\approx 1.30 \times 10^{11}$ p/b (left) and $\approx 1.40 \times 10^{11}$ p/b (right) at injection.

injection energy[3]. This blow-up is probably caused by a fast instability right after injection, since in some cases losses for the corresponding bunches could be observed on the Fast Beam Current Transformer (FBCT). It was tried to stabilize the beam by increasing the chromaticity and increasing the gain of the transverse feedback. However during the available machine study sessions in 2012, stable beam conditions for an intensity of $\approx 1.40 \times 10^{11}$ p/b or higher were not achieved. Further studies and optimization would be needed to see if the observed instability can be cured by optimizing the chromaticity and the transverse damper settings. Although it cannot be concluded from any direct measurement, the observations of the losses and emittance blow-up of trailing bunches of the train in combination with the dynamic pressure rise always observed with the 25 ns beam are strong indications for EC effects.

The spatial EC distribution was measured in the presence of a dipole field using dedicated Electron cloud strip detectors with vacuum chambers reproducing those of the two types of SPS dipole chambers (see Sec. 8.5.2). Consistently with numerical simulations (see Sec. 8.1), it was observed that the electrons are concentrated in the center for low bunch intensities, while for increasing intensity the region covered by the EC gets wider with most of the electrons located in two outer stripes. It should be emphasized that the SPS vacuum chambers were

3 These measurements were performed on a modified magnetic cycle with a 300 ms longer flat bottom during another machine development session.

never conditioned with 25 ns beams with high bunch intensities in the past, and thus these outer regions exhibit probably a higher SEY. Therefore, an improvement of the beam quality and reduction of the pressure rise might be obtained gradually after operating the machine extensively with these beam conditions, as for example during a scrubbing run.

In future machine development sessions and scrubbing runs (2014-2015), it will be studied whether these issues can be mitigated by machine conditioning. If not, the LIU project aims at coating the SPS vacuum chambers with a thin film of amorphous Carbon, which provides an SEY close to unity and therefore suppresses the EC.

8.4 EXPERIMENTAL STUDIES: VACUUM OBSERVATIONS

Apart from the coherent and incoherent effects on the beam, the dynamic pressure rise is the only other observable which can be used to qualify the present state of conditioning of the SPS ring. When the nominal 25 ns LHC beam is injected into the SPS, an evident pressure rise is observed on most of the gauges in the ring. In order to study this phenomenon during the scrubbing run, the pressure readings of all Penning gauges available in the accelerator were stored with a sampling rate of 1 Hz instead of the usual logging interval of one minute.

In this section we will often focus on the following selected pressure gauges:

- gauges 12940, 22940, 32940, 42940, 52940, and 62940, i.e. one in each arc located at equivalent positions between two MBB type magnets;
- gauge 51460, which has been employed for the experiment on the aC coated drift tube (see [29]);
- gauge 51780, which shows the highest pressure rise in the ring with 25 ns beam;
- gauge 51824, which is the nearest to the strip detectors (see section 8.5.2).

Figure 8.10 shows the typical behavior of the pressure on these gauges during the long flat bottom cycle with 25 ns beam. The pressure grows during the injection phase and tends to level off when the total intensity remains constant. When the beam is dumped or extracted, the pressure decreases with a time constant of a few seconds.

Figure 8.11 shows the pressure rise (defined as the difference between the maximum and the minimum pressure recorded during the cycle) on all gauges along the ring for the same cycle. The pressure rise in the six arcs are the same order of magnitude ($\sim 10^{-8}$ mbar), while those observed near Point 5 peak to much higher values ($\sim 10^{-6}$ mbar).

8.4.1 *Effect of the beam intensity*

Figure 8.12 shows the pressure rise at some selected gauges as a function of the number of injected batches. The point at zero intensity corresponds to the pressure recorded right before the first injection. The other points show the maximum pressure measured along the long FB cycle for different number of injections (batches made of 72 bunches with the nominal 225 ns gaps between them). The measurement has been performed both with the Q26 and the Q20 optics and no significant difference has been observed. In particular, for both optics almost no pressure increase is observed when a single batch is injected, while for more than one batch in the machine the pressure rise increases almost linearly with the total intensity.

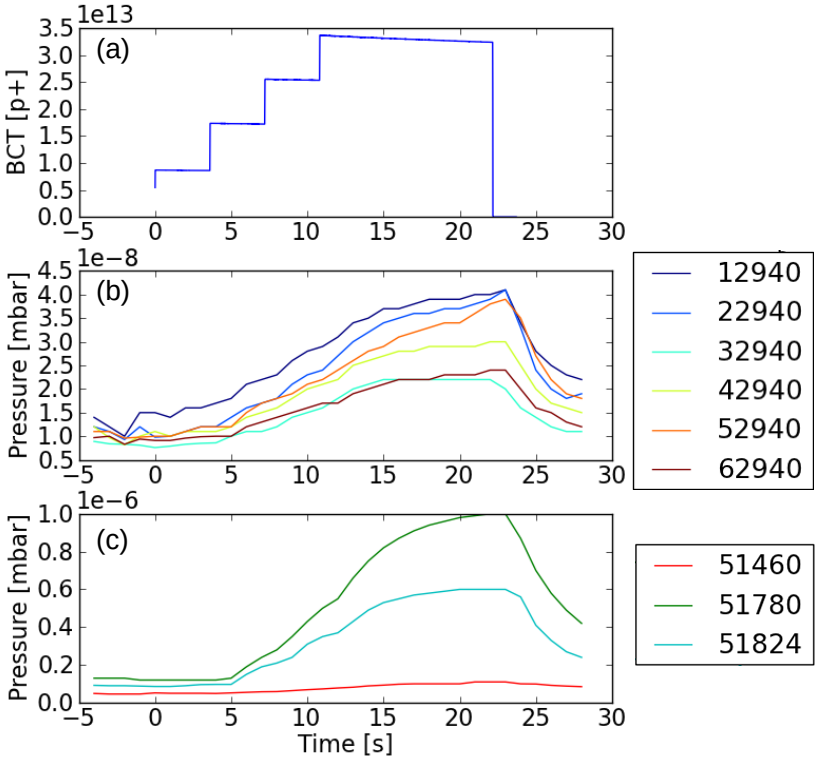

Figure 8.10: Beam intensity and pressure evolution on selected gauges when the nominal 25 ns beam is injected into the SPS: (a) total beam intensity; (b) pressure gauges in the arcs, (c) pressure gauges close to Point 5.

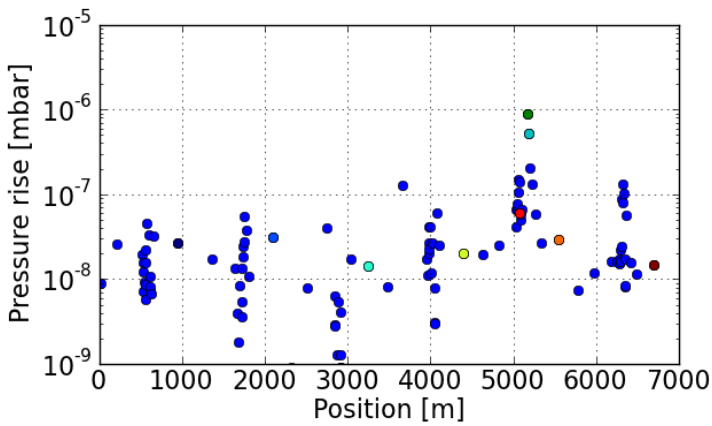

Figure 8.11: Typical pressure rise profile observed on all gauges along the ring with nominal 25 ns beam (four batches) at 26 GeV.

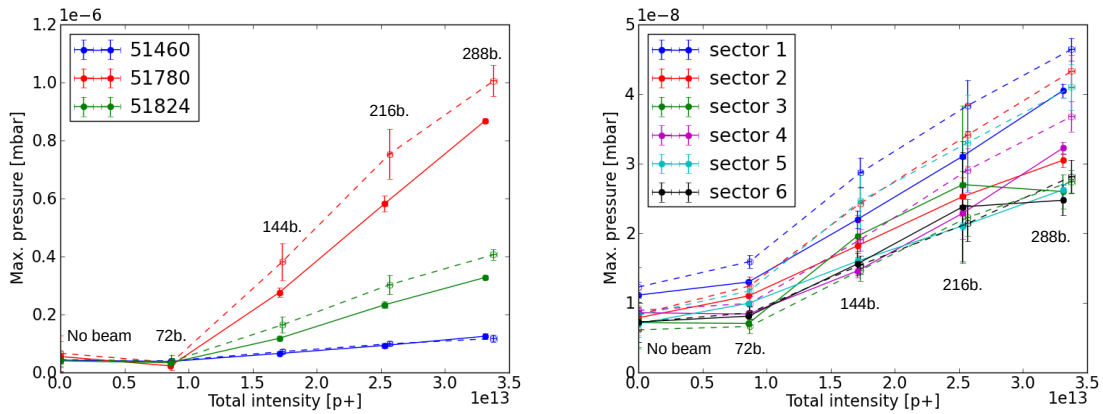

Figure 8.12: Pressure at gauges near Point 5 (on the left) and in the arcs (on the right) for 1 to 4 batches of 72× 25 ns spaced bunches with nominal bunch intensity. Comparison between nominal optics (dashed lines) and Q20 (continuous lines).

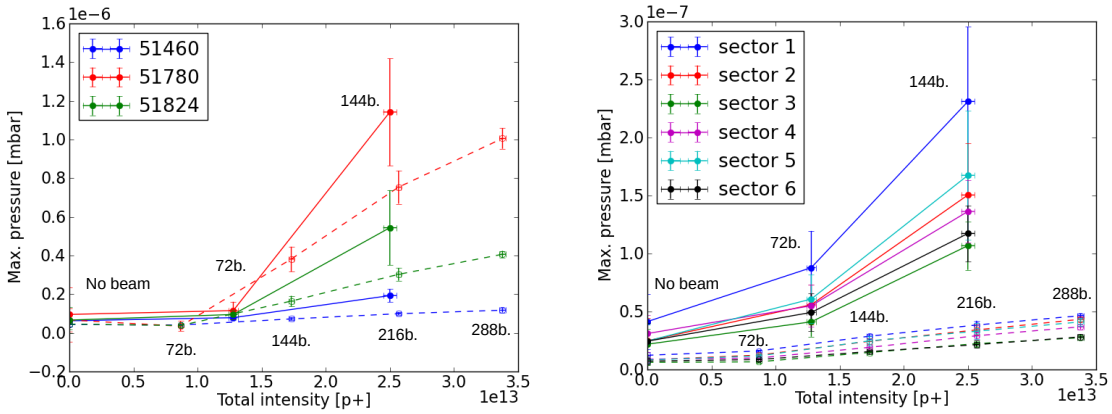

Figure 8.13: Pressure at gauges near Point 5 (on the left) and in the arcs (on the right) for different number of batches of 72× 25 ns spaced bunches with nominal (dashed lines) and ultimate (continuous lines) bunch intensity.

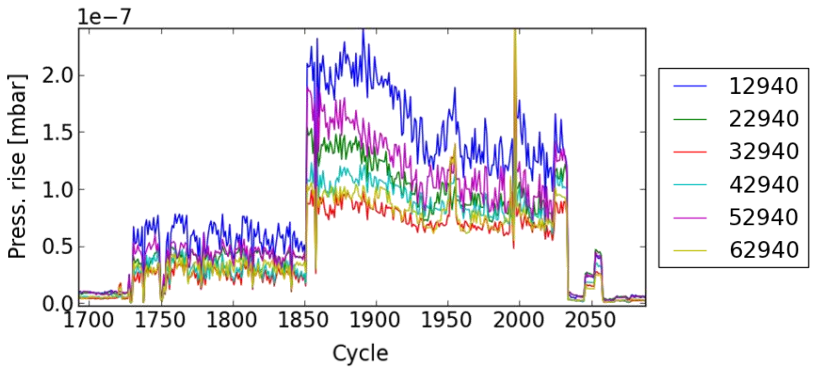

Figure 8.14: Pressure rise evolution with ultimate intensity 25 ns beam (one batch injected for cycles from 1730 to 1850, two batches from 1850 to 2040). Indications of conditioning can be observed.

In Fig. 8.13 we plot the dependence of the pressure on the number of injected batches for the 25 ns beam with ultimate intensity ($1.8 \cdot 10^{11}$ppb). In this case the pressure rise on the gauges near Point 5 is about 50% higher compared to what is observed with nominal intensity. A much larger increase (by up to one order of magnitude) is observed on the gauges in the arcs, while the difference is much smaller in the gauges close to Point 5.

A possible explanation for these observations can be the following. Around Point 5 there is a lot of equipment used for machine studies (e.g. crystal collimation, beam beam long range compensator wire, electron cloud diagnostics). The observed strong pressure rise suggests that a significant EC is already present in this region with nominal beam intensity due to the lack of accumulated conditioning (components freshly installed or frequently vented for interventions) and due to the presence of materials with high Secondary Emission Yield like aluminum. On the other hand, the arcs show a much lower pressure activity with 25 ns beam with nominal intensity, consistently with the significant amount of scrubbing which was accumulated over the last years (e.g. during scrubbing runs in 2002, 2003, 2004, 2006, 2007 and 2008).

The pressure rise observed in the arcs is extremely small (by a factor 10^4) below the value observed in the SPS in the early 2000, when the LHC type beams were injected in the SPS for the first time. These observations confirm that the noticeable improvements in beam quality observed over the years (see Sec. 8.3) is a consequence of the the mitigation of the EC achieved by the scrubbing run policy adopted over the previous years.

The observations with the *ultimate* intensity 25 ns beam do not contradict this picture since when the 25 ns beam with $1.8 \cdot 10^{11}$ppb is injected in the SPS, the EC in the bending magnets covers a region of the horizontal aperture that is wider than the region conditioned by the nominal intensity beam (see also Sec. 8.5.2). This allows for the formation of a strong EC in the unconditioned part of the chamber inner surfaces, which may be the origin of the strong pressure rise. This explanation is also consistent with the conditioning of the dynamic pressure rise observed during the 25 ns ultimate intensity run (see Fig. 8.14).

8.4.2 *Effect of losses*

The analysis of the pressure data stored during the scrubbing run has also shown a significant correlation between the pressure rise in the arcs and slow beam losses. In Figs. 8.15 and 8.16 we display two cases in which losses are much stronger than in a typical cycle. An important pressure rise is observed when the losses are larger. In Fig. 8.15 the losses occur when lowering the RF voltage, while in Fig. 8.16 they are due to a transverse instability triggered with low chromaticity. Such pressure rise is likely to be directly related to vacuum desorption from particle losses rather than to the EC. The correlation between losses and the pressure behavior is another indication that the SPS arcs are in a good conditioning state with respect to the EC for the nominal bunch intensity. On the other hand, the vacuum observations on the gauges near Point 5 seem to confirm that the pressure rise in that region is dominated by the EC, since in this region the pressure decreases as soon as losses start (see Figs. 8.15(c) and 8.16(c)). This can be understood as related to the reduced EC activity caused by beam degradation and loss.

Observations on the cycle with the ramp from 26 GeV to 450 GeV seem consistent with the explanation given before. In these cases (see Fig. 8.17) the losses are strongly reduced during the ramp (after the initial capture losses) with a consequent reduction of the pressure rise in

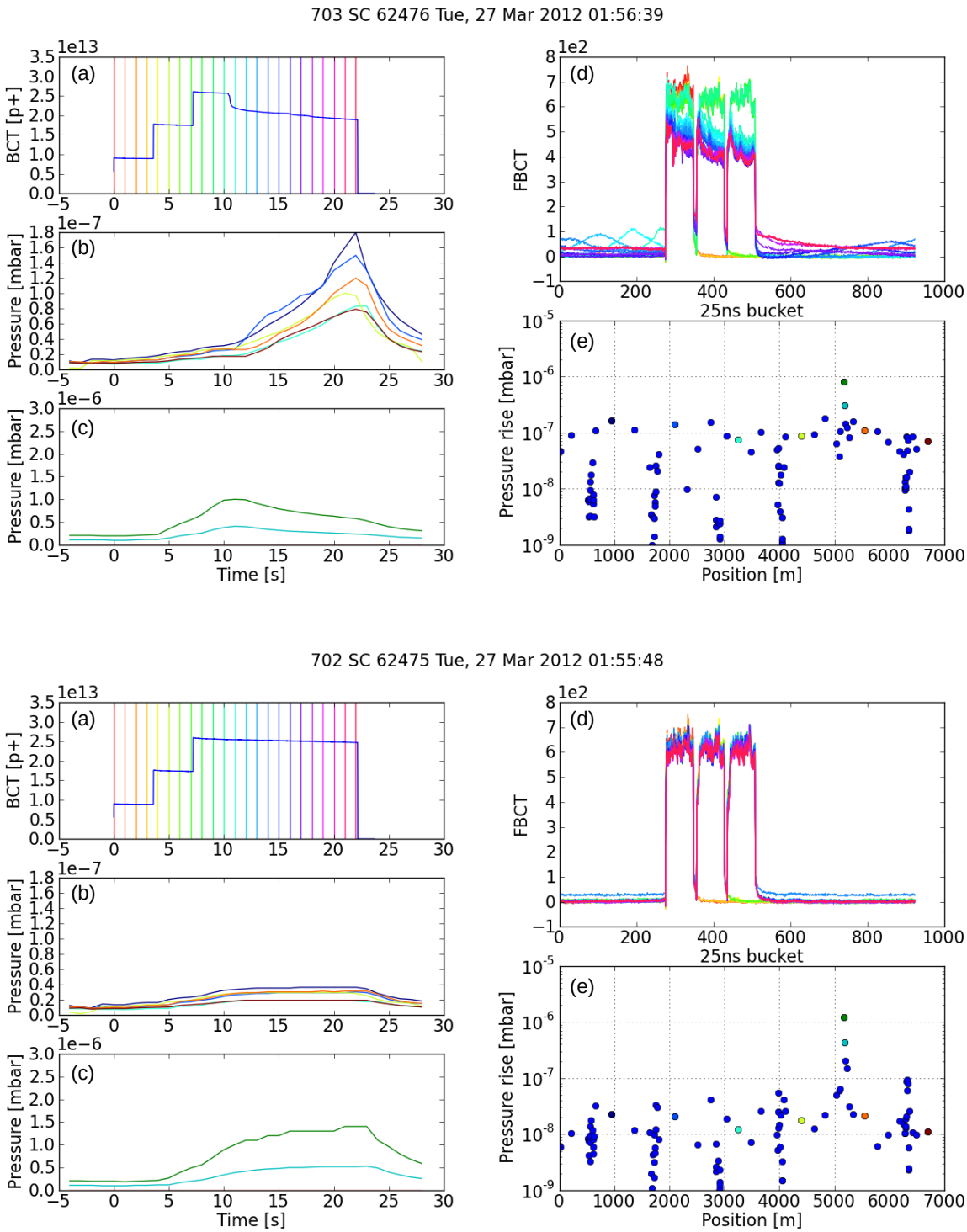

Figure 8.15: Pressure behavior during a cycle with 200 MHz voltage reduced 11 s after the first injection (top). A cycle with nominal RF program is shown for comparison (bottom). In the subplots: (a) total beam intensity; (b) pressure evolution in the arcs; (c) pressure evolution near Point 5; (d) bunch intensity (one trace per second corresponding to the vertical lines in (a), not calibrated); (e) pressure rise along the ring.

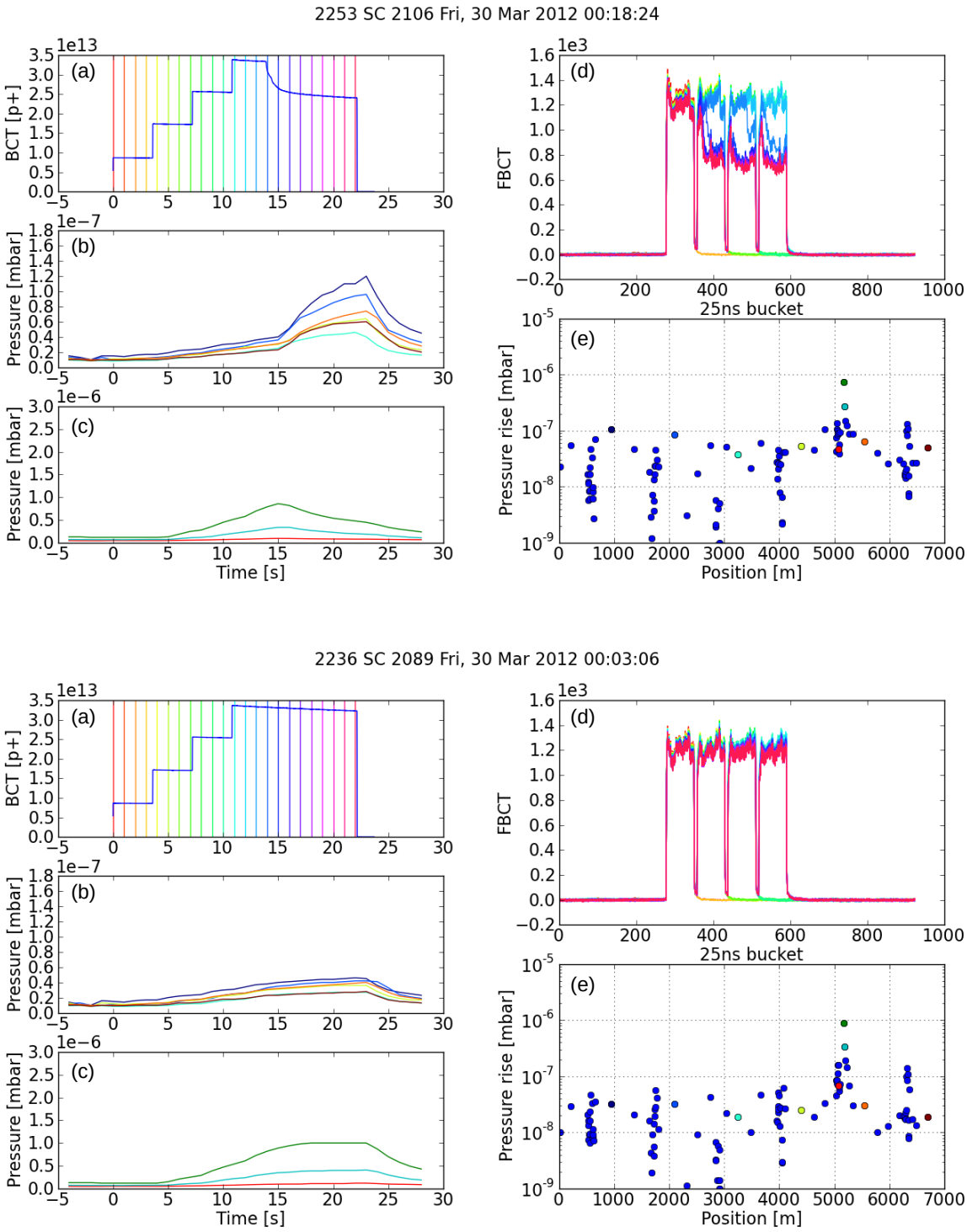

Figure 8.16: Pressure behavior during a cycle when the beam becomes unstable 14s after the first injection, due to the reduction of vertical chromaticity (top). A cycle with nominal chromaticity program is shown for comparison (bottom). In the subplots: (a) total beam intensity; (b) pressure evolution in the arcs; (c) pressure evolution near Point 5; (d) bunch intensity (one trace per second corresponding to the vertical lines in (a), not calibrated); (e) pressure rise along the ring.

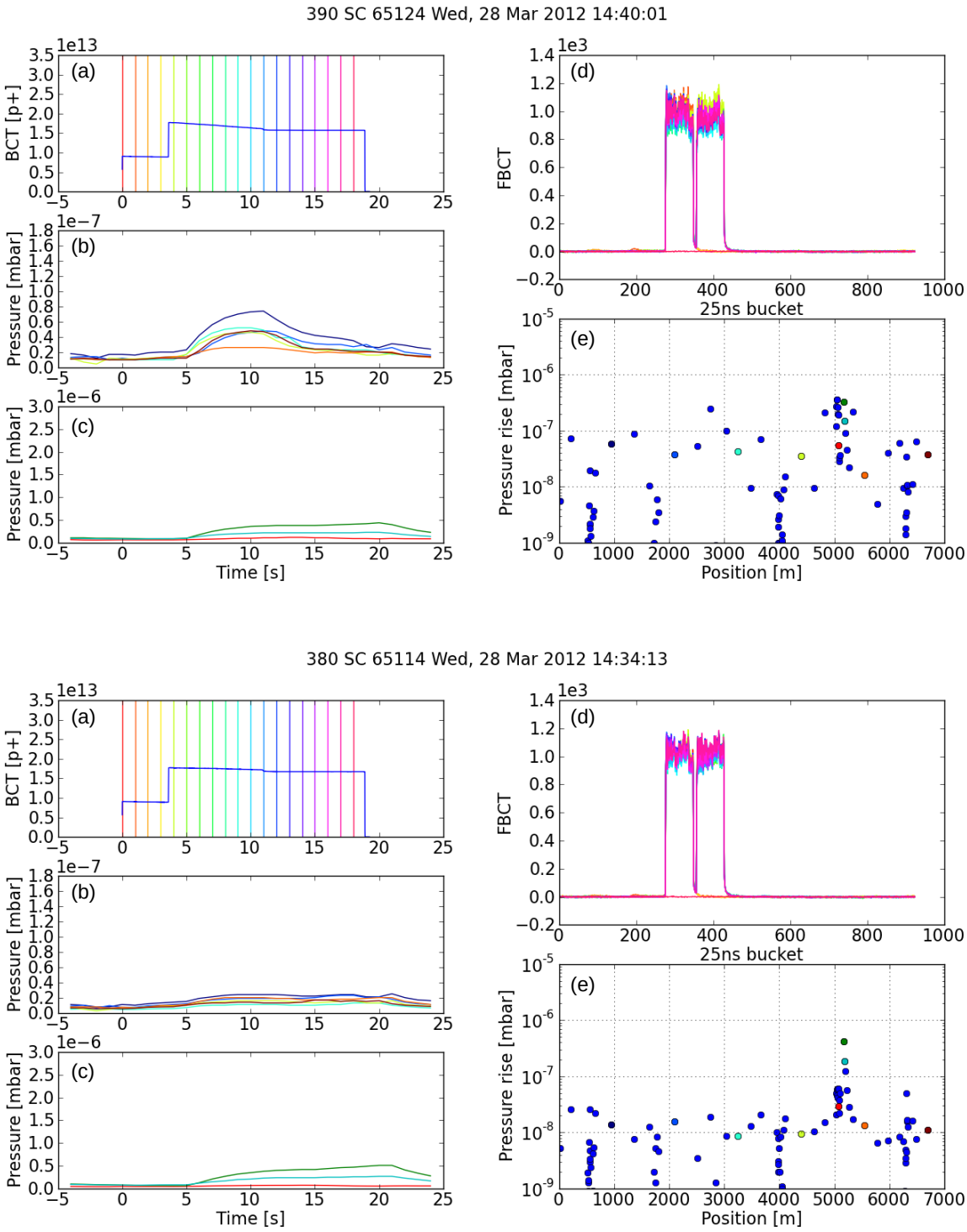

Figure 8.17: Pressure behavior when slow losses occur after the second injection and the beam is accelerated from 26 GeV to 450 GeV starting from $t = 11\,s$ (top). A cycle with weaker losses is shown for comparison (bottom). In the subplots: (a) total beam intensity; (b) pressure evolution in the arcs; (c) pressure evolution near Point 5; (d) bunch intensity (one trace per second corresponding to the vertical lines in (a), not calibrated); (e) pressure rise along the ring.

the arcs. On the other hand, only a small effect is observed on the gauges near Point 5 due to the weak dependence of the EC on the beam energy.

8.4.3 *Effect of the filling pattern*

Figures 8.18 and 8.19 show the pressure behavior for two different filling patterns having the same bunch intensity and number of bunches as in the nominal beam but differently arranged. In the case depicted in Fig. 8.18, the last two batches are displaced from the rest of the train. This gives an evident reduction of the pressure rise on the gauges near Point 5 consistently with the presence of EC in that region. Only a small reduction of the pressure rise can be noticed in the arcs. This can be explained either with a contribution of EC to the pressure rise, or with the slight reduction of losses which is also observed with this filling pattern (compare Fig. 8.18a top and bottom) and thus may also not be related to EC.

In Fig. 8.19 we present the pressure evolution for the *microbatch* filling scheme [137]. The pressure rise is much weaker in this case, both near Point 5 and in the arcs. However the two situations may not be directly comparable, since six injections instead of four are needed to complete the "microbatch" scheme and, as a consequence, the final total intensity stays in the ring for a significantly shorter time. To be noted that, in the microbatch case, the same pressure behaviour is observed both in the arcs and in Point 5. This hints to the suppression of the EC also in Point 5 with this scheme, and a pressure rise dominated by beam losses all along the SPS.

8.5 EXPERIMENTAL STUDIES: MEASUREMENTS WITH DEDICATED EC EQUIPMENT

During the scrubbing run and the MDs with 25 ns beam, setup and data acquisition with EC dedicated equipment for direct EC detection have been performed. The results of these measurements are summarized in the following subsections.

8.5.1 *Shielded pickup*

Shielded pickups are among the few devices which allow the measurement of the EC flux with a bunch by bunch time resolution. A device very similar to the one installed in the PS [92] was tested in the SPS in 2008 and has been re-installed in the ring for the 2012 Scrubbing Run. A remote control exploiting the LAN connection to a scope has been setup in order to acquire the pickup signal from the CCC as well as to allow automatic acquisitions. As in 2008 the signal is very noisy, probably due to the long cables going from the pickup location to the rack with the electroncs in BA5. Fortunately it is possible to filter out the noise by isolating the frequency components around 40 MHz (for the 25 ns bunch spacing) to extract some information on the EC rise-time. Typically a good result can be obtained with a band-pass filter from 20 MHz to 90 MHz.

In Fig. 8.20 we show the shielded pickup acquisitions for different delays of the last batch from the rest of the train. It can be noticed that the first batch shows a much weaker signal compared to the second batch. Moreover the cleaning effect of different gaps between the second and the third batch can also be observed comparing Fig. 8.20 left and right.

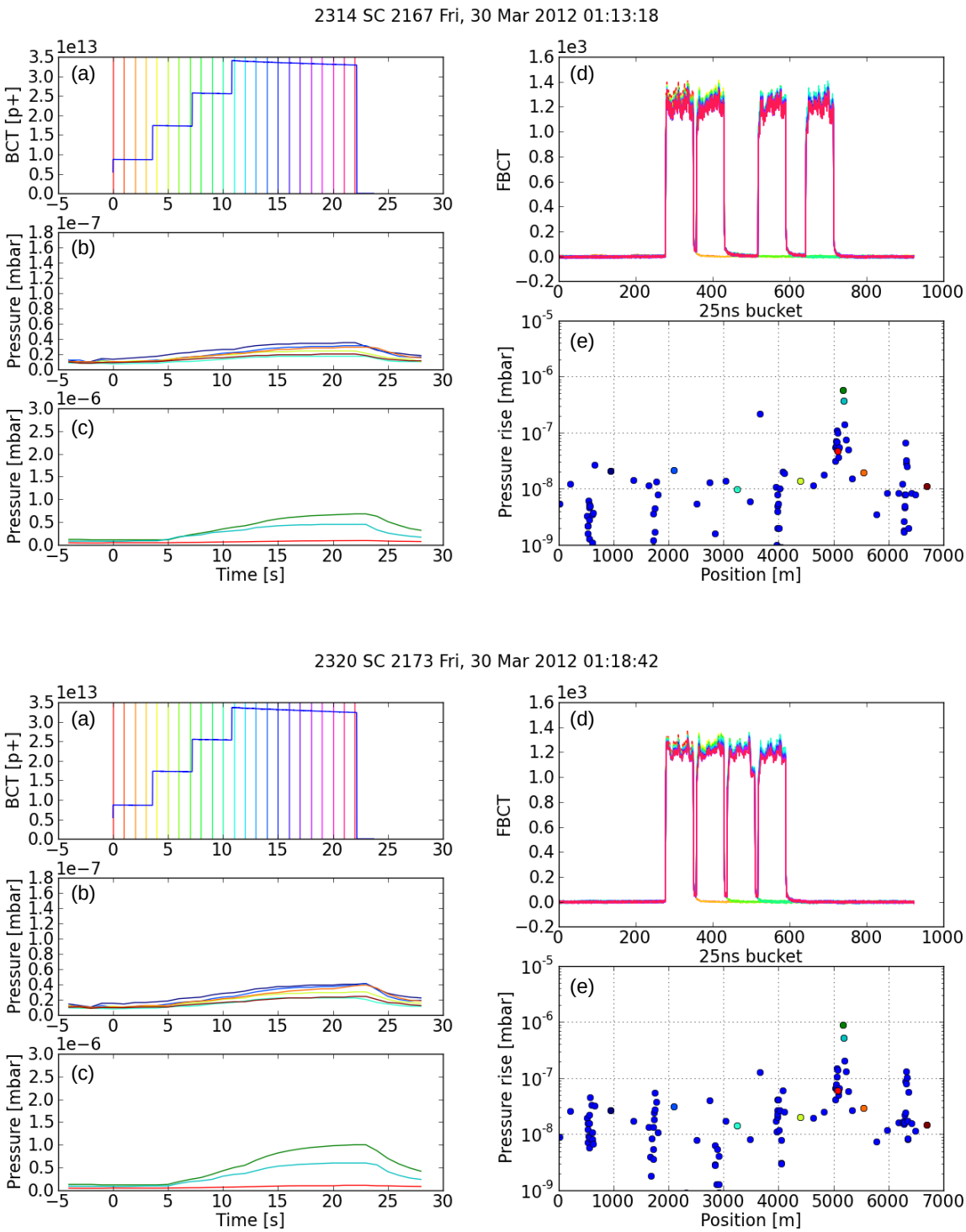

Figure 8.18: Pressure behavior with increased batch spacing (top). A cycle with the nominal filling pattern is shown for comparison (bottom). In the subplots: (a) total beam intensity; (b) pressure evolution in the arcs; (c) pressure evolution near Point 5; (d) bunch intensity (one trace per second corresponding to the vertical lines in (a), not calibrated); (e) pressure rise along the ring.

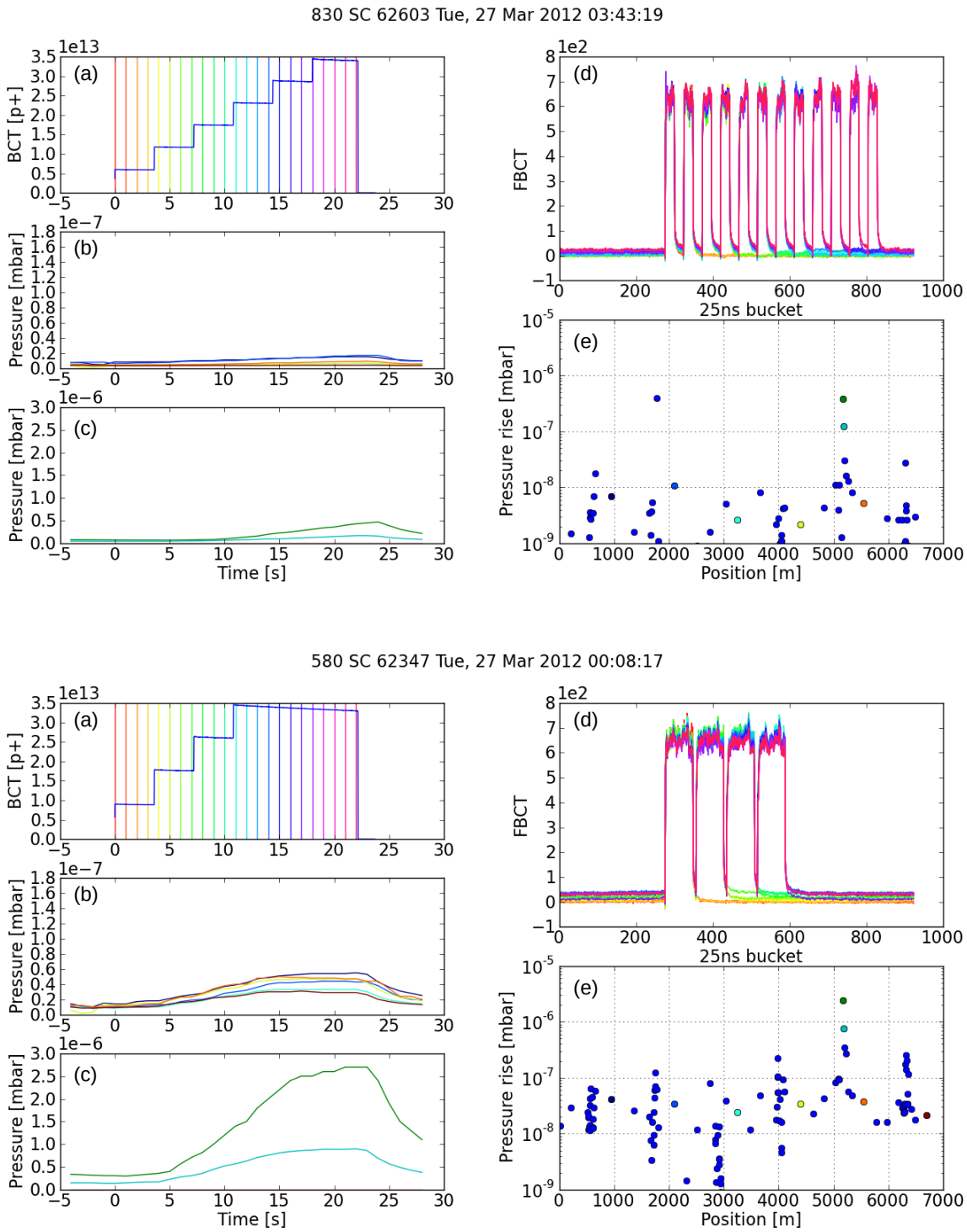

Figure 8.19: Pressure behavior with the microbatch filling pattern (top). A cycle with the nominal filling pattern is shown for comparison (bottom). In the subplots: (a) total beam intensity; (b) pressure evolution in the arcs; (c) pressure evolution near Point 5; (d) bunch intensity (one trace per second corresponding to the vertical lines in (a), not calibrated); (e) pressure rise along the ring.

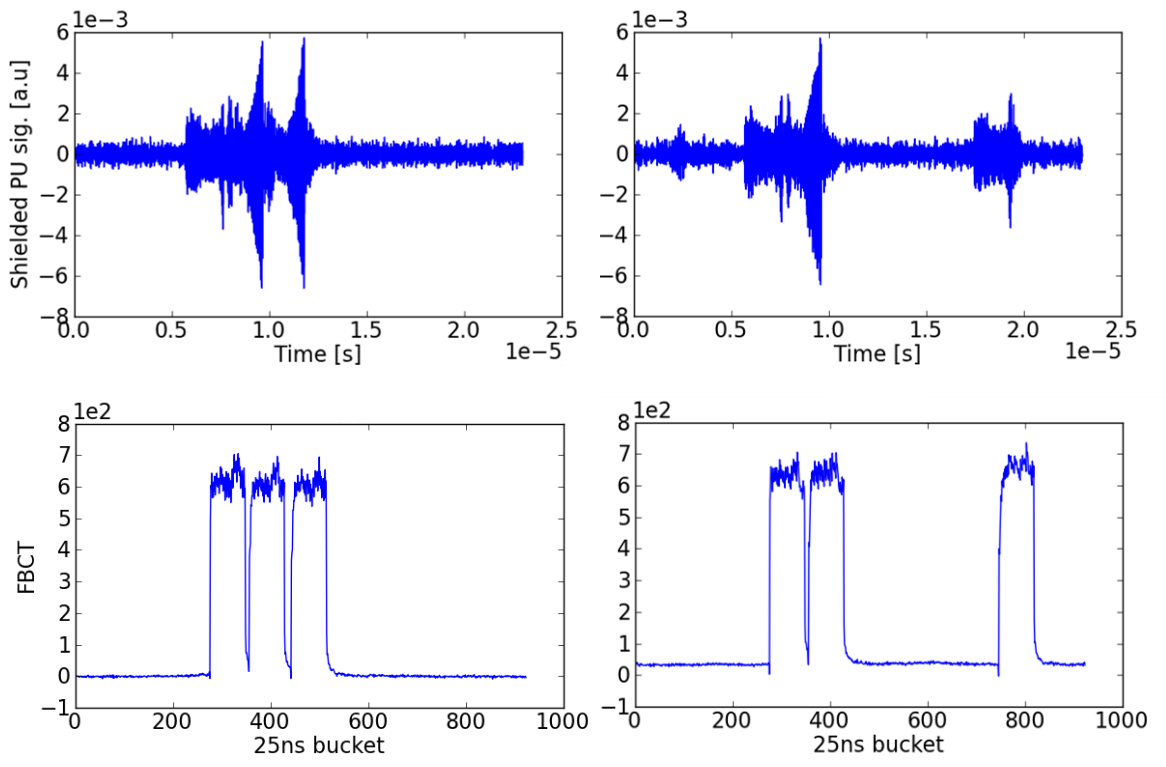

Figure 8.20: Shielded pick-up signal (filtered around 40MHz) and FBCT acquisition for two different delays of the last batch from the rest of the train.

8.5.2 *Strip detectors*

Strip detectors (also called Electron Cloud Monitors - ECM) are a powerful tool to study the EC formation, which allow measuring the spatial distribution of the electrons impinging on the chamber's wall. A full description of the strip detectors installed in the SPS can be found in [131].

In 2012 an ECM measurement campaign has been started in order to investigate the EC formation in the SPS bending magnets. For this purpose stainless steel liners, both with MBA and MBB-like chamber shapes, have been installed in the ECMs. A vertical magnetic field with of $B = 0.12\,\mathrm{T}$ (corresponding about to the bending field in the SPS main dipoles at 26 GeV) has been applied in the chambers for all the measurements. The SPS ECMs do not allow for time resolution of the EC build-up signal on the turn-by-turn time scale since the EC signal on each channel needs to be averaged over tens, or even hundreds, of milliseconds. Sometimes, when the electron flux is very small, the acquired signal can be slightly negative due to offset errors introduced by the measurement electronics.

Effect of bunch intensity

The EC profile has been measured both in the MBA and the MBB chamber types for 25 ns beams with different bunch intensities (one train of 72 bunches). The results of these tests are shown in Fig. 8.21. No EC flux is observed in either chamber type for intensities lower than 3×10^{10} ppb. For relatively small intensities (3×10^{10} ppb to 5×10^{10} ppb) the electrons

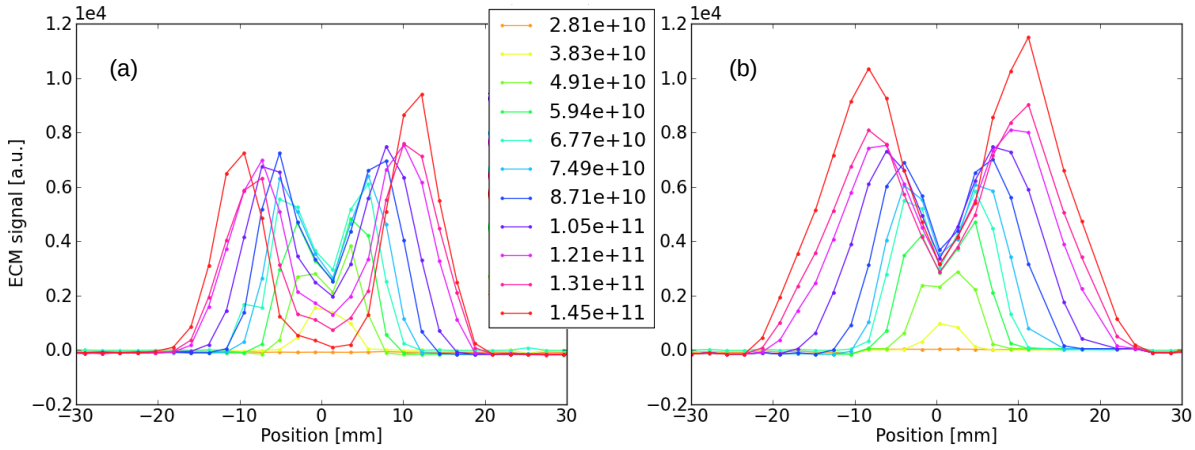

Figure 8.21: Horizontal distribution of the electron flux in two strip detectors with MBA (a) and MBB (b) shaped chambers for 72 25 ns spaced bunches with different bunch intensities.

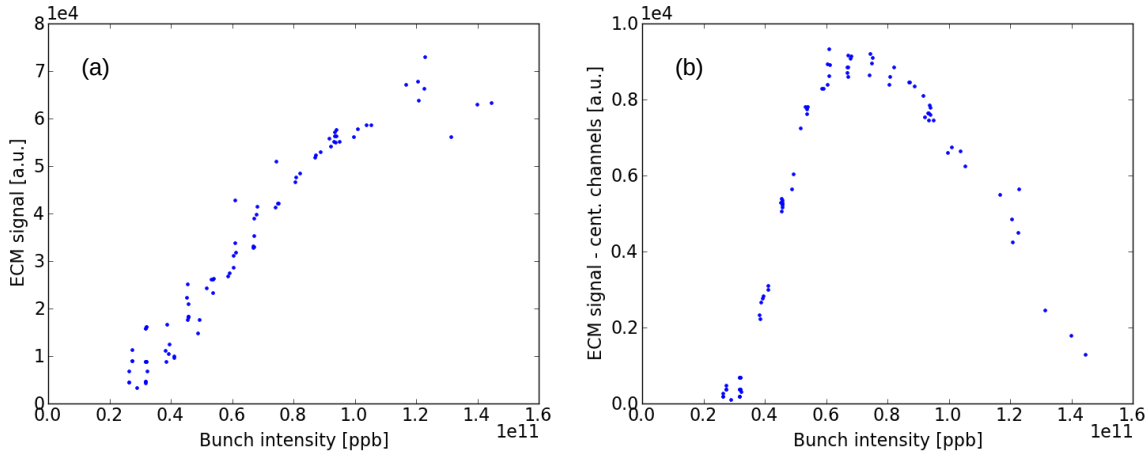

Figure 8.22: Sum of the signals of all channels (a) and of the two central channels (b) on a strip detector with MBA shaped chamber as function of the bunch intensity.

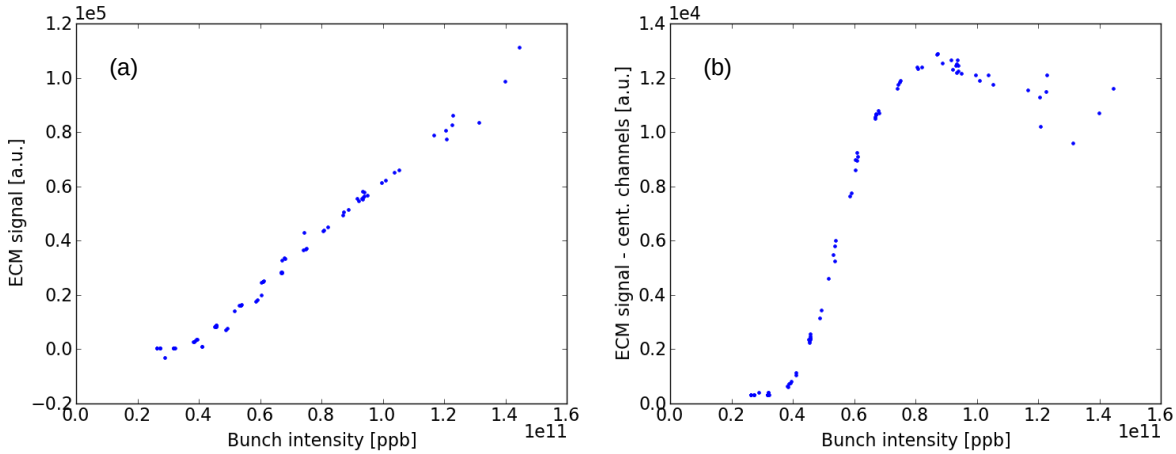

Figure 8.23: Sum of the signals of all channels (a) and of the two central channels (b) on a strip detector with MBB shaped chamber as function of the bunch intensity.

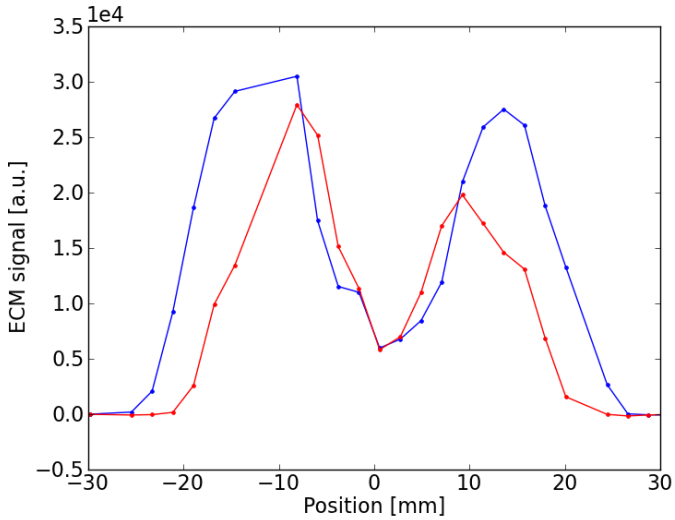

Figure 8.24: Horizontal distribution of the electron flux in a detector with MBB shaped chambers for 72 bunches spaced by 25 ns with nominal (red curve) and ultimate (blue curve) bunch intensities (the scale is different than in other figures).

are confined within a thin stripe around the beam location, while for higher intensities the two stripes configuration typical for the EC build-up in bending magnets with LHC beams becomes more evident. Comparing Figs. 8.21 (a) and 8.21 (b) we notice that the EC in the MBA chamber is significantly weaker than in the MBB: Not only the region covered by EC is thinner but also the peak and the integrated flux are smaller.

For both chambers the two stripes tend to moderately grow both in peak value and in thickness and they also move further apart from the beam when the bunch intensity is increased. Furthermore, for intensities higher than nominal the electron flux in the region closest to the beam (in a range $\Delta x = 1$ cm) remains almost constant for the MBB and is clearly decreasing for the MBA chambers (see Figs. 8.22 and 8.23). These effects can be understood recalling that the Secondary Electron Yield is not a monotonic function of the energy of the electrons hitting the wall, determined by the kick imparted by the beam on the electrons. As a consequence, the maxima of the electron flux (the stripes) are the locations at which the energy received by the electrons matches the maximum of the SEY curve. In the central region of the beam pipe, the electrons receive a kick from the passing bunch which is strong enough to be in the decreasing region of the SEY curve so that for higher intensity the multipacting may become less efficient on a surface with uniform SEY.

ECM measurements have also been acquired on an MBB liner with 25 ns beam with ultimate bunch intensity. A comparison with the nominal bunch intensity is shown in Fig. 8.24. These two curves can be compared, as they were acquired over the same MD session. However, the y-scale of this plot cannot be compared with that of the plots previously displayed, because of the use of different electronic boards for the acquisitions.

Effect of the number of bunches and of the filling pattern

Even if the strip detectors do not provide bunch-by-bunch information about the EC build-up, indirect information about the EC rise-time during the train passage can be inferred from measurements with different number of bunches. The results of this type of measurements

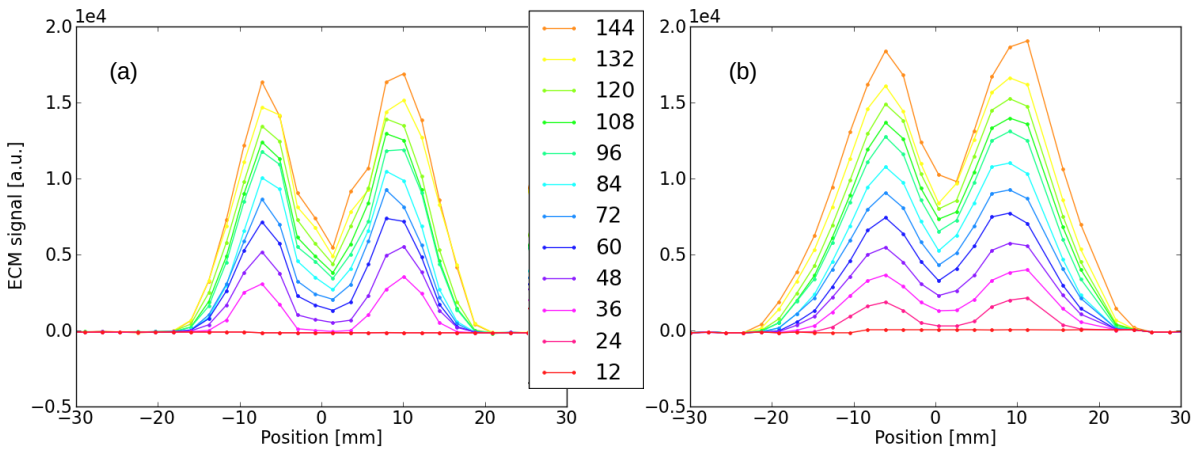

Figure 8.25: Horizontal distribution of the electron flux as function of the number of bunches in two strip detectors with MBA (a) and MBB (b) shaped chambers.

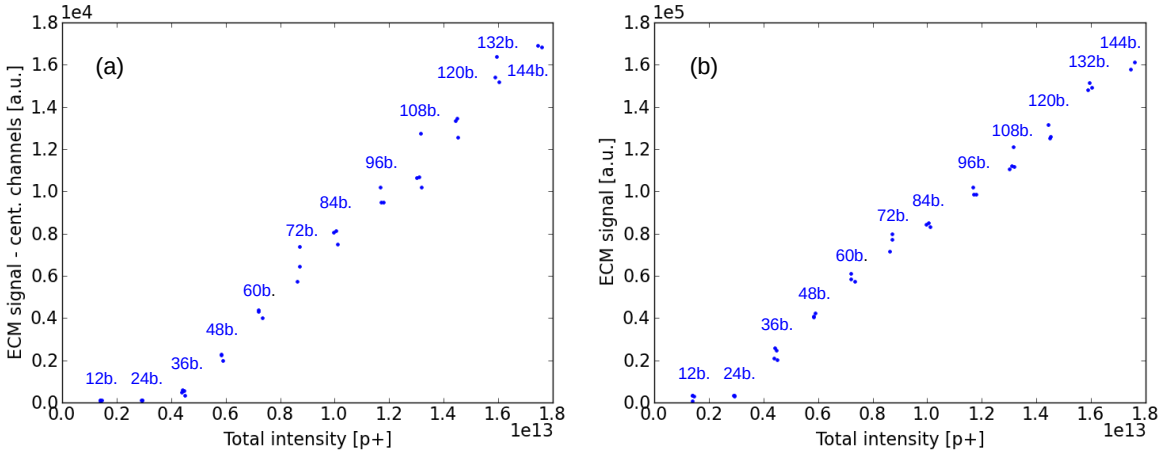

Figure 8.26: Sum of the signals of all channels (a) and of the two central channels (b) on a strip detector with MBA shaped chamber as function of the number of bunches.

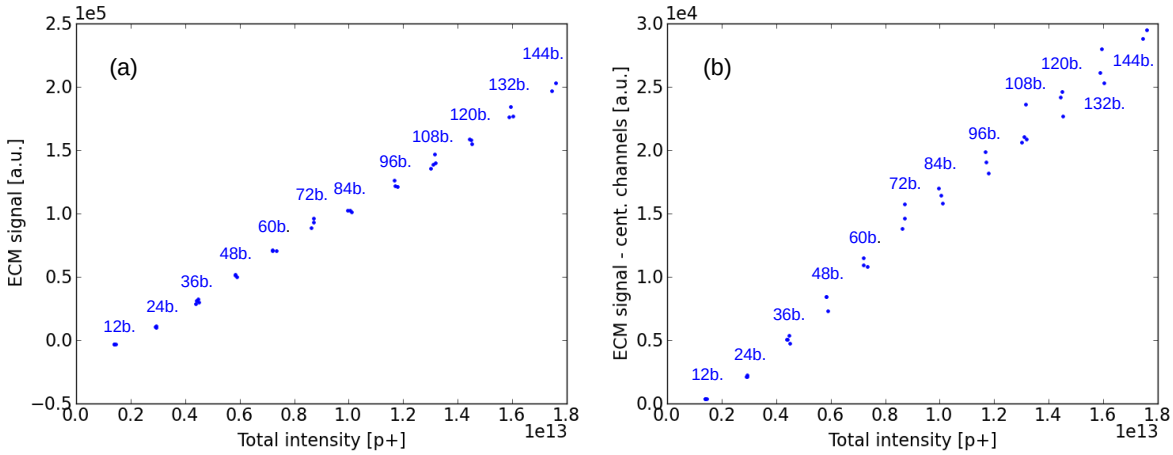

Figure 8.27: Sum of the signals of all channels (a) and of the two central channels (b) on a strip detector with MBB shaped chamber as function of the number of bunches.

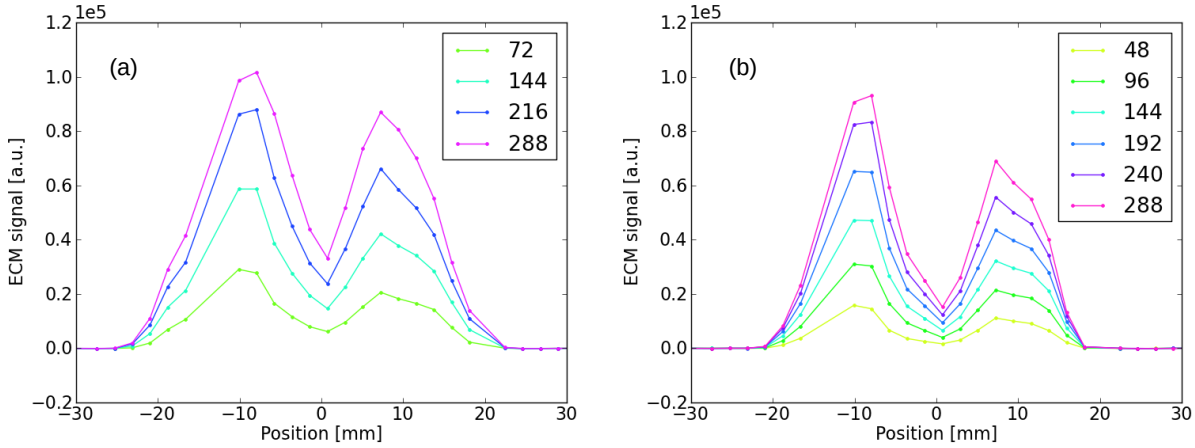

Figure 8.28: Horizontal distribution of the electron flux (a) for the nominal filling pattern (one to four batches of 72 bunches, 225 ns gaps between batches) and (b) for the *microbatch* filling pattern (2 to 12 batches of 24 bunches, 625 ns gaps between batches) in the MBB shaped chamber.

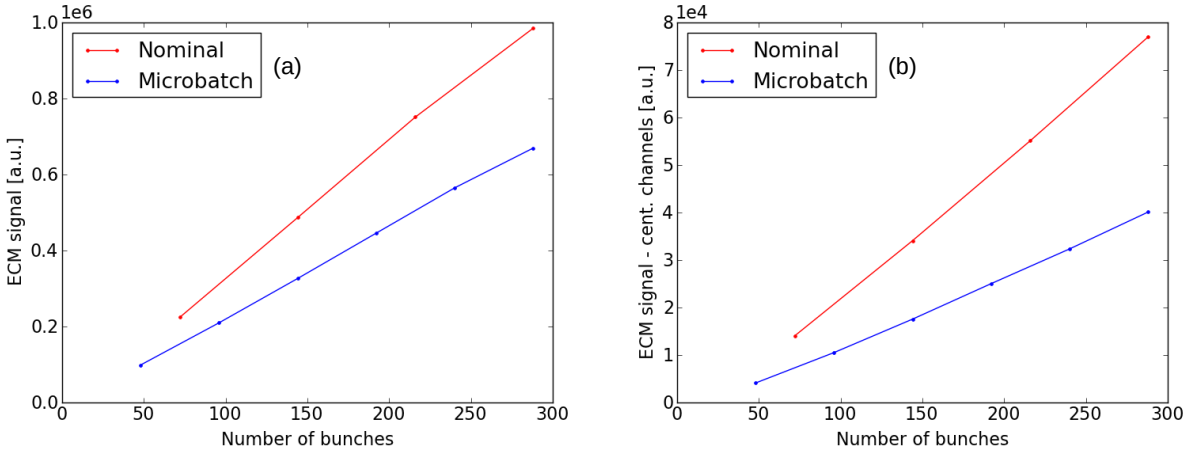

Figure 8.29: Sum of the signals of all channels (a) and of the three central channels (b) on a strip detector with MBB shaped chamber for the nominal and the microbatch filling pattern.

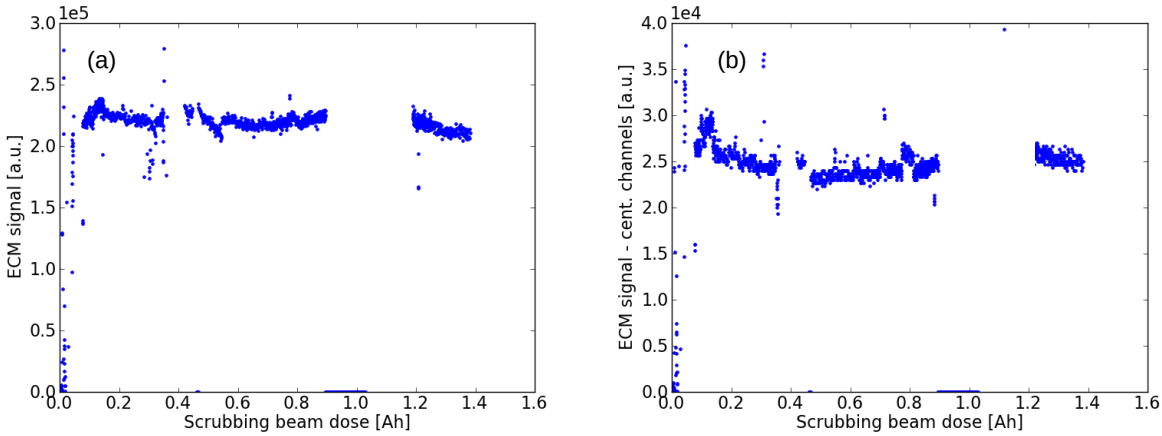

Figure 8.30: Evolution of the sum of the signals of all channels (a) and of the two central channels (b) during the 2012 scrubbing run on a strip detector with MBB shaped chamber. (Only dose accumilated with long FB cycle with Q26 optics is considered)

(using the 25 ns beam with nominal intensity) are plotted in Figs. 8.25, 8.26 and 8.27. No EC signal is observed with 12 bunches for both chambers. With 24 bunches the signal is measurable in the MBB but not in the MBA. This confirms experimentally that the EC build up is more severe in MBB chambers than in MBAs (see Sec 8.1). The 225 ns gap between the two trains of 72 bunches is not sufficient to introduce a complete reset of the EC between batches. Fig. 8.25 also shows that the separation between the two stripes depends only on the bunch intensity and not on the total number of bunches.

A possibility for the mitigation of the EC effects on the 25 ns beam is to group bunches in shorter trains with larger spacing between them. In this direction the *microbatch* filling (made of trains of 24 bunches with 625 ns gaps) scheme has been tested in the SPS during the scrubbing run. Related observations on the strip detector with an MBB like chamber are presented in Fig. 8.28. A consistent decrease on the overall electron flux was measured, more pronounced in the region closest to the beam (where a twofold reduction is observed) rather than in the region of the stripes (see also in Fig. 8.29).

Scrubbing observations on the liners

Scrubbing effects have been observed on the liners installed in the strip detectors. This can help to understand the beam induced conditioning process in presence of an external strong magnetic field. However it has to be taken into account that this behavior might not represent the scrubbing process as it takes place in the SPS bending magnets, because of the horizontal confinement of the electrons in the dipolar magnetic field and the presence of the holes for the electron detection which might significantly affect (probably slow down) the conditioning process.

In 2012, most of the 25 ns beam has been accumulated during the scrubbing run. Despite this, the signal on the ECM stayed almost constant during the entire scrubbing week (see Fig. 8.30). This has been later understood to be due to the fact that the liner was already exposed to a comparable amount of 25 ns beam before the scrubbing run (without magnetic field applied) for vacuum conditioning of equipment installed during the Christmas technical stop. This has been confirmed during the MD block in week 17, when two new stainless steel

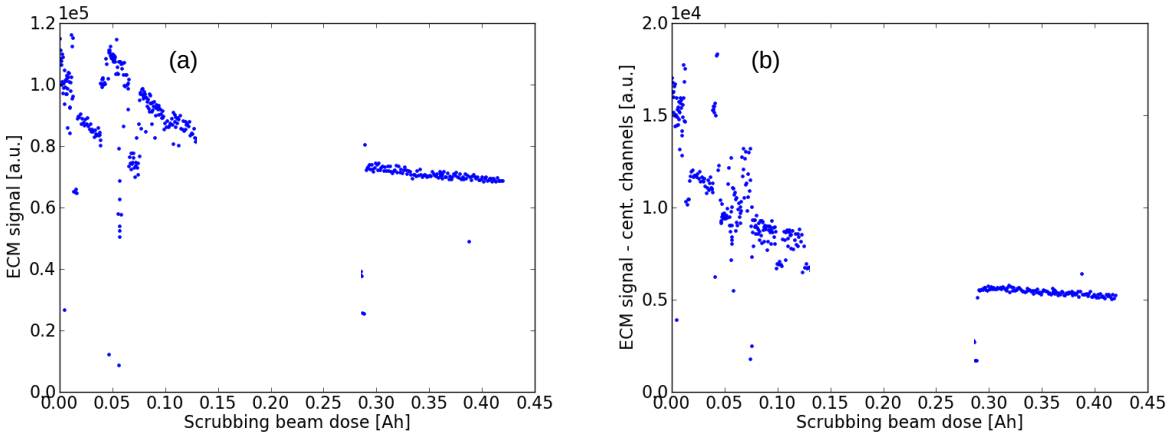

Figure 8.31: Evolution of the sum of the signals of all channels (a) and of the two central channels (b) during a few hours exposition to 25 ns beam on a strip detector with MBA shaped chamber installed just before the MD session.

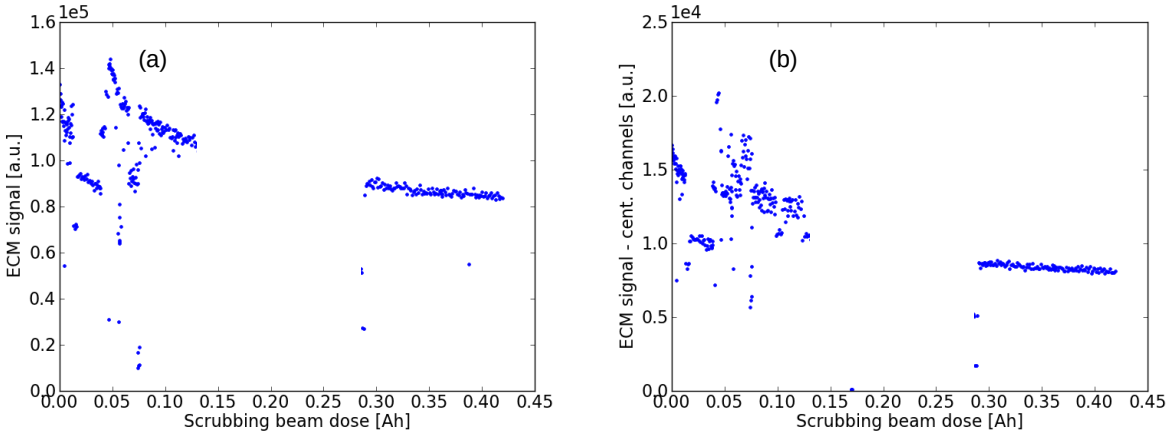

Figure 8.32: Evolution of the sum of the signals of all channels (a) and of the two central channels (b) during a few hours exposure to 25 ns beam on a strip detector with MBB shaped chamber installed just before the MD session.

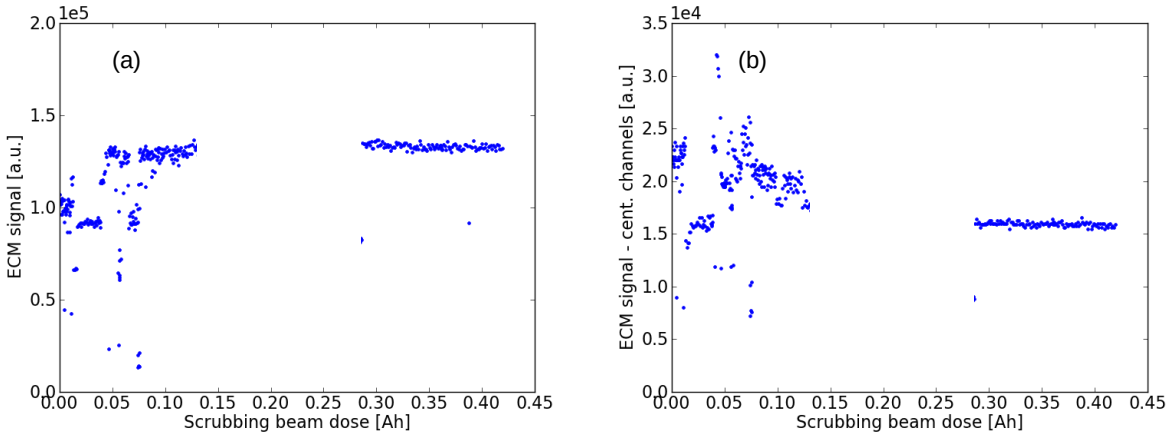

Figure 8.33: Evolution of the sum of the signals of all channels (a) and of the two central channels (b) during a few hours exposition to 25 ns beam on a strip detector with MBB shaped chamber already conditioned with 25 ns beam.

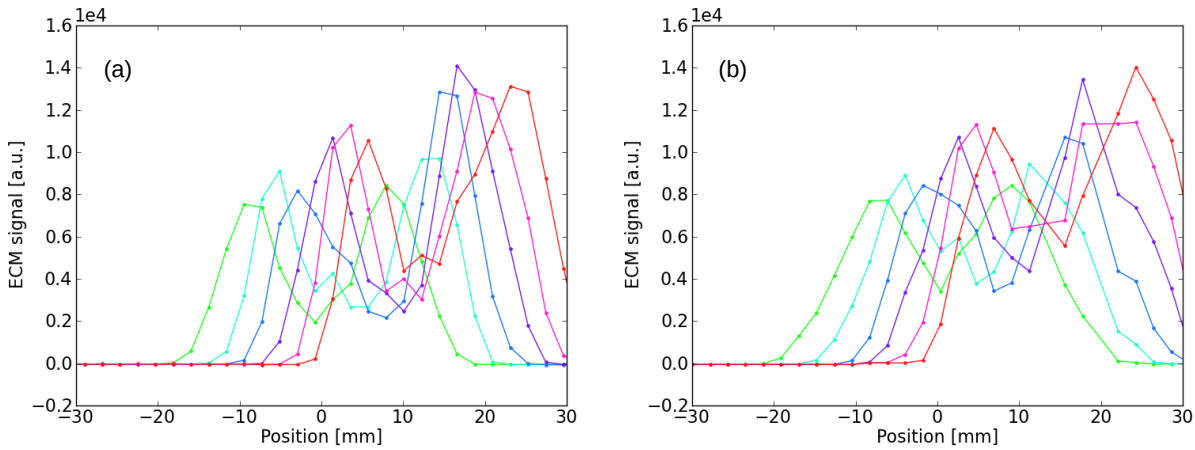

Figure 8.34: Horizontal distribution of the electron flux after conditioning with 25 ns beam in two strip detectors with MBA (a) and MBB (b) shaped chambers for different horizontal displacements of the beam.

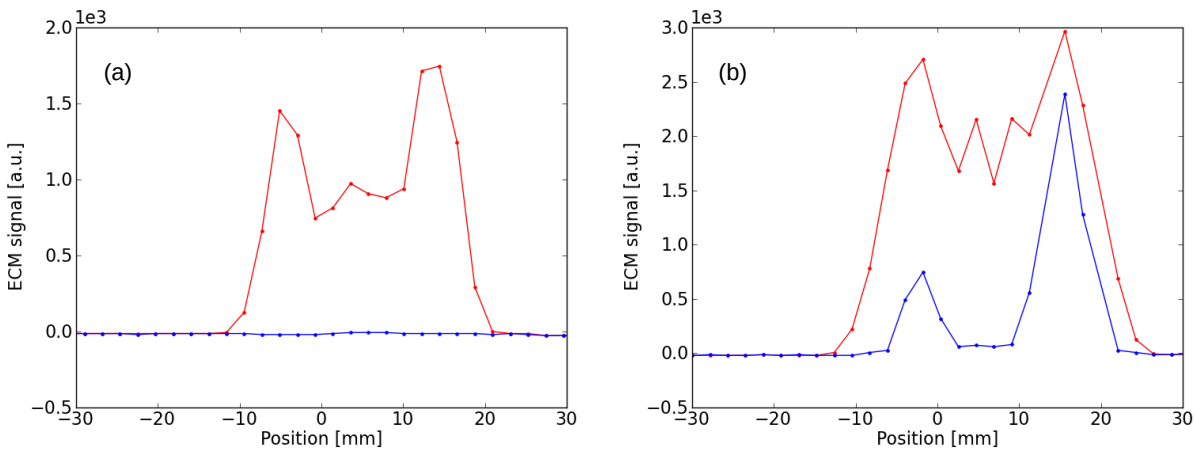

Figure 8.35: Horizontal distribution of the electron flux in two strip detectors with MBA (a) and MBB (b) shaped chambers measured with 50ns beam before (red curve) and after conditioning (blue curve) with 25 ns beam.

liners (with MBA and MBB profiles) have been installed in the SPS. On this occasion a much shorter amount of beam time has been sufficient to observe the scrubbing effect on both newly installed liners (see Figs. 8.31 and 8.32). Moreover the reduction observed on the EC flux in the region closer to the beam is stronger than the one observed on the total flux. At the same occasion, no further conditioning effect was observed on the liner already present in the machine during the scrubbing run (see Fig. 8.33), even if it was vented the day before for the installation of the new liners (the three ECMs are in the same vacuum sector).

The strip detectors also allow identifying the horizontal part of the chamber conditioned by the scrubbing process. Figure 8.34 shows the measured electron flux when the beam is horizontally displaced in the ECM chamber: a consistent enhancement of the signal is observed in the regions which are not affected by the EC in normal operation (green curve).

In the conditioning experiment of week 17, measurements with beam with 50 ns spacing were taken before and after the accumulation of the scrubbing dose with the 25 ns beam (see

Fig. 8.35). On the MBA chamber the EC with 50ns beam was completely suppressed by the given scrubbing dose with 25 ns. On the other hand, the EC in the MBB was strongly reduced but was still present, confirming again that EC is more severe in the MBBs rather than in the MBAs as also predicted by simulation studies [134].

8.6 DOUBLET SCRUBBING BEAM

In the framework of the LIU project we have been asked to investigate the possibility of improving the efficiency of the beam induced scrubbing process in the SPS by defining a beam configuration specifically tailored for this purpose and compatible with the different constraints imposed by the different subsystems both of the SPS and of the pre-injectors.

Exploratory studies in this direction were performed in 2011 when different options compatible with the beam types attainable in the SPS were investigated. In particular, the options of enhancing the EC via deliberately increasing the fraction of uncaptured beam or with tighter bunch spacings such as 5 ns, hybrid (10+15) ns or (20+5) ns, which can be accommodated in the 200 MHz main SPS RF system, were the object of detailed EC simulation campaigns to compare their potential [134]. The outcome of these studies indicated that one of the most promising techniques for EC enhancement consists of creating beams with the aforementioned hybrid bunch spacings with about nominal charge per bunch, i.e. 1.1×10^{11} ppb.

The higher frequency of the beam electric field with a shorter time for the EC decay between subsequent bunch passages is the underlying reason for the EC enhancement with the hybrid bunch spacings. However, the techniques initially envisioned to produce these beams, i.e. slip stacking in the SPS or RF manipulations in the pre-injector Proton Synchrotron (PS), turned out to be inapplicable due to technical limitations of the RF systems in the two accelerators.

At this point, a novel production scheme was proposed to create a beam with the required (20+5) ns spacing. Long bunches (10 ns full bunch length) in 25 ns spaced trains could be injected from the PS on the unstable phase of the 200 MHz SPS RF system. Ramping up the RF voltage shortly after injection from 1 MV to 3 MV such as to capture the long bunches in two neighboring buckets would then result in the generation of 5 ns spaced "doublets" out of each incoming PS bunch.

This scheme was successfully tested in the SPS with a single bunch first, and then with a train of 72 bunches with 25 ns bunch spacing [133]. Figure 8.36 shows the doublet creation in the SPS, with the bunch splitting effectively taking place in the first 50 turns and the readjustment of the bunches to their buckets in the following few synchrotron periods. Another test took place in 2013, in which a second PS train was injected into the SPS while one train of doublets was already circulating. The goal of this test was to prove that the decrease-increase of the RF voltage required for the injection of the second train would not cause excessive capture losses for the circulating beam.

Electron cloud simulations run with PyECLOUD in preparation of this doublet experiment showed that doublets can provide larger scrubbing doses and have significantly lower mutipacting thresholds than nominal 25 ns beams, as long as their intensity is above 1.5×10^{11}p/doublet. This is illustrated in Fig. 8.37 both for the MBA and MBB dipole magnets.

The enhacement effect should be mostly visible in the region of SEY below 1.55 for the MBA and below 1.25 for the MBB (i.e. the mutipacting threshold for nominal 25 ns beams).

For a direct comparison between the two beam types, a standard 25 ns beam with 1.7×10^{11} p/b and a doublet beam with the same intensity per doublet were injected on consecutive

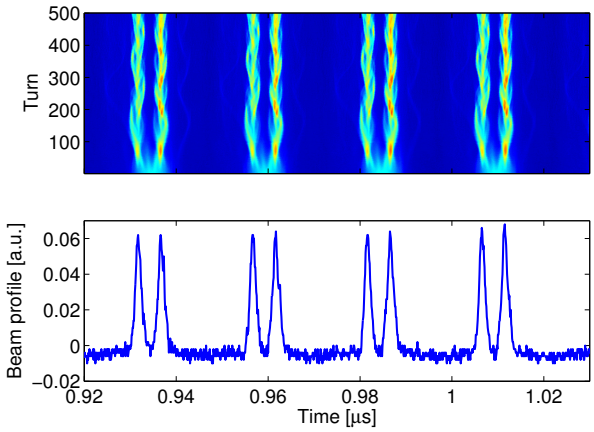

Figure 8.36: Longitudinal beam profile (zoom on four of the 72 bunches): measured evolution during the first 500 turns after injection (top) and snapshot at turn 500 (bottom).

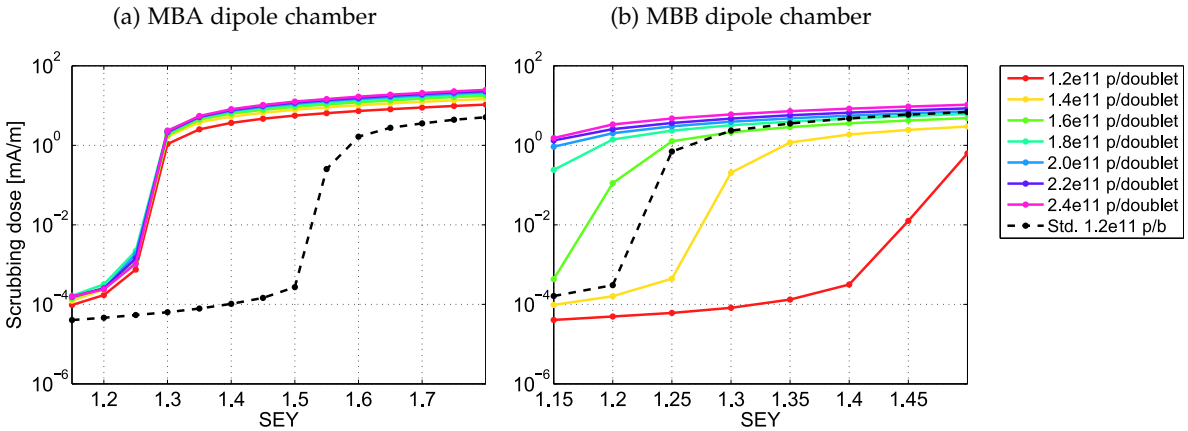

Figure 8.37: Electron scrubbing flux in the SPS MBA and MBB dipole chambers as a function of the maximum SEY for different values of the intensity per doublet (solid lines, colors labeled) in comparison with the nominal 25 ns beam (dashed line).

SPS cycles, each with a length of 4 s. The effect of the enhanced EC in the SPS with doublet beams was immediately observed with a dynamic pressure rise in the arcs that was about four times the value measured with the standard beam. Furthermore, the signals from the ECMs (both MBB and MBA chamber types) also provided a direct measurement of the stronger EC production, as displayed in Fig. 8.38. However, albeit increasing the electron flux on the chamber walls, the doublet beam covers a different region compared to the two stripes created by the standard beam. This observation was already anticipated by build up simulations with a high degree of accuracy, as shown in Fig. 8.39. The consequence is that radial steering in the dipoles is needed in order to scrub the required part of the SPS chambers with the doublet beam.

The proof-of-principle of the production and efficiency of the doublet beam in the SPS, as well as the validation of our simulation tools for predictions, was an essential milestone to consider this beam as a future option for scrubbing the SPS after LS1.

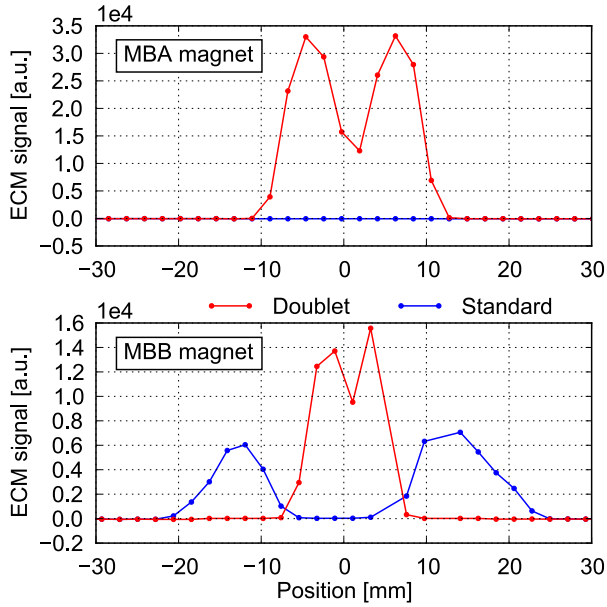

Figure 8.38: Electron signal from the SPS electron cloud monitors in an MBA-type chamber (top) and MBB-type chamber (bottom) as a function of the horizontal position. The blue traces are the measured signals with the standard 25 ns beam and the red traces are those from the doublet beam.

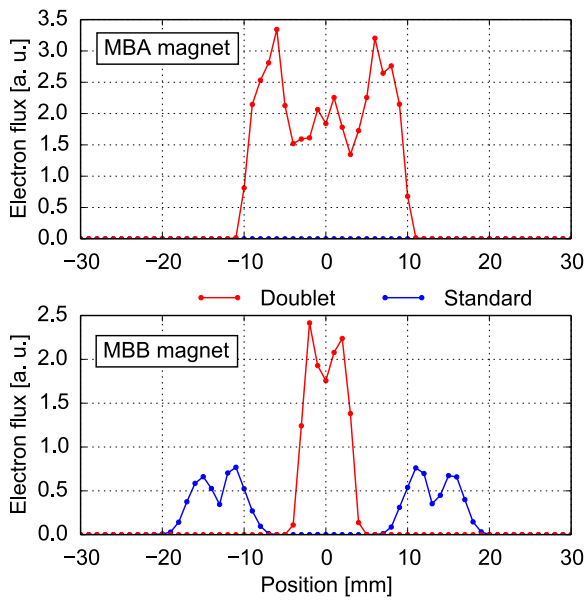

Figure 8.39: Simulated electron flux to the wall of an MBA-type chamber with SEY=1.5 (top) and an MBB-type chamber with SEY=1.3 (bottom) as a function of the horizontal position for the standard 25 ns beam (1.7×10^{11} p/b, blue trace) and a doublet beam (1.7×10^{11} p/doublet, red trace).

SUMMARY AND CONCLUSIONS

EC effects in the LHC and in the last two rings of its injector chain (PS and SPS) have been addressed with numerical simulation and experimental studies.

A new simulation code, PyECLOUD, has been developed in order to cope with the different and often complex simulation scenarios necessary for a correct understanding of the EC observations in CERN accelerators. The development of PyECLOUD resulted from an in-depth analysis of previously available tools in order to identify possible improvement and optimization paths. The code was written in a more modern language with respect to the existing tools, allowing for strongly enhanced flexibility and reliability. In the process, several key features were also redesigned.

In particular, the field generated by the traveling beam is pre-computed on a suitable map at the initialization stage and interpolated at the different MP locations at each time step, with a substantial impact both on simulation accuracy and speed. The possibility to compute the beam field using a Finite Difference (FD) algorithm allows the simulation of arbitrarily shaped chambers. The Space Charge (SC) field within the EC itself is computed using a Particle In Cell (PIC) method in order to also allow for the simulation of arbitrary chamber shapes. The electron tracking is performed using a semi analytic algorithm optimized for strong magnetic field conditions, which allows having time steps comparable or even larger than the cyclotron period with important advantages in terms of computation time. A novel approach is introduced for the management of the number of MPs, which allows an adaptive change of the MP size during the simulation while preserving the full phase space distribution of the EC. This allows correctly modeling the electron avalanche multiplication process while keeping a reasonable computational burden.

The modular structure of the code (implemented in Python using an object-oriented approach) allowed a smooth development of the features necessary to address complex simulation scenarios, like the EC buildup in quadrupoles or combined function magnets and with two counter-rotating beams in the same chamber. Moreover the possibility to deal with beams with thousands of bunches and with non-idealities like non-uniform bunch populations and bunch lengths along the beam turned out to be crucial for the correct understanding of machine experimental observations.

The impact of the introduced improvements on the simulator's reliability, accuracy and speed were immediately evident and PyECLOUD quickly became the reference tool for electron cloud simulations for CERN machines, covering a variety of devices and beam conditions. In particular a full characterization for different beam conditions has been performed for the LHC main magnets (dipoles and quadrupoles), for the SPS dipoles and for the PS main (combined function) magnets.

In parallel with this modeling and simulation work, an intense experimental activity was carried out, which involved the LHC and the last two synchrotrons of its injector chain, i.e. the PS and the SPS. Its main goals were the qualification of the EC formation in the three accelerators and of its impact on the quality of the proton beam, the collection of experimental data for the validation and the improvement of our simulation models, and the definition and experimental validation of possible EC mitigation strategies.

At the LHC EC effects were observed during the first three years of beam operation (Run 1, 2010-2012), becoming more and more severe while moving to tighter bunch spacing. EC effects with 50 ns bunch spacing could be successfully mitigated through beam induced scrubbing and these beams could be used for most of the integrated luminosity production with 7-8 TeV Center of Mass (CoM) energy in 2011-12.

After the 2013-14 machine shutdown (LS1) the LHC will be able to run at 13-14 TeV CoM energy and it will be necessary to move to the design bunch spacing of 25 ns in order to reach the design luminosity within the pileup limits required by the LHC experiments.

Up to now, the 25 ns beam has been used only for test purposes, and as expected from simulation studies, due to the smaller multipacting threshold, EC effects proved to be significantly more severe compared to the 50 ns case. Therefore our studies mainly focused on experiments carried out with beams with 25 ns bunch spacing.

Both in 2011 and in 2012 several hours of machine time were devoted to scrubbing fills with 25 ns beams at injection energy (450 GeV), in order to test the possibility of improving the machine performance via beam induced scrubbing. Due to the non-ideal beam conditions during these periods, it was found to be not trivial to qualify the scrubbing evolution. For this purpose we developed a method for the reconstruction of the SEY of the beam chambers based on the comparison of PyECLOUD simulations (setup with the bunch-by-bunch beam parameters measured in the machine) against the heat load measured in the cryogenic magnets.

Estimations performed with this method showed that the accumulated electron dose could decrease the SEY of the dipole chambers from an initial value of about 2.2 down to values slightly above 1.4, very close to the estimated multpacting threshold. These estimations could be crosschecked using bunch-by-bunch energy loss measurements (estimated through RF stable phase) and instability observations, finding a remarkably good agreement.

An important piece of information on the evolution of the scrubbing process came from the analysis of the heat load measured in the Stand Alone Modules (SAMs). From this we could infer that the heat load distribution over the LHC arcs was changing during the scrubbing periods. During the 2011 scrubbing tests and the first scrubbing fills in 2012 the heat load measured in the LHC arcs was dominated by the contribution of the dipole magnets, which extend over 85% of the total arc length. At later stages, a significant amount of the total heat load was actually coming from the quadrupole magnets, despite they constitute less than 10% of the total arc length. This could be understood through PyECLOUD simulations, which showed a significantly lower multipacting threshold for the quadrupoles compared to the dipoles.

At this later stage, in spite of remaining signs of the presence of EC in the machine, the scrubbing process significantly slowed down and no further improvement could be identified over the last few fills. Beam quality measurements (proton losses, transverse emittance blowup) confirmed the behavior inferred from the heat load.

Despite not being sufficient to fully suppress the EC at injection energy, the conditioning accumulated during the scrubbing run was sufficient to allow accelerating for the first time beams with 25 ns beams in trains of 48, 72, or 96 bunches, up to 4 TeV. On these occasions we could study the dependence of the EC buildup in the LHC on the beam energy. In fact we could notice an increase of the EC activity for larger beam energies, especially in the dipole magnets. As shown by the simulation studies, possible factors contributing to the observed

dependence are the stronger photoemission due to synchrotron radiation, the variation of the bunch length and the decrease of the beam size inherent with the beam acceleration.

The impact of the EC on the beam degradation during the physics stores (4 TeV) was studied by looking at the evolution of the bunch by bunch emittance from the specific luminosity. Despite the stronger EC activity at high energy, the beam quality during the high energy stores did not exhibit any signs of degradation that could be attributed to EC. This can be explained with the increased beam rigidity of the beam at 4 TeV.

Nevertheless, the heat load values measured along the ramp showed that the achieved conditioning might not be sufficient to run with the nominal number of bunches due to the limited cooling capacity of the cryogenic system. In order to provide a further scrubbing step in a reasonable time we investigated the possibility of resorting to a dedicated "scrubbing beam" configuration. PyECLOUD simulations showed that the "doublet scheme" that we developed for the same purpose at the SPS looks even more attractive for the LHC.

The studies also addressed the EC effects observed in the LHC common regions, where the two counter-rotating beams share the same chamber. With this respect two cases were treated in detail.

The first of them was a room temperature common vacuum chamber having 800 mm diameter installed on both sides of the ALICE experiment. During 2011 operation with 50 ns bunch spacing an important pressure rise was noticed in these chambers with a significant impact on the background for the ALICE experiment. The analysis of the pressure data showed a quite singular behavior i.e. a severe pressure increase observed only when the two rings of the LHC are completely filled. PyECLOUD simulations were used to study the EC buildup in these devices and we could show that when (and only when) the two rings are completely filled, a complete decay of the EC between subsequent turns cannot take place. The EC can then pile up over subsequent turns with a strong enhancement of the electron flux on the wall and therefore of the pressure rise.

The second device equipped with a common chamber that was analyzed in detail is the final focusing triplet installed at the four experimental regions. These are the only cryogenic magnets in the ring where a strong heat load could still be observed during the operation with 50 ns beams in 2012, despite the conditioning accumulated during physics operation and during the scrubbing tests with 25 ns beams. PyECLOUD simulations showed that, especially with 50 ns beams, the presence of two counter rotating beams strongly enhances the EC buildup and provokes a significant decrease of the multipacting threshold. Comparing the simulated heat load against the measured values it was possible to infer that, in 2012, the SEY value of the inner surface of the beam screen was between 1.2 and 1.3. Simulations also showed that, for SEY values in this range, no EC buildup should be observed with only one beam with 50 ns spacing circulating in the LHC. These predictions could be confirmed by machine experiments conducted in these beam conditions.

Concerning the LHC injectors, the experimental activity at the PS aimed at identifying possible limitations related to EC for the production of the high intensity and high brightness beams foreseen by the LHC Injectors Upgrade (LIU) project. Several measurements under different beam conditions have been collected using a shielded pickup installed in one of the straight sections of the ring. The comparison of these measurements against PyECLOUD simulation results allowed pinning down the value of the SEY in the pick-up chamber to a value close to 1.6. The studies also addressed beam instabilities observed when storing in the ring a bunch train with 25 ns spacing. Transverse position measurements over several

subsequent turns showed a clear coupled bunch motion, stronger in the horizontal plane with a faster growth rate for bunches at the tail of the train. All these features point towards EC effects being the main driving mechanisms for the observed instabilities. Finally, the MD activity at the PS addressed the possibility to mitigate the EC effects by specifically tailoring the RF manipulations on the beam without affecting the beam quality at extraction. The first results in this direction looked very encouraging.

At the SPS, as EC effects have been observed since the early years of 2000's with 25 ns beams, the operation with this type of beams relies on beam-induced scrubbing. Since 2002, scrubbing runs with 25 ns beams were carried out almost every year of operation in order to condition (scrub) the inner surfaces of the beam pipes and therefore mitigate the EC effect. Thanks to the conditioning achieved with these scrubbing runs, during the 2012 run the SPS could deliver to the LHC beams with 50 ns spacing (bunch intensities up to 1.6×10^{11} ppb) and with 25 ns spacing (nominal bunch intensity of 1.2×10^{11} ppb) without any visible beam degradation coming from EC. On the other hand, as for the PS, it is necessary to identify possible limitations for the production of the LIU beams.

The experiments conducted during several MD sessions in 2012 served the two main purposes of collecting measurements in order to crosscheck and improve our simulation models and of assessing the present performance limitations of the SPS with respect to EC effects.

Concerning the first aspect, several measurements under various beam conditions have been collected in different EC dedicated experiments. In particular, the range of bunch intensities between 0.3×10^{11} ppb and 1.4×10^{11} ppb has been explored in order to study by means of strip detectors the dependence of the EC build-up on the bunch population for both MBA and MBB dipole magnets. The results are consistent with the predictions of the simulation models: the intensity increase leads to a widening of the region covered by the EC but at the same time the region closer to the beam (which should be the most critical concerning beam quality) has a decrease in the electron population. A stronger flux is observed in the outer regions of the chambers which were not reached by the scrubbing performed with the nominal bunch intensity.

Concerning the qualification of performance limitations coming from EC, this was carried out mainly with measurements of the pressure along the ring and of the beam parameters. Pressure observations confirm that, with nominal beam parameters, the arcs do not show strong vacuum activity compared to what was observed in the first years of SPS operation with 25 ns beams. Strong pressure rise (most probably due to EC) is presently only observed in regions with equipment which expose high SEY materials (e.g. aluminum) to the beam or are frequently vented and lose conditioning. Instead a significantly stronger pressure rise was observed when moving to intensities larger than nominal. Actually when increasing the bunch intensity up to 1.4×10^{11} ppb (for the nominal filling pattern wit 288 bunches) a fast transverse instability, most probably driven by EC, could be observed at injection energy, causing emittance blowup and particle losses on the trailing bunches of the train. Future studies will address the question if this effect can be effectively mitigated by beam induced scrubbing.

For this purpose, we studied the possibility of preparing a dedicated beam for the EC mitigation through beam induced scrubbing. PyECLOUD simulations were performed to compare different options and the most promising, the so-called "doublet" beam could be experimentally validated in the accelerator. A novel production scheme was proposed to create a beam with the required (20+5) ns spacing, which was successfully tested in the SPS.

The enhancement of the electron flux was confirmed by the pressure rise observed all along the machine as well as by direct EC measurements on the strip detectors installed in the ring. The proof-of-principle of the production and efficiency of the doublet beam in the SPS, as well as the validation of our simulation tools for predictions, was an essential milestone to consider this beam as a future option for scrubbing at the SPS and, most probably, also at the LHC.

BIBLIOGRAPHY

[1] F. M. Mako and P. Weilhammer, "A High-Current Micro-Pulse Electron Gun," *Proceedings of the 15th IEEE Particle Accelerator Conference, Washington, DC, USA,* , 1993.

[2] J. Vaughan, "Multipactor," *Electron Devices, IEEE Transactions on*, vol. 35, pp. 1172–1180, Jul 1988.

[3] R. A. Kishek, Y. Y. Lau, L. K. Ang, A. Valfells, and R. M. Gilgenbach, "Multipactor discharge on metals and dielectrics: Historical review and recent theories," *Physics of Plasmas (1994-present)*, vol. 5, no. 5, pp. 2120–2126, 1998.

[4] A. Woode and J. Petit, "Investigations into multipactor breakdown in satellite microwave payloads," *ESA Journal*, vol. 14, pp. 467–478, 1990.

[5] "Proceedings of ECLOUD'02: Mini Workshop on Electron Cloud Simulations for Proton and Positron Beams, Geneva, Switzerland, edited by G.Rumolo and F.Zimmermann," *CERN-2002-001*, 2002.

[6] "Proceedings of ECLOUD'04: 31st Advanced ICFA Beam Dynamics Workshop on Electron-Cloud Effects, Napa, CA, USA , edited by M. Furman, S. Henderson and F. Zimmermann," *CERN-2005-001*, 2005.

[7] "Proceedings of ECLOUD'07: International Workshop on Electron Cloud Effects, Ithaca, New York, edited by H. Fukuma, E. S.Kim and K. Ohmi," 2007.

[8] "Proceedings of ECLOUD'10: ICFA Advanced Beam Dynamics Workshop on electron cloud physics, Ithaca, New York, edited by K. Smolenski," 2010.

[9] "Proceedings of ECLOUD'12: Joint INFN-CERN-EuCARD-AccNet Workshop on Electron-Cloud Effects, La Biodola, Isola d'Elba, Italy, edited by R. Cimino, G.Rumolo and F.Zimmermann," *CERN-2013-02*, 2013.

[10] W. Fischer, M. Blaskiewicz, J. Brennan, H. Huang, H.-C. Hseuh, V. Ptitsyn, T. Roser, P. Thieberger, D. Trbojevic, J. Wei, S. Y. Zhang, and U. Iriso, "Electron cloud observations and cures in the relativistic heavy ion collider," *Physical Review Special Topics-Accelerators and Beams*, vol. 11, no. 4, p. 041002, 2008.

[11] H. Fukuma, "Electron Cloud Observations and Predictions at KEKB, PEP-II and SuperB Factories," *Proceedings of ECLOUD12: Joint INFN-CERN-EuCARD-AccNet Workshop on Electron-Cloud Effects, La Biodola, Isola d'Elba, Italy*, 2012.

[12] M. Zobov, D. Alesini, A. Drago, A. Gallo, S. Guiducci, C. Milardi, A. Stella, S. De Santis, T. Demma, and P. Raimondi, "Operating experience with electron cloud clearing electrodes at DAFNE," *Proceedings of ECLOUD12: Joint INFN-CERN-EuCARD-AccNet Workshop on Electron-Cloud Effects, La Biodola, Isola d'Elba, Italy*, 2012.

[13] G. Rumolo, F. Ruggiero, and F. Zimmermann, "Simulation of the electron-cloud build up and its consequences on heat load, beam stability, and diagnostics," *Phys. Rev. ST Accel. Beams*, vol. 4, p. 012801, Jan 2001.

[14] G. Peach, "Ionization of atoms and positive ions by electron and proton impact," *Journal of Physics B: Atomic and Molecular Physics*, vol. 4, no. 12, p. 1670, 1971.

[15] M. E. Rudd, Y. K. Kim, D. H. Madison, and J. W. Gallagher, "Electron production in proton collisions: total cross sections," *Rev. Mod. Phys.*, vol. 57, pp. 965–994, Oct 1985.

[16] J. D. Jackson, *Classical electrodynamics*. New York, NY: Wiley, 3rd ed. ed., 1999.

[17] A. Hofmann, *The Physics of Synchrotron Radiation*. Cambridge Monographs on Particle Physics, Nuclear Physics and Cosmology, Cambridge University Press, 2004.

[18] E. Willett, *The Basics of Quantum Physics: Understanding the Photoelectric Effect and Line Spectra*. The Library of Physics, Rosen Publishing Group, 2004.

[19] F. Zimmermann, "Synchrotron radiation in the LHC Arcs - Monte Carlo Approach," *LHC-PROJECT-NOTE-237*, 2000.

[20] F. Zimmermann and A. Rossi, "Synchrotrotron Radiation in the LHC Experimental Insertions," *LHC-Project-Report-675*, 2003.

[21] V. Baglin, I. R. Collins, and O. Gröbner, "Photoelectron Yield and Photon Reflectivity from Candidate LHC Vacuum Chamber Materials with Implications to the Vacuum Chamber Design," *Proceedings of the 6th European Particle Accelerator Conference, Stockholm, Sweden*, 1998.

[22] B. Henrist, N. Hilleret, M. Jiménez, C. Scheuerlein, M. Taborelli, and G. Vorlaufer, "Secondary electron emission data for the simulation of electron cloud," *Mini Workshop on Electron Cloud Simulations for Proton and Positron Beams, CERN, Geneva, Switzerland*, 2002.

[23] V. Baglin, I. Collins, B. Henrist, N. Hilleret, and G. Vorlaufer, "A Summary of Main Experimental Results Concerning the Secondary Electron Emission of Copper," *LHC Project Report 472*, 2002.

[24] R. Cimino, I. R. Collins, M. A. Furman, M. Pivi, F. Ruggiero, G. Rumolo, and F. Zimmermann, "Can Low-Energy Electrons Affect High-Energy Physics Accelerators?," *Phys. Rev. Lett.*, vol. 93, p. 014801, Jun 2004.

[25] R. Cimino and I. Collins, "Vacuum chamber surface electronic properties influencing electron cloud phenomena," *Applied Surface Science*, 2004.

[26] A. Kuzucan, H. Neupert, M. Taborelli, and H. Störi, "Secondary Electron Yield on Cryogenic Surfaces as a Function of Physisorbed Gases," *Proceedings of the IPAC11 International Particle Accelerator Conference, San Sebastian, Spain*, 2011.

[27] R. Cimino, M. Commisso, D. R. Grosso, T. Demma, V. Baglin, R. Flammini, and R. Larciprete, "Nature of the decrease of the secondary-electron yield by electron bombardment and its energy dependence," *Phys. Rev. Lett.*, vol. 109, p. 064801, Aug 2012.

[28] R. Larciprete, D. R. Grosso, M. Commisso, R. Flammini, and R. Cimino, "Secondary electron yield of Cu technical surfaces: Dependence on electron irradiation," *Phys. Rev. ST Accel. Beams*, vol. 16, p. 011002, Jan 2013.

[29] H. Bartosik, G. Iadarola, G. Rumolo, F. Caspers, M. Driss Mensi, S. Federmann, M. Holz, H. Neupert, and M. Taborelli, "Electron Cloud and Scrubbing Studies for the SPS in 2012," *CERN-ATS-Note-2013-019 MD*, 2013.

[30] J. M. Jiménez, G. Arduini, P. Collier, G. Ferioli, B. Henrist, N. Hilleret, L. Jensen, K. Weiss, and F. Zimmermann, "Electron cloud with LHC-type beams in the SPS: A review of three years of measurements," *Mini Workshop on Electron Cloud Simulations for Proton and Positron Beams, CERN, Geneva, Switzerland*, Apr 2003.

[31] D. Halliday, R. Resnick, and J. Walker, *Fundamentals of Physics*. John Wiley & Sons, 2010.

[32] R. J. Macek, A. A. Browman, J. E. Ledford, M. J. Borden, J. F. O'Hara, R. C. McCrady, L. J. Rybarcyk, T. Spickermann, T. J. Zaugg, and M. T. F. Pivi, "Electron cloud generation and trapping in a quadrupole magnet at the Los Alamos proton storage ring," *Phys. Rev. ST Accel. Beams*, vol. 11, p. 010101, Jan 2008.

[33] A. Chao, *Physics of Collective Beam Instabilities in High Energy Accelerators*. Wiley Series in Beam Physics and Accelerator Technology, Wiley, 1993.

[34] K. Li and G. Rumolo, "Review of Beam Instabilities in the Presence of Electron Clouds in the LHC," *Proceedings of the IPAC11 International Particle Accelerator Conference, San Sebastian, Spain*, 2011.

[35] K. Li, H. Bartosik, X. Buffat, W. Höfle, G. Iadarola, M. Kuhn, N. Mounet, and G. Rumolo, "LHC injection instabilities," *Presentation at 2-day internal review of LHC performance limitations during run I, 25-26. September 2013, CERN*.

[36] G. Bregliozzi, G. Lanza, V. Baglin, and J. M. Jimenez, "Vaccum Pressure Observations during 2011 Proton Run," *Proceedings of the Evian 2011 LHC Beam Operation Workshop, Evian, France*, 2011.

[37] L. Tavian, "Performance Limitations of the LHC Cryogenics: 2012 Review and 2015 Outlook," *Proceedings of the Evian 2012 LHC Beam Operation Workshop, Evian, France*, 2012.

[38] W. Höfle, "Observations of the electron cloud effect on pick-up signals in the SPS," *10th Workshop on LEP-SPS Performance, Chamonix, France*, 2000.

[39] F. Zimmermann, "A Simulation Study of Electron-Cloud Instability and Beam-Induced Multipacting in the LHC," *LHC Project Report 95*, 1997.

[40] F. Zimmermann, "Electron Cloud Simulations for SPS and LHC," *Proceedings of the Chamonix X LHC workshop, Chamonix, France*, 2000.

[41] G. Rumolo and F. Zimmermann, "Practical User Guide for ECLOUD," *CERN-SL-Note-2002-016 (AP)*, 2003.

[42] M. de Berg, M. van Kreveld, M. Overmars, and O. Schwarzkopf, *Computational Geometry: Algorithms and Applications*. Springer-Verlag, second ed., 2000.

[43] M. Bassetti and G. A. Erskine, "Closed expression for the electrical field of a two dimensional Gaussian charge," *CERN-ISR-TH/80-06*, 1980.

[44] M. A. Furman, "The electron-cloud effect in the arcs of the LHC," *CERN - LHC Project Report 180*, May 1998.

[45] T. Cormen, C. Leiserson, R. Rivest, and C. Stein, *Introduction To Algorithms*. MIT Press, 2001.

[46] O. Haas, "Electron Cloud Modeling and Coupling to Tracking Codes," *Presentation at the joined CERN/TU Darmstadt e-cloud meeting , 16 December 2013, CERN*.

[47] C. K. Birdsall and A. B. Langdon, *Plasma physics via computer simulation*. New York: Taylor and Francis, first ed., 2005.

[48] G. Iadarola and G. Rumolo, "Electron cloud in the CERN accelerators (PS, SPS, LHC)," *Proceedings of ECLOUD12: Joint INFN-CERN-EuCARD-AccNet Workshop on Electron-Cloud Effects, La Biodola, Isola d'Elba, Italy*, 2012.

[49] G. Maury Cuna, G. Rumolo, F. Zimmermann, and G. Iadarola, "Simulation of electron-cloud heat load for the cold arcs of the Large Hadron Collider," *Proceedings of the IPAC12 International Particle Accelerator Conference, New Orleans, USA*, 2012.

[50] F. Caspers, S. Gilardoni, E. Mahner, G. Rumolo, C. Yin Vallgren, and G. Iadarola, "Comparison between electron cloud build-up measurements and simulations at the cern ps," *Proceedings of the IPAC12 International Particle Accelerator Conference, New Orleans, USA*, 2012.

[51] C. M. Bhat, H. Damerau, S. Hancock, E. Mahner, F. Caspers, G. Iadarola, T. Argyropoulos, and F. Zimmermann, "Dependence of e-cloud on the longitudinal bunch profile: studies in the PS & extension to the HL-LHC," *Proceedings of ECLOUD12: Joint INFN-CERN-EuCARD-AccNet Workshop on Electron-Cloud Effects, La Biodola, Isola d'Elba, Italy*, 2012.

[52] O. S. Bruning, P. Collier, P. Lebrun, S. Myers, R. Ostojic, J. Poole, and P. Proudlock, *LHC Design Report*. Geneva: CERN, 2004.

[53] K. Wille, *The Physics of Particle Accelerators: An Introduction*. The Physics of Particle Accelerators: An Introduction, Oxford University Press, 2000.

[54] G. Arduini, D. Banfi, J. Barranco, H. Bartosik, R. Bruce, O. Bruning, R. Calaga, F. Cerutti, H. Damerau, R. De Maria, L. Esposito, L. Fartoukh, M. Fitterer, M. Garoby, S. Gilardoni, M. Giovannozzi, G. Goddard, G. Gorini, M. Lamont, E. . Metral, N. Mounet, T. Pieloni, S. Redaelli, L. Rossi, G. Rumolo, E. Todesco, R. Tomas, F. Zimmermann, and A. Valishev, "How to Maximize the HL-LHC performance," *Proceedings of the Review of the LHC and Injector Upgrade Plans Workshop (RLIUP), 29-31 October 2013 Archamps, Switzerland*.

[55] M. Kuhn, G. Arduini, J. Emery, A. Guerrero, W. Höfle, V. Kain, F. Roncarolo, M. Sapinsky, M. Shaumann, and R. Steinhagen, "LHC Emittance Preservation during the 2012 Run," *Proceedings of the Evian 2012 LHC Beam Operation Workshop, Evian, France*, 2012.

[56] G. Rumolo, O. Dominguez, and F. Zimmermann, "E-cloud simulations for SPS (update)," *Presentation at the SPS Upgrade Study Team Meeting, 16 Dec. 2010, CERN*.

[57] A. N. Andronov, A. S. Smirnov, I. D. Kaganovich, E. A. Startsev, Y. Raitses, and V. I. Demidov, "Secondary electron emission yield in the limit of low electron energy," *Proceedings of ECLOUD12: Joint INFN-CERN-EuCARD-AccNet Workshop on Electron-Cloud Effects, La Biodola, Isola d'Elba, Italy*, 2012.

[58] M. Belhaj, J. Roupie, O. Jbara, J. Puech, N. Balcon, and D. Payan, "Electron emission at very low electron impact energy: experimental and Monte-Carlo results," *Proceedings of ECLOUD12: Joint INFN-CERN-EuCARD-AccNet Workshop on Electron-Cloud Effects, La Biodola, Isola d'Elba, Italy*, 2012.

[59] V. Baglin, J. Bojko, O. Gröbner, B. Henrist, N. Hilleret, C. Scheuerlein, and M. Taborelli, "The Secondary Electron Yield of Technical Materials and its Variation with Surface Treatments," *Proceedings of the 7th European Particle Accelerator Conference, Vienna, Austria*, 2000.

[60] J. Jimenez, G. Arduini, V. Baglin, G. Bregliozzi, P. Chiggiato, S. Claudet, and G. Lanza, "Vacuum and Cryogenics observations for different bunch spacing," *Proceedings of the Chamonix 2011 Workshop on LHC Performance, Chamonix, France*, 2011.

[61] G. Arduini, V. Baglin, H. Bartosik, G. Bregliozzi, P. Chiggiato, S. Claudet, O. Domínguez, J. Jimenez, G. Lanza, K. Li, H. Maury, E. Métral, T. Pieloni, F. Roncarolo, G. Rumolo, B. Salvant, L. Tavian, F. Zimmermann, and U. Iriso, "Beam observations with different bunch spacing and overall synthesis," *Proceedings of the Chamonix 2011 Workshop on LHC Performance, Chamonix, France*, 2011.

[62] G. Arduini, E. Métral, F. Zimmermann, E. Shaposhnikova, S. Claudet, L. Tavian, V. Baglin, G. Bregliozzi, J. Jimenez, and G. Lanza, "50 and 75 ns operation in the LHC: Vacuum and Cryogenics observations," *CERN-ATS-Note-2011-046 MD*, 2011.

[63] B. Goddard, G. Arduini, V. Baglin, W. Bartmann, H. Bartosik, P. Baudrenghien, C. Bracco, G. Bregliozzi, S. Claudet, K. Cornelis, L. Drosdal, W. Höfle, D. Jacquet, L. Jensen, J. Jimenez, V. Kain, G. Lanza, K. Li, M. Meddahi, E. Métral, G. Rumolo, B. Salvant, E. Shaposhnikova, L. Tavian, J. Uythoven, D. Valuch, W. Venturini, and J. Wenninger, "Injection into LHC of bunches at 25 ns spacing," *CERN-ATS-Note-2011-050 MD*, 2011.

[64] H. Bartosik and W. Höfle, "Analysis of bunch by bunch oscillations with bunch trains at injection into LHC at 25 ns bunch spacing," *CERN-ATS-Note-2012-027 MD (LHC)*, 2012.

[65] O. Domínguez, K. Li, G. Arduini, E. Métral, G. Rumolo, F. Zimmermann, and H. M. Cuna, "First electron-cloud studies at the large hadron collider," *Phys. Rev. ST Accel. Beams*, vol. 16, p. 011003, Jan 2013.

[66] G. Rumolo, G. Arduini, V. Baglin, H. Bartosik, N. Biancacci, P. Baudrenghien, G. Bregliozzi, P. Chiggiato, S. Claudet, R. De Maria, J. Esteban-Müller, M. Favier, C. Hansen, W. Höfle, J. M. Jimenez, V. Kain, G. Lanza, K. S. B. Li, G. H. I. Maury Cuna, E. Métral, G. Papotti, T. Pieloni, F. Roncarolo, B. Salvant, E. N. Shaposhnikova, R. J.

Steinhagen, L. J. Tavian, D. Valuch, W. Venturini Delsolaro, F. Zimmermann, U. Iriso, O. Domínguez, E. Koukovini-Platia, N. Mounet, C. Zannini, and C. M. Bhat, "Electron Cloud observation in the LHC," *Proceedings of the IPAC11 International Particle Accelerator Conference, San Sebastian, Spain*, Sep 2011.

[67] J. F. Esteban Müller, P. Baudrenghien, T. Mastoridis, G. Papotti, E. Shaposhnikova, and D. Valuch, "Electron cloud observations through synchronous phase measurements," *CERN-ATS-Note-2012-036 PERF*, 2012.

[68] G. Rumolo, G. Iadarola, O. Domínguez, G. Arduini, H. Bartosik, S. Claudet, J. Esteban-Müller, F. Roncarolo, E. Shaposhnikova, and L. Tavian, "Electron Cloud Effects in the LHC in 2011," *Proceedings of the Evian 2011 LHC Beam Operation Workshop, Evian, France*, 2011.

[69] G. Rumolo, G. Iadarola, O. Domínguez, G. Arduini, H. Bartosik, S. Claudet, J. Esteban Müller, F. Roncarolo, E. Shaposhnikova, and L. Tavian, "LHC experience with different bunch spacings in 2011 (25, 50 and 75 ns)," *Proceedings of the Chamonix 2012 Workshop on LHC Performance, Chamonix, France*, 2012.

[70] G. Arduini, H. Bartosik, N. Biancacci, X. Buffat, O. Dominguez, G. Iadarola, E. Métral, G. Rumolo, B. Salvant, C. Zannini, F. Roncarolo, J. Esteban Müller, W. Höfle, E. Shaposhnikova, D. Valuch, S. Cettour-Cave, V. Kain, S. Redaelli, M. Barnes, W. Bartmann, C. Bracco, B. Goddard, S. Claudet, L. Tavian, V. Baglin, G. Bregliozzi, R. Kersevan, and G. Lanza, "25 ns studies in the LHC – MD held on 14/10/2011," *CERN-ATS-Note-2012-042 MD*, 2012.

[71] J. F. Esteban-Müller, P. Baudrenghien, G. Iadarola, T. Mastoridis, G. Papotti, G. Rumolo, E. Shaposhnikova, and D. Valuch, "Synchronous Phase Shift at LHC," *Proceedings of ECLOUD12: Joint INFN-CERN-EuCARD-AccNet Workshop on Electron-Cloud Effects, La Biodola, Isola d'Elba, Italy*, 2012.

[72] H. Bartosik, W. Höfle, G. Iadarola, Y. Papaphilippou, and G. Rumolo, "Benchmarking HEADTAIL with electron cloud instabilities observed in the LHC," *Proceedings of ECLOUD12: Joint INFN-CERN-EuCARD-AccNet Workshop on Electron-Cloud Effects, La Biodola, Isola d'Elba, Italy*, 2012.

[73] G. Iadarola, G. Arduini, H. Bartosik, and G. Rumolo, "Electron Cloud Effects in 2012 in the LHC," *Proceedings of the Evian 2012 LHC Beam Operation Workshop, Evian, France*, 2012.

[74] J. Esteban Müller and E. Shaposhnikova, "Synchronous phase measurements in the LHC for electron cloud observations," *CERN-ACC-NOTE-2013-0007*, 2013.

[75] G. Iadarola, G. Arduini, V. Baglin, H. Bartosik, J. Esteban Müller, G. Rumolo, E. Shaposhnikova, L. Tavian, F. Zimmermann, O. Domínguez, and G. Maury Cuna, "Electron Cloud and Scrubbing Studies for the LHC," *Proceedings of the IPAC13 International Particle Accelerator Conference, Shanghai, China*, 2013.

[76] G. Iadarola, G. Arduini, H. Bartosik, and G. Rumolo, "Elecron cloud effects," *Presentation at 2-day internal review of LHC performance limitations during run I, 25-26. September 2013, CERN*.

[77] M. Lamont, "The first years of LHC operation for luminosity production," *Proceedings of the IPAC13 International Particle Accelerator Conference, Shanghai, China*, 2013.

[78] R. Jacobsson, "Future wishes and constraints from the experiments at the LHC for the proton-proton program," *Proceedings of the ICFA Mini-Workshop on Beam-Beam Effects in Hadron Colliders (BB2013), Cern, Switzerland*, 2013.

[79] H. Bartosik, G. Arduini, T. Argyropoulos, T. Bohl, S. Cettour-Cave, K. Cornelis, J. Esteban Muller, W. Hofle, Y. Papaphilippou, G. Rumolo, B. Salvant, and E. Shaposhnikova, "Increasing instability thresholds in the SPS by lowering transition energy," *Proceedings of the IPAC12 International Particle Accelerator Conference, New Orleans, USA*, 2012, and references therein.

[80] Y. Papaphilippou, G. Arduini, T. Argyropoulos, W. Bartmann, H. Bartosik, T. Bohl, C. Bracco, S. Cettour-Cave, K. Cornelis, L. Drosdal, J. Esteban Müller, B. Goddard, A. Guerrero, W. Höfle, V. Kain, G. Rumolo, B. Salvant, E. Shaposhnikova, H. Timko, D. Valuch, G. Vanbavinckhove, J. Wenninger, and E. Gianfelice-Wendt, "Operational Performance of the LHC Proton Beams with the SPS Low Transition Energy Optics," *Proceedings of the IPAC13 International Particle Accelerator Conference, Shanghai, China*, 2013.

[81] O. Domínguez, *Electron cloud studies for the LHC and future proton colliders*. PhD thesis, Ecole Polytechnique, Lausanne, Sep 2013.

[82] G. Arduini, T. Bohl, K. Cornelis, W. Höfle, E. Métral, and F. Zimmermann, "Beam observations with electron cloud in the CERN PS and SPS complex," *31st Advanced ICFA Beam Dynamics Workshop on Electron-Cloud Effects, Napa, CA, USA*, Apr 2005.

[83] G. Rumolo and F. Zimmermann, "Electron cloud simulations: beam instabilities and wakefields," *Phys. Rev. ST Accel. Beams*, vol. 5, p. 121002, Dec 2002.

[84] M. J. Barnes, "Update on MKI Vacuum, Proposal for 25ns MD, and Outlook," *Presentation at LHC Machine Committee (LMC) meeting, 2 October 2012, CERN*.

[85] H. Damerau, A. Findlay, S. Gilardoni, and S. Hancock, "RF Manipulations for Higher Brightness LHC-Type Beams," *Proceedings of the IPAC13 International Particle Accelerator Conference, Shanghai, China*, 2013.

[86] G. Rumolo, G. Iadarola, H. Bartosik, and G. Arduini, "Possible strategy for scrubbing LHC for 25 ns operation," *Presentation at LHC Machine Committee (LMC) meeting, 27 November 2013, CERN*.

[87] R. Bossart, J. Bosser, L. Burnod, R. Coisson, E. D'Amico, A. Hofmann, and J. Mann, "Observation of visible synchrotron radiation emitted by a high-energy proton beam at the edge of a magnetic field," *Nuclear Instruments and Methods*, vol. 164, no. 2, pp. 375 – 380, 1979.

[88] G. Iadarola and G. Rumolo, "Electron cloud build-up in the inner triplets (IP1-5)," *Presentation at Electron Cloud meeting, 10 September 2013, CERN*.

[89] G. Iadarola, O. Dominguez, and G. Rumolo, "e-cloud in 800mm chamber in IP2," *LHC Background Study Group meeting 19 March 2012, CERN*.

[90] R. Cappi, M. Giovannozzi, E. Métral, G. Métral, G. Rumolo, and F. Zimmermann, "Electron cloud buildup and related instability in the cern proton synchrotron," *Phys. Rev. ST Accel. Beams*, vol. 5, p. 094401, Sep 2002.

[91] R. Steerenberg, G. Arduini, E. Benedetto, A. Blas, W. Höfle, E. Métral, M. Morvillo, C. Rossi, and C. Rumolo, "Nominal LHC Beam Instability Observations in the CERN Proton Synchrotron," *Proceedings of the 22nd Particle Accelerator Conference, Albuquerque, NM, USA*, 2007.

[92] E. Mahner, T. Kroyer, and F. Caspers, "Electron cloud detection and characterization in the cern proton synchrotron," *Phys. Rev. ST Accel. Beams*, vol. 11, p. 094401, Sep 2008.

[93] S. Gilardoni, S. Bart Pedersen, C. Bertone, N. Biancacci, A. Blas, S. Damjanovic, D. Bodart, J. Borburgh, P. Chiggiato, H. Damerau, J. Devine, T. Dobers, M. Gourber-Pace, S. Hancock, A. Huschauer, G. Iadarola, L. Lopez Hernandez, A. Masi, S. Mataguez, E. Métral, M. Paoluzzi, S. Persichelli, S. Pittet, C. Rossi, S. Roesler, G. Rumolo, B. Salvant, R. Steerenberg, G. Sterbini, J. Vollaire, R. Wasef, L. Ventura, C. Yin Vallgren, and M. Migliorati, "The PS Upgrade Program: Recent Advances," *Proceedings of the IPAC13 International Particle Accelerator Conference, Shanghai, China*, 2013.

[94] G. Iadarola, H. Damerau, S. Gilardoni, G. Rumolo, G. Sterbini, C. Yin Vallgren, M. Pivi, and S. Rioja-Fuentelsaz, "Electron Cloud Studies for the Upgrade of the CERN PS," *Proceedings of the IPAC13 International Particle Accelerator Conference, Shanghai, China*, 2013.

[95] S. Rioja Fuentelsaz, G. Iadarola, and G. Rumolo, "Electron Cloud Studies for the PS," *Presentation at LIU-PS meeting, 6 August 2013, CERN*.

[96] G. Iadarola, H. Bartosik, H. Damerau, S. Rioja Fuentelsaz, S. Pivi, G. Rumolo, and G. Sterbini, "Electron Cloud Studies for the PS," *Presentation at Machine Studies Working Group meeting, 9 April 2013, CERN*.

[97] A. Blas, S. Gilardoni, and G. Sterbini, "Beam Tests and Plans for the Cern PS Transverse Damper System," *Proceedings of the IPAC13 International Particle Accelerator Conference, Shanghai, China*, 2013.

[98] H. Damerau, S. Hancock, T. Kroyer, E. Mahner, and M. Schokker, "Electron Cloud Mitigation by Fast Bunch Compression in the CERN PS," *Proceedings of the 11th European Particle Accelerator Conference, Genoa, Italy*, 2008.

[99] G. Arduini, "Observations in the SPS: beam emittance, instabilities," *10th Workshop on LEP-SPS Performance, Chamonix*, 2000.

[100] J. M. Jiménez, G. Arduini, K. Cornelis, G. Moulard, M. Pivi, and K. Weiss, "Electron cloud: SPS vacuum observations with LHC type beams," *10th Workshop on LEP-SPS Performance, Chamonix, France*, Jan 2000.

[101] G. Arduini, "Observations on transverse instabilities," *Proceedings of the Chamonix XI LHC workshop, Chamonix, France*, 2001.

[102] M. Jiménez, "SPS vacuum observations and electron scrubbing with LHC beams," *11th Workshop of the LHC, Chamonix, France*, 2001.

[103] G. Arduini, K. Cornelis, W. Höfle, G. Rumolo, and F. Zimmermann, "Transverse Behaviour of the LHC Proton Beam in the SPS: an Update," *19th IEEE Particle Accelerator Conference, Chicago, IL, USA*, Jun 2001.

[104] G. Arduini, "Electron cloud and ion effects," *8th European Particle Accelerator Conference, Paris, France*, Jun 2002.

[105] K. Cornelis, "The Electron Cloud Instability in the SPS," *Mini Workshop on Electron Cloud Simulations for Proton and Positron Beams, CERN, Geneva, Switzerland*, 2002.

[106] G. Arduini, P. Baudrenghien, T. Bohl, P. Collier, K. Cornelis, W. Höfle, T. P. R. Linnecar, E. Shaposhnikova, J. Tückmantel, and J. Wenninger, "Status of the LHC proton beam in the CERN SPS," *CERN-SL-2002-054-OP*, Jun 2002.

[107] G. Arduini, P. Collier, B. Dehning, G. Ferioli, B. Henrist, L. Jensen, J. M. Jimenez, J. M. Laurent, R. Rumolo, K. Weiss, and F. Zimmermann, "Measurement of the electron cloud properties by means of a multistrip detector in the CERN SPS," *8th European Particle Accelerator Conference, Paris, France*, Jun 2002.

[108] J. M. Jiménez, G. Arduini, V. Baglin, P. Collier, G. Ferioli, H. Henrist, N. Hilleret, B. Jenninger, L. Jensen, J. M. Laurent, A. Rossi, K. Weiss, and F. Zimmermann, "Electron Cloud Studies and Analyses at SPS for LHC-Type Beams," *20th IEEE Particle Accelerator Conference, Portland, OR, USA*, May 2003.

[109] K. Cornelis, "LHC Beams in the SPS: The Way Through the Clouds," *Workshop on LHC performance, Chamonix, France*, Mar 2003.

[110] G. Arduini, K. Cornelis, W. Höfle, G. Rumolo, and F. Zimmermann, "The Electron Cloud Instability of the LHC Beam in the CERN SPS," *20th IEEE Particle Accelerator Conference, Portland, OR, USA*, Jun 2003.

[111] G. Arduini, P. Baudrenghien, T. Bohl, P. Collier, K. Cornelis, W. Höfle, T. P. R. Linnecar, E. Shaposhnikova, J. Tückmantel, and J. Wenninger, "The LHC Proton Beam in the CERN SPS: an Update," *20th IEEE Particle Accelerator Conference, Portland, OR, USA*, Jun 2003.

[112] J. M. Jiménez, G. Arduini, P. Collier, G. Ferioli, B. Henrist, N. Hilleret, L. Jensen, J. M. Laurent, K. Weiss, and F. Zimmermann, "Electron Cloud Studies and Beam Scrubbing Effect in the SPS," Tech. Rep. LHC-Project-Report-634. CERN-LHC-Project-Report-634, CERN, Geneva, Apr 2003.

[113] G. Arduini, "LHC beams in the SPS: where do we stand?," *1st LHC Project Workshop, Chamonix, France*, Jan 2004.

[114] D. Schulte and F. Zimmermann, "Electron cloud build-up simulations using ecloud," *31st Advanced ICFA Beam Dynamics Workshop on Electron-Cloud Effects, Napa, CA, USA*, 2004.

[115] G. Arduini, V. Baglin, T. Bohl, B. Jenninger, M. Jiménez, J. M. Laurent, D. Schulte, F. Ruggiero, and F. Zimmermann, "Electron-Cloud Build-Up Simulations and Experiments at CERN," *9th European Particle Accelerator Conference, Lucerne, Switzerland*, Aug 2004.

[116] J. M. Jiménez, "The latest news on electron cloud and vacuum effects," *1st LHC Project Workshop, Chamonix, France*, Jan 2004.

[117] E. Benedetto, G. Rumolo, D. Schulte, and F. Zimmermann, "Simulated Emittance Growth due to Electron Cloud for SPS and LHC," *9th European Particle Accelerator Conference, Lucerne, Switzerland*, Aug 2004.

[118] J. M. Jiménez, B. Henrist, N. Hilleret, J. M. Laurent, D. Schulte, and F. Zimmermann, "LHC and SPS Electron Cloud Studies," *AIP Conf. Proc.*, vol. 773, 2005.

[119] D. Schulte, G. Arduini, V. Baglin, J. M. Jimenez, and F. Zimmermann, "Electron Cloud Measurements in the SPS in 2004," *Proceedings of the 21st IEEE Particle Accelerator Conference, Knoxville, TN, USA*, 2005.

[120] E. Benedetto, G. Arduini, B. Feng, G. Franchetti, A. F. Ghalam, T. C. Katsouleas, K. Ohmi, F. Roncarolo, G. Rumolo, and F. Zimmermann, "Effect of Lattice and Electron Distribution in Electron-Cloud Instability Simulations for the CERN SPS and LHC," *21st IEEE Particle Accelerator Conference, Knoxville, TN, USA*, Jul 2005.

[121] G. Rumolo, G. Arduini, E. Métral, E. Chapochnikova, R. Calaga, G. Papotti, and B. Salvant, "Experimental studies on the SPS electron cloud," *CARE-HHH-APD Workshop on Finalizing the Roadmap for the Upgrade of the CERN and GSI Accelerator Complex, CERN, Geneva, Switzerland*, 2008.

[122] G. Rumolo, G. Arduini, E. Benedetto, R. Calaga, E. Métral, G. Papotti, B. Salvant, and E. Shaposhnikova, "Experimental Study of the Electron Cloud Instability at the CERN SPS," *11th European Particle Accelerator Conference, Genoa, Italy*, Aug 2008.

[123] G. Rumolo, G. Arduini, E. Métral, E. Shaposhnikova, E. Benedetto, R. Calaga, G. Papotti, and B. Salvant, "Dependence of the Electron-Cloud Instability on the Beam Energy," *Phys. Rev. Lett.*, vol. 100, p. 144801, 2008.

[124] G. Rumolo, "Simulation study of electron cloud build up in the SPS MKD kickers," *CERN-BE-Note-2009-029*, Aug 2009.

[125] E. N. Shaposhnikova, G. Arduini, J. Axensalva, E. Benedetto, S. Calatroni, P. Chiggiato, K. Cornelis, P. Costa-Pinto, B. Henrist, J. M. Jiménez, E. Mahner, G. Rumolo, M. Taborelli, and C. Yin Vallgren, "Experimental Studies of Carbon Coatings as Possible Means of Suppressing Beam Induced Electron Multipacting in the CERN SPS," *Particle Accelerator Conference 2009, Vancouver, Canada*, May 2009.

[126] G. Rumolo, "Electron cloud effects for PS2, SPS and LHC," *Final CARE-HHH Workshop on Scenarios for the LHC Upgrade and FAIR, Chavannes-de-Bogis, Switzerland*, 2009.

[127] J. R. Thompson, J. M. Byrd, W. HÃ¶fle, and G. Rumolo, "Initial results of simulation of a damping system for electron cloud-driven instabilities in the cern sps," *Particle Accelerator Conference 2009, Vancouver, Canada*, May 2009.

[128] J. D. Fox, T. Mastorides, G. Ndabashimiye, C. H. Rivetta, D. Van Winkle, J. Xu, J. M. Byrd, J. L. Vay, W. Höfle, G. Rumolo, and R. de Maria, "Feedback techniques and sps ecloud instabilities - design estimates. feedback techniques and ecloud instabilites - design estimates," *Particle Accelerator Conference 2009, Vancouver, Canada*, May 2009.

[129] C. Yin Vallgren, P. Chiggiato, P. Costa Pinto, H. Neupert, G. Rumolo, E. Shaposhnikova, M. Taborelli, and S. Kato, "Performance of Carbon Coatings for Mitigation of Electron Cloud in the SPS," *2nd International Particle Accelerator Conference, San Sebastian, Spain*, Dec 2011.

[130] C. Yin Vallgren, S. Calatroni, P. Chiggiato, P. Costa Pinto, H. Neupert, M. Taborelli, G. Rumolo, E. Shaposhnikova, and W. Vollenberg, "Recent Experimental Results on Amorphous Carbon Coatings for Electron Cloud Mitigation," *49th ICFA Advanced Beam Dynamics Workshop on Electron Cloud Physics, Ithaca, New York, Usa*, Oct 2011.

[131] C. Yin Vallgren, G. Arduini, J. Bauche, S. Calatroni, P. Chiggiato, K. Cornelis, P. Costa Pinto, B. Henrist, E. Metral, H. Neupert, G. Rumolo, E. Shaposhnikova, and M. Taborelli, "Amorphous carbon coatings for the mitigation of electron cloud in the CERN Super Proton Synchrotron," *Phys. Rev. Spec. Top. Accel. Beams*, vol. 14, p. 071001. 11 p, Jul 2011.

[132] S. Federmann, F. Caspers, and E. Mahner, "Measurements of electron cloud density in the CERN Super Proton Synchrotron with the microwave transmission method," *Phys. Rev. Spec. Top. Accel. Beams*, vol. 14, no. 1, p. 012802, 2011.

[133] G. Iadarola, H. Bartosik, M. Driss Mensi, H. Neupert, G. Rumolo, and M. Taborelli, "Recent Electron Cloud Studies in the SPS," *Proceedings of the IPAC13 International Particle Accelerator Conference*, 2013.

[134] G. Iadarola and G. Rumolo, "Recent electron cloud simulation studies for the SPS," *Presentation at LIU-SPS Electron Cloud Review, 11 January 2012, CERN*.

[135] R. Garoby, S. Hancock, and J. L. Vallet, "Demonstration of Bunch Triple Splitting in the CERN PS," Aug 2000.

[136] H. Bartosik, T. Argyropoulos, G. B, G. Iadarola, G. Rumolo, and E. Shaposhnikova, " Can we ever reach the HL-LHC requirements with injectors?," *Proceedings of the Review of the LHC and Injector Upgrade Plans Workshop (RLIUP), 29-31 October 2013 Archamps, Switzerland*.

[137] S. Fartoukh, "Micro-batch filling scheme for pacman cancellation," *Presentation at HL-LHC / LIU Joint Workshop, 30 March 2012, CERN*.